LEABHARLANN CHOLÁISTE NA TRÍONÓIDE, BAILE ÁTHA CLIATH | TRINITY COLLEGE LIBRARY DUBLIN
Ollscoil Átha Cliath | The University of Dublin

Terms and Conditions of Use of Digitised Theses from Trinity College Library Dublin

Copyright statement

All material supplied by Trinity College Library is protected by copyright (under the Copyright and Related Rights Act, 2000 as amended) and other relevant Intellectual Property Rights. By accessing and using a Digitised Thesis from Trinity College Library you acknowledge that all Intellectual Property Rights in any Works supplied are the sole and exclusive property of the copyright and/or other IPR holder. Specific copyright holders may not be explicitly identified. Use of materials from other sources within a thesis should not be construed as a claim over them.

A non-exclusive, non-transferable licence is hereby granted to those using or reproducing, in whole or in part, the material for valid purposes, providing the copyright owners are acknowledged using the normal conventions. Where specific permission to use material is required, this is identified and such permission must be sought from the copyright holder or agency cited.

Liability statement

By using a Digitised Thesis, I accept that Trinity College Dublin bears no legal responsibility for the accuracy, legality or comprehensiveness of materials contained within the thesis, and that Trinity College Dublin accepts no liability for indirect, consequential, or incidental, damages or losses arising from use of the thesis for whatever reason. Information located in a thesis may be subject to specific use constraints, details of which may not be explicitly described. It is the responsibility of potential and actual users to be aware of such constraints and to abide by them. By making use of material from a digitised thesis, you accept these copyright and disclaimer provisions. Where it is brought to the attention of Trinity College Library that there may be a breach of copyright or other restraint, it is the policy to withdraw or take down access to a thesis while the issue is being resolved.

Access Agreement

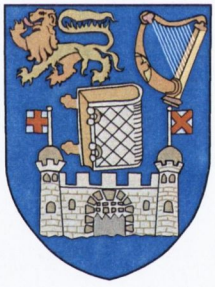
By using a Digitised Thesis from Trinity College Library you are bound by the following Terms & Conditions. Please read them carefully.

I have read and I understand the following statement: All material supplied via a Digitised Thesis from Trinity College Library is protected by copyright and other intellectual property rights, and duplication or sale of all or part of any of a thesis is not permitted, except that material may be duplicated by you for your research use or for educational purposes in electronic or print form providing the copyright owners are acknowledged using the normal conventions. You must obtain permission for any other use. Electronic or print copies may not be offered, whether for sale or otherwise to anyone. This copy has been supplied on the understanding that it is copyright material and that no quotation from the thesis may be published without proper acknowledgement.

Förster Resonant Energy Transfer in Nanocrystal Quantum Dot Structures

by
Manuela Lunz

A thesis submitted for a degree of
Doctor of Philosophy
to the University of Dublin



School of Physics
Trinity College Dublin
University of Dublin
Ireland

December 2010

TRINITY COLLEGE
10 APR 2012
LIBRARY DUBLIN
9395

Declaration

This thesis has not been submitted as an exercise for a degree at this or any other university. The work described in this thesis is entirely my own, with exception of assistance recognised in the acknowledgements and the collaborative work noted in the publications. I agree that Trinity College may lend or copy this thesis on request.

Manuela Lunz

Summary

Förster resonant energy transfer (FRET) is an energy transfer mechanism based on dipole-dipole interactions. FRET occurs in photosynthetic active organisms and is used in artificial structures to create energy flow in sensors, light-harvesting and light-emitting devices. It requires a spectral overlap of the energy donor and acceptor, the reason why semiconductor quantum dots (QDs) with their tunable, discrete energy level structure are ideal building blocks for FRET structures. Most FRET theories have been developed for donor and acceptor molecules, that are much smaller than QDs and don't show an inhomogeneous broadening. Although theoretical investigations have shown that these basic theories can also be used to describe FRET between QDs, only few comparisons of experiment and theory have been reported in literature. However, a detailed analysis and understanding of FRET between QDs are necessary to optimize the above mentioned FRET applications. Therefore, the objective of this thesis is to characterise FRET in different QD structures and to compare the observed trends with theoretical calculations. The layer-by-layer assembled structures discussed here, prepared with CdTe QDs of different sizes acting as energy donors and acceptors, are characterized by steady-state absorption and photoluminescence spectroscopy as well as by time-resolved photoluminescence measurements.

Concentration dependent optical properties were observed for monodispersed QD monolayers, which have been attributed to energy transfer in literature. Modelling with FRET theory clearly shows that these concentration dependent effects are mediated by FRET. Furthermore, it is shown that the probability for FRET in monodispersed structures, which reaches up to 80%, can be controlled by the QD concentration as well as the self-overlap of the QDs' absorption and emission features. The same theory is applied to characterise the dependence of FRET in a mixed donor-acceptor monolayer on the acceptor QD concentration and good agreement with theory is found if the QD size is taken into account in form of exclusion zones around the donors. These exclusion zones limit the FRET efficiency in QD structures, but for high acceptor:donor ratios FRET efficiencies of 90% and FRET rates of up to $(0.5\ \text{ns})^{-1}$ can be achieved due to the large acceptor concentration.

FRET in a separated donor-acceptor QD bilayer structure was also investigated. An unexpected donor concentration dependence of the FRET efficiency is observed. Quantitative agreement with FRET theory can only be achieved when donor intra-ensemble energy transfer is taken into account. Two ways of including donor intra-ensemble energy transfer in theoretical calculations are discussed. FRET rates as fast as $(1.2\ \text{ns})^{-1}$ are measured in the bilayer structure with a minimum donor-acceptor separation of 3.6 nm.

Theories predict that the FRET efficiency and rate can be enhanced by interaction

with surface plasmons. Surface plasmons are supported by gold nanoparticles. To examine the effect of surface plasmons, the impact of the gold nanoparticles on the QD emission must also be characterised. The observed emission and lifetime in an acceptor-gold-donor sandwich structure depend on both the separations between the constituents and the gold nanoparticle concentration. Clear signatures for surface plasmon enhanced FRET are observed and indicate a large enhancement of the FRET rate to $(2.0\ \text{ns})^{-1}$ for a minimum donor-acceptor separation of 22 nm. For comparison a separated donor-acceptor bilayer and a mixed donor-acceptor monolayer on a gold nanoparticle layer are also investigated. Neither of these structures show surface plasmon effects as strong as those observed for the sandwich structure, which is in agreement with theory.

Acknowledgements

At this point I would like to thank all the people who contributed to the success of this thesis in many different ways and who have been very important to me during my four years in Dublin:

My supervisor **Dr. Louise Bradley** for giving me the opportunity to pursue my PhD in this exciting field of nano-photonics, for her advice and all the time we spent discussing data and the physics hidden behind the numbers.

All the people who have been working on the project during my time in Trinity. **Vamsi Komarala** for helping me get started in the lab, with the sample preparation and characterization. **Muamer Kadic** for all his help, ideas and passion to try new things as well as all our scientific and not so scientific discussions. **Loic Bodiou** for his interest in my progress and the discussions about our work. In particular, **Clare Higgins** for being a great colleague and friend. All the students that came to work with us for a few weeks over the summer or longer. And last but not least, **Graham Murphy** and **Xia Zhang**, whom I wish all the best in continuing in my tracks!

All past and current members of the **Semiconductor Photonics Group**. Those involved with work on nanocrystal QDs for their help in the lab and answers to my questions, in particular Yury and Sasha Rakovich as well as Jing Jing Wang for all their support with the confocal. All the others in the group who worked on different topics but still showed interest in what I was doing and sometimes even asked questions about it! To all of you: Thanks for the good time especially at the Photonics conferences in Galway and particularly Kinsale!

The chemistry students on the third floor, who were never tired of answering all our chemistry-related questions. Most of all **Wei-Yu (Tim) Chen, Stephen Byrne** and **Valerie Gerard** in the group of **Prof. Yurii Gun'ko**, who provided us with nanocrystal QDs and never turned down any of our "special" requests. **Deirdre Ledwith** and **Damian Aherne** for preparing metal nanoparticles for some of our surface plasmon experiments.

Dr. Vladimir Lesnyak and **Dr. Nikolai Gaponik** in the Physical Chemistry group at TU Dreseden, Germany for also supplying us with nanocrystal QDs.

Prof. Andrey Rogach and **Dr. Andrei Susha**, City University Hong-Kong, China, for the large stock of colloidal gold nanoparticles.

Robert Gunning for the measurements of the polyelectrolyte layer thickness.

Leona Mulvey at the Centre for Microscopy and Analysis, for the investigation of QD monolayer samples by mass spectroscopy.

The team of technicians in the **workshop**: David Grouse, Pat Murphy, Gordon O'Brien, Dave O'Mahoney and Mick Reilly; for all the "little" bits and pieces they made for our lab. **Ken Concannon** and **Alan O'Meara** for their help with any computer-related issues. **Gillian Gunning** and **Chris Smith** for all the posters they printed for me.

John Kelly, the first point to turn to when trying to find out how to do something or whom to ask; **Una Dowling, Jeanette Cummins, Robbie Gallagher, Marie Kinsella, Rebecca Owens, Ciara Scanlon** and **Colm Stephens** for the answers to all administrative questions.

Clelia Pagano, Egle Passante and **Natacha Vanattou** for the International Dinners (!!!), all their support and the good time we had together.

My flatmates with whom I have been sharing our apartment in the "big yellow house", in particular: **Grainne Egan, Sandra Fickert, Michelle O'Brien, Claire Rubotham** and **Christine Schnell**. Thanks for all the nice chats, cooking together or just hanging out in the living room!

All my friends back in Germany and around the world for keeping in touch despite some very long periods of silence.

Very special thanks go to my parents **Annegret** and **Wolfgang Lunz**, my sister **Christiane** and brother **Andreas** for their never ceasing support, encouragements and listening to me when I needed someone to talk to. It was very reassuring that even though far away I could always count on you.

List of Publications and Conference Contributions

Publications

- *"Two dimensional Förster Resonant Energy Transfer in a Mixed Quantum Dot Monolayer: Experiment and Theory"*; Manuela Lunz, A. Louise Bradley, Wei-Yu Chen and Yurii K. Gun'ko; Journal of Physical Chemistry C **2009**, *113*, pp. 3084-3088

- *"Förster Resonant Energy Transfer in Quantum Dot Structures"*; Manuela Lunz, A. Louise Bradley, Wei-Yu Chen and Yurii K. Gun'ko; IEEE ICTON **2009** proceedings, DOI: 10.1109/ICTON.2009.5185310

- *"Förster Resonant Energy Rransfer in Quantum Dot Layers"*; Manuela Lunz, A. Louise Bradley, Wei-Yu Chen and Yurii K. Gun'ko; PLMCN 9 proceedings, Superlattices and Microstructures **2010**, *47*, pp. 98-102

- *"Influence of Quantum Dot Concentration on Förster Resonant Energy Transfer in Monodispersed Nanocrystal Quantum Dot Monolayers"*; Manuela Lunz, A. Louise Bradley, Wei-Yu Chen, Valerie A. Gerard, Stephen J. Byrne, Yurii K. Gun'ko, Vladimir Lesnyak and Nikolai Gaponik; Physical Review B **2010**, *81*, 205316

- *"FRET in Self-Assembled CdTe Quantum Dot Nanoclusters"*; Clare Higgins, Manuela Lunz, A. Louise Bradley, Valerie A. Gerard, Stephen J. Byrne and Yurii K. Gun'ko; IEEE ICTON **2010** proceedings, DOI: 10.1109/ICTON.2010.5549025

- *"Influence of Intra-Ensemble Energy Transfer on the Properties of Nanocrystal Quantum Dot Structures and Devices"*; Manuela Lunz, A. Louise Bradley, Wei-Yu Chen, Valerie A. Gerard, Stephen J. Byrne, Yurii K. Gun'ko, Vladimir Lesnyak and Nikolai Gaponik; IEEE ICTON **2010** proceedings, DOI: 10.1109/ICTON.2010.5549154

- *"Influence of Localised Surface Plasmons on Energy Transfer between Quantum Dots"*; Manuela Lunz, A. Louise Bradley, Wei-Yu Chen, Valerie A. Gerard, Stephen J. Byrne, Yurii K. Gun'ko, Vladimir Lesnyak, Nikolai Gaponik, Andrei S. Susha and Andrey L. Rogach; IEEE ICTON **2010** proceedings, DOI: 10.1109/ICTON.2010.5549280

- *"Energy Transfer in Colloidal CdTe Quantum Dot Nanoclusters"*; Clare Higgins, Manuela Lunz, A. Louise Bradley, Valerie A. Gerard, Stephen J. Byrne, Yurii K. Gun'ko, Vladimir Lesnyak and Nikolai Gaponik; Optics Express **2010**, *18*, 24486

- *"Concentration Dependence of Förster Resonant Energy Transfer between Donor and Acceptor Nanocrystal Quantum Dot Layers - Impact of Donor-Donor Interactions"*; Manuela Lunz, A. Louise Bradley, Wei-Yu Chen, Valerie A. Gerard, Stephen J. Byrne, Yurii K. Gun'ko, Vladimir Lesnyak and Nikolai Gaponik (submitted for publication in Physical Review B)

Conference Contributions - Oral Presentations and Posters

The name of the person who gave the presentation is underlined if they were not the first author of the submitted contribution.

- *"Off-resonance Surface Plasmon Enhanced Spontaneous Emission from CdTe Quantum Dots"*; Vamsi K. Komarala, Manuela Lunz, Muamer Kadic, A. Louise Bradley, Stephen J. Byrne, Yurii K. Gun'ko, Tony Donnelly, James G. Lunney, Andrei S. Susha, Andrey L. Rogach; International School of Quantum Electronics 44th Course: Advances on nanophotonics, 22nd June - 2nd July 2007, Erice, Italy (poster presentation)

- *"Surface Plasmon Enhanced Spontaneous Emission from CdTe Quantum Dots"*; Manuela Lunz, Muamer Kadic, Vamsi K. Komarala, A. Louise Bradley, Stephen J. Byrne, Yurii K. Gun'ko, Tony Donnelly, James G. Lunney, Andrei S. Susha, Andrey L. Rogach; Photonics Ireland, 24th - 26th September 2007, Galway, Ireland (poster presentation)

- *"Förster Resonant Energy Transfer Between CdTe Quantum Dots Near Gold Nanoparticles"*; Manuela Lunz, Vamsi K. Komarala, Yury Rakovich, A. Louise Bradley, Stephen J. Byrne, Yurii K. Gun'ko, Andrei S. Susha and Andrey L. Rogach; 3rd International Conference on Nanomaterials and Nanomanufacturing, 17th - 18th December 2007, Dublin, Ireland (oral presentation)

- *"Förster Resonant Energy Transfer in a Mixed CdTe Quantum Dot Layer"*; Manuela Lunz, A. Louise Bradley, Tim (Wei-Yu) Chen, Yurii K. Gun'ko; 14th International Conference on Solid Films and Surfaces, 30th June - 4th July 2008, Dublin, Ireland (2nd place in poster competition)

- *"Theory of Förster Resonant Energy Transfer in Two Dimensions Applied to a Mixed Quantum Dot Monolayer"*; Manuela Lunz, A. Louise Bradley, Tim (Wei-Yu) Chen, Yurii K. Gun'ko; Workshop on Optical Properties of Coupled Semiconductor and Metallic Nanoparticles, 21st - 25th July, Dresden, Germany (poster presentation)

- *"Theory of Förster Resonant Energy Transfer in Two Dimensions Applied to a Mixed Quantum Dot Monolayer"*; Manuela Lunz, A. Louise Bradley, Tim (Wei-Yu) Chen and Yurii K. Gunko; 22nd General Conference of the Condensed Matter Division of the European Physical Society, 25th - 29th August 2008, Rome, Italy (poster prize)

- *"Förster Resonant Energy Transfer In a Mixed Quantum Dot Monolayer"*; Manuela Lunz, Louise Bradley, Tim (Wei-Yu) Chen, Yurii K. Gun'ko; Semiconductor and Integrated Optoelectronics (SIOE), 6th - 8th April 2009, Cardiff, Wales (poster presentation)

- *"Förster Resonant Energy Transfer in Quantum Dot Layers"*; Manuela Lunz, A. Louise Bradley, Wei-Yu Chen, Yurii K. Gun'ko; 9th International Conference on Physics of Light-Matter Coupling in Nanostructures, 16th - 20th April 2009, Lecce, Italy (oral presentation)

- *"Förster Resonant Energy Transfer in Quantum Dot Structures"*; Manuela Lunz, A. Louise Bradley, Wei-Yu Chen, Yurii K. Gun'ko; 1st Annual Conference on 'Sub-Wavelength Photonics' of COST MP0702 (in conjunction with ICTON11), 28th June 2nd July 2009, Island of São Miguel, Azores, Portugal (oral presentation)

- *"Tranverse versus Vertical Förster Resonant Energy Transfer: Concentration Dependence in Quantum Dot Layer Structures"*; Manuela Lunz, A. Louise Bradley, Wei-Yu Chen Stephen J. Byrne and Yurii K. Gun'ko; Optics of Excitons in Confined Systems, 7th - 11th September 2009, Madrid, Spain (poster presentation)

- *"Förster Resonant Energy Transfer between Semiconductor Quantum Dot Layers"*; Manuela Lunz, A. Louise Bradley, Wei-Yu Chen and Yurii K. Gun'ko; Photonics Ireland, 14th - 16th September 2009, Kinsale, Ireland (invited presentation)

- *"Concentration Dependence of the Optical Properties of Monodisperse Colloidal Quantum Dot Monolayers"*; Manuela Lunz, Clare Higgins, A. Louise Bradley, Valerie A. Gerard, Stephen J. Byrne, Yurii K. Gun'ko, Vladimir Lesnyak and Nikolai Gaponik; Quantum Dot, 26th - 30th April 2010, Nottingham, England (poster presentation)

- *"Surface Plasmon Effects on Förster Resonant Energy Transfer in Colloidal Quantum Dot Structures"*; Manuela Lunz, A. Louise Bradley, Valerie A. Gerard, Stephen J. Byrne, Yurii K. Gun'ko, Vladimir Lesnyak and Nikolai Gaponik; Quantum Dot, 26th - 30th April 2010, Nottingham, England (oral presentation)

- *"Influence of the Donor Concentration on Förster Resonant Energy Transfer between Donor / Acceptor Quantum Dot Layers"*; Manuela Lunz, A. Louise Bradley,

Valerie A. Gerard, Stephen J. Byrne, Yurii K. Gun'ko, Vladimir Lesnyak and Nikolai Gaponik; Quantum Dot, 26th - 30th April 2010, Nottingham, England (poster presentation)

- *"Influence of Localised Surface Plasmons on Energy Transfer Between Quantum Dots"*; Manuela Lunz, Louise Bradley, Wei-Yu Chen, Valerie A. Gerard, Stephen J. Byrne, Yurii K. Gun'ko, Vladimir Lesynak, Nikolai Gaponik, Andrei S. Susha and Andrey L. Rogach; 2nd Annual Conference on 'Sub-Wavelength Photonics' of COST MP0702 (in conjunction with ICTON12), June 27th - 1st July 2010, Munich, Germany (invited presentation)

- *"Influence of Intra-Ensemble Energy Transfer on the Properties of Nanocrystal Quantum Dot Structures and Devices"*; Manuela Lunz, Louise Bradley, Wei-Yu Chen, Valerie A. Gerard, Stephen J. Byrne, Yurii K. Gun'ko, Vladimir Lesynak, Nikolai Gaponik; 2nd Annual Conference on 'Sub-Wavelength Photonics' of COST MP0702 (in conjunction with ICTON12), Munich, Germany (oral presentation)

- *"FRET in Self-Assembled CdTe Quantum Dot Nanoclusters"*; Clare Higgins, Manuela Lunz, A. Louise Bradley, Valerie A. Gerard, Stephen J. Byrne, Yurii K. Gun'ko, Vladimir Lesnyak and Nikolai Gaponik; 2nd Annual Conference on 'Sub-Wavelength Photonics' of COST MP0702 (in conjunction with ICTON12), June 27th - 1st July 2010, Munich, Germany (oral presentation)

Contents

Declaration i
Summary iii
Acknowledgements v
List of Publications and Conference Contributions vii

1 Motivation **1**

2 Background **5**
2.1 Quantum Dots 6
2.1.1 Optical Properties of Nanocrystal Quantum Dots 6
2.1.2 Applications 9
2.1.3 Surface Plasmon Enhanced Photoluminescence 10
2.2 Förster Resonant Energy Transfer 11
2.2.1 FRET Theory 13
2.2.2 FRET in QD Systems 17
2.2.3 Surface Plasmon Enhanced FRET 20

3 Sample Preparation and Characterization **23**
3.1 Sample preparation 23
3.1.1 Materials 23
3.1.2 Substrate Treatment 26
3.1.3 Principle of Layer-by-Layer Technique 26
3.1.4 Sample Preparation 28
3.2 Absorption 29
3.2.1 Polyelectrolyte Layer Thickness 30
3.2.2 Quantum Dot Concentration 31
3.2.3 Gold Nanoparticle Concentration 34
3.3 Photoluminescence 36
3.3.1 Quantum Yield 38
3.3.2 Förster Radius 40
3.4 Time-resolved Photoluminescence 41

4 FRET in QD Monolayers **45**
4.1 Monodispersed QD Monolayers 46
4.1.1 Concentration Effects on Optical Properties 46
4.1.2 Theoretical modelling 53
4.1.3 Effect of Self-Overlap 56
4.2 Mixed donor - acceptor monolayer 59
4.2.1 Mixed QD Monolayer - One Example 60
4.2.2 Concentration Dependence and Theoretical Modelling 65

4.2.3 Relative Quantum Efficiency 68
4.3 Conclusion 74

5 FRET between separated donor-acceptor QD layers **77**
5.1 FRET in Bilayer Structure 78
5.2 Distance dependence 81
5.2.1 FRET Efficiency and Acceptor Enhancement 83
5.2.2 Relative Quantum Efficiency 85
5.3 Acceptor concentration dependence 87
5.3.1 FRET Efficiency and Acceptor Enhancement 89
5.3.2 Relative Quantum Efficiency 91
5.4 Donor concentration dependence 92
5.4.1 FRET efficiency 95
5.4.2 FRET efficiency in Bilayers with Different Donor QDs 105
5.4.3 Relative Quantum Efficiency 107
5.5 Conclusion 109

6 Surface Plasmon Effects on FRET in QD Structures **111**
6.1 Monodispersed QD Monolayers in Proximity to Gold Nanoparticle Layers 112
6.1.1 Surface Plasmon Effects on Donor QDs 112
6.1.2 Surface Plasmon Effects on Acceptor QDs 117
6.2 Acceptor-Gold-Donor Sandwich Structure 121
6.2.1 Comparison of Different Donor QDs 123
6.2.2 Acceptor-Gold Distance Dependence 127
6.2.3 Gold-Donor Distance Dependence 135
6.2.4 Gold Concentration Dependence 138
6.3 Different Sample Geometries 146
6.3.1 Separate Donor-Acceptor Bilayer on Gold 147
6.3.2 Mixed Donor-Acceptor Monolayer on Gold 151
6.3.3 Comparison 153
6.4 Conclusion 154

7 Conclusions **157**
7.1 Summary of Results 157
7.2 Outlook 161

Appendix **165**
A.1 Quantum Dot Layer Concentration 165
A.2 Quantum Dot Spectra 167

Bibliography **173**

1 Motivation

Climate change, sustainability and carbon footprint are some of the key words of our time. Although claims that we will run low in fossil fuels, such as oil and natural gas, within the 21st century have been revoked [1], it is generally accepted that the generation of electricity by combustion of fossil fuels is one of the most important sources of the greenhouse gas CO_2, the main factor for global warming [2]. Furthermore, it has been discussed that the consequences of the rising global temperature, such as the melting of the polar ice caps and glaciers and the resulting rise in sea level, might not be reversible if temperatures rise by more than 2°C above pre-industrial levels [2, 3, 4]. It has, for example, been predicted that for medium greenhouse gas emissions, the September sea-ice cover in the arctic oceans might disappear well before 2100 [5], which could have drastic ecological and economic effects. A global effort is underway to try to limit the emission of greenhouse gases, with the Kyoto protocol that aimed at a reduction of the greenhouse gases emitted worldwide by at least 5.0% compared to the 1990 levels by 2012 [6]. Negotiations continue on a future agreement for even more drastic reductions in an attempt to keep the rise in the average global temperature below 2°C [7]. In order to realize these goals on minimizing the effects of global warming on the worldwide climate as well as to extend the availability of limited, non-renewable resources, such as fossil fuels, regenerative energy sources and more sustainable means of energy production and consumption have to be explored in greater detail and further developed [1, 2, 8].

The majority of the electricity used worldwide is produced by fossil fuels. In 2008 approximately 66% of the global power was provided by fossil fuels and 14% were generated in nuclear power plants, while renewable energy sources, such as hydropower, geothermal, wind and solar, only provided for a total of 20% [1]. Emphasis on renewable energy sources, such as wind and solar electricity, will improve the sustainability of the global power supply. The efficiency of photovoltaic devices is, however, still relatively low and the manufacturing costs for bulk-type semiconductor solar cells are high. Therefore, many research groups are focusing on increasing the light-to-electricity conversion efficiency and / or reducing the cost of producing solar cells [9]. One idea is to use semiconductor nanocrystal quantum dots (QDs) with tunable, broad absorption bands in solar cells to improve the absorption of sunlight by extending the wavelength range over which the devices are able to absorb light [10, 11]. Furthermore, the QDs can also be used to efficiently funnel the absorbed energy into other parts of the photovoltaic

device via non-radiative Förster resonant energy transfer (FRET) [12, 13], very similar to how energy is brought to the reaction centres in plant leaves or photosynthetic active organisms in nature [14, 15].

It is, however, not only important to produce electricity in a more sustainable way, but reduction of the overall power consumption is also an important factor [1]. Therefore, the development of more effective appliances using less power while maintaining or even improving their performance is essential. Approximately 19% of the power produced worldwide is used for electric lighting [16]. However, most lamps are fitted with incandescent bulbs that are more efficient in generating heat than light. Increasing the efficiency of lamps in converting energy into light will have a large impact on the global energy consumption. Therefore, incandescent bulbs with very poor efficiencies of below 10% and generating light with 10 lm/W (lumen per Watt) have started to be phased out in many countries. Alternative light sources, such as energy saving lamps or high-intensity discharge lamps, offer much better efficiencies. However, the lighting structures with the most promising future are light-emitting diodes (LEDs). Commercially available LEDs already have efficiencies higher than 50%, providing up to 100 lm/W, and continuing research and developement should be able to increase this even further [2, 17, 18]. LEDs also have long lifetimes and by changing the material combination used in these solid-sate lighting structures, the colour of the emitted light can be adjusted easily. However, changing the main material the LED is made of can affect their efficiency. Therefore, it has been suggested to incorporate semiconductor QDs into or to deposit them onto LED structures to generate white light by incorporating QDs with different emission wavelengths [19, 20, 21] or by colour conversion via energy transfer [22, 23, 24].

Semiconductor nanocrystal QDs have unique optical properties [25, 26], such as broad absorption bands and narrow emission, that can be easily tuned by changing their size or material, making them very suitable for applications such as light-emitting and photovoltaic devices, as discussed above. Furthermore, they offer also great advantages for structures in which energy flow is created by FRET, which requires a good spectral overlap to transfer energy from a donor to an acceptor species. FRET can not only be employed for colour conversion and light-harvesting, but this energy transfer mechanism is also used to measure distances on the nano-scale [27, 28] and is the mechanism on which the operation of many nano-sensors is based [29, 30, 31].

To optimize the performance of all these devices it is important to understand FRET in systems in which QDs act as donors and / or acceptors. Since the first experimental report on FRET in a QD solid [32], research has mostly focused on the demonstration of the above mentioned applications as well as on the increase of the FRET rate, discussed in more detail in chapter 2. Therefore, the objective of this thesis is to analyse the factors

influencing FRET in QD structures and, in particular, to determine the differences in comparison to FRET in molecular systems, for which most basic FRET theories have been developed. Furthermore, interaction with surface plasmons, supported by gold nanoparticles, are investigated as means to enhance the range of the FRET interaction between QDs, in terms of the FRET efficiency and rate.

In **chapter 2**, the optical properties of nanocrystal QDs as well as their potential applications are presented. Furthermore, the effect of surface plasmons supported by metal nanoparticles on the photoluminescence of fluorophores, and in particular of QDs, is discussed. In the second part of this chapter, the FRET mechanism is explained and the equations for calculation of the FRET rate and efficiency as used in the subsequent chapters are summarized. Then, FRET in QD structures is discussed, including a summary of applications, an outline of the advantages of QDs over molecular dyes and a detailed review of some of the major reports on FRET in QD structures in the literature. Finally, the current state-of-the-art theoretical and experimental work on surface plasmon enhanced FRET between dyes and QDs is presented.

In **chapter 3** the materials as well as the technique used to prepare the QD layer structures are presented. The first section is followed by a detailed description of the analysis of the measured absorption and photoluminescence spectra as well as the time-resolved photoluminescence decays measured for all samples. In particular, it is explained how the QD and gold nanoparticle concentrations, quantum yield and the Förster radius have been determined from the absorption and photoluminescence spectra.

The experiments on QD monolayers are presented in **chapter 4**. This chapter is divided into two parts. The first part is concerned with monodispersed QD monolayers for which intra-ensemble energy transfer is investigated as a function of the QD concentration as well as the self-overlap of the QD ensemble and compared with FRET theory. In the second part the FRET signatures observed in mixed donor-acceptor QD monolayers are discussed and the acceptor concentration dependence of the FRET efficiency, acceptor enhancement and the overall emission intensity are modelled based on FRET theory.

In **chapter 5** the distance as well as acceptor and donor concentration dependences in a separated donor-acceptor QD bilayer structure are presented. In the comparison with FRET theory the impact of donor intra-ensemble energy transfer on donor-acceptor FRET is highlighted and two ways of including this effect in the basic FRET theory are presented. Furthermore, it is outlined how the influence of the donor concentration on the donor-acceptor FRET efficiency, arising from the competition of these two energy transfer processes, can be reduced.

In the first part of **chapter 6** the impact of surface plasmons, supported by gold nanoparticles, on the optical properties of QD monolayers are discussed. Then, the

experimental results on FRET between donor and acceptor QDs in proximity to gold nanoparticles are presented. In the second part, the distance and gold nanoparticle concentration dependences in a acceptor-gold-donor sandwich structure are characterised in detail. The third and last part of this chapter is concerned with the surface plasmon effects on FRET in a separated donor-acceptor bilayer and a mixed donor-acceptor monolayer on gold. For both structures the distance dependence is presented.

In **chapter 7**, the main conclusions are discussed and some suggestions for future research are outlined.

2 Background

Semiconductor quantum dots (QDs) are semiconductor material with a spatial confinement in three dimensions. Due to this confinement, the allowed electron and hole states are no longer represented by the energy bands typical for semiconductor bulk material, but the the electronic structure of the QDs is described by discrete energy levels [25, 33, 34]. Unlike for one- or two-dimensional confinement in quantum wells and wires respectively, the confinement is "complete" and therefore only few electron and hole pairs can be created in semiconductor QDs at the same time [34]. The physics behind the quantization of the energy levels arising from the confinement can be understood in analogy to the quantum mechanical problem of a particle in a box and has been discussed in detail in books and reviews on QDs, as for example in references [25, 33].

Based on the results for particles trapped in a box potential, one can easily understand that the lowest energy level - corresponding to the first excited energy state of a QD - depends on the material of the QD, influencing the height of the potential well, and the size of the QD, representing the width of the potential well. The relaxation of excitons in QDs to this first excited state occurs usually on the time-scale of picoseconds or faster [35, 36, 37, 38]. The recombination of the excitons in this first excited state can be radiative, causing the different emission colours of QDs with different sizes shown in Figure 2.1, or non-radiative. The discrete, tunable energy levels of the QDs make them interesting fluorophores suitable for use in many different kinds of applications as outlined in section 2.1.2 and in particular also for studies of Förster resonant energy

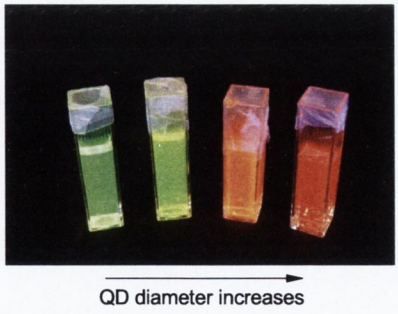


Figure 2.1: Solutions of CdTe nanocrystal quantum dots (QDs) in aqueous solution with different diameters ranging from approximately 2 to 4 nm.

transfer (FRET), as it requires a good overlap between the energy donors and acceptors used, as explained in section 2.2.

2.1 Quantum Dots

Semiconductor QDs can be created in different ways, which are divided into top-down and bottom-up fabrication techniques [25, 33]. QDs can be achieved by strain-driven island growth by molecular beam epitaxy or vapour deposition techniques [33], resulting in high-quality material that can be easily incorporated into semiconductor devices grown by the same techniques. Alternatively, they can be chemically synthesized, where the synthesis is carried out in solution starting with a precursor solution and the growth of the QDs is controlled via the solution temperature as well as the ratio of the different QD material components and the stabilizing ligand [25]. QDs synthesised in the latter way are often referred to as nanocrystal QDs, colloidal QDs or just nanocrystals. The low temperature at which the growth of the colloidal QDs occurs, is favourable for the formation of semiconductor nanocrystals with a low number of lattice defects. This QD preparation technique also offers the possibility to functionalize the QDs by changing their surface chemistry by reactions in solution. Furthermore, with colloidal chemistry high-quality nanocrystals can be prepared at lower costs than by the epitaxial growth techniques and incorporated into optoelectronic devices by spin-coating, drop-casting and as closely-packed films prepared by the Langmuir-Blodgett and layer-by-layer assembly techniques [26, 39, 40].

2.1.1 Optical Properties of Nanocrystal Quantum Dots

The first publications on nanocrystal QDs were published in the 1980s [41, 42, 43, 44]. Since then many advances in the synthesis of colloidal QDs have been reported to increase their quantum yields, for example by adding a shell of a second, wider band-gap material to improve the confinement and the reduce the number of defects at the core surface [45], and to reduce the blinking of QDs, the fluctuation between "on" and "off" states in the emission of a single QD, by increasing the shell thickness or engineering their energy band-gap profile [46, 47, 48].

In this thesis, "core-only" CdTe nanocrystal QDs stabilized by thioglycolic acid (TGA) in aqueous solution, shown in Figure 2.1, were used for the preparation of the FRET structures under investigation. Using "core-only" QDs reduces the QD centre-to-centre separation, which is important for the observation of FRET due to its strong distance dependence, discussed below. Furthermore, CdTe nanocrystals can be synthesized directly in water [49, 50, 51], making them bio-compatible and allowing for a water-based processing, for example with the layer-by-layer (LbL) technique [52, 53] used here and

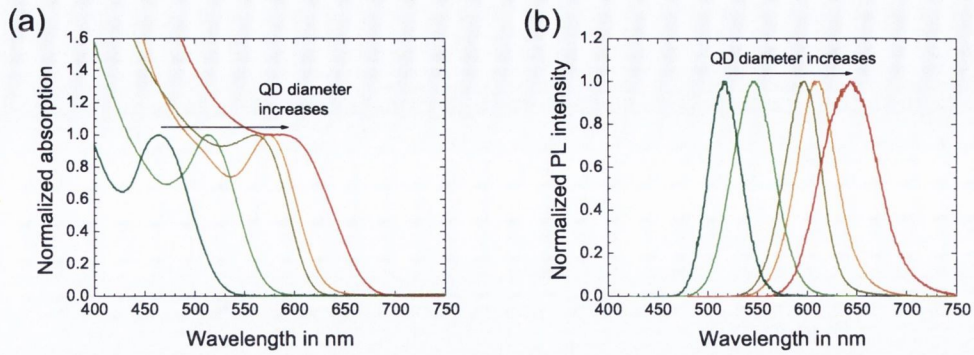


Figure 2.2: (a) Absorption spectra of CdTe quantum dots (QDs) samples in water with different QD diameters. (b) Photoluminescence (PL) spectra of the same QDs in solution as shown in (a) for excitation at 400 nm. The size of the QDs in solution increases for the spectra shown from dark green, light green, dark yellow, orange to red.

discussed in detail in section 3.1 in the next chapter.

Normalized absorption and emission spectra of aqueous CdTe QDs of different sizes are shown in Figure 2.2(a) and (b) respectively. The distinct first absorption peak as well as the emission peak wavelength shift to the red with increasing QD size due to the weaker electron and hole confinement can be clearly observed [25, 26, 51]. By changing the size of the TGA stabilized CdTe QDs from 2 to 5 nm, the QD emission can be tuned in the visible wavelength range from 500 nm to 700 nm [51, 54]. Using a different stabilizer, for example mercaptopropionic acid, the QD size can be further increased, resulting in CdTe QDs emitting at wavelength of up to 800 nm.

The size of the QDs determines the electronic structure and in particular the energy of the 1s-1s transition, reflected in the wavelength position of the first absorption peak. By evaluating the QD size from TEM measurements and comparing it to the wavelength or energy of the first absorption peak, sizing curves for CdTe QDs have been established [55, 51] , and good agreement with theory was found [51]. Empirical expressions for the dependence of the size dependence of the first absorption peak wavelength as well as the extinction coefficient of CdTe QDs have been established [55], so that the size and the concentration of CdTe QDs in solution can be determined from their absorption measurements alone (see also section 3.2.2).

As can be seen in Figure 2.2, the absorption and emission spectra of the QD samples are fairly broad, with values of the full width at half maximum (FWHM) of the order of 30 to 40 nm. Usually, very narrow emission lines would be expected for single QDs, but finite lifetimes, dephasing by low-energy acoustic phonons and scattering at surfaces and defects give rise to a homogeneous broadening of the QD absorption and emission peaks [25]. Moreover, the spectra shown in Figure 2.2 were measured for QD ensembles, that

also show inhomogeneous broadening mainly due to the distribution of sizes present in the nanocrystal ensemble. Furthermore, differences in shape, defect concentration, surface structures, variations in stoichiometry and charge also add to the inhomogeneous broadening [25]. As the inhomogeneous broadening arises mainly from the size distribution present in the sample, the FWHM of the spectral features of the QD ensemble can be reduced by size fractionation methods with size-selective precipitation being the most common procedure, rather than exclusion chromatography or gel electrophoresis [40, 56].

Comparing the peak wavelength of the first absorption peak and the emission of the smallest QDs represented by the dark green line in Figure 2.2, it can be seen that the peak emission at 516 nm (2.403 eV) occurs further to the red than the first absorption peak at 465 nm (2.666 eV). This energy difference is also referred to as the Stokes shift and with a value of 263 meV it is particularly large for this sample compared to values reported in literature [51, 57]. However, it has also been found that the Stokes shift, for the different size fractions of one QD solution, is increasing with decreasing QD size [51, 57]. This explains why such a large Stokes shift is observed for the smallest QDs, whereas those for the other QDs shown in Figure 2.2 are smaller, for example 150 meV for the second smallest QDs (light green line) and 127 meV for the second largest QD sample (orange line). The Stokes shift arises from exciton-phonon interactions as well as electron-hole exchange interactions and is influenced by the crystal fields and the particle shape [25, 26]. These effects lead to a splitting of the lowest excitonic energy level into states with high oscillator strength, to which the energy is absorbed and they therefore feature in the absorption spectrum, and states with a lower energy and smaller oscillator strength, to which energy cannot be absorbed as well as to the absorbing states but to which the excitons relax after excitation so that radiative recombination occurs from this state, which is therefore visible in the emission spectrum [25, 26].

The time-dependent photoluminescence decays for nanocrystals in solution should be mono-exponential, only determined by the intrinsic exciton recombination rate of the nominally monodispersed QD ensemble. However, due to interaction with the environment but mostly as a consequence of the variations of the defect concentration from QD to QD in the ensemble, multi-exponential PL decay traces are commonly observed for CdTe nanocrystal ensembles even in solution [34, 51]. The emission decrease on the short time scales is associated with holes becoming trapped in surface defect states [51, 58, 59]. Typical PL lifetimes for TGA stabilized CdTe QDs range from 10 to 20 ns in solution. For larger CdTe QDs, stabilized with mercaptopropionic acid, even longer PL lifetimes as well as a transition to mono-exponential decays can be observed, as the hole energy level associated with the lowest excitonic state is shifting to energies lower than the hole trap state with increasing nanocrystal size [51].

Reducing the number of defects, mostly located on the surface, by improving the synthesis of the nanocrystals is of great interest as this will not only result in longer PL lifetimes but also larger quantum yields, Q, defined in equation (2.1).

$$Q = \frac{\text{emitted Photons}}{\text{absorbed Photons}} = \frac{k_r}{k_r + k_{nr}} \tag{2.1}$$

Q describes the probability with which an absorbed photon will be emitted by the material and can be determined in comparison to a luminescent standard such as Rhodamine 6G for CdTe QDs [60], as explained in section 3.3.1. The quantum yield can also be expressed in terms of the radiative and non-radiative exciton decay rates k_r and k_{nr} as shown in the second part of equation (2.1). Reducing the defect concentration in the QDs corresponds to a decrease in k_{nr} which consequently increases Q, the probability for radiative decay. Typical quantum yields for the QDs used in this thesis vary from 5% to 45%, but in the state-of-the-art synthesis quantum yields of up to 80% can be achieved for thiol-capped "core-only" CdTe QDs [54].

2.1.2 Applications

As mentioned above, colloidal QDs are attractive luminescent components for applications due to their easy, cost-efficient synthesis and processing. Furthermore they offer many advantages over molecular dyes [61, 62]. First of all, QDs have broad absorption bands, allowing for multiplexing - based on the possibility to excite several, different QDs at the same time - and excitation at wavelengths far enough removed from their emission to avoid contamination of the QD emission signal by excitation light. Moreover, they have a narrow emission band that can be tuned over a large range of wavelengths from the UV to the near Infrared [61], making them ideal for applications where specific spectral emission properties are required, such as in FRET and plasmonic structures discussed below. Furthermore, QDs show a higher photostability than dyes and are less prone to chemical degradation. Additionally, high quantum yields and long emission lifetimes can be achieved as mentioned above.

Therefore, nanocrystal QDs have been proposed to replace molecular dyes in many different types of applications and a few examples are given in the following. Colloidal QDs have, for example, been employed as biological labels [62, 63] and as building blocks for solution based nano-sensors based on FRET, discussed in more detail below, [30, 61]. For fluorescent labelling and nano-sensors, multiplexing has been demonstrated where the signals of different QDs emitting at different wavelength were recorded in a single measurement with a fixed excitation wavelength [63, 64]. Nanocrystal QDs have also been demonstrated as part of optoelectronic devices, such as light emitting diodes [21, 22, 65, 66] and lasers [67], as well as photodetectors [11, 68] and photovoltaic

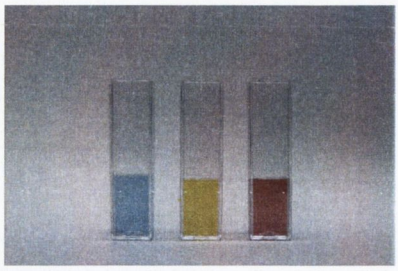


Figure 2.3: Metal nanoparticles in solution (left to right): gold nanoboxes, silver nanoparticles with a diameter of 2 to 3 nm, gold nanoparticles with a diameter of approximately 4 nm.

devices [10, 11, 69], where the QDs are used for the efficient absorption of light that is consecutively transformed into carriers.

2.1.3 Surface Plasmon Enhanced Photoluminescence

It has been suggested that the emission of fluorophores, molecules as well as QDs, can be enhanced in the proximity of metal nanoparticles due to the enhanced field of localized surface plasmon (SP) resonances [70, 71, 72]. The SPs give rise to a new feature in the absorption and scattering spectra compared to the bulk metal, which gives colloidal metal particle solutions their distinct colour, shown in Figure 2.3.

The optical properties of the fluorophore in proximity to the metal nanoparticle are influenced by energy transfer to the particle and the field enhancement arising from the excitation of surface plasmons. Due to the different distance dependences of these processes, emission quenching due to energy transfer is dominating in close proximity to the metal nanoparticle and photoluminescence enhancements will only be observed at a certain separation to the metal nanoparticle where the quenching is small but the field enhancement is still large enough to positively affect the emission of the fluorophores [34, 72]. Therefore, the photoluminescence enhancement depends strongly on the size, shape and material of the metal particle as well as the particle separations and the geometry of the structure investigated. Typical surface plasmon distance dependent effects, including quenching and enhancement, have been observed in experiments with single particles [73, 74] as well as for ensemble measurements with molecules [75] and QDs on metal nano-island films or layers of colloidal metal nanoparticles [76, 77, 78]. For QD layers, a maximum intensity enhancement of 3 to 10 has been observed at separations of 11 and 7 nm on silver nano-island films and gold nanoparticle layers, respectively [76, 77]. However, there have been many more reports on either photoluminescence quenching or enhancement for different types of metal nanoparticles and luminescent materials [79,

80, 81, 82, 83, 84, 85, 86]. An enhancement factor of 30 was observed for the emission of CdSe/ZnS nanocrystals dispersed in a 35 nm thick polymer film on triangular gold nanostructures [83] and a maximum enhancement of the integrated emission intensity by a factor of 33 was reported for samples with CdSe QDs and colloidal gold nanopartices with a diameter of 18 nm [85].

It has been shown that the emission quenching by energy transfer to the metal particle can be described by Förster resonant energy transfer to a surface [80, 81, 84, 86], discussed in section 2.2 below. Emission enhancement can be either attributed to enhanced absorption of the fluorophores for excitation in resonance with the surface plasmon resonance or to enhanced emission for fluorophores emitting at wavelengths of the surface plasmon resonance [87, 88]. Emission enhancement has also been attributed to interaction with the scattering component of the extinction coefficient of the metal nanoparticles [77]. For CdTe nanoparticles, silver nanoparticles can lead to enhanced absorption or pumping while gold nanoparticles could resonantly enhance the emission. It has been suggested that gold and silver nanoparticles could be used to enhance the performance of light-harvesting structures, such as photovoltaic and photosynthetic structures [87, 89].

2.2 Förster Resonant Energy Transfer

Förster Resonant Energy Transfer (FRET) is a non-radiative energy transfer mechanism mediated by dipole-dipole interactions. This mechanism is occurring naturally as part of the light-harvesting process in plants and photosynthetic active bacteria [14, 15], but has also been engineered in artificial structures during the last two decades. The first theoretical description of the process was outlined by Theodor Förster in 1948 [90], who evaluated the electronic coupling between a donor state and a quasi-continuum of acceptor states on the basis of the Fermi Golden rule, and since then it has been widely explored theoretically and experimentally. FRET has, for example, been implemented in energy funneling structures [12, 13, 91, 92, 93], light-emitting devices [20, 22, 23, 24] and sensing structures [29, 30, 31, 94].

The basic idea of FRET is depicted schematically in Figure 2.4. The donor and acceptor states are shown as electron and hole states representing the donor and acceptor as semiconductor quantum dots, but the following description of the FRET process can be applied in the same way to energy transfer between donor and acceptor molecules. In a first step, the donor is excited, for example by light as shown in the schematic (blue wavy arrow), and then relaxes quickly (black arrows) into its first excited state (solid green lines). The radiative or non-radiative decay of the energy from this first excited donor state occurs with an average lifetime $\tau_D = 1/(k_r + k_{nr})$ in the absence of the acceptor. However, if a suitable acceptor with an excited state in resonance (solid green

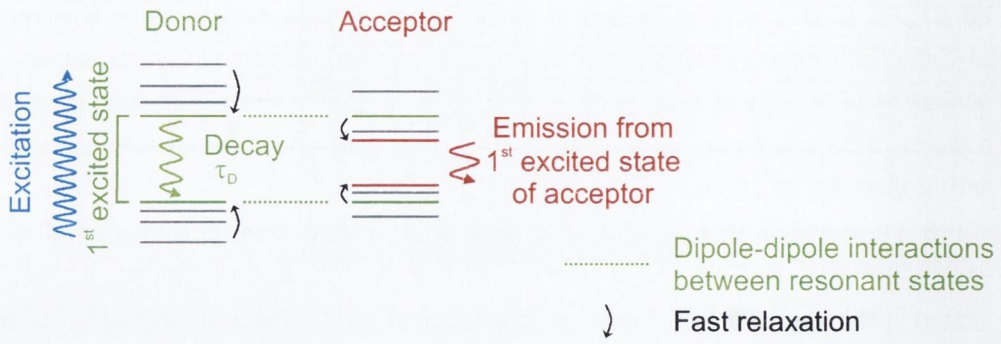


Figure 2.4: Schematic representation of resonant energy transfer from an excited donor (green) to an acceptor (red) via dipole-dipole interactions (dotted lines). The energy relaxation from the higher excited states, after excitation of the donor (indicated by the blue arrow) and the energy transfer to the acceptor, to the respective first excited states (green and red solid lines respectively) occurs on very short time scales and this fast relaxation is indicated by the black arrows.

line) is found in proximity to the donor, the energy from the first excited donor state can be transferred resonantly to this acceptor state with a rate k_{FRET} by dipole-dipole interactions (indicated by the dotted green line). The acceptor relaxes quickly into its first excited state, preventing a back-transfer of the energy to the donor, and then decays either radiatively or non-radiatively.

The prerequisites for this type of non-radiative energy transfer are a spectral overlap of donor and acceptor states, normally the donor emission and the acceptor absorption, and a small separation of the donor and acceptor of the order of 1 to 10 nm [14, 95], due to the strong distance dependence of the FRET process, discussed in the next section. Assuming that fluorescent molecules or particles are used as donors and acceptors, the typical signatures for energy transfer are the observation of a donor emission quenching and an acceptor emission enhancement. In the ideal case the acceptor would not be excited at the same time as the donors, so that in the absence of FRET no acceptor emission would be seen, and any acceptor emission signal could then be used as a direct indication for energy transfer. Furthermore, as FRET represents another decay channel the donor lifetime τ_{DA} in the presence of acceptors is reduced, as can be seen from equation (2.2):

$$\tau_{DA} = \frac{1}{k_r + k_{nr} + k_{\mathrm{FRET}}} = \frac{1}{\tau_D^{-1} + k_{\mathrm{FRET}}} \tag{2.2}$$

The acceptor lifetime τ_{AD} in proximity to a suitable donor may be increased due to the additional pumping by the donors, as the energy transfer can last over longer time-scales than the short excitation pulse normally used for time-resolved emission measurements.

Additionally, if the energy is transferred with a high efficiency, it can also cause the emission of the acceptors to increase even after the excitation has been switched off, resulting in a so-called rise-time in the time-dependence of the acceptor emission. For broad donor and acceptor ensembles, some parts of the donor ensemble might transfer energy more efficiently to a particular part of the acceptor ensemble than others. This will lead to a stronger quenching or enhancement of parts of the donor and acceptor ensembles respectively, so that the energy transfer can also give rise to shifts in the donor and / or acceptor ensemble emission peak wavelength.

Two other important energy transfer mechanisms are radiative energy transfer, when a photon is emitted by the donor and re-absorbed by the acceptor, and tunnelling, which occurs via an exchange mechanism facilitated by the spatial overlap of donor and acceptor wavefunctions [96, 97]. Radiative energy transfer can occur over very long distances but does not cause a decrease of the donor lifetime as the energy is transferred to the acceptor by a photon that has been emitted from the donor with its typical lifetime τ_D, and can therefore be easily distinguished from FRET [14, 95]. Tunnelling, on the other hand, is also giving rise to a lifetime decrease, but shows a different distance dependence than FRET and normally only occurs for donor-acceptor separations on the sub-nanometer scale [96, 97]. For donor-acceptor separations larger than 2 nm, tunnelling can normally be excluded as a possible energy transfer mechanism, but for verification distance or temperature dependent measurements can be carried out to differentiate between tunnelling and FRET [98, 99].

2.2.1 FRET Theory

As mentioned above, energy is transferred via the Förster mechanism from donor to acceptor states in resonance. The resonance of the states is described by the spectral overlap J of the donor emission $I_D(\lambda)$ and the acceptor absorption, determined by its extinction coefficient $\epsilon_A(\lambda)$. The spectral overlap is calculated with equation (2.3) by integration over the area-normalized donor emission $\hat{I}_D(\lambda)$ and $\epsilon_A(\lambda)$.

$$J = \int_0^\infty \epsilon_A(\lambda) \cdot \hat{I}_D(\lambda) \cdot \lambda^4 d\lambda \tag{2.3}$$

The units of J calculated with equation (2.3) are $\frac{\mathrm{nm}^4}{\mathrm{M \cdot cm}}$, if ϵ_A is included in $\mathrm{M}^{-1}\mathrm{cm}^{-1}$ and λ in nm. The typical interaction distance of FRET, the Förster radius R_0, is not only strongly dependent on J but also the donor quantum yield Q_D as can be seen from equation (2.4).

$$R_0 = 0.0211 \cdot \left(\frac{\kappa^2 \cdot Q_D}{n^4} \cdot J \right)^{1/6} \tag{2.4}$$

It furthermore depends on the orientation factor κ^2, typically 2/3 for randomly oriented donor and acceptor dipoles, as well as the refractive index n of the surrounding medium. The Förster radius is calculated with equation (2.4) in nm, by including J in $\frac{\text{nm}^4}{\text{M}\cdot\text{cm}}$.

FRET Between a Single Donor and Acceptor

The FRET rate for energy transfer between a single donor and acceptor, separated by a distance r_{DA}, is equal to the donor decay rate, $\tau_D^{-1} = k_r + k_{nr}$, for $r_{DA} = R_0$ as shown in equation (2.5).

$$k_{\text{FRET}} = \tau_D^{-1} \cdot \left(\frac{R_0}{r_{DA}}\right)^6 \tag{2.5}$$

Typical values for R_0 range between 1 and 10 nm [14, 95] and due to the r_{DA}^{-6} distance dependence of the energy transfer mediated via dipole-dipole interactions, the energy transfer is only observed for donor-acceptor separations on the nanometer length scale. The efficiency of energy transfer via the FRET mechanism, E_{FRET}, is defined as the ratio of the FRET rate, k_{FRET}, over all donor decay rates, as shown in the first part of equation (2.6).

$$E_{\text{FRET}} = \frac{k_{\text{FRET}}}{k_r + k_{nr} + k_{\text{FRET}}} = \frac{k_{\text{FRET}}}{\tau_D^{-1} + k_{\text{FRET}}} = 1 - \frac{\tau_{DA}}{\tau_D} \tag{2.6}$$

By replacing the decay rates with the donor emission lifetimes, as shown in equation (2.6), an expression for E_{FRET} is obtained that can be used to determine the FRET efficiency simply by comparing the donor lifetimes measured for the donor alone, τ_D, and in presence of the acceptor, τ_{DA}. Taking into account the definition of k_{FRET} in equation (2.5), the FRET efficiency can also be written in dependence of R_0 and the donor-acceptor separation, r_{DA}, as shown in equation (2.7).

$$E_{\text{FRET}} = \frac{R_0^6}{R_0^6 + r_{DA}^6} \tag{2.7}$$

Knowing R_0 or carrying out relative measurements for different separations r_{DA}, equation (2.7) can be applied to use the measurement of the FRET efficiency, via the lifetime ratio in equation (2.6), to determine distances on the nanoscale [27, 28]. For $r_{DA} = R_0$, the FRET efficiency is equal to 50%.

FRET Systems with Multiple Acceptors

Equations (2.5) and (2.7) only apply to single donor-acceptor pairs. If a donor can interact with several acceptors, numbered i, k_{FRET} for this one donor is the sum of all FRET rates k_i, representative of the energy transfer to the i^{th} acceptor for a donor-

acceptor separations r_i:

$$k_{\mathrm{FRET}} = \sum_i k_i = \tau_D^{-1} \cdot \sum_i \left(\frac{R_0}{r_i}\right)^6 . \tag{2.8}$$

This means that instead of equation (2.5), equation (2.8) has to be used in a system with multiple acceptors. It also shows, that with increasing number of acceptors around a donor, the energy transfer from this donor becomes faster and therefore more likely.

$$E_{\mathrm{FRET}} = \frac{1}{1 + \left[\sum_i (R_0/r_i)^6\right]^{-1}} \tag{2.9}$$

Equation (2.9), giving the FRET efficiency in the structure with multiple acceptors, shows that unless all donor-acceptor separations r_i are known, the FRET efficiency for structures with multiple acceptors cannot be estimated via R_0.

FRET in Two Dimensions

To characterize the FRET process in planar systems with random donor-acceptor distributions, Wolber and Hudson applied Förster's original theory to a two-dimensional structure by starting with equation (2.8) and integrating over a plane of acceptors [100]. Furthermore, they included an exclusion zone with radius R_{ex} in their calculations, to allow for applications to biological systems in which donors and acceptors can be separated by a minimum distance due to pores or lipid membranes. The equation they obtained for the time-dependent donor intensity $I_{DA}(t)$ in the presence of acceptors is reproduced in equation (2.10). It is including the incomplete Gamma function $\gamma(x, y) = \int_0^y z^{x-1} e^{-z} dz$, arising from the integration over the acceptor plane for radii ranging between R_{ex} and infinity.

$$I_{DA}(t) = \exp\Bigg\{ -\frac{t}{\tau_D} - \pi \cdot R_0^2 \cdot c_{Acc} \cdot \gamma\left(2/3, (R_0/R_{ex})^6 \cdot (t/\tau_D)\right) \cdot \left(\frac{t}{\tau_D}\right)^{1/3} + \pi \cdot R_{ex}^2 \cdot c_{Acc} \cdot \left[1 - e^{-(R_0/R_{ex})^6 \cdot (t/\tau_D)}\right] \Bigg\} \tag{2.10}$$

As can be seen, the donor emission decay (I_{DA}) depends on the undisturbed donor lifetime (τ_D), the acceptor concentration (c_{Acc}), the Förster radius (R_0) and the exclusion zone radius (R_{ex}). The donor decay in absence of acceptors, $I_D(t) = \exp\{-t/\tau_D\}$, is becoming faster due to energy transfer, represented by the negative second term in the exponent shown in equation (2.10). However, due to the exclusion zone, which limits the interaction between donor and the acceptor, the effect of the energy transfer on the

donor decay is reduced, shown by the positive sign of the third term in the exponent. For the evaluation of the efficiency of the process, the yield $q_r = \int I_{DA}dt / \int I_D dt$ can be calculated by numerical integration of equation (2.11). The yield q_r is also equal to the lifetime ratio τ_{DA}/τ_D and is therefore related to the FRET efficiency via $E_{\mathrm{FRET}} = 1 - q_r$.

$$q_r = \int_0^\infty e^{-\lambda} \cdot \exp\left[-\pi \cdot C \cdot \gamma\left(2/3, \lambda/r^6\right) \cdot \lambda^{1/3}\right] \cdot \exp\left[\pi \cdot C \cdot r^2 \cdot \left(1 - e^{-\lambda/r^6}\right)\right] d\lambda \quad (2.11)$$

The q_r in equation (2.11) is written in dependence of a dimensionless concentration $C = c_{Acc} \cdot R_0^2$ and $r = R_{ex}/R_0$, which corresponds to $r = \alpha^{1/6}$ in the original work by Wolber and Hudson [100]. After numerical integration of equation (2.11), q_r can also be approximated by a two-exponential decay in dependence of the concentration C for a particular r. Using equations (2.10) and (2.11) to fit the donor emission decay as well as the concentration dependence of the lifetime ratio $q_r = \tau_{DA}/\tau_D$, information on R_0 and R_{ex} can be obtained from time-resolved donor emission measurements. Furthermore, equations (2.10) and (2.11) can not only be applied to a two-dimensional structure, but they also describe the case of energy transfer between two planes of separated donor and acceptor layers.

Separated Donor-Acceptor Layer Structure

Analytical expressions for the FRET rate and efficiency can also be obtained for FRET in a separated donor-acceptor layer structure. Taking into account homogeneously distributed acceptors in a plane, the sum in equation (2.8) can be converted into the surface-integral shown in equation (2.12):

$$k_{\mathrm{FRET}} = \tau_D^{-1} \cdot c_{Acc} \cdot \int_0^\infty (R_0/r)^6 \, dS \; . \quad (2.12)$$

The integration can be extended to ∞ as the probability for FRET is decreasing quickly with increasing donor-acceptor separation r. Carrying out the integration leads to equation (2.13) for the FRET rate, showing that the typical r^{-6} FRET distance dependence turns into a R_{ex}^{-4} distance dependence for the interaction of a donor with a plane of acceptors.

$$k_{\mathrm{FRET}} = \frac{c_{Acc} \cdot \pi \cdot R_0^6}{2 \cdot R_{ex}^4 \cdot \tau_D} \quad (2.13)$$

In equation (2.13), R_{ex} represents the separation of the donor and acceptor planes, rather than the actual donor-acceptor separation, and, in line with the presentation of the calculations of Wolber and Hudson, indicates the minimum distance between the donors and acceptor in the structure. With the above expression for k_{FRET} and equation

(2.6) the FRET efficiency is calculated to be

$$E_{\mathrm{FRET}} = \frac{1}{1 + \frac{2 \cdot R_{ex}^4}{c_{Acc} \cdot \pi \cdot R_0^6}} \,. \tag{2.14}$$

Equation (2.14) shows that the FRET efficiency in the separated donor-acceptor bilayer structure depends strongly on the donor-acceptor layer separation R_{ex} and the acceptor concentration c_{Acc}, but not the donor concentration c_{Don}.

2.2.2 FRET in QD Systems

As mentioned before, FRET has been used for energy funnelling in light-harvesting structures that mimic photosynthesis and could be used in photovoltaic structures [12, 13, 91, 92, 93]. FRET can also be implemented to achieve colour conversion or to generate white light for light-emitting devices [20, 22, 23, 24]. Furthermore, the change in donor and acceptor emission signatures upon creation of energy flow by FRET or its disruption can be used as a signal in nano-sensors [29, 30, 31, 61, 94, 101, 102]. While these sensors are one-way senors that cannot be reused, schemes have also been proposed for FRET sensors based on conformational or spectral changes due to the binding of a ligand or differences in the surrounding pH [103, 104]. These latter sensors are also able to monitor temporal changes. The earliest FRET structures were created with molecular dyes but recently also many of these applications including QDs as donors and / or acceptors have been proposed and demonstrated.

Molecular Dyes vs. Quantum Dots

As outlined above, QDs offer many advantages over dyes such as higher photostability, broad absorption bands and tunable emission wavelength [61, 62]. Therefore, QDs are very attractive for FRET as the tunable emission wavelengths of the donor QDs and / or broad absorption band of the acceptor QD enables the optimization of the spectral overlap in FRET structures with donor and / or acceptor QDs. Moreover, the tunable optical properties of the QDs also allow for the reduction of cross talk in donor QD - acceptor dye FRET structures. The broad QD absorption bands also cause a parallel excitation of donors and acceptors in FRET assemblies for which QDs are used as donors and acceptors, but this can be taken into account in the FRET analysis by comparing to reference measurements of the emission for pure donor and acceptor samples.

However, there are also some drawbacks in using QDs for FRET. First of all the diameter of the QDs is of the same order of magnitude as the typical Förster radii of 1 to 10 nm [14, 95]. Hence, the QD size limits the minimum separation between donor and acceptor and creates an exclusion zone around the donors which reduces the maximum

FRET rate and efficiency in this system. This limitation can be overcome by creating QD assemblies with high acceptor:donor ratios to increase the FRET efficiency [30, 105, 106, 107]. Furthermore, the QD ensembles show an inhomogeneous broadening and follow different optical selection rules as molecules do. Therefore, it was unclear if the basic FRET theories developed for molecules could also be directly applied to describe FRET in QD structures [108, 109]. However, in recent years it has been shown theoretically that energy transfer, in particular the rate, in QD structures can be appropriately described by the basic FRET theory [109, 110, 111, 112]. Even though a good understanding of the FRET process in QD structure is essential for the characterization of FRET in QD structures and the optimization of QD FRET devices, only few reports on the comparison of theory and experiment can be found in the literature [32, 108, 113, 114].

Reports on FRET in QD Structures

The first observation of FRET between QDs was reported by Kagan et al. [32, 113], who investigated energy transfer in a closely packed three-dimensional donor-acceptor QD solids and showed that it was mediated by the Förster mechanism. They also presented evidence for energy transfer within a monodispersed QD solid. Intra-ensemble energy transfer has also been observed by Crooker et al. [108], who reported on a wavelength-dependent lifetime in their monodispersed QD solid, as well as by Achermann et al. [115], who determined a FRET rate as fast as $(50\ \text{ps})^{-1}$ for a monodispersed QD layer prepared by the Langmuir-Blodgett technique. The cause for this energy transfer within the QD ensemble has been attributed to the overlap of the inhomogeneously broadened QD absorption and photoluminescence bands, but was not investigated in detail in these publications. In section 4.1 of this thesis, also published in reference [116], it is verified that this intra-ensemble energy transfer is mediated by FRET due to the self-overlap of the QD absorption and emission spectra and it is shown that it can be strongly influenced by the QD concentration in the structure.

Furthermore, Crooker et al. also demonstrated a first graded energy structure in order to increase the FRET rate, which was determined to be $(0.75\ \text{ns})^{-1}$. Achermann et al. were able to further increase k_{FRET} in their graded donor-acceptor bilayer structure to $(120\ \text{ps})^{-1}$ and found that in order to explain their observations, donors from within the third shell in a hexagonally-ordered structure had to be transferring energy to a central acceptor QD [115]. The highest FRET rates in QD structures so far were reported by Franzl et al., who deposited layers of oppositely charged CdTe QDs right on top of each other to reduce the QD centre-to-centre separation and achieved an average FRET rate of $(50\ \text{ps})^{-1}$ and FRET efficiencies of 80% in this way [117].

The qualitative agreement of the distance dependence of the FRET rate in a separated donor-acceptor layer structures, similar to the graded donor-acceptor structures

discussed in the aforementioned publications, with the R_{ex}^{-4} trend expected from equation (2.13) was however only demonstrated in 2008 by Kim et al. [114]. At about the same time, Chen et al. reported on the observation of the decrease of the FRET efficiency with increasing QD separation due to stretching of mixed donor-acceptor layers on an elastomeric film [118].

Earlier confirmation of the Förster-like energy transfer in CdTe QD solids was reported by Wuister et al., who investigated the temperature dependence of the acceptor rise-time, which reflects the energy transfer rate [99]. They found a trend in good qualitative agreement with energy transfer via dipole-dipole interactions and could exclude tunnelling as a possible energy transfer mechanism. Further temperature dependent measurements for separated CdSe/ZnS donor and acceptor layer structures revealed the existence of two different temperature regions, one at larger temperatures showing an increase in the FRET rate with increasing temperature similar to the observations of Wuister et al. and another at lower temperatures for which a constant FRET rate was observed, attributed to the break down of the thermal equilibrium between the bright and dark excitonic states due to the larger energy level splitting as in the CdTe QDs [119].

Even though good qualitative agreement between FRET theory and distance and temperature dependent measurements has been demonstrated, little has been reported on concentration dependences [99] even though the donor and acceptor concentrations can have an important impact, for example on the overall light output from a mixed QD film [120]. Therefore, the work carried out in this thesis further completes the above presented picture of energy transfer in QD structures by analysing the acceptor concentration-dependent FRET in a mixed donor-acceptor monolayer (section 4.2) and a separated donor-acceptor bilayer structure (section 5.3). Moreover, it is demonstrated that by including the donor and acceptor QD radii in form of exclusion zones around the donors in the theoretical calculations good quantitative agreement of the observed FRET signatures with theory is obtained for donor-acceptor [107] as well as monodispersed QD monolayer structures [116], as discussed in chapter 4. Furthermore, in section 5.4, it is shown that donor intra-ensemble energy transfer can lead to a donor concentration dependence that is not expected from FRET theories for molecules and two ways on how to include this effect in theory are suggested.[1]

Apart from solid QD structures, solution-based nano-assemblies of charged QDs were also investigated in the literature [80, 121, 122, 123]. For clusters of oppositely charged QDs, energy transfer for assemblies with single donor or single acceptor QDs can be studied, depending on the charge state of the donor or acceptor QDs. For clusters of oppositely charged CdSe/ZnS QDs, good agreement of the donor PL quenching and acceptor PL enhancement with theory were found [80]. Furthermore, in a detailed

[1] Parts of these results have been submitted for publication

investigation of the lifetime in clusters prepared from oppositely charged CdTe QDs an impact of donor intra-ensemble energy transfer on donor-acceptor FRET was also observed [123], in line with the effect discovered for donor-acceptor bilayer structures discussed in section 5.4. This observation allows for an analysis of the cluster composition without the need for high-resolution microscopy, as the formation of donor-acceptor and donor-donor nanoclusters can be monitored from the changes in donor lifetime and the acceptor PL enhancement.

2.2.3 Surface Plasmon Enhanced FRET

To overcome the limitations on the FRET efficiency due to the large size of the QDs, surface plasmons supported by metal nanoparticles can be used to enhance the FRET rate and efficiency in QD structures. It has been proposed that large enhancements of the energy transfer based on dipole-dipole interactions of donor and acceptor molecules, represented as point-dipoles, can be observed in proximity to solid-state particles [124, 125]. The enhancement factor is predicted to strongly decrease with increasing molecule-particle separations but can be high for donor-acceptor separations of up to approximately 70 nm [125]. It furthermore depends on the shape of the particle as well as the angular orientation of the molecules with respect to the particle.

First observations of surface plasmon enhanced energy transfer have already been reported for dye-systems [126, 127, 128], while in reference [129] the energy transfer rate is decreased in the presence of the metal nanoparticles. Zhang et al. report on the increase of the FRET efficiency, determined from the relative donor and acceptor emission, from 22% to 87% for energy transfer between two dye molecules linked by a rigid double strand of DNA [126]. This is compared to a decrease of the relative donor-acceptor separation r_{DA}/R_0 from 1.1 to 0.75 and as r_{DA} is supposedly unchanged in this system, this would correspond to an increase of R_0 by 47%. Furthermore, based on the values of the FRET efficiency and the measured lifetimes an increase of the FRET rate from $(62.5\text{ns})^{-1}$ to $(2.9\text{ns})^{-1}$ was determined for this system. They further report that larger enhancement effects are observed for the larger donor-acceptor separations over which the FRET efficiency is small, larger silver particle sizes with diameter increasing from 15 to 40 to 80 nm, which is attributed to the larger near-field of the bigger particles, and by increasing the distance between the silver nanoparticle and donor-acceptor assembly from two to ten nanometers, in line with the typical surface plasmon distance dependence [127]. Similar observations with an increase of the FRET efficiency from 12 to 56% corresponding to an increase of R_0 from 5.4 nm to 7.8 nm are discussed by Lessard-Viger et al., who investigate energy transfer between donor and acceptor dyes deposited in separated silica sheels around silver nanoparticles with a diamtere of 47 nm [128]. In contrast, Reil et al. report on a decrease of the FRET rate for

randomly distributed donor and acceptor fluorophores on metal nanoparticles fabricated by electron beam lithography with diameters varying from 30 to 80 nm [129]. The observed acceptor intensity increase is attributed to a direct surface plasmon emission enhancement despite the decrease in FRET efficiency, which is reflected in an increase of the donor emission, despite the quenching by the metal nanoparticles. This clearly shows that a good understanding of the donor / acceptor - metal nanoparticle interaction, outlined in section 2.1.3, is necessary for a detailed analysis of the modification of FRET by surface plasmons.

Theoretical calculations by Govorov et al., for surface plasmon mediated FRET between a donor and an acceptor QD, predict that the strongest enhancement of the FRET rate will be observed for metal nanoparticles positioned between donor and acceptor QDs [130]. Furthermore, they show that the emission spectra for QD FRET assemblies in proximity to metal nanoparticles are dominated by quenching of the donor and acceptor QDs luminescence and that surface plasmon enhanced FRET will only lead to small variations in the donor and acceptor emission peak intensities even for large enhancement factors of the FRET rate of up to 50. Therefore, the observation of surface plasmon enhanced FRET from steady-state PL is suggested to be rather difficult and time-resolved measurements should also be carried out. For both types of measurements it is important to determine the influence of the metal nanoparticles on the donor and acceptor emission properties, in order to be able to differentiate between direct surface plasmon enhanced or quenched emission and the modification of FRET.

The lifetime data for a mixed donor-acceptor CdTe QD monolayer deposited at different separations to a gold nanoparticle layer is presented by Komarala et al. [131]. The decrease of the donor lifetime in the presence of the acceptors on quartz and on the gold nanoparticle layer, suggest that surface plasmon enhanced FRET decreases the donor lifetime from 5.7 ns in the absence of acceptors (on gold and quartz) to 2.1 ns, compared to 4.4 ns for the mixed QD monolayer on quartz. This corresponds to an increase of the FRET efficiency by a factor of 2.7 from 23 to 63% in proximity to the gold nanoparticles with a diameter of approximately 7 nm. Furthermore, the acceptor intensity shows a typical surface plasmon distance dependence with a maximum at one of the intermediate QD-gold nanoparticle separations investigated, no acceptor QD on gold reference data is shown. Su et al. have investigated a similar system with mixed donor-acceptor CdSe/ZnS films and silver nanoparticles with silica shells of different thicknesses to probe the QD-silver nanoparticle distance dependence for nanoparticle diameters of 40 and 110 nm [132]. They observe strong donor PL quenching and acceptor enhancement as well as a decrease of the donor lifetime and an increase of the acceptor lifetimes in proximity to the silver nanoparticles in comparison with a mixed QD layer in the absence of the silver nanoparticles. Larger PL enhancement effects are

observed for the 110 nm silver nanoparticle, attributed to the dipole and quadrupolar resonances observed in the absorption spectrum. Also here, a typical surface plasmon distance dependence of the FRET efficiency determined from the acceptor:donor PL ratio is observed. However, due to the lack of reference data for donor or acceptor-only monolayers with and without silver nanoparticles, it is not clear by how much the FRET efficiencies determined in this way is actually different from the FRET efficiency that would be observed in the absence of the silver nanoparticles and it is also difficult to establish whether this effect is due to direct surface plasmon PL enhancement and quenching or the influence on the FRET process. In reference [133], Wang et al. study FRET between type I CdSe/ZnS QDs and type II CdSe/ZnTe QDs. By adding gold nanoparticles with a diameter of approximately 20 nm to their mixed film, they observe a further quenching of the donor emission and an increased acceptor enhancement compared to the quenching and enhancement observed in the mixed donor-acceptor film. As the direct quenching of the donor QDs by the gold nanoparticles is negligibly small, the increased donor quenching is attributed to surface plasmon enhanced FRET. This is further confirmed by the excitation wavelength dependence of the acceptor enhancement, which shows the same shape as the gold nanoparticle absorption spectrum. Moreover, the donor lifetime in the mixed film with gold nanoparticles is decreasing upon additional excitation in resonance with the gold nanoparticle absorption during the time-resolved measurements, an effect that is not observed for the mixed film with donor and acceptor QDs only and a donor film with gold nanoparticles. This is a clear indication of surface plasmon mediated FRET and the FRET efficiency is determined to be increasing from 30% to 60% for resonant excitation with the surface plasmon absorption feature. The increase in the acceptor lifetime in the mixed film with gold nanoparticles over the values observed for a pure acceptor and a mixed film also confirm that the observed acceptor enhancement is due to increased energy transfer from the donor QDs and not caused by direct surface plasmon interaction, which should cause the lifetime to decrease.

As can be seen, the experimental investigation of surface plasmon enhanced FRET has only just started, probably because the analysis of surface plasmon mediated energy transfer is very complex, as outlined above. Therefore, it is important to understand well FRET in pure QD systems, discussed in chapters 4 and 5, and characterise the metal nanoparticle-QD interaction, analysed in section 6.1, before investigating the impact of surface plasmons on the energy transfer process between donor and acceptor QDs, presented in sections 6.2 and 6.3.

3 Sample Preparation and Characterization

The structures under investigation were prepared by a layer-by-layer (LbL) technique [52, 53] based on the electrostatic self-assembly of oppositely charged nanoparticles and macromolecules. This deposition technique allows one to build complex layer structures on the scale of nanometers simply by immersion of a substrate in solutions with different, charged particles. A detailed description of the materials used and the preparation of the structures investigated is given in the first part of this chapter. In the subsequent sections the characterization of the samples by means of absorption and photoluminescence (PL) spectroscopy as well as by time-resolved PL measurements is outlined.

3.1 Sample preparation

The LbL sample preparation technique is based on the assembly of oppositely charged particles onto a substrate by electrostatic interaction. Alternatingly, positively and negatively charged particles can be deposited into layers on different types of materials and different shapes of substrates - including curved surfaces and microspheres [40, 53, 134, 135] - making this a very versatile deposition technique. Structures prepared by LbL assembly have already been reported for applications such as light emitting and guiding structures [19, 136, 137, 138], photovoltaic structures [139, 140, 141] as well as sensors and detectors [142, 143, 144]. Additionally, due to the possibility of controlling the layer structure on the nanometer scale, the LbL technique is also valuable for the investigation of energy transfer processes [23, 114, 145] and the interaction of fluorophores with surface plasmons [76, 77, 78].

3.1.1 Materials

Ideally the substrates used for the LbL assembly should be at least slightly charged to facilitate the attraction and deposition of the initial layers. However, after the deposition of a few layers, the surface charge will be mostly influenced by the charge density of the particles used to prepare the layers rather than the initial surface charge of the substrate. Therefore, polyelectrolyte (PE) layers were deposited as initial layers (buffer layer) that

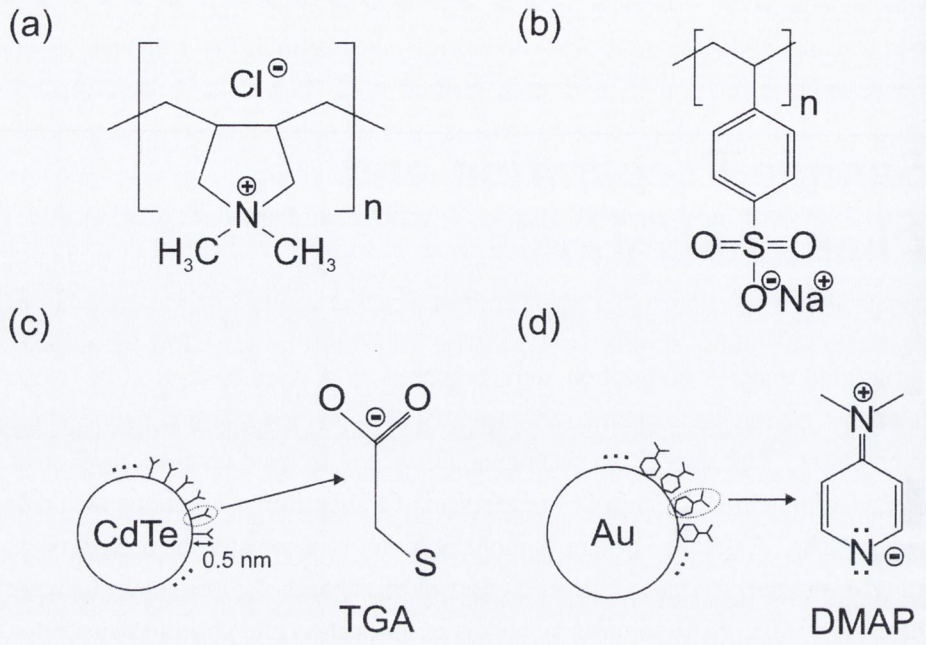


Figure 3.1: Chemical structure formula of one repetition unit of the polyelectrolytes Poly(diallyldimethylammonium chloride) (a) and Poly(sodium 4-styrene sulfate) (b). Schematic drawing of a CdTe nanocrystal quantum dot stabilized by thioglycolic acid (TGA) (c) and a colloidal gold nanoparticle stabilized by 4-dimethylaminopyridine (DMAP) (d). The size of the chemical structures of the polyelectrolyte repetition units and the stabilizing molecules of the nanoparticles is not to scale.

serve to establish a strongly and homogeneously charged surface onto which the actual, functional structure was deposited. The PE layers were also used to form spacer layers of variable thickness between the semiconductor and metal nanoparticle layers. The PE bilayers used here consist of a positively charged poly(diallyldimethylammonium chloride) (PDDA) and negatively charged Poly(sodium 4-styrene sulfate) (PSS) layer. The chemical structure of the PDDA and PSS repetition units are shown in Figure 3.1(a) and (b) respectively.

In solution the PSS and PDDA chains are stretched out due to the repulsion of the positive and negative charge on each of their repetition units respectively. Therefore, they form very thin layers when deposited onto a substrate by the LbL deposition technique. By adding salt to the PE solutions, for example NaCl, the counterions Cl^- or Na^+ get attracted to the PDDA or PSS chains respectively. The counterions screen the charge on the repetition units so that the polyelectrolytes are now able to curl up [146]. When layers are deposited from PE solutions containing salt thicker layers are formed.

The thickness of the PE layers can therefore be tuned by the amount of salt added to the solution used for the LbL deposition.

The polyelectrolytes used for the preparation of the samples investigated in this thesis were obtained from Sigma Aldrich, PSS in powder form with a molecular weight of approximately 70, 000 and a 20 wt% solution of PDDA in water, with a molecular weight of 100,000 to 200,000. Millipore water with a resistance of 18.2 $M\Omega/cm^2$ was used for the preparation of the LbL solutions. To vary the thickness of the PE layers different volumes of a 3 M NaCl solution[1] were added to the LbL solutions used for depositing the PE layers. The PDDA solution was used as purchased and a PSS stock solution was prepared from the PSS powder by dissolving it in water in an ultrasonic bath:

PSS (stock solution): 543 mg PSS powder in 10 ml millipore water.

To deposit approximately 7 nm thick bilayers, PE solutions with a concentration of 0.5 M NaCl were used:

PDDA (LbL solution): 170 μl PDDA + 1 ml NaCl (3 M) + 5 ml millipore water
PSS (LbL solution): 560 μl PSS (stock solution) + 1 ml NaCl (3 M) + 4.5 ml millipore water

Thinner PE bilayers with a thickness of approximately 3 nm were deposited using 0.1 M NaCl PE solutions:

PDDA (LbL solution): 170 μl PDDA + 0.2 ml NaCl (3 M) + 5.8 ml millipore water
PSS (LbL solution): 560 μl PSS (stock solution) + 0.2 ml NaCl (3 M) + 5.3 ml millipore water

Colloidal CdTe QDs stabilized by thioglycolic acid (TGA), emitting at different wavelengths in the visible spectral region due to a variation of their diameter, were obtained from Prof. Yurii Gun'ko's group in the chemistry department of Trinity College Dublin, Ireland and from Dr. Vladymir Lesnyak and Dr. Nikolai Gaponik from the Technical University in Dresden, Germany. The QDs were synthesized according to standard procedures [49, 50, 51]. The TGA ligand introduces a negative charge to the QD surface, see Figure 3.1(c). Due to this negative charge the QDs are suitable for the LbL deposition technique [147] and were deposited onto PDDA layers.

Colloidal gold nanoparticles (NPs) with a diameter of approximately 4 nm were obtained from Dr. Andrei Susha and Prof. Andrey Rogach, who are currently working at the City University in Hong Kong. The gold NPs were stabilized by 4-dimethylaminopyridine (DMAP) [148], giving them a positive surface charge, see Figure 3.1(d), so that they could be deposited onto PSS layers.

[1] NaCl solution (3 M): 1.75 g NaCl in 10 ml millipore water

3.1.2 Substrate Treatment

The structures investigated here are deposited on 1.2 by 1.5 cm quartz substrates with a thickness of 1.5 mm. Quartz has been chosen as the transparent substrate for the optical characterization due to its low autofluorescence compared to standard glass slides for excitation close to 400 nm.

If the substrates have been used before, they are first cleaned in aqua regio[2] in a fume hood. The semiconductor and metal particles are dissolved by the acid. The substrates are left in the aqua regio for 10 minutes, then washed with soap and rinsed with water to remove any remaining acid off the surface.[3]

A negative charge is introduced on the surface of cleaned or new substrates by a chemical treatment with NaOH, the steps of which are outlined below. During this procedure the substrates are placed in a teflon stand that allows them to stand upright in a beaker and prevents them from sticking together. The beaker with the substrates is then filled with the different solutions and kept in an ultrasonic bath for the times given below to optimize the effect of the procedure:

1. Keep substrates in soap-free (millipore) water 10 min
2. 1 M NaOH (4 – 5 g of NaOH in 75 ml H2O) 15 min
3. Ethanol + NaOH (some NaOH pellets in Ethanol) 15 min
4. Rinse each substrate with millipore water
5. Fresh millipore water 10 min

After the treatment the quartz slides are best kept in the stand in millipore water to maintain a well charged surface and to avoid contamination of the slides with dust and scratches on the surface. Before starting the LbL deposition the substrates are taken out of the water and dried.

3.1.3 Principle of Layer-by-Layer Technique

For the preparation of a LbL-structure on a negatively charged substrate, it is first immersed in a solution with positively charged particles for some time so that the particles can assemble onto the surface, see Fig 3.2(a). PDDA was used to form the first layer for the structures investigated here. The particles will be attracted by the oppositely charged substrate and form a layer on the surface. As more and more particles deposit into the layer, the surface charge changes from negative to positive as indicated in Figure 3.2(b). Due to this charge inversion only a very thin layer of material is deposited as the positive particles are no longer attracted by the substrate but repelled. This is why, with the LbL

[2] Aqua regio: acid mix of HNO_3 : HCl of 1 : 3

[3] The aqua regio has to be disposed of as hazardous material, as it contains the dissolved Cd and Te from the QDs.

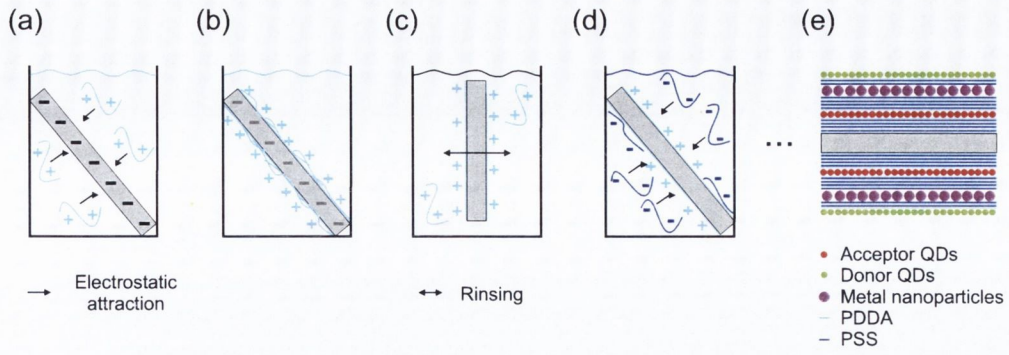


Figure 3.2: Basic steps of the sample preparation with the layer-by-layer technique. (a) Immersion of a negatively charged substrate (grey) in a solution with positively charged particles or molecules (light blue). (b) Deposition of a positively charged layer on the substrate and charge inversion. (c) Removal of loosely bound particles and molecules during rinsing. (d) Subsequent immersion in a solution with negatively charged particles or molecules (dark blue) and formation of layer with negative charge. (e) Example of a final structure built up from PDDA (light blue) and PSS (dark blue) polyelectrolyte and including quantum dots (QDs) (green and red) as well as metal nanoparticles (purple).

technique, it is possible to deposit monolayers of charged particles or macromolecules that are only a few nm thick. Once the layer has formed, the substrate is taken out of the solution and rinsed in water (or a different solvent, depending on the materials used) to remove all loosely bound particles from the substrate as schematically shown in Figure 3.2(c). Only particles attached to the substrate by strong electrostatic interaction will remain in the layer. Therefore, the rinsing is important to ensure the formation of monolayers rather than multilayers. It also helps to prevent the cross-contamination of the different solutions used in the deposition.

Then, the substrate is immersed into a solution with negatively charged particles, usually PSS for the second layer. The negatively charges particles will assemble onto the surface in the same way as the positively charged ones due to the charge inversion, as shown in Figure 3.2(d). After the deposition of the negative particles the substrate will be rinsed again before the immersion of the substrate into a solution with positively charged particles, usually PDDA for the third layer. By repeating the immersion in solutions of oppositely charged particles structures with different combinations of positively, here PDDA or metal NPs, and negatively, here PSS or QDs, charged particle layers can be obtained in a fairly simple way. An example of one of the structures investigated, a donor-gold-acceptor sandwich structure, is schematically depicted in Figure 3.2(e). Due to the nature of the LbL process, the sample structure is deposited on the front as well as on the back of the substrate.

3.1.4 Sample Preparation

The first step for the deposition of each structure investigated was the deposition of a PE buffer layer consisting of two or four bilayers from 0.5 M and 0.1 M NaCl PE solutions respectively. For the deposition the substrates were immersed in the PDDA and PSS LbL solutions alternatingly for 10 minutes and rinsed for 1 minutes between each immersion step. After deposition of the buffer layer gold NPs can be deposited directly onto the PE bilayers. In order to deposit QDs onto the slides, an additional PDDA layer had to be deposited first. Details on the concentrations of the gold NP and QD solutions and the immersion times for the LbL deposition are discussed later. In the following the different types of structures investigated are summarized, the PE layers were deposited from PE solutions with 0.1 M NaCl concentration if not stated otherwise:

Monodispersed QD monolayer: A PDDA layer was deposited onto the PE buffer layer before immersing the sample into the QD solution. These samples were used as reference samples for the more complex structures. The concentration of the QDs in the layers was varied by changing the immersion time in the QD solution.

Mixed QD monolayer: After the deposition of a PDDA layer on the PE buffer layer (0.5 M NaCl), the sample was immersed in a solution containing different ratios of small donor and large acceptor QDs.

Separated donor-acceptor bilayer structure: After depositing a PDDA layer on top of the PE buffer layer, an acceptor QD layer was prepared. The sample was rinsed carefully and the homogeneity of the QD layer was checked with a UV lamp. Then, a PE spacer, consisting of a varying number of PE bilayers (usually between 0 and 7) and a final PDDA layer, was deposited on top of the acceptor QD monolayer. In the end the structure was immersed in the donor QD solution to form the final layer. The acceptor QDs were deposited as the first layer, as the donor QDs seemed to be washed off the structure when covered with an additional PE layer, probably because of the lower charge due to the smaller size.

QD monolayer on gold: On the PE buffer layer one gold NP layer (all PE solutions used for the preparation of this structure contained 0.1 M NaCl) or three layers of gold NPs with intermediate PSS layers (all PE layers in this structure were prepared from solutions with 0.5 M NaCl concentration) were deposited and covered with a varying number of PE bilayers. The QD layer, either donor or acceptor QDs, was deposited last.

Mixed QD monolayer on gold: As for the QD monolayer on gold, the gold NPs were deposited onto the PE buffer layer. Structures with either one gold layer (0.1 M NaCl) or three gold layers (0.5 M NaCl) with intermediate PSS layers were prepared. After the deposition of a varying number of PE bilayers on top of the gold NPs, the sample was immersed into a solution containing donor and acceptor QDs for the deposition of

a mixed donor-acceptor QD layer.

Separated donor-acceptor bilayer on gold: A single gold NP layer was formed on the PE buffer layer and covered with a varying number of PE bilayers. Then an acceptor QD layer was deposited, followed by a PDDA layer and the final donor QD layer.

Acceptor-gold-donor sandwich structure: On top of the PE buffer layer a PDDA layer was formed to enable the deposition of an acceptor QD layer.Then PE bilayers were added to the structure and a gold NP layer was deposited.On top of the gold layer more PE bilayers were deposited and finally covered with a donor QD layer. This structure is schematically depicted in Figure 3.2(e).

To monitor the build up of the more complex structures, in particular those including metal NP layers, the samples were left to dry in air after each NP layer deposition and characterized by absorption measurements. If QDs had already been incorporated into the structure PL spectra were recorded as well. The completed structures were all left to dry over night and then fully characterized the next day.

3.2 Absorption

The absorption spectra of the samples were usually taken first to obtain information about the concentration of the different NPs and sometimes the thickness of the PE layers. These measurements were carried out on a double-beam UV-Vis Recording Spectrometer (Shimadzu UV-2401 PC). The spectra of the NP solutions and layers were recorded between 350 and 800 nm with a resolution of 0.5 nm. To monitor the thickness of the polyelectrolyte layers, the absorption spectra were taken down to a wavelength of 200 nm as the characteristic absorption peak of PSS occurs at approximately 226 nm.

The absorption $A(\lambda)$ of a material is characterized by Lambert-Beer's law:

$$A(\lambda) = \epsilon(\lambda) \cdot l \cdot c \ . \tag{3.1}$$

It shows that the absorption of a sample depends on the extinction coefficient $\epsilon(\lambda)$ of the materials contained in the sample, the concentration of the material c as well as the length l of the light path, the distance over which the light can interact with the material. In case of a solid material l is the sample thickness and for the solutions investigated it is 1 cm, the inner dimension of a standard cuvette. If l and $\epsilon(\lambda)$ of the material are known, the concentration of the material can be determined by measuring the absorption. Alternatively, if the concentration and extinction coefficient of the material under investigation are known, the thickness of a material can be determined by the absorption measurement or at least one can compare the thicknesses of different samples made from the same material (corresponding to the same $\epsilon(\lambda)$) at the same concentration.

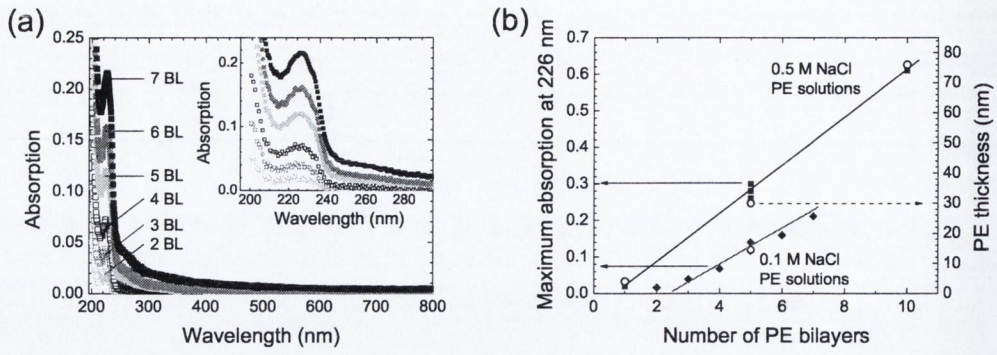


Figure 3.3: (a) Absorption of 2 to 7 polyelectrolyte (PE) bilayers (BL) deposited from PDDA and PSS solutions containing 0.1 M NaCl. The inset shows a close up of the PE absorption peak at 226 nm. (b) Dependence of the absorption values at 226 nm on the number of PE bilayers deposited from solutions containing 0.5 M NaCl (solid squares) and 0.1 M NaCl (solid diamonds). The respective thicknesses determined by X-ray diffraction (open circles) for some of the samples are shown on the right-hand-axis. The lines are included as guide to the eyes to highlight the linear increase of the absorption and thickness with increasing number bilayers for the two salt concentrations.

3.2.1 Polyelectrolyte Layer Thickness

The change of the overall PE thickness with increasing number of bilayers deposited on a quartz substrate can be monitored by measuring the PSS absorption peak at approximately 226 nm. In Figure 3.3(a) the absorption spectra for samples with 2 to 7 PE bilayers (on front and back of the sample), deposited by LbL from PE solutions containing 0.1 M NaCl, can be seen. It is important to note that the absorption increases with decreasing wavelength between 800 and 226 nm, the position of the PE peak, and that this increase becomes stronger for a larger number of deposited bilayers. This has to be taken into account when analysing the absorption spectra of structures containing many PE bilayers, typically more than 5 or 6. In the inset of Figure 3.3(a), a close-up of the PSS absorption peak at 226 nm is shown and the increase of the peak absorption with increasing number of deposited PE bilayers can be seen clearly, indicating that the thickness of the deposited polyelectrolyte is increasing as expected.

To determine the absolute values of the PE bilayer thickness, the thickness of a few PE bilayer samples were also determined by X-ray diffraction.[4] As can be seen in Figure 3.3(b) the dependence of the absorption peak value at 226 nm (solid squares, left-hand axis) and the thickness of the PE layers (open circles, right-hand axis), deposited from solutions with 0.5 M NaCl concentration, on the number of bilayers follow the same,

[4]The X-ray diffraction measurements were carried out by Robert Gunning in the School of Physics, Trinity College Dublin, Ireland.

linear trend. This shows that, as assumed from Lambert-Beer's law in equation (3.1), the change in thickness of the PE layers can be monitored by absorption measurements. From the X-ray diffraction measurements, the average thickness of a bilayer deposited from a 0.5 M NaCl PE solution was determined to be approximately 7 nm.

As mentioned above, by decreasing the salt content in the PE solutions used for the LbL deposition the thickness of the layers can be decreased. The absorption peak values of the PE samples shown in Figure 3.3(a) are also shown in Figure 3.3(b) (solid diamonds, left-hand axis). Their absorption is decreased compared to the PE layers deposited from 0.5 M NaCl solutions, but also follow a linear trend with increasing number of deposited bilayers. The PE thickness determined for a 5 bilayer sample deposited from 0.1 M NaCl PE solution is also included in Figure 3.3(b). As can be seen the absorption of the 5 BL sample is decreased by a factor of approximately two compared to the 0.5 M NaCl sample with 5 bilayers. The thickness of (14.2 ± 0.5) nm, determined by X-ray diffraction, explains the decrease of the absorption peak very well. The average thickness of PE layers deposited from PE solutions with 0.1 M NaCl was determined to be approximately 3 nm.

3.2.2 Quantum Dot Concentration

From the absorption spectra of the nanoparticle solutions one can obtain information about the nanoparticle size and concentration. As already mentioned, the size of colloidal QDs can be determined from the centre wavelength of the first absorption peak. For CdTe QDs, this can be done with the help of the sizing curve given in Ref. [55]. From the solution spectra shown in Figure 3.4(a), values of 2.7 nm and 3.5 nm are obtained for the Don1 and Acc2 QD diameters respectively. The position and absorption value of the first absorption peak, 0.167 at 514 nm for Don1 and 0.224 at 575 nm for Acc2, are indicated by lines in the Figure. In their article Yu et al. also studied the relation between the value of the extinction coefficient at the wavelength of the first absorption peak and the QD size. Based on the fitting curve of the extinction coefficient $\epsilon\left(\lambda_{peak}\right)$ in dependence of the QD diameter (equation (5) in reference [55]), extinction coefficients $\epsilon_{Don1}\left(\lambda_{peak}\right) = 8.2 \times 10^4\ \mathrm{M^{-1}cm^{-1}}$ and $\epsilon_{Acc2}\left(\lambda_{peak}\right) = 1.4 \times 10^5\ \mathrm{M^{-1}cm^{-1}}$ were obtained for Don1 and Acc2 QDs respectively. Knowing the extinction coefficient of the QDs, the molar concentration c_{sol} of the CdTe QDs in solution can be determined via Lambert-Beer's law. The concentration determined for the Don1 and Acc2 QD solutions shown in Figure 3.4(a) are 3.5 10^{-6} M and 2.7 10^{-6} M respectively.

After the deposition in a layer, $\epsilon\left(\lambda\right)_{peak}$ of the QDs should not have changed, so that the concentration of the QDs in the layer can be determined by comparison with the spectrum of these QDs in solution, as shown in Figure 3.4(b). The molar concentration of the QDs in the monolayer c_{ML} can be obtained with equation (3.2) by multiplying

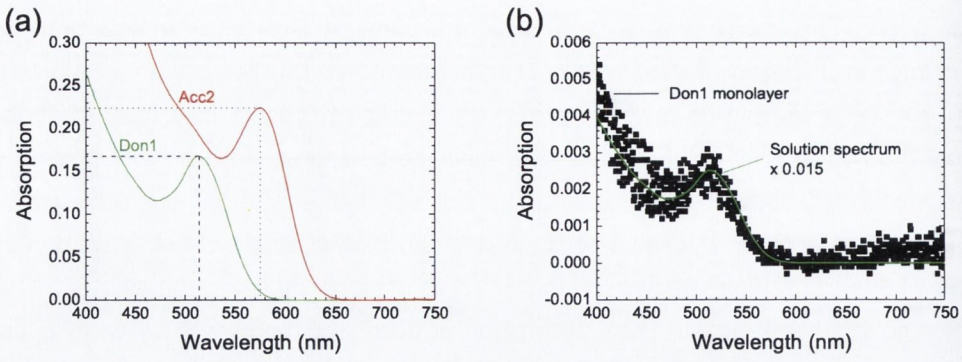


Figure 3.4: (a) Absorption spectra of a donor (Don1) and acceptor (Acc2) QD solutions. The wavelength as well as the absorption value of the first absorption peak are indicated by lines. (b) Absorption spectrum of a Don1 QD monolayer (ML, black squares), fitted by the Don1 solution spectrum (green line) also shown in (a).

the concentration of the QDs in solution, c_{sol}, with the ratio of the absorption values at the first absorption peak $\frac{A_{ML}(\lambda_{peak})}{A_{sol}(\lambda_{peak})}$ and the ratio of the absorption path length $\frac{1\text{cm}}{d_{QD}}$, which is the 1 cm length of the cuvette in case of the solution and the QD diameter d_{QD} for a QD monolayer. Additionally a factor $\frac{1}{2}$ has to be taken into account as the QD layers are deposited on both sides of the sample. Finally the molar concentration can be converted into a QD surface density by a factor of $N_A \cdot 10^3 \frac{\text{l}}{\text{m}^3} \cdot d_{QD}$, where N_A is the Avogadro constant:

$$\begin{aligned} c_{ML} &= \frac{A_{ML}(\lambda_{peak})}{A_{sol}(\lambda_{peak})} \cdot c_{sol} \cdot \frac{1\text{ cm}}{d_{QD}} \cdot \frac{1}{2} \cdot N_A \cdot 10^3 \frac{\text{l}}{\text{m}^3} \cdot d_{QD} \\ &= \frac{A_{ML}(\lambda_{peak})}{A_{sol}(\lambda_{peak})} \cdot c_{sol} \cdot 3.011 \times 10^{24}\ . \end{aligned} \tag{3.2}$$

c_{ML} is obtained in m^{-2} when including c_{sol} in $\frac{\text{mol}}{\text{l}}$, equivalent to M, in equation (3.2). For the Don1 monolayer shown in Fig 3.4(b), the ratio of absorption values was found to be 0.015 and a QD concentration in the layer of $1.6 \times 10^{17}\ \text{m}^{-2}$ was determined with an approximate error of $\pm 0.2 \times 10^{17}\ \text{m}^{-2}$.

To verify the suitability of evaluating the concentration of the QDs in the layers by comparison of the absorption spectra with those in solution, the QD concentration was determined for two samples exemplarily by mass spectroscopy.[5] Details on the analysis can be found in Appendix A.1.

The concentration of the QDs in the LbL assembled layers can be varied by using a solution with a low QD concentration for the deposition and by varying the immersion

[5]The investigation of the samples with an Inductively Coupled Plasma - Mass Spectrometer was carried out by the Centre for Microscopy and analysis in Trinity College Dublin

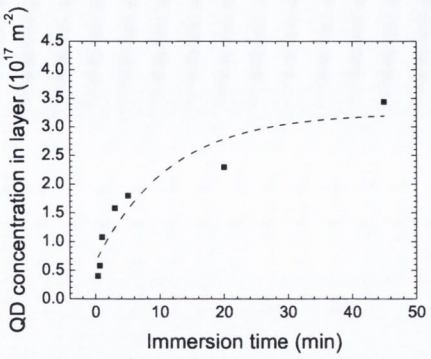


Figure 3.5: Dependence of the QD concentration in the deposited LbL layers from a solution with a Don1 QD concentration of 1.5×10^{-6} M on the immersion time. The line is included as a guide to the eye.

time, as published in [116]. For the smaller donor QDs a concentration of 1.5×10^{-6} M and for the larger acceptor QDs concentrations of 0.3 to 0.5×10^{-6} M were used. A typical dependence of the QD concentration in the layer on the immersion time is shown in Figure 3.5 for Don1 layers. For the formation of complete monolayers higher concentrations of at least 3×10^{-6} M for the donors and 1×10^{-6} M for the acceptors were used with immersion times of 10 to 20 minutes.

To vary the concentration ratio of the donor and acceptor QDs in mixed monolayers, solutions with different acceptor:donor ratios were used for the deposition, as also outlined in [107]. For layers with a low acceptor:donor ratio, less than 1:3, small volumes of acceptor QDs were added to a 2.0×10^{-6} M donor solution. To obtain larger ratios, small amounts of donor QDs were added to an acceptor QD solution with a concentration of 2.0×10^{-6} M.

The concentration of the donor and acceptor QDs in the mixed monolayers or structures with separated donor and acceptor QD layers were determined by fitting the measured absorption spectrum of the mixed monolayer or bilayer with a linear combination of the spectra recorded for monodispersed donor and acceptor QD reference monolayers as shown in Figure 3.6. As can be seen the measured spectrum of a QD bilayer structure (black squares) can be well reproduced by a weighted sum of the donor and acceptor reference spectra (shown in the inset) with factors 1.1 and 0.8 for the donor and acceptor contribution respectively (blue line).

For structures with many layers an increasing PE absorption background had to be taken into account. To facilitate the fitting of the absorption spectra of more complex structures, in particular those including gold NPs, absorption spectra were taken after each nanoparticle deposition step for the dried sample. In this way the QD and gold NP concentrations could be determined individually after each deposition step. Small varia-

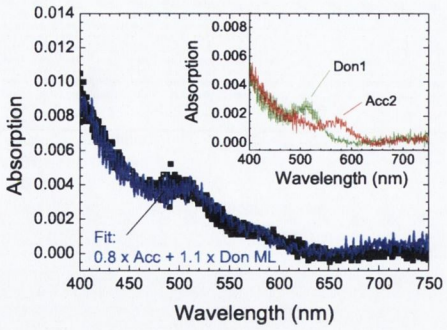


Figure 3.6: Absorption spectrum of a donor-acceptor QD bilayer structure (black squares). The reference spectra used for the fit (blue line) are shown in the inset. The measured bilayer spectrum can be well reproduced by a linear combination of the donor (Don, green line) and acceptor (Acc, red line) monolayer spectra.

tions, in particular decreases of the concentrations or increases of the surface plasmon peak absorption after the deposition of further layers, were determined by fitting of the absorption spectrum of the full structure.

3.2.3 Gold Nanoparticle Concentration

The absorption spectrum of the gold NP solution and a gold NP layer shown in Figure 3.7(a) are dominated by the surface plasmon (SP) resonance of the gold NPs. The NP solution contained 110 μl of the original gold NP stock solution diluted in 3 ml millipore water. From a fit with Mie-theory [149, 150, 151], the size of the NPs in solution can be determined. A MatLab program was used to calculate the wavelength-dependence of the extinction, scattering and absorption cross sections for different diameters of gold NPs based on Mie-theory [150, 151]. In this program the dielectric properties of small gold NPs were obtained from the bulk values [152] as outlined in literature [151, 153].

As can be seen in Figure 3.7(a) a good agreement with the measured gold NP solution spectrum was obtained for the absorption calculated from the extinction cross section for gold NPs with a diameter of 4 nm. The value of the extinction cross section is 1.601 nm^2 at the peak wavelength of the surface plasmon feature, corresponding to a molar extinction coefficient of $4.19 \times 10^6 M^{-1} cm^{-1}$. The measured maximum absorption value for the gold solution is 0.403 at 518 nm (indicated by the dotted line). Taking into account the length of the cuvette of 1 cm, a concentration of the gold NP solution of 9.6×10^{-8}M was determined from Lambert-Beer's law, given in equation (3.1). The concentration of the gold NP stock solution was estimated to be 2.7×10^{-6}M. Both values depend crucially on the real size of the gold NPs and the absolute value might

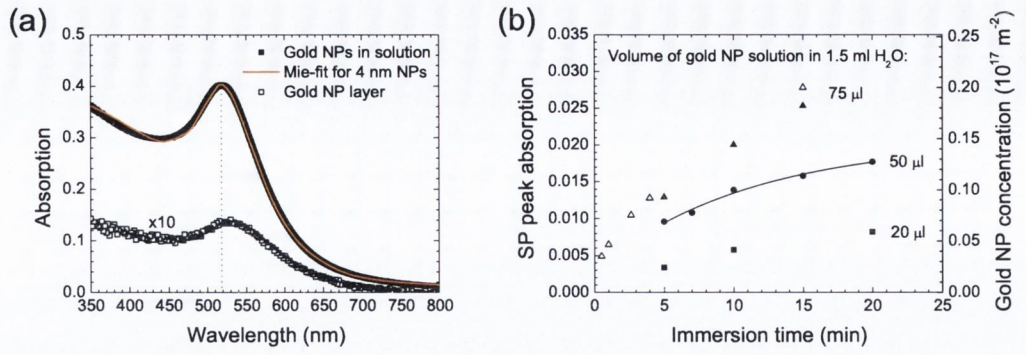


Figure 3.7: (a) Absorption spectrum of a 9.6×10^{-8} M gold nanoparticle (NP) solution (solid black squares) and a gold NP layer (open black squares, multiplied by $\times10$) deposited from a 8.7×10^{-8} M gold NP solution for 10 minutes immersion time. The orange line represents a calculation of the gold NP extinction spectrum with Mie-theory for a NP diameter of 4 nm. The dotted line indicates the maximum in the measured solution spectrum. (b) Dependence of the surface plasmon (SP) peak absorption value on the immersion time for layers deposited from gold NP solutions with different concentrations (3.6×10^{-8} M - solid squares; 8.7×10^{-8} M - solid circles; 1.3×10^{-7} M - triangles). On the right-hand-axis the approximate NP concentration in the layer is shown. The data represented by solid symbols was measured for samples prepared on the same day and open triangles indicate data recorded for samples prepared more than a year later.

actually be different as the fitting with Mie-theory does not take into account any size distribution or non-spherical particles [151]. However, as only this one gold NP solution has been used for all experiments, rather than interpreting the gold NP concentrations as absolute numbers the values can be used for a relative comparison of the gold NP concentration for the different samples prepared.

The gold monolayer absorption spectrum (multiplied by $\times10$) shown in Figure 3.7(a) was deposited by immersion for 10 minutes in a gold NP solution with a concentration of 8.7×10^{-8} M. As can be seen, the SP absorption peak value is slightly shifted to the red, compared to that of the solution, due to dipole-dipole interactions between the closely-packed gold NPs in the layer [154, 155, 156]. Due to this red-shift a fitting with Mie-theory cannot be used to determine the gold NP concentration in the layer, c_{AuML}, directly. However, with equation (3.3), a rough estimation of c_{AuML} was made from the absorption value A_{AuML}, at the SP peak wavelength λ_{peak} in the monolayer, using the molar extinction coefficient determined for the solution. With Lambert-Beer's law a concentration of

$$c_{AuML} = \frac{A_{AuML}\left(\lambda_{peak}\right)}{4.19\times10^{6}} \cdot \frac{1}{2} \cdot 6.022\times10^{24}\ \mathrm{m}^{-2} = 1.0\times10^{16}\ \mathrm{m}^{-2} \qquad (3.3)$$

is obtained. This corresponds to a sub-monolayer coverage, as with a diameter of 4 nm a maximum concentration of 7.2×10^{16} m^{-2} can be achieved in a single layer.

The concentration of the gold NPs in the layers was varied by changing the immersion time, as for the QD deposition, or by changing the concentration of the NPs in the solution used for the deposition. As shown in Figure 3.7(b) the concentration of the NPs in the layer, represented by the surface plasmon peak absorption, increases with increasing immersion time for a constant concentration in solution. The concentration increases faster with time when the samples are immersed in solutions with higher gold NP concentrations for the deposition. In addition, absorption peak values measured for a set of samples prepared more than a year later (open triangles) with respect to the other samples (solid symbols) is shown. As can be seen the absorption values measured for the samples prepared from the same concentration but over a year apart show similar absorption values, indicating that the gold NP solution only changed very little over time. In addition to the surface plasmon absorption peak value, the concentration is also given on the right-hand-axis in Figure 3.7(b). However, as mentioned above, this should not be understood as an absolute value but is only an approximate estimation of the actual NP concentration in the layer that will only be used for comparison of samples prepared from the same gold NP solution.

3.3 Photoluminescence

The photoluminescence (PL) and PL excitation (PLE) spectra of the QD solutions and layer structures were recorded with a Perkin-Elmer LS 55 fluorescence spectrometer. A pulsed Xenon lamp was used as light source and provided a variable excitation wavelength for the PL and PLE measurements. PL spectra of the QD samples were usually recorded with an excitation wavelength of 400 nm, at which all donor and acceptor QDs absorb well, and at 470 nm, the excitation wavelength used for time-resolved PL measurements discussed in the following section. For the acquisition of the solution spectra usually neutral density filters with transmission of 1 or 10% were used in the detection path to reduce the intensity of the emission and avoid saturation of the detector signal. Due to the reduced quantum yield and lower QD concentration, the measurement of the PL spectra of the layer structures could be carried out without filters.

The PL spectrum of the Don1 QD solution (squares) is shown in Figure 3.8(a) along with its absorption spectrum (line) (see also Figure 3.4(a)). As can be seen the Stokes shift, indicated by the short lines and arrow, between the first absorption and PL peaks is quite significant, in this particular case about 35 nm or 121 meV. The width of the PL peak is dominated by the inhomogeneous broadening due to the size distribution present in the QD samples. The inhomogeneous broadening can be described by the full

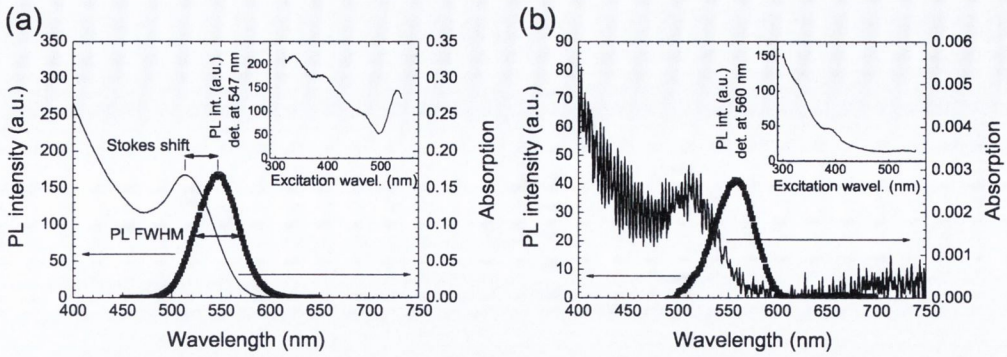


Figure 3.8: (a) Photoluminescence (PL) spectrum of the Don1 QD solution (solid squares), recorded with a 1% transmission filter. The absorption spectrum (line) of the solution is shown as well and the arrows indicate the Stokes shift beween the first absorption and PL peak as well as the full width at half maximum (FWHM) of the PL peak. The inset shows the photoluminescence excitation (PLE) spectrum of the solution recorded at an emission wavelength of 547 nm. (b) PL (solid squares), recorded without neutral density filter, and absorption spectra (line) of a Don1 QD monolayer. The inset shows the PLE spectrum of the monolayer recorded at an emission wavelength of 560 nm.

width at half maximum (FWHM) of the PL peak, indicated by the arrow in 3.8(a). The FWHM is extracted from a fit with a Gaussian curve. The ratio of the FWHM and the centre emission wavelength or energy, in this case $\frac{163\text{meV}}{2.269\text{eV}} = 7.2\%$, is representative of the size distribution. The typical values for the QDs used here are between 6 and 9%.

In the inset of Figure 3.8(a), the PLE spectrum of the Don1 solution recorded at the peak emission wavelength of 547 nm is shown. One can clearly see the first absorption feature at 531 nm for the QDs emitting at 547 nm, it occurs slightly shifted compared to the first absorption feature shown in Figure 3.8(a). The PLE intensity increases with decreasing wavelength due to the increasing absorption coefficient of the QDs with increasing energy. Additional features in the PLE spectrum are attributed to an efficient, resonant excitation of excited QD states.

In Figure 3.8(b) the PL and absorption spectra (also shown in Figure 3.4(b)) of a Don1 QD monolayer are shown. Compared to the solution spectrum shown in Figure 3.8(a), the PL peak is shifted to the red and the origin of this red-shift will be discussed in detail in section 4.1. In the inset of Figure 3.8(b) the PLE spectrum of the Don1 monolayer detected at 560 nm is shown. Again the equivalent of the first absorption peak can be seen at high wavelength, but it is much smaller compared to the peak seen in the solution PLE spectrum. The most dominant feature in the monolayer PLE spectrum occurs at 390 nm which is thought to be due to polyelectrolyte emission recorded for the layer structures rather than an increased emission from the QDs.

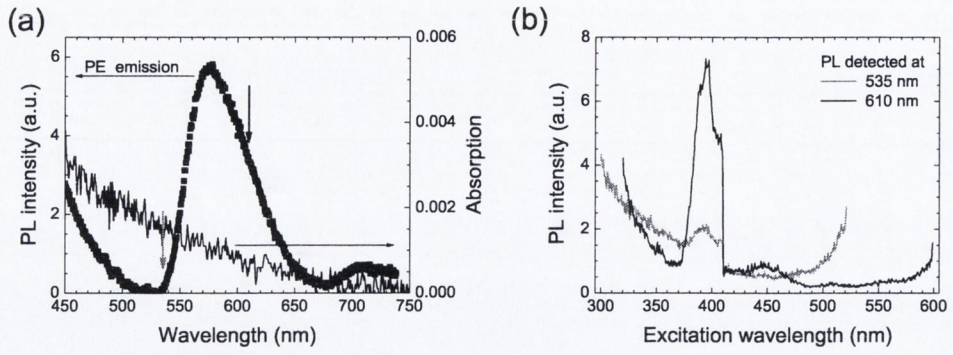


Figure 3.9: (a) Photoluminescence (PL) (solid squares) and absorption spectra (line) of a 8 polyelectrolyte (PE) bilayer sample. The grey and black arrow indicate the emission wavelength at which the PL excitation spectra (grey and black line) shown in (b) were recorded.

Some of the features visible in the PL and PLE measurements of the layer structures are attributed to emission from the PE layers [157]. In particular for excitation at 400 nm, emission in the range between 540 and 650 nm has been observed as can be seen in the polyelectrolyte spectrum recorded for a 8 BL sample shown in Fig. 3.9(a). The PE background emission has been removed from the measured QD spectra where possible. Also shown in Figure 3.9(b) are two PLE spectra recorded for the 8 BL polyelectrolyte sample at 535 and 610 nm, typical donor and acceptor emission wavelengths. As can be seen, the feature at 390 nm observed in the QD monolayer PLE spectrum shown in the inset of Figure 3.8(b) can be assigned to PE emission.

3.3.1 Quantum Yield

The quantum yield Q of a material is defined as the ratio of the number of emitted to the number of absorbed photons. It is a value that can be used to compare the emission efficiency of different materials if excited under the same conditions and is therefore also referred to as quantum efficiency. As it is difficult to evaluate the absolute number of absorbed and emitted photons, the quantum yield Q_{sample} of the QD solutions and or layers is determined by comparison to a Rhodamine 6G standard sample with a quantum yield of $Q_{\text{Rho}} = 95\%$. [60]. Due to the difference in extinction coefficient and concentration (as well as absorption path length when comparing a QD layer to the Rhodamine 6G solution), the number of absorbed photons for the QD sample and the Rhodamine 6G standard in solution will be different. This difference is taken account of by the ratio of the sample and Rhodamine absorption at the excitation wavelength $\frac{A_{\text{Rho}}(\lambda_{ex})}{A_{\text{sample}}(\lambda_{ex})}$. The number of emitted photons is determined by integrating over the PL spectra of the QD sample $I_{\text{sample}}(\lambda)$ and the Rhodamine sample $I_{\text{Rho}}(\lambda)$, shown in Figure 3.10.

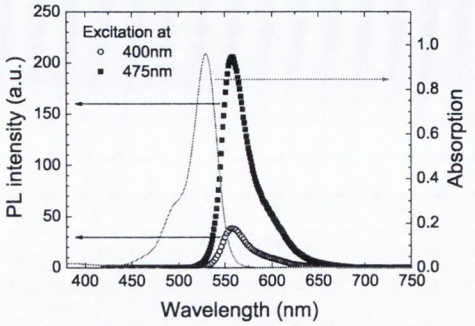


Figure 3.10: Absorption (grey line, right-hand axis) and photoluminescence (PL) spectra (left-hand axis, recorded with a neutral density filter with 1% transmission for 400 nm (solid squares) and 475 nm (open cirlces) excitation of a Rhodamine 6G solution.

The integration was carried out between 500 and 700 nm, covering the whole emission range of all QD samples as well as of the Rhodamine. To facilitate the evaluation of the quantum yield the emission spectra of the sample of interest and the standard are recorded with the same excitation wavelength. This ensures that the excitation intensity is the same in both cases. Additionally, as the QDs and the Rhodamine are dissolved in different solvents, water and ethanol respectively, the difference in refractive index n of 1.333 and 1.329 has to be corrected for.

$$Q_{\text{sample}} = \frac{A_{\text{Rho}}(\lambda_{ex})}{A_{\text{sample}}(\lambda_{ex})} \cdot \frac{\int_{500nm}^{700nm} I_{\text{sample}}(\lambda)\, d\lambda}{\int_{500nm}^{700nm} I_{\text{Rho}}(\lambda)\, d\lambda} \cdot \left(\frac{n_{\text{sample}}}{n_{\text{Rho}}}\right)^2 \cdot Q_{\text{Rho}} \qquad (3.4)$$

From the Rhodamine absorption and PL spectra shown in Figure 3.10 the following values were obtained for the calculation of the quantum yield:

Rhodamine absorption:

0.0167 at 400 nm

0.1004 at 475 nm

Integrated PL (from 500 to 700 nm, for 1% transmission) filter:

1635 for 400 nm excitation

8828 for 475 nm excitation .

Including these values in equation (3.4) gives equation (3.5), which can be used to evaluate the quantum yield Q_{sol} for solutions:

$$Q_{\text{sol}} = \frac{0.0167}{A_{\text{sol}}(\lambda_{ex})} \cdot \frac{\int_{500nm}^{700nm} I_{\text{sol}}(\lambda)\, d\lambda}{1635} \cdot \left(\frac{1.333}{1.329}\right)^2 \cdot 0.95\ . \qquad (3.5)$$

To determine the quantum yield Q_{ML} for QD monolayers an additional factor $\frac{0.7}{0.5}$ takes

into account the different contributions of the layers at the front and back of the samples to the PL spectrum (factor 0.7 determined experimentally) and the absorption spectrum. Additionally, a refractive index $n = 1.5$ for the ligand and surrounding polyelectrolyte is used, instead of that for water. The integrated PL value might have to be adjusted by a factor of 0.1 or 0.01 if the QD PL spectra of the layers or solutions were recorded with a 10% or no transmission filter. From the spectra of the Don1 QD monolayer shown in Figure 3.8 a quantum yield

$$Q_D = \frac{0.0167}{0.0047} \cdot \frac{2065}{1635} \cdot 0.01 \cdot \left(\frac{1.5}{1.329}\right)^2 \cdot \frac{0.7}{0.5} \cdot 0.95 \approx 8\%$$

was determined.

3.3.2 Förster Radius

For the analysis of Förster resonant energy transfer (FRET) and the modelling of its distance and concentration dependences of the process, the Förster radius R_0 is an important parameter to know, as discussed in section 2.2.1. R_0 can be calculated with equation (2.4) via the spectral overlap J of the donor emission and acceptor absorption. The equation to calculate J by integrating over the area-normalized donor PL spectrum $\hat{I}_D(\lambda)$ and the acceptor extinction spectrum $\epsilon_A(\lambda)$ is given in (2.3) and repeated here for convenience:

$$J = \int_0^\infty \epsilon_A(\lambda) \cdot \hat{I}_D(\lambda) \cdot \lambda^4 d\lambda \; . \tag{3.6}$$

The area-normalized Don1 solution PL spectrum and the Acc2 solution extinction spectrum, obtained from the acceptor absorption spectrum by adjusting the value at the first absorption spectrum to the value of the extinction coefficient obtained from the fitting curve given in [55], are both shown in Figure 3.11. The overlap integral calculated with equation (3.6) for these two QD solutions with a program written in MatLab is $J = 1.19 \times 10^{-16} \frac{\text{nm}^4}{\text{M·cm}}$.

With equation (2.4) R_0 can then be calculated for this value of J with a volume-weighted refractive index n =2.1 and $\kappa^2 = 2/3$ for randomly oriented dipoles:

$$R_0 = 0.0211 \cdot \left(\frac{2/3 \cdot Q_D}{2.1^4} \cdot 1.19 \times 10^{-16}\right)^{1/6} ,$$

in dependence of the donor quantum yield, Q_D. For the Don1 solution $Q_D = 32\%$ and for the monolayer shown in Figure 3.8(b) $Q_D = 8\%$. Therefore, R_0 would be (4.8 ± 0.2) nm in solution, but taking into account the reduction of the QD quantum yield in the layers R_0 for Don1 and Acc2 reduces to (3.8 ± 0.2) nm. In addition to the reduction

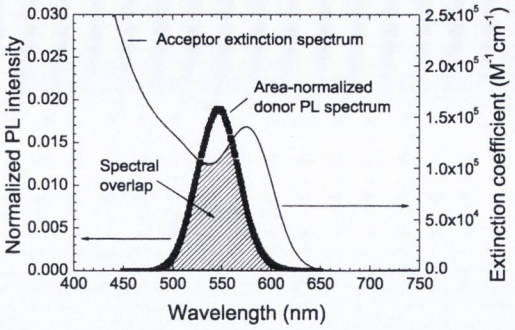


Figure 3.11: Area-normalized photoluminescence (PL) spectrum (solid squares) of the Don1 QD solution and extinction spectrum (line) of the Acc2 QD solution, converted from the absorption spectrum shown in Fig. 3.4(a). The shaded area indicates the spectral overlap of the donor and acceptor QDs.

in quantum yield, also the red-shift of the donor emission in the layer can be taken into account by calculating the overlap including the area-normalized donor PL spectrum of a donor monolayer rather than the solution spectrum. However, the effect on the value of R_0 is less important than that of the quantum yield and lies within the estimated error of 0.2 nm.

As can be seen in Figure 3.8(a), there is also a significant overlap of the Don1 emission with its own absorption, which is referred to as self-overlap in the following. This self-overlap arises from the large inhomogeneous broadening and a small Stokes shift and can lead to FRET within the QD ensemble if the QDs are sufficiently close to each other. To calculate R_0 and therefore the typical interaction distances for this intra-ensemble FRET, the overlap J can be evaluated for the area-normalized donor PL and the extinction spectrum of the same QD sample (in solution). For the Don1 sample the self-overlap, evaluated with equation (3.6) in the same way as the donor-acceptor overlap described above, is $3.32\times10^{-15}\,\frac{\mathrm{nm}^4}{\mathrm{M\cdot cm}}$ and an intra-ensemble R_0 of (2.8 ± 0.2) nm is obtained for Don1 monolayers. The influence of the self-overlap and intra-ensemble energy transfer on the optical properties of QD monolayers is presented in chapter 4 and its impact on donor-acceptor FRET is discussed in chapter 5.

3.4 Time-resolved Photoluminescence

The time-resolved PL decays were measured using a PicoQuant Microtime200 time-resolved confocal microscope system with 150 ps time-resolution. For excitation picosecond laser pulses at 470 nm were provided by a LDH-480 laser head, controlled by a PDL-800B driver(PicoQuant). The average excitation power was set to approximately 16 nW and pulse repetition rates of 5 or 10 MHz were used depending on the length

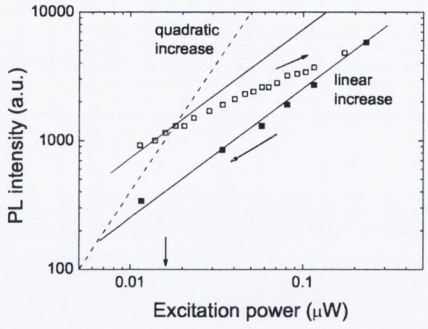


Figure 3.12: Dependence of the measured time-integrated intensity on the excitation power with the fluoresecence lifetime imagine microscopy system. Measurements were taken by increasing (open squares) and decreasing (solid squares) power. The solid and dashed lines represent a linear and quadratic increase with power respectively.

of the PL decay. The time-resolved signal was recorded with a single-photon avalanche diode (Perkin Elmer - SPCM-AQR, later replaced by a single-photon avalanche diode of the PDM series from Micro Photon Devices) via a 40x magnification objective. The PL decays were measured over areas of 80 by 80 μm^2 (150 $\times$ 150 pixels) with an integration time of 4 ms per pixel.

Under these experimental conditions the time-integrated PL intensity of a typical QD monolayer sample increases linearly with pump power as shown in Fig. 3.12, ensuring that only single excitons are generated in each QD. This also shows that at an excitation power of 16 nW not all QDs are excited at the same time. The sub-linear increase of the intensity at higher excitation powers measured for increasing power (open squares) is attributed to photobleaching of the QDs. No such effect was observed when decreasing the intensity quickly back to the initial power value (solid squares).

For spectral resolution, broad band filters with a FWHM of approximately (70 ± 5) nm were placed in front of the detector. Filters with nominal central wavelengths of 500, 550, 600 and 650 nm were used. The transmission spectra for these filters are shown in Figure 3.13. For the analysis of donor-acceptor FRET, signals recorded with the 500 and 600 or 650 nm filter were used to characterize the donor and acceptor decays respectively.

The time-dependence of the PL decays $I(t)$ was fitted by a two-exponential decay curve given in equation (3.7).

$$I(t) = I_1 \cdot e^{-t/\tau_1} + I_2 \cdot e^{-t/\tau_2} + I_0 \tag{3.7}$$

I_0 represents the background intensity of the measurement, I_1 and I_2 are the two

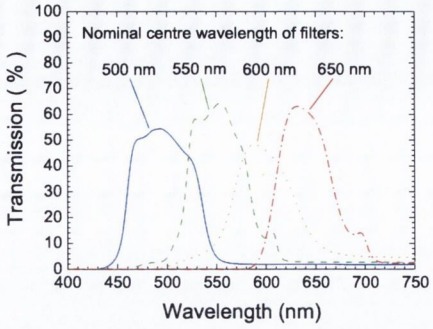


Figure 3.13: Transmission spectra of the 500 (solid blue line), 550 (dashed green line), 600 (dotted orange line) and 650 nm (dash-dot red line) filters. The wavelength represents the nominal centre wavelength, which is different from the actual centre wavelength measured in the transmission spectra.

intensity amplitudes for the exponential decays with two different lifetimes τ_1 and τ_2. An intensity-weighted average lifetime τ_{avg} is then calculated with (3.8) from the fitting parameters.

$$\tau_{avg} = \frac{I_1 \cdot \tau_1^2 + I_2 \cdot \tau_2^2}{I_1 \cdot \tau_1 + I_2 \cdot \tau_2} \tag{3.8}$$

All lifetimes mentioned in the following are intensity-weighted average lifetimes calculated with equation (3.8) if not stated otherwise.

The fit of the normalized PL decay measured with a 500 nm filter for a Don1 QD monolayer is shown as an example in Figure 3.14. The decay as measured, before normalization, is shown in the inset. For the emission on the blue side of the Don1 QD monolayer an average lifetime $\tau_{\text{blue}} = 4.8$ ns was calculated from the two-exponential decay fit.

In Figure 3.15(a) the PL decays of the 8 BL polyelectrolyte (PE) sample measured without filter (black line) as well as with a 500 nm (blue line) and a 650 nm filter (red line) are shown. Compared to the PL decay recorded for the QD monolayer, the maximum intensity of the PE emission decay is very low and the decays are very short for the measurements with filters. Therefore, the PE emission should usually not make a large contribution to the measured QD decays. The normalized PE PL decay measured without filter is shown in Figure 3.15(b) and a lifetime $\tau_{\text{avg}} = 4.5$ ns was determined from the two-exponential fit.

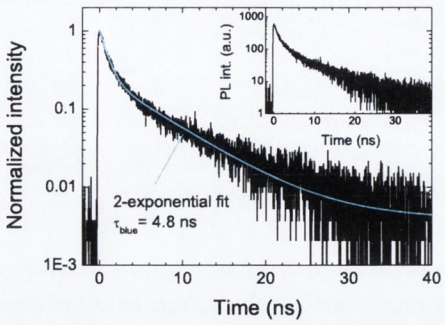


Figure 3.14: Time-resolved photoluminescence (PL) decay (black line) of a Don1 QD monolayer recorded with the 500 nm filter. A two-exponential fit (light-blue line) was used to calculate the average lifetime τ_{blue} on the blue side of the Don1 ensemble emission spectrum. In the inset the PL decay curve before normalization is shown.

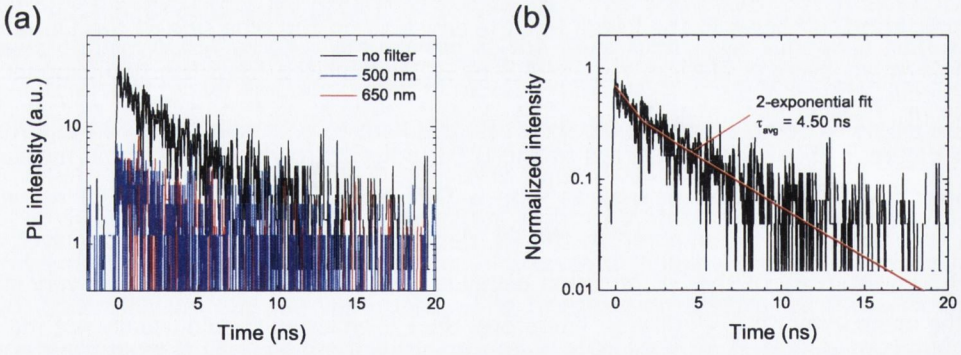


Figure 3.15: (a) Time-resolved PL decays of a 8 BL polyelectrolyte sample measured without filter (black line), with 500 nm (blue line) and with 600 nm (red line) filter. (b) Normalized PL decay of the 8 BL polyelectolyte sample measured without filter (black line) and two-exponential fit (red line) of the measured data.

4 FRET in QD Monolayers

As discussed in section 2.1.2, colloidal QDs have been proposed for many different types of applications and in particular for those that make use of FRET to generate energy flow, as QDs offer many advantages over molecular dyes commonly used in these structures. There have been reports on energy transfer within nominally monodispersed QD ensembles for mostly three-dimensional QD structures [99, 108, 113, 115, 158], but no detailed investigation of the influence of the QD concentration or the inhomogeneous broadening on intra-ensemble FRET has been carried out. However, intra-ensemble energy transfer has an effect on the spectral and dynamic properties of the QD emission and can therefore impact on device performance. This is particularly important for applications which require spectrally matched material such as FRET-sensors or energy funelling structures. Additionally, FRET theories have mainly been developed for molecular systems, where the fluorophores can be represented as point-dipoles, and for a long time it has not been clear if these theories can be directly applied to FRET structures containing QDs, due to their larger size, their inhomogeneous broadening and optical selection rules [108, 109]. Recent theoretical works [109, 110, 111, 112] have confirmed that standard FRET theory can be applied to semiconductor QDs, but very few and only qualitative comparisons of experiment and theory have been reported [108, 113, 114]. However, it is important to understand FRET in QD systems in more detail to enable accurate characterization of FRET in QD structures, reliable modelling of QD structures and optimization of device performance, not only for FRET QD structures but any system containing nanocrystal QDs.

In this thesis FRET in QD structures was investigated in detail. This chapter is concerned with FRET in QD monolayer structures. Firstly, a detailed study of FRET within monodispersed QD monolayers will be presented. In particular, the dependence of intra-ensemble energy transfer on QD concentration and inhomogeneous broadening of the QD ensemble will be analysed and these two parameters are found to allow for the control of intra-ensemble FRET at room-temperature. Then, FRET in a mixed donor-acceptor monolayer will be discussed and the concentration dependence of the FRET efficiency, acceptor enhancement and total PL emission will be presented. For both structures, the monodispersed and mixed QD monolayers, a theory of FRET in two dimensions taking into account exclusion zones around the donors [100] is applied to model the concentration dependence of the FRET process. The exclusion zones

are used to take into account the size of the QDs. The good agreement with theory shows that the observed energy transfer in the QD structures is mediated by the Förster mechanism and that it is appropriate to calculate the Förster radius from the spectral overlap of the inhomogeneously broadened QD spectra.

4.1 Monodispersed QD Monolayers

In this section, monodispersed QD monolayers prepared by the LbL technique from four different QD samples: Don1, Don2, Don3 and Acc2; are going to be characterized in detail. Parts of this section have been published and are reproduced with permission from M. Lunz et al., Physical Review B, 81, 205316, 2010. Copyright 2010 by the American Physical Society. The figures taken from this publication are indicated by a reference to the article in the caption.

The absorption (line, right-hand axis) and PL spectra (squares, left-hand axis) of the four QD solutions are shown in Figure 4.1. The Don1, Don2 and Don3 QDs emit in the green spectral range and the emission of Acc2 is in the red. The details on the emission wavelength, PL full-width-at-half-maximum (FWHM), the position of the first absorption peak as well as the Stokes shift can be found in Table 4.1. Comparing the values in energy for the different QDs, it can be seen that the PL FWHM for Don1 and Acc2 are significantly larger than their Stokes shift. The two parameters are similar for Don2, and for Don3 the PL FWHM is smaller than the Stokes shift. The QD sizes and concentrations in solution were determined from the absorption spectra as discussed in section 3.2.2. The smaller donor QDs have diameters of 2.7 nm (Don1), 2.2 nm (Don2) and 1.9 nm (Don3). The diameter of the Acc2 QDs is 3.5 nm. The concentrations are 3.5×10^{-6}M for the Don1 solution shown in Figure 4.1(a), 4.9×10^{-6}M for Don2 (b), 6.1×10^{-6}M for Don3 (c) and 2.7×10^{-6}M for the Acc2 solution (d).

4.1.1 Concentration Effects on Optical Properties

Monolayers of the three donor QDs were prepared with concentrations between 0.4×10^{17} m^{-2} and 3.5×10^{17} m^{-2}. The concentrations of the Acc2 QD monolayers were varied from 0.2×10^{17} m^{-2} to 0.7×10^{17} m^{-2}. The Acc2 concentration range is smaller than that for the donor QD monolayers, as less Acc2 QDs are needed to form a closely packed QD monolayer due to their larger size.

The absorption (line, right-hand axis) and PL spectra (solid squares, left-hand axis) of monolayers with concentrations of approximately 2.4×10^{17} m^{-2} for the donor QDs and 0.7×10^{17} m^{-2} for the Acc2 monolayer are shown in Figure 4.2. For comparison the PL spectra of the respective QD solutions have been included as well (open squares), with the peak intensity of the solution spectra normalized to that of the monolayers. As

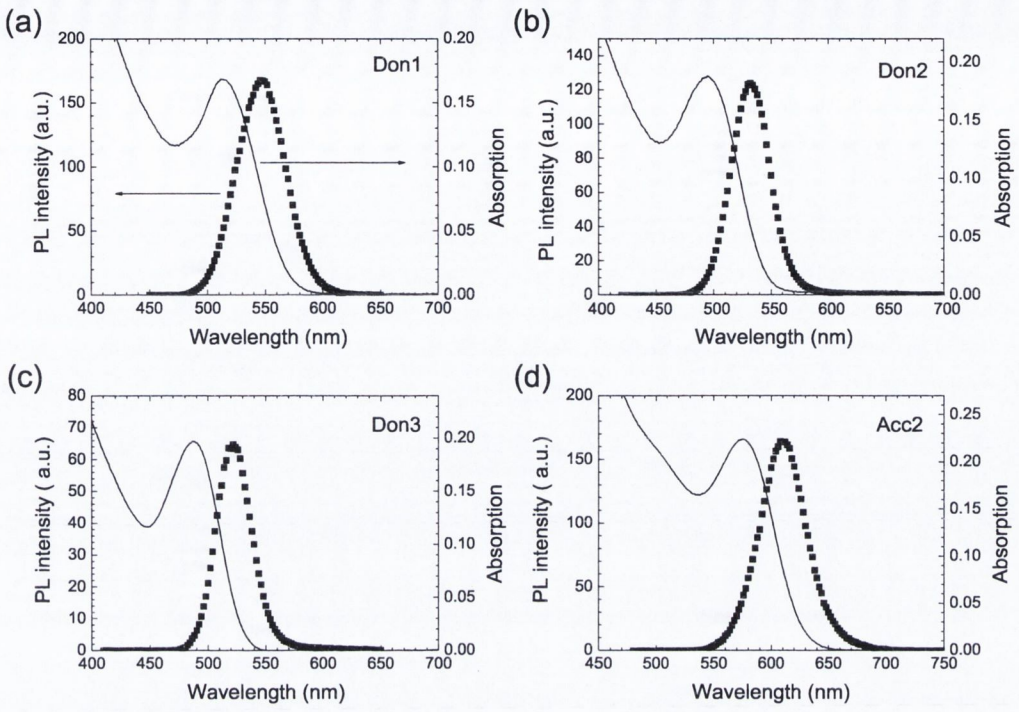


Figure 4.1: Photoluminescence (PL) (squares, left-hand axis) and absorption spectra (line, right-hand axis) for solutions of: Don1 (a), Don2 (b), Don3 (c) and Acc2 QDs (d). The wavelength scale for the Acc2 spectra is shifted 50 nm to the red. Figures (a), (b) and (c) are reproduced with permission from M. Lunz et al., Physical Review B, 81, 205316, 2010. Copyright 2010 by the American Physical Society.

QD Sample	PL peak (nm / eV)	PL FWHM (nm / eV)	First absorption peak (nm / eV)	Stokes shift (nm / eV)
Don1	546.5 / 2.269	50 / 208	514.0 / 2.412	32.5 / 143
Don2	532.0 / 2.331	40 / 175	495.0 / 2.505	37.0 / 174
Don3	522.0 / 2.375	36 / 164	486.5 / 2.538	35.5 / 170
Acc2	610.0 / 2.033	49 / 163	575.5 / 2.145	34.5 / 121

Table 4.1: Optical properties of Don1, Don2, Don3 and Acc2 QD solutions: PL peak position, PL FWHM, position of first absorption peak and Stokes shift in wavelength and energy.

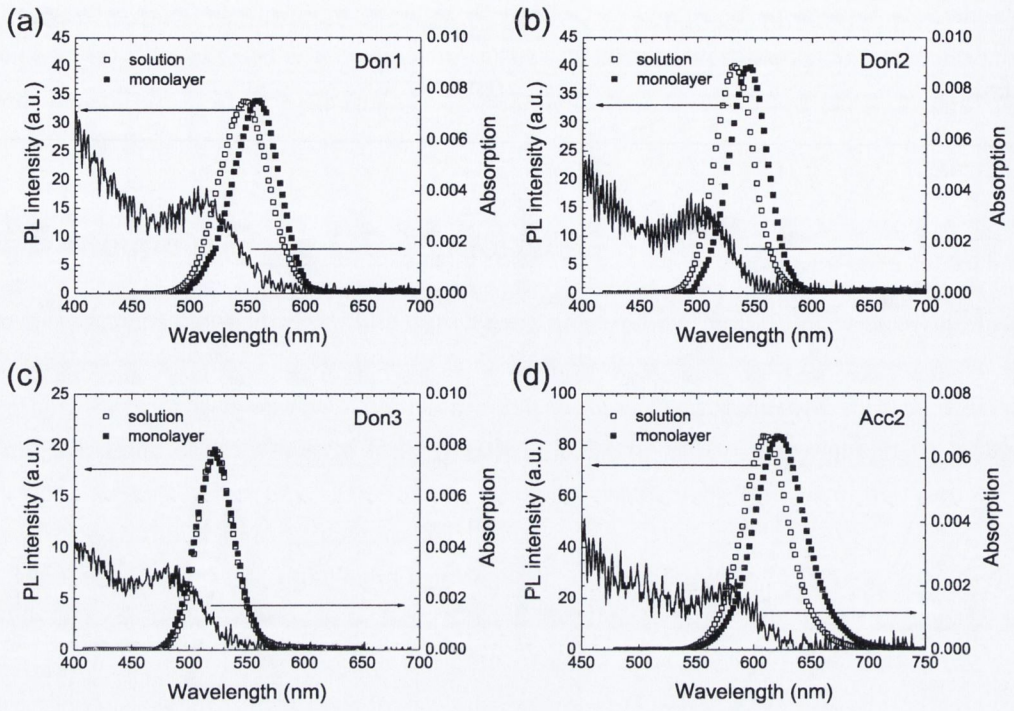


Figure 4.2: PL emission spectra (left-hand axis) of QD monolayers (solid squares) and solutions (open squares), with the solution peak intensity normalized to that of the monolayer for comparison. The QD monolayer absorption spectra (lines, right-hand axis) are also included. The spectra are shown for Don1 (a), Don2 (b), Don3 (c) and Acc2 (d).

can be seen, for the Don1, Don2, and Acc2 monolayers the PL peak is shifted to the red by more than 10 nm compared to the emission of the respective solutions, whereas for the Don3 monolayer no shift of the emission peak is observed. This red-shift observed for three out of the four QD samples is attributed to energy transfer within the QD monolayers and is going to be investigated in detail in this section.

The spectrally integrated PL intensities (solid squares, left-hand axis) as well as the PL peak positions (open circles, right-hand axis) in dependence of the QD concentration in the monolayers are presented in Figure 4.3. As expected, the integrated PL intensity of the monolayers increases with increasing concentration. The mostly linear increase with concentration, as indicated by the dashed lines included in each graph, shows that the quantum yield of the QDs in the monolayer is not changing with concentration. For Don1, Figure 4.3(a), the PL intensity seems to increase more slowly at high concentrations which could indicate a decrease in the quantum yield, but more data at high concentrations would be necessary to confirm the trend. From the slope of the lines shown in Figures 4.3 (a) to (d), the average monolayer quantum yields were determined

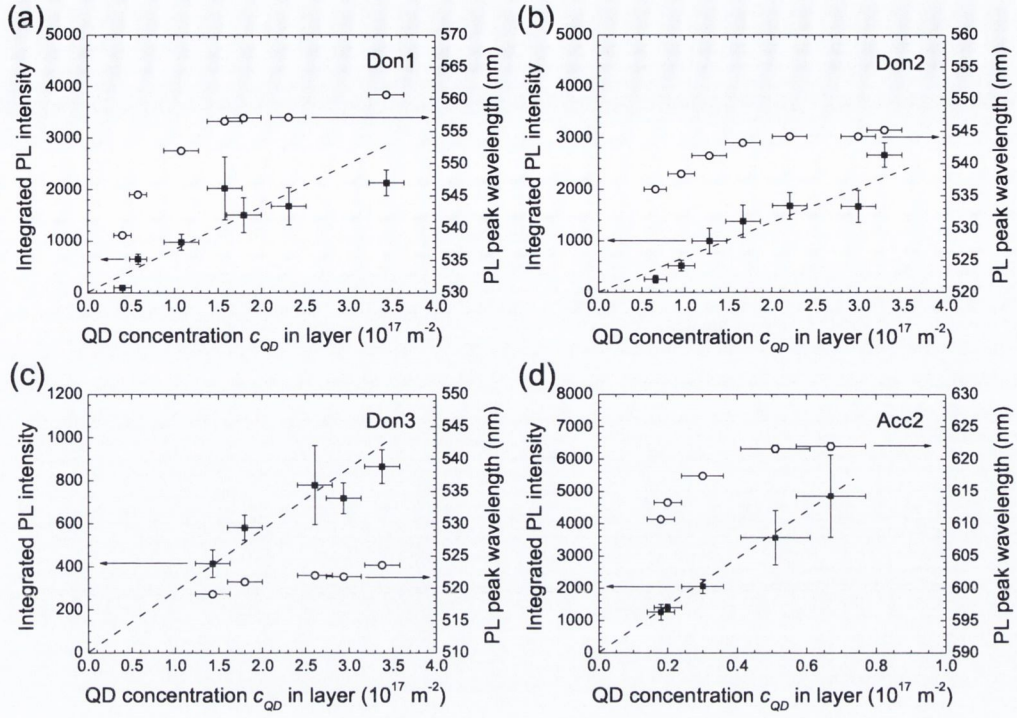


Figure 4.3: Dependence of the spectrally integrated PL intensity (solid squares, left-hand-axis) and the PL peak wavelength (open circles, right-hand-axis) on the QD concentration in the monolayers for Don1 (a), Don2 (b), Don3 (c) and Acc2 (d). The dashed lines indicate the mostly linear dependence of the integrated PL intensity on the QD concentration. Figures (a), (b) and (c) are reproduced with permission from M. Lunz et al., Physical Review B, 81, 205316, 2010. Copyright 2010 by the American Physical Society.

to be 5.3% for Don1, 4.5% for Don2, 3.0% for Don3 and 11% for Acc2 respectively.

Comparing the peak emission wavelengths determined for the monolayers with different QD concentrations in Figure 4.3, it can be seen that the PL emission wavelength shifts to the red with increasing QD concentration. The effect is the most significant for Don1 (Figure 4.3(a)), for which a peak shift of 16 nm is observed from 545 nm at a concentration of 0.6×10^{17} m^{-2} to 561 nm at 3.4×10^{17} m^{-2}. Over the same concentration range, the PL peak of the Don2 monolayers (Figure 4.3(b)) only shifts from 536 to 545 nm, corresponding to a change of 9 nm. For Don3 (Figure 4.3(c)) no reliable measurements at low concentration were possible due to its low quantum yield. Comparing the PL peak shift of the donor QD monolayers between 1.4 and 3.4×10^{17} m^{-2}, one can see that with a red-shift of 6 nm the effect is again largest for Don1. Don2 and Don3 both show shifts of 4 nm only. However the Don3 emission wavelength in the monolayers only varies around 522 nm, the PL peak wavelength measured for the Don3 solution, whereas the emission peak wavelength of the Don2 monolayers with the highest QD

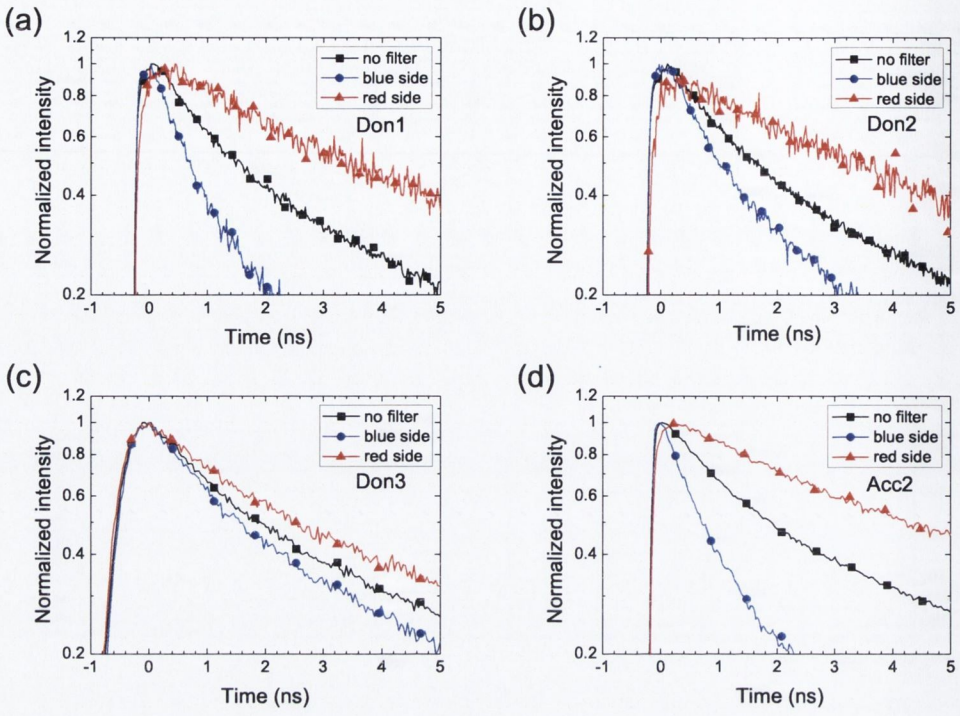


Figure 4.4: PL intensity decays of the overall ensemble emission (black line, squares) as well as for the blue (blue line, circles) and red side (red line, triangles) of the ensemble emission spectrum in donor QD layers with $c_{QD} \approx 2.4 \times 10^{17}\mathrm{m}^{-2}$ (Don1 (a), Don2 (b), Don3 (c)) and an Acc2 monolayer with a concentration $c_{QD} \approx 0.7 \times 10^{17}\mathrm{m}^{-2}$ (d). Figures (a), (b) and (c) are reproduced with permission from M. Lunz et al., Physical Review B, 81, 205316, 2010. Copyright 2010 by the American Physical Society.

concentrations is shifted by 13 nm compared to solution. For Acc2 (Figure 4.3(d)) the PL peak shifts by 12 nm from 611 nm at $0.2{\times}10^{17}$ m^{-2} to 622 nm at $0.7{\times}10^{17}$ m^{-2}, corresponding to a shift of 12 nm at the highest concentration investigated compared to the emission peak wavelength in solution. Therefore, the dependence of the PL peak wavelength on the concentration in the Acc2 monolayers is similar to those observed for Don1 and Don2. A red-shift, as seen in Figures 4.2 and 4.3, is a signature of energy transfer from the blue, high-energy side of the inhomogeneously broadened QD ensemble emission spectrum (smaller QDs) to the red, low-energy side (larger QDs). Changes in QD size or shape can be ruled out as the origin of the red-shift, as this would also have an impact on the absorption spectra and should affect all QDs including Don3. Surface effects due to chemical reactions can also be excluded as the QDs are well passivated by their TGA ligand shell.

In order to obtain more information about the underlying energy transfer mechanism, time-resolved PL measurements have been carried out. In Figure 4.4 (a) to (c) the PL

decays of Don1, Don2 and Don3 monolayers with an approximate concentration c_{QD} of $2.4\times10^{17}\mathrm{m}^{-2}$ are shown for measurements without a filter (black squares), with a 500 nm filter (blue circles) and a 600 nm filter (red triangles). The 500 nm filter was used to record the time-dependence of the emission on the blue side of the donor QD ensemble emission and the 600 nm filter to measure the signal on the red side. The respective emission decays for an Acc2 monolayer with $c_{QD} \approx 0.7\times10^{17}\mathrm{m}^{-2}$ can be seen in Figure 4.4(d); the PL decays on the blue and red sides of the Acc2 QD ensemble emission were recorded with the 550 and 650 nm filters respectively. All decays are shown over the first 5 ns only.

It can be clearly seen that for all QDs the PL decays on the blue side are shorter than those recorded without a filter and that the decays on the red side are longer. The difference between the time-traces measured on the blue and red side of the ensemble emission spectrum is largest for the Don1 and Acc2 monolayers, a little smaller for Don2 and much reduced for the Don3 monolayer. Furthermore, for Don1, Don2 and Acc2 the intensity maximum of the decays measured on the red side of the ensemble emission spectrum occurs at a later time than that of the decays measured on the blue side or without a filter. This time-delay is approximately 0.28 ns for the two donor QD monolayers and 0.25 ns for the Acc2 sample. No such effect is observed for the Don3 monolayer. A so-called rise-time in the emission decay on the red side of the ensemble emission spectrum is another indication for energy transfer from the smaller to the larger QDs, emitting on the blue and red side of the ensemble emission spectrum respectively.

The PL lifetimes on the blue and red side of the ensemble emission spectrum, τ_{blue} and τ_{red}, were calculated from the measured PL decays as described in section 3.4. In Figure 4.5 (a) to (d) the concentration dependences of τ_{blue} (solid squares, left-hand axis) and the lifetime difference between the blue and the red side, $1-\tau_{\mathrm{blue}}/\tau_{\mathrm{red}}$, are shown for the Don1, Don2, Don3 and Acc2 monolayers (open circles, right-hand axis).

Considering, firstly, the trends for Don1, one can see in Figure 4.5(a) that τ_{blue} decreases from 9.0 ns at a concentration of 0.4×10^{17} m^{-2} to 2.2 ns at 3.4×10^{17} m^{-2}, corresponding to a reduction of 75%. And while at low concentrations the lifetime difference is very small, $1-\tau_{\mathrm{blue}}/\tau_{\mathrm{red}}$ increases to almost 75% at the highest concentration investigated. The decrease of τ_{blue} with increasing concentration shows that the energy transfer from the blue to the red side of the QD ensemble emission is not of radiative nature but mediated by a non-radiative energy transfer mechanism.

Dexter transfer describes energy transfer by an exchange mechanism, i.e. tunneling [96, 97]. It requires the overlap of the donor and acceptor wavefunctions and usually only occurs over short distances of less than 1 nm. The minimum QD centre-to-centre separation is determined by the QD size and the thickness of the ligand shell, which is larger than 2 nm for all samples investigated here. In particular, for QD monolayers with

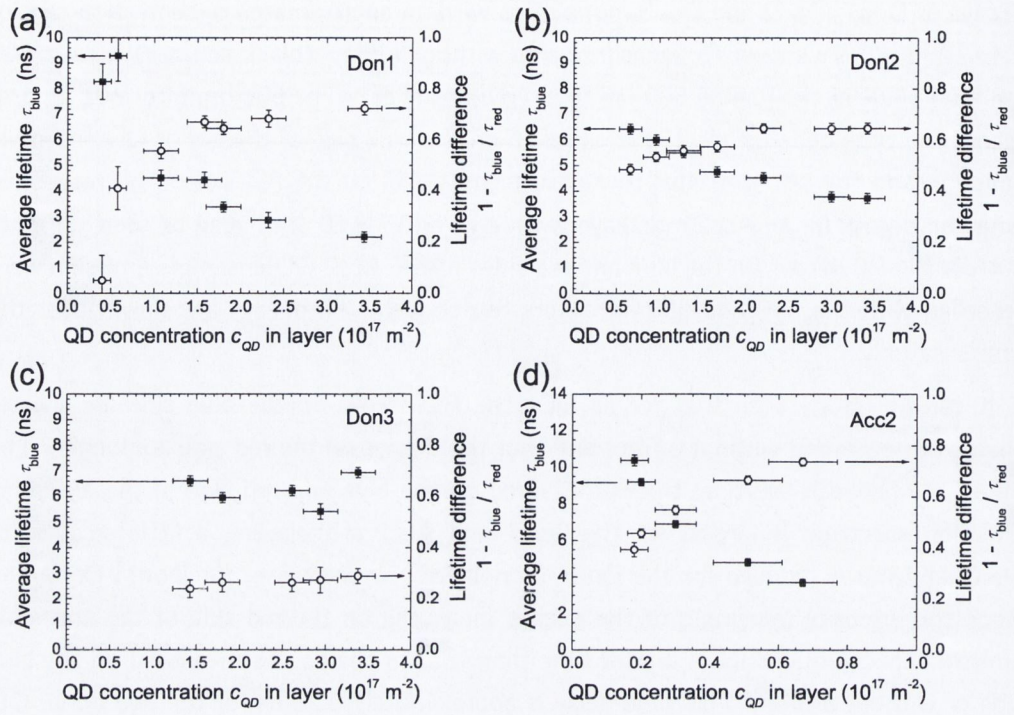


Figure 4.5: QD concentration dependence of the average lifetime τ_{blue} on the blue side of the ensemble emission spectrum (solid squares, left-hand axis) as well as of the lifetime difference between the red and blue sides, $1-\tau_{\text{blue}}/\tau_{\text{red}}$, (open circles, right-hand axis) for Don1 (a), Don2 (b), Don3 (c) and Acc2 (d). Figures (a), (b) and (c) are reproduced with permission from M. Lunz et al., Physical Review B, 81, 205316, 2010. Copyright 2010 by the American Physical Society.

low concentrations of approximately 0.5×10^{17} m^{-2}, the QD centre-to-centre separation is as large as 4.5 nm. Hence, Dexter transfer can be excluded as a possible energy transfer mechanism. The most likely origin of the observed concentration dependent effects is therefore Förster resonant energy transfer (FRET) based on dipole-dipole interactions, which can give rise to energy transfer over distances on the nanometer scale [14, 90, 95].

Even though the lifetime difference $1-\tau_{\text{blue}}/\tau_{\text{red}}$ and the decrease of τ_{blue} with concentration indicate that the energy transfer in the closely packed Don1 monolayers must be very efficient, they do not represent the actual FRET efficiency E_{FRET}. To calculate E_{FRET} at a concentration c_{QD}, $\tau_{\text{blue}}(c_{QD})$ has to be compared with an undisturbed value of the lifetime measured on the blue side of the ensemble emission spectrum, τ^0_{blue}:

$$E_{\text{FRET}} = 1 - \tau_{\text{blue}}(c_{QD}) / \tau^0_{\text{blue}} \,.$$

However, the decrease of τ_{blue} by 75% over the concentration range investigated, as

well as $1 - \tau_{blue}/\tau_{red} = 75\%$ at $c_{QD} = 3.4 \times 10^{17}$ m^{-2}, indicates that FRET efficiencies of at least 75% can be obtained in closely packed Don1 monolayers.

For Don2 (Figure 4.5(b)) τ_{blue} decreases a little less strongly than for Don1, from 6.4 ns at 0.7×10^{17} m^{-2} to 3.8 ns at 3.3×10^{17} m^{-2}, and the difference of τ_{blue} and τ_{red} increases only to 65% at 3.3×10^{17} m^{-2}. The concentration effects on the lifetimes for Don3 (Figure 4.5(c)) are fairly small. The PL lifetime τ_{blue} seems to be almost independent of the concentration, varying around a value of approximately 6.1 ns, and even at the highest concentration investigated the lifetime difference $1 - \tau_{blue}/\tau_{red}$ only reaches 30%. For Acc2 (Figure 4.5(d)) the dependence of τ_{blue} on the QD concentration in the monolayers is again quite strong and the values decrease from 10.4 ns at 0.2×10^{17} m^{-2} to 3.7 ns at 0.7×10^{17} m^{-2}. This corresponds to a decrease of τ_{blue} by 64% over the concentration range investigated. The lifetime difference of the blue and red side of the ensemble emission spectrum increases to 75% at 0.7×10^{17} m^{-2}, similar to the value reached for closely packed Don1 monolayers.

4.1.2 Theoretical modelling

For a more detailed characterization of the energy transfer in the monodispersed QD monolayers, a theoretical model of FRET between randomly distributed donors and acceptors in two dimensions, taking into account exclusion zones around the donors, is applied [100]. In colloidal nanocrystal QD structures, the QD size and the length of the stabilizing ligand give rise to a minimum QD centre-to-centre separation that can be included in the theoretical calculations in form of an exclusion zone. The theory is described in detail in section 2.2.1. Equation (2.11), reproduced as equation (4.1) below, is used to model the decrease of the lifetime τ_{blue} with increasing QD concentration c_{QD}, as presented in Figure 4.5. The exclusion zone radius, R_{ex}, the Förster radius, R_0, and the initial, undisturbed lifetime, τ^0_{blue}, are used as fitting parameters.

$$q_r = \int_0^\infty e^{-\lambda} \cdot \exp\left[-\pi \cdot C \cdot \gamma\left(2/3, \lambda/r^6\right) \cdot \lambda^{1/3}\right] \cdot \exp\left[\pi \cdot C \cdot r^2 \cdot \left(1 - e^{-\lambda/r^6}\right)\right] d\lambda \quad (4.1)$$

For a better comparison of the lifetime trends observed for the four different QD samples, the data is shown in form of the lifetime yield, $q_r = \tau_{blue}(c_{QD})/\tau^0_{blue}$, in Figure 4.6(a) and (b) for the donor samples and the Acc2 monolayers respectively. The measured lifetime τ_{blue} is converted into a lifetime yield by division with the value of τ^0_{blue} obtained from the modelling (value given in Table 4.2). In accordance with the concentration dependence of τ_{blue} shown in Figure 4.5, the decrease of the lifetime yield (shown in Figure 4.6(a)) with increasing QD concentration is the strongest for

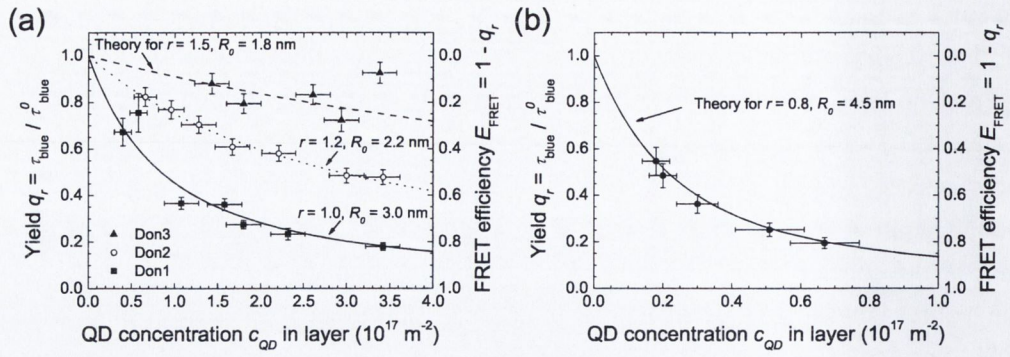


Figure 4.6: Measured (symbols) and calculated (lines) lifetime yield q_r (left-hand axis) as a function of the QD concentration c_{QD} for Don1 (solid squares), Don2 (open circles), Don3 (solid triangles) (all in (a)) and Acc2 (solid circles) (b). The corresponding values of the FRET efficiency E_{FRET} can be read off the right-hand axis. The values of the Förster radius R_0 and the ratio $r = R_{ex}/R_0$ used for the calculation of the trends are indicated next to the corresponding lines. Figure (a) is reproduced with permission from M. Lunz et al., Physical Review B, 81, 205316, 2010. Copyright 2010 by the American Physical Society.

the Don1 monolayers (solid squares); it is less strong but still quite significant for Don2 (open circles) and smallest for Don3 (solid triangles). The yield determined for the Acc2 monolayers, shown in Figure 4.6(b), is also observed to strongly decrease with increasing QD concentration, showing an impact of the QD concentration on the lifetime similar to that seen for the Don1 monolayers. This finding is in agreement with the similarity of the other FRET signatures observed for the Don1 and Acc2 QDs.

The best fits of the theoretically calculated yields to the data are shown as lines in Figure 4.5 and the values of R_0 and $r = R_{ex}/R_0$ used for the modelling are given next to the respective lines. The fitting parameters used to obtain the best agreement with the measured concentration dependence of the lifetime are summarized in Table 4.2 for all four QDs. As mentioned above, R_{ex} is determined by the relatively large size of the QDs and the length of the stabilizing ligand, 0.5 nm in the case of TGA [159]. As the ligand shells of two QDs can interpenetrate [145, 159] the length of the ligand is only included once in the calculation of the exclusion zone radius R_{ex}. The QD diameter d has been determined for all four QD samples from their absorption spectra in solution (shown in Figure 4.1) and the values of d and R_{ex} are given in Table 4.2. The value of R_{ex} used in the modelling was kept within ± 0.3 nm of the exclusion zone radius determined from the donor QD size and within ± 0.4 nm for the larger Acc2 QDs. As can be seen for all four QDs the experimentally observed trends can be well reproduced by the theoretical model over the whole concentration range. This shows that the decrease

	Obtained from QD spectra			Obtained from lifetime data		
QD Sample	d (nm) $\pm$ 10%	R_{ex} (nm) $\pm$ 10%	R_0 (nm) $\pm$ 10%	R_{ex} (nm) $\pm$ 10%	R_0 (nm) $\pm$ 10%	τ^0_{blue} (ns) $\pm$ 0.3 ns
Don1	2.7	3.2	2.8	3.0	3.0	12.3
Don2	2.2	2.7	2.5	2.7	2.2	7.8
Don3	1.9	2.4	2.0	2.7	1.8	7.5
Acc2	3.5	4.0	3.7	3.6	4.5	19.6

Table 4.2: QD diameter (d), exclusion zone radius (R_{ex}) and Förster radius (R_0) as determined from the absorption and emission spectra of the QD samples; fitting parameters R_{ex}, R_0 and undisturbed lifetime (τ^0_{blue}) used for the theoretical modelling of the concentration dependence of the lifetime τ_{blue}. The errors on the values are given below the column headings.

of the lifetime measured on the blue side of the QD ensemble emission with increasing concentration can be fully explained within FRET theory. No deviation of the data from the theoretically calculated trend is observed at high concentrations, corresponding to closely packed monolayers and the smallest centre-to-centre separation possible for these QDs. Therefore, it can be concluded that even when the QDs are in close proximity no significant contribution of Dexter transfer, influencing the energy transfer from the blue to the red side of the QD ensemble, is observed and that intra-ensemble energy transfer is dominated by FRET.

The validity of the application of the theoretical model can be further confirmed by the comparison of the R_0 obtained from the fitting of the lifetime data with that calculated from the spectral self-overlap as described in section 3.3.2. It is important to note that the self-overlap should be calculated from the spectra of the QD solution, for which no effect of intra-ensemble transfer is observed. The red-shift of the PL emission peak in the monolayers is a consequence of the intra-ensemble transfer and using the monolayer PL spectra in the calculation of the self-overlap would result in a reduced value of the overlap and an underestimation of R_0. The self-overlap calculated for the solution spectra shown in Figure 4.1 are

$3.32 \times 10^{-15} \frac{nm^4}{M \cdot cm}$ for Don1,
$1.40 \times 10^{-15} \frac{nm^4}{M \cdot cm}$ for Don2,
$0.67 \times 10^{-15} \frac{nm^4}{M \cdot cm}$ for Don3 and
$7.65 \times 10^{-15} \frac{nm^4}{M \cdot cm}$ for Acc2.

The spectral self-overlap of the Acc2 QD ensemble is larger than those of the donor QDs, because of the larger size of the Acc2 QDs, giving rise to a larger extinction cross section, and an emission at higher wavelengths than for the donor QDs, which both increase the value of the spectral overlap.

The values for R_0 calculated from the self-overlap of the QDs in solution are also given in Table 4.2. A good agreement, within the estimated error ranges, is found for R_{ex} and R_0 determined from the spectral properties of the QDs with the values used for the modelling of the lifetime data in Figure 4.6. The values obtained for Acc2 show a larger deviation, which is attributed to a larger error in determining the characteristic values arising from their larger size and the larger spectral overlap value calculated for these QDs. The overall good agreement of the two sets of parameters confirms that intra-ensemble energy transfer is mediated by the FRET mechanism and that no other process has to be taken into account to explain the measured concentration dependence of τ_{blue}. Therefore, it can be concluded that tunnelling between QDs or surface effects due to direct contact of the QDs have a negligible effect on the optical properties of monolayers prepared with this type of chemically stabilized QDs.

The FRET efficiency E_{FRET} can be calculated as $1 - q_r$ and these values are indicated on the right-hand axis of Figure 4.6. It is important to note that the dependence of the lifetime difference, $1 - \tau_{\text{blue}}/\tau_{\text{red}}$, on the QD concentrations, shown in Figure 4.5, follows a trend similar to that of the FRET efficiency for all four QD samples. Therefore, even though the lifetime difference is not equivalent to E_{FRET}, it can still be used as an indicator for the probability of FRET at any given concentration.

The FRET efficiency of Don1 and Acc2 monolayers increases to values over 80% in monolayers with high QD concentrations, due to the large self-overlap of these QDs, arising from a relativley large inhomogeneous broadening and a small Stokes shift. As can be seen, E_{FRET} is reduced for lower concentrations, providing the possibility to tune the FRET efficiency in monodispersed QD structures via the QD concentration. The maximum FRET efficiency that is observed at high concentrations for the Don2 and Don3 samples, approximately 55% and 30%, is reduced compared to that of the Don1 monolayers. This indicates that, as expected from theory, the FRET efficiency also strongly depends on the spectral overlap. As the self-overlap increases from Don3 to Don2 to Don1, corresponding to a decrease of the PL FWHM and / or an increase in the Stokes shift, an increased FRET efficiency and a stronger effect of the QD concentration on the optical properties of the QD monolayers is observed.

4.1.3 Effect of Self-Overlap

The impact of the self-overlap on intra-ensemble FRET has been investigated in more detail by extending the study of the optical properties of monodispersed QD monolayers to ten different green-emitting QDs, including Don1, Don2 and Don3 discussed in detail above. The size of the QDs varies between 1.0 and 2.8 nm and their PL peak wavelength range from 511 to 553 nm. To compare the effect of energy transfer within the QD ensembles for monolayers prepared from these ten QD samples, the lifetime difference

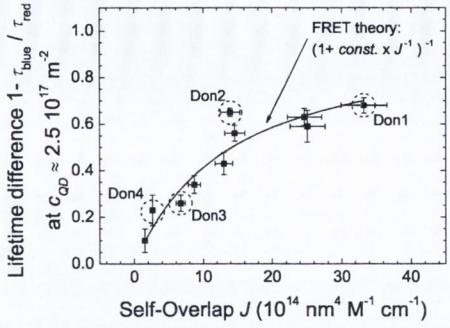


Figure 4.7: Lifetime difference of the blue and red side of the QD ensemble emission (squares) for monolayers with a concentration $c_{QD} \approx 2.5 \times 10^{17}$ m^{-2} as a function of the self-overlap J for ten different QD samples. The theoretically calculated trend (line) is based on the dependence of the FRET efficiency on the self-overlap J. Reproduced with permission from M. Lunz et al., Physical Review B, 81, 205316, 2010. Copyright 2010 by the American Physical Society.

on the blue and red side of the QD ensemble emission, $1 - \tau_{blue}/\tau_{red}$, has been determined experimentally for monolayers with similar concentrations. As discussed above, the lifetime difference does not represent the actual FRET efficiency, but follows a similar concentration dependence and can therefore be used as an indicator for the probability of intra-ensemble energy transfer. To evaluate E_{FRET}, it is necessary to determine τ^0_{blue} by modelling $\tau_{blue}(c_{QD})$. This would require the measurement of τ_{blue} for at least two monolayers with different QD concentrations, including one relatively low concentration, to enable a reliable fitting of the lifetime decrease with concentration. Therefore, it is more convenient to instead determine the lifetime difference, $1 - \tau_{blue}/\tau_{red}$, at a single concentration and to use this quantity to evaluate the different levels of intra-ensemble FRET for the ten samples.

The lifetime difference, measured for monolayers with a concentration of approximately 2.5×10^{17} m^{-2}, is shown as a function of the self-overlap J for the ten different QD samples in Figure 4.7. As can be seen, $1 - \tau_{blue}/\tau_{red}$ increases with increasing J. This clearly shows that for QD ensembles with a larger self-overlap, intra-ensemble FRET has a stronger impact on the optical properties of QD monolayers, as already suggested by the comparison of the Don1, Don2 and Don3 monolayers.

The dependence of E_{FRET} on the self-overlap J:

$$E_{FRET} = \frac{1}{1 + \left[\sum_i (R_0/r_i)^6\right]} = \frac{1}{1 + \text{const.} \cdot J^{-1}}\,, \tag{4.2}$$

where r_i represents the distance between one QD and its i^{th} neighbour, can be used to

fit $1 - \tau_{blue}/\tau_{red}$ as a function of J. If one assumes that only nearest neighbours will interact with each other via FRET, because of the relatively small R_0 compared to the QD separations, the constant in equation (4.2) can be simplified to

$$\text{const.} = \left(\frac{r_{DA}}{0.0211}\right)^6 \frac{n^4}{6 \cdot \kappa^2 Q_D} \,. \tag{4.3}$$

The separation r_{DA} has to be included in nm in equation (4.3) as J is calculated in units of $\text{nm}^4/(\text{M} \cdot \text{cm})$. The next-neighbour separation r_{DA} between the QDs is approximately R_{ex}, as closely packed layers are formed at $c_{QD} \approx 2.5 \times 10^{17}\ \text{m}^{-2}$. The average R_{ex} for all ten QD samples is 2.7 nm and the average quantum yield $Q_D = 2\%$. Including a refractive index of 2.1 and $\kappa^2 = 2/3$, as outlined in section 3.3.2, the constant given in equation (4.3) is of the order of 1.1×10^{15}. The best agreement with the data, shown as a line in Figure 4.7, was obtained for const.$= 1.4 \times 10^{15}$. This value agrees well with the expected one considering that the data is based on measurements of QDs with different sizes and quantum yields. It also confirms that it is valid to use the lifetime difference measured at a single concentration, rather than the FRET efficiency which is be more difficult to determine, to evaluate the probability for intra-ensemble energy transfer in monodispersed QD structures.

The comparison of the ten QD samples and the good agreement with FRET theory clearly show that, as already suggested for other mainly three-dimensional monodispersed QD structures [99, 108, 113, 115, 158], intra-ensemble transfer arises from the overlap of the first absorption peak and the PL emission of the inhomogeneously broadened QD ensembles. Choosing the spectral properties of the QD sample and carefully tuning the QD concentration in any QD structure therefore presents another means to control intra-ensemble FRET other than by temperature [158].

Intra-ensemble energy transfer in monodispersed QD structures, that are, for example, used as components for FRET structures, light-emitting devices or energy funelling structures, can affect device performance and have an impact on measurement results, as will be presented in section 5.4 of the next chapter. As temperature tuning is not very practical for QD based devices, it is important to choose QDs with a low self-overlap where intra-ensemble transfer could pose a problem for experiments and applications. As can be seen in Figure 4.7, low levels of intra-ensemble FRET can be expected for green-emitting QDs with a self-overlap smaller than $1.0 \times 10^{15}\ \text{nm}^4/(\text{M} \cdot \text{cm})$. The self-overlap is mainly influenced by the Stokes shift and the PL FWHM. In order to decrease the overlap, usually a stronger size selection is carried out to reduce the PL FWHM, which will also reduce the overall luminescence of the sample. Furthermore, the quantum yield seems to be decreasing for QDs with increasing Stokes shift [51]. Therefore, the advantages of using QDs with a small self-overlap over a high quantum

yield have to be considered.

It is important to note that the data shown in Figure 4.7 can only be used as a reference curve for green-emitting QDs and monolayers with concentrations of approximately 2.5×10^{17} m^{-2}. For example for a monolayer of Acc2 QDs ($J = 7.65 \times 10^{15}$ $nm^4/(M \cdot cm)$) with $c_{QD} = 0.7 \times 10^{17}$ m^{-2}, a lifetime difference of 75% was determined. However, at the relatively low concentration of $c_{QD} = 0.7 \times 10^{17}$ m^{-2} a maximum lifetime difference of 50% was observed for Don1 QDs with the highest self-overlap of the green-emitting QDs investigated (see Figure 4.5(a)). As mentioned above, due to their larger size and emission wavelength, larger values of the self-overlap can be obtained for Acc2 QDs than for the smaller green-emitting QDs, explaining why a larger lifetime difference is observed for Acc2 than for Don1 at the same QD concentration. Furthermore, Acc2 QDs have a larger minimum centre-to-centre separation and only lower concentrations can be achieved in the closely packed monolayers due to their larger size. Therefore, Acc2 cannot be included in the comparison of the lifetime difference for the smaller green-emitting QDs, but a different reference curve has to be used. For nanocrystal QDs of different sizes and / or materials emitting in a different wavelength range, as well as for different QD structures, equations (4.2) and (4.3) can be adopted to estimate the self-overlap for which low levels of intra-ensemble FRET will occur.

4.2 Mixed donor - acceptor monolayer

In the following, energy transfer between donor and acceptor QDs in mixed donor-acceptor monolayers will be discussed. Parts of this chapter have been published and are reproduced with permission from Journal of Physical Chemistry C 2009, 113, 3084 Copyright 2009 American Chemical Society.

The mixed monolayers were prepared from QD solutions containing varying concentration ratios of Don3 and Acc1 QDs. The Don3 solution spectra were presented above in Figure 4.1(c) and the Acc1 solution spectra are shown in Figure A.2 in appendix A.2. The Acc1 QDs have a diameter of approximately 3.5 nm and their emission is centred at 610 nm in solution. As discussed above the optical properties of the Don3 monolayers do not show any strong concentration dependence. Therefore, effects on the donor lifetime due to small donor concentration variations can be neglected and a constant, average donor reference lifetime, measured on the blue side of the Don3 ensemble emission spectrum, of $\tau_D = 6.1$ ns is used in the FRET analysis.

In principle, similar energy transfer signatures as in the monodispersed monolayers are expected for the mixed donor-acceptor monolayers. However, in the monodispersed monolayers the energy donating and energy accepting QDs all contributed to the same emission peak. Don3 and Acc1 were chosen as donor and acceptor QDs for this study as

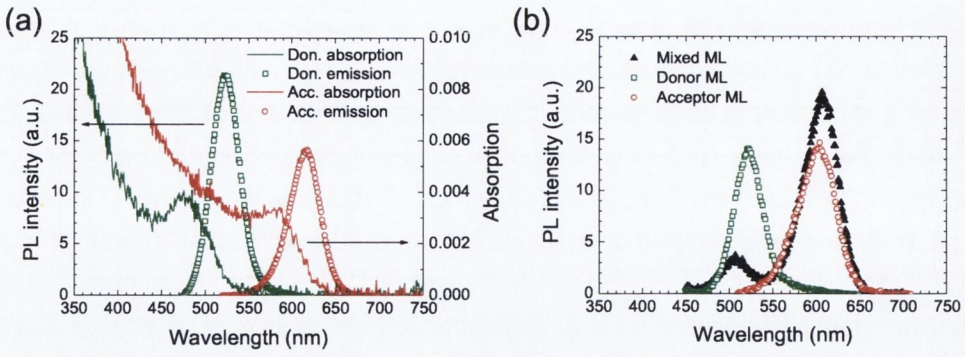


Figure 4.8: (a) Photoluminescence (PL) (open symbols, left-hand-axis) and absorption spectra (lines, right-hand-axis) for a Don3 (green squares and line) and an Acc1 (red circles and line) monolayer. (b) PL spectra of a mixed Don3-Acc1 monolayer (ML) (solid black triangles) as well as of donor (Don.) and acceptor (Acc.) QD reference monolayers (open green squares and open red circles respectively) at the same concentrations as in the mixed monolayer. Reproduced with permission from Journal of Physical Chemistry C 2009, 113, 3084 Copyright 2009 American Chemical Society.

there is a good overlap of the Don3 emission with the Acc1 absorption, but at the same time both PL peaks are spectrally well separated, as can be seen from the monolayer absorption and PL spectra shown in Figure 4.8(a). Therefore, the energy transfer process can be investigated in more detail in the mixed donor-acceptor QD monolayers as the influence of FRET on the optical properties of the donor and acceptor QDs can be distinguished more clearly than in the monodispersed QD monolayers.

From the absorption and emission spectra of the Don3 and Acc1 monolayers shown in Figure 4.8(a) quantum yields of $Q_D = 4\%$ and $Q_A = 1\%$ were determined respectively. Additionally, a Förster radius $R_0 = (3.3 \pm 0.2)$ nm was determined for the donor-to-acceptor energy transfer in the monolayers from the spectral overlap of the donor emission and the acceptor absorption.

4.2.1 Mixed QD Monolayer - One Example

Figure 4.8(b) shows an example of a PL spectrum measured for a mixed QD monolayer with donor and acceptor concentrations $c_{\mathrm{Don}} = (2.6 \pm 0.2) \times 10^{17}$ m^{-2} and $c_{\mathrm{Acc}} = (0.6 \pm 0.1) \times 10^{17}$ m^{-2} respectively, corresponding to an acceptor:donor ratio of 1:4.5 (solid black triangles). Don3 (open green squares) and Acc1 (open red circles) monolayer reference samples, with similar concentrations of donor or acceptor QDs as in the mixed monolayer, are also included for comparison. Small differences in concentration were adjusted for by weighting the reference PL spectra with the respective concentration ratios determined from the absorption spectra. As expected for energy transfer from

the Don3 to the Acc1 QDs, the donor emission is quenched and the acceptor emission is enhanced in the mixed monolayer. The donor PL is decreased by (77 ± 11) % compared to that of the reference monolayer, and the acceptor emission is increased by (31 ± 8) %. Additionally, a relatively large blue-shift of the Don1 PL peak by 14 nm is observed compared to the emission in the pure monolayer. This indicates that the larger donors, emitting on the red side of the Don1 ensemble emission spectrum, transfer energy more efficienctly to the Acc1 QDs, probably because they overlap directly with the first absorption peak of the acceptors. In the mixed monolayer, the acceptor emission peak is shifted a little to the red, by 2 to 3 nm, but the shift is not as strong as for the donor QDs.

The photoluminescence excitation (PLE) spectra recorded at the donor emission peak in the mixed monolayer and the pure Don3 reference are shown in the inset of Figure 4.9(a). For the pure Don3 monolayer (green line) an increase of the emission intensity at high excitation wavelengths between approximately 480 and 500 nm can be clearly seen, corresponding to the first absorption peak of the QDs emitting at the detection wavelength of 522 nm. The additional feature at 390 nm is attributed to a polyelectrolyte emission as discussed in section 3.3. The donor PLE spectrum for the mixed monolayer (black line) is recorded at 508 nm due to the blue-shift of the donor emission peak. For all excitation wavelengths, the emission intensity of the donors in the mixed monolayer is much lower than for the Don3 monolayer, clearly showing the quenching of the donor emission in the presence of the acceptor QDs. The ratio of the donor PLE measured for the mixed monolayer and the pure Don3 reference sample is shown in Figure 4.9(b) (green line). The peak at wavelengths longer than 450 nm is a consequence of the different detection wavelengths used to measure the PLE spectra. As the PLE spectrum for the donors in the mixed monolayer is measured at a lower detection wavelength, corresponding to the emission from smaller Don3 QDs, the increase due to excitation in resonance with the first absorption peak begins at a lower wavelength than for the PLE spectrum recorded for the reference monolayer. This blue-shifted first absorption peak is seen as a peak in the ratio of the PLE spectra, a red-shift would be observed as a dip. No other significant feature is observed in the donor PLE ratio.

The acceptor PLE spectra, recorded at similar wavelengths for the mixed monolayer and the pure Acc1 reference sample, are shown in the main panel of Figure 4.9(a). The increase in the acceptor emission in the presence of donor QDs can be seen in the PLE spectrum of the mixed monolayer (black line), which shows higher emission intensities than the Acc2 monolayer (red line) at low excitation wavelength up to 550 nm. More importantly, an additional feature is observed in the acceptor PLE spectrum measured in the mixed monolayer for excitation wavelengths between 450 and 500 nm. For the Acc1 reference monolayer only a monotonic decrease of the emission intensity

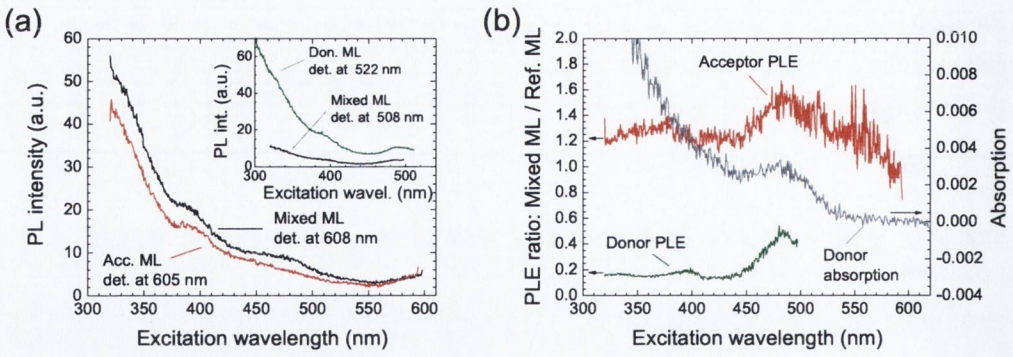


Figure 4.9: (a) Acceptor PL excitation (PLE) spectra of the mixed monolayer (black line) and the acceptor monolayer (red line) detected at the acceptor peak emission wavelength, 608 nm and 605 nm respectively. The inset shows the donor PLE spectra recorded at 508 nm for the mixed QD monolayer (black line) and at 522 nm for the donor monolayer (green line). (b) Ratios of the donor (green line) and acceptor (red line) PLE spectra of the mixed monolayer and pure reference layers (left-hand axis). The absorption spectrum (grey line, right-hand axis) of a donor reference monolayer is shown as well.

is detected in this wavelength range. This feature can be seen even more clearly in the ratio of the two PLE spectra shown in Figure 4.9(b) (red line). It is interesting to note that this new feature occurs at the same wavelengths as the peak in the donor PLE ratio and the first absorption peak of the Don3 absorption spectrum, also included in the Figure for comparison (grey line, right-hand axis). The PLE ratio shows that at low excitation wavelengths the acceptor PL emission is enhanced by a factor of 1.3, the same value as determined from the PL spectra. The acceptor emission in the mixed monolayer is further enhanced when exciting in resonance with the first donor absorption peak as the Don3 QDs absorb energy very efficiently in this wavelength range and consequently more energy can be transferred to the Acc1 QDs. Therefore, the additional feature in the acceptor PLE spectrum, coinciding with the absorption peak of the donor QDs, is another important signature of energy transfer in the mixed QD monolayer. At wavelengths higher than the first donor absorption peak, the acceptor enhancement decreases and the PLE ratio tends towards 1, as a decreasing number of Don3 QDs can be excited in this wavelength range and therefore less energy transfer occurs.

Figure 4.10(a) shows the donor PL decays, recorded with a 500 nm filter, of the mixed monolayer with a donor:acceptor ratio of 1:4.5 (black line) and of a Don3 reference sample (green line), with a similar donor QD concentration as in the mixed monolayer. As expected for energy transfer via the FRET mechanism, the donor decay in the presence of the acceptors is reduced compared to that of the pure donor monolayer. The decrease

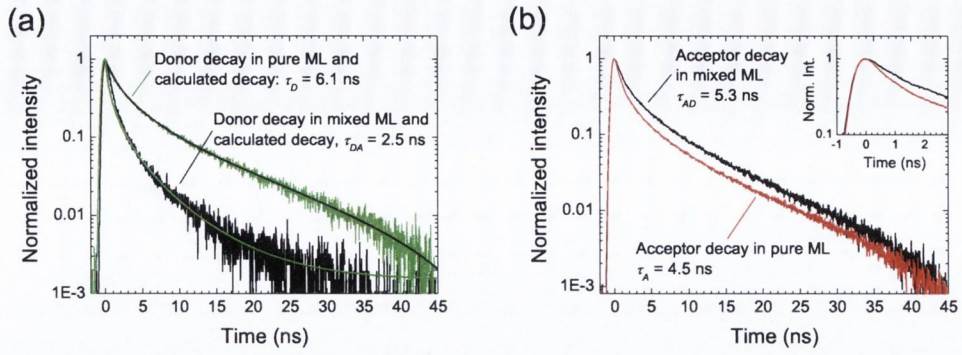


Figure 4.10: (a) Time-resolved donor PL decays in the monodispersed donor monolayer (ML) (green line) and in the mixed QD ML (black line). The thin lines are fits of the data with multi-exponential decay curves. (b) Acceptor PL decays in the monodispersed acceptor reference ML (red line) and in the mixed QD ML (black line). The inset shows a close-up of the acceptor decays over the first 3 ns. (a) is reproduced with permission from Journal of Physical Chemistry C 2009, 113, 3084 Copyright 2009 American Chemical Society.

of the donor lifetime from $\tau_D = 6.1$ ns, in the reference sample, to $\tau_{DA} = 2.5$ ns, in the mixed monolayer, corresponds to a FRET efficiency of $(59 \pm 8)\,\%$ and a FRET rate $k_{FRET} = \tau_{DA}^{-1} - \tau_D^{-1} = (1.8 \pm 0.3\ \text{ns})^{-1}$ at this acceptor concentration.

The theory of FRET in two dimensions developed by Wolber and Hudson [100], that was applied to model the concentration dependence of the lifetime τ_{blue} in the monodispersed QD monolayers, can be applied to fit the donor decay in the presence of the acceptor QDs in a mixed monolayer. The decays on the blue side of the QD ensemble emission in the monodispersed monolayers could not be fitted in this way as it was not possible to measure a reference decay in absence of energy transfer. The Don3 reference decay shown in Figure 4.10(a) is fitted with a multi-exponential decay curve (black curve). For the fitting of the donor decay in the mixed QD monolayer, each of the exponential terms of the fitting curve for the pure donor monolayer is modified according to equation (2.10) discussed in section 2.2.1:

$$I_{DA}(t) = \exp\left\{ -\frac{t}{\tau_D} - \pi \cdot R_0^2 \cdot c_{Acc} \cdot \gamma\left(2/3, (R_0/R_{ex})^6 \cdot (t/\tau_D)\right) \cdot \left(\frac{t}{\tau_D}\right)^{1/3} + \pi \cdot R_{ex}^2 \cdot c_{Acc} \cdot \left[1 - e^{-(R_0/R_{ex})^6 \cdot (t/\tau_D)}\right] \right\}$$

where τ_D is the characteristic lifetime of the respective exponential term. The Förster radius, R_0, exclusion zone radius, R_{ex}, and acceptor concentration, c_{Acc}, are used as fitting parameters. The best agreement with the measured decay was obtained for

$R_0 = (3.6 \pm 0.3)$ nm, $R_{ex} = (2.9 \pm 0.2)$ nm and $c_{Acc} = (0.75 \pm 0.1) \times 10^{17}$ m^{-2}. As can be seen in Figure 4.10(a), the fit reproduces the donor decay in the mixed monolayer very well. Additionally, the values of R_0, R_{ex} and c_{Acc} as extracted from the fit of the time-resolved donor PL decay agree well with those determined from the spectral measurements of the pure and mixed monolayers ($R_0 = (3.3 \pm 0.2)$ nm, $R_{ex} = (3.2 \pm 0.3)$ nm and $c_{Acc} = (0.6 \pm 0.1) \times 10^{17}$ m^{-2}). For donor PL decays in mixed monolayers with different acceptor:donor ratios, good agreement of the fit with FRET theory and data was obtained for the same R_0 and R_{ex} values (within error).

The most important parameters characterizing the FRET process are its efficiency, rate and its characteristic interaction distance, the Förster radius (R_0). The FRET efficiency and rate are usually determined from the time-resolved donor decays. As outlined in section 3.3.2, PL and absorption measurements of the QDs are needed to obtain not only the donor emission and acceptor absorption spectra but also the other parameters, such as the donor quantum yield and the acceptor extinction coefficient, that are necessary to calculate R_0 from the spectral overlap. Therefore, the calculation of R_0 via the spectral overlap is prone to errors, in particular as one compares information from measurements that are usually carried out on different experimental setups where different sample areas might be investigated under different pumping and collection conditions. Furthermore, in the case of FRET between QDs, it was not clear whether the overlap of the donor emission had to be calculated with the first acceptor absorption peak only or if the full absorption spectrum should be taken into account. Therefore, it was important to find a way to independently verify the value of R_0 calculated via the spectral overlap. The fitting of the donor decays with FRET theory taking into account exclusion zones around the donors offers not only the possibility to confirm the value of R_0 but also enables the calculation of all important FRET parameters from time-resolved measurements only. The good agreement of the theoretically calculated and measured decay curves show that it is appropriate to determine R_0 via the spectral overlap of the donor emission with the full acceptor absorption spectrum. Furthermore, it confirms that, in line with the findings for the monodispersed QD monolayers, the impact of FRET on the time-resolved donor decay can be adequately described by a theory of FRET developed for molecules, if the QD size is included in the calculations in form of an exclusion zone around the donors.

The acceptor decays, measured with a 600 nm filter, of the mixed monolayer with an acceptor:donor ratio of 1:4.5 as well as the corresponding acceptor reference decay (measured without filter) are shown in Figure 4.10(b). In the presence of donor QDs the acceptor decay (black line) is longer than for the pure acceptor monolayer (red line) and the lifetime is increased from $\tau_A = 4.5$ ns to $\tau_{AD} = 5.3$ ns, reflecting the enhanced acceptor emission due to energy transfer. In the inset a close-up of the first

three nanoseconds of the acceptor decays is shown, but no rise-time due to feeding from the donors is observed. This is most likely due the spectral region covered in these measurements. With the 600 nm filter the emission of almost all acceptors is recorded rather than only that from the red-side of the acceptor ensemble spectrum.

4.2.2 Concentration Dependence and Theoretical Modelling

The FRET efficiencies E_{FRET} for mixed monolayers with different acceptor:donor ratios as a function of the acceptor concentration are shown in Figure 4.11(a). The corresponding number of acceptors per donor are shown on the top axis. As expected from theory, E_{FRET} is increasing with increasing acceptor concentration, as more acceptors per donor are available to receive energy. It should be noted that the FRET efficiency in the mixed monolayer follows a concentration dependence similar to that of the FRET efficiency determined for the monodispersed QD monolayers, shown in Figure 4.6. At the highest acceptor concentrations investigated, $c_{Acc} > 1.5 \times 10^{17}$ m^{-2}, FRET efficiencies of over 90% were achieved. The corresponding FRET rates were determined to be as fast as $(0.5 \text{ ns})^{-1}$. This rate is similar to what has been reported in literature, even though in highly optimized systems faster FRET rates of $(0.2 \text{ ns})^{-1}$ [115] and $(0.07 \text{ ns})^{-1}$ [145] have already been observed. The FRET rate in the mixed monolayers could be optimized by using donor QDs with a higher quantum yield, to increase R_0, and by decreasing the QD diameters, to reduce R_{ex}.

Theoretically calculated trends of the acceptor concentration dependence of the FRET efficiency, obtained with equation (2.11), also given as equation (4.1) on page 53, are also shown in Figure 4.11(a). The calculation has been carried out for $R_0 = 3.6$ nm and different ratios of $r = R_{ex}/R_0$, namely 0.7, 0.8, 0.9 and 1.0. The best agreement of theory and data is obtained for $R_0 = 3.6$ nm and a ratio of $r = 0.8$, again confirming the values of R_0 and R_{ex} obtained from the spectral data and the fit of the time-resolved data. This shows once more, that FRET theory can explain the donor lifetime changes due to energy transfer very well if the QD size is taken into account in form of an exclusion zone. Furthermore, the good agreement of the values of R_0 and R_{ex} extracted from the spectral data, the fitting of the time-resolved donor decays and the concentration dependence of the FRET efficiency validate the use of either of the methods to calculate the Förster radius, which is an important parameter in the analysis of FRET and not always easy to determine reliably.

The acceptor PL enhancement, $E_{Enh} = I_{AD}/I_A - 1$, was determined from the integrated acceptor PL decays of the mixed monolayer sample, I_{DA}, and of a monodispersed acceptor monolayer, I_A, with a similar acceptor concentration as in the mixed layer. The integrated acceptor PL decays were used instead of the integrated PL spectra, as the acceptor PL intensities in the spectra recorded for samples with low acceptor concentra-

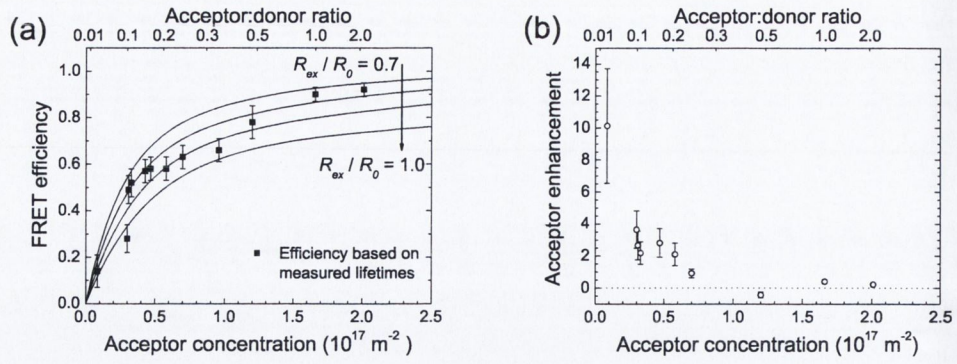


Figure 4.11: (a) Acceptor concentration dependence of the FRET efficiency (solid black squares) calculated from the donor lifetime decrease in the mixed QD monolayers. The experimentally determined efficiency follows the trend predicted by theory (lines) for a ratio R_{ex} / $R_0 \approx 0.8$. The corresponding number of acceptor QDs per donor QD in the mixed layer is given on the top axis. (b) Acceptor concentration dependence of the acceptor PL enhancement in the mixed QD monolayer. (a) is reproduced with permission from Journal of Physical Chemistry C 2009, 113, 3084 Copyright 2009 American Chemical Society.

tions were too low to allow for a reliable determination of the acceptor enhancement. As can be seen in Figure 4.11(b), the measured E_{Enh} is decreasing with increasing acceptor concentration, showing a trend opposite to that of the FRET efficiency.

A constant acceptor PL enhancement is expected at very low acceptor:donor ratios. At these ratios the number of acceptors is so small that some of the donor QDs are too far away from any suitable acceptor QD to be able to transfer energy to any acceptor. Therefore, the number of donor QDs that can transfer energy to a particular acceptor, and consequently E_{Enh}, should be constant for these acceptor:donor ratios.

The acceptor enhancement determined for the mixed QD monolayers continues to increase up to an acceptor:donor ratio of 1:33, the lowest ratio investigated. This means that not only the nearest neighbour QDs can transfer energy to an acceptor QD, but that at least 33 donors can funnel energy into a central acceptor. Achermann et. al [115] have reported similar observations for FRET in Langmuir-Blodgett assembled QD films. Assuming a short-range hexagonally ordered structure, they determined that donors located in up to the third shell around an acceptor must be able to participate in energy transfer to this acceptor in order to explain their experimental results. In such a hexagonally ordered structure 33 donors would be arranged in three shells around a central acceptor. Therefore, it can be concluded that also in the structures investigated here, acceptors can receive energy from donors as far as in the third shell.

At a first glance, the opposite trend of acceptor PL enhancement and FRET efficiency

is quite surprising, as the highest acceptor enhancement of 10 is observed at the lowest acceptor concentration investigated at which E_{FRET} is just $\approx 15\%$. However, considering that the number of donors per acceptor is decreasing with increasing acceptor concentration in the mixed monolayer (corresponding to an increasing acceptor:donor ratio as shown on the top axis), the trend of the acceptor enhancement reflects the number of donors available to transfer energy to a particular acceptor rather than the probability of energy being transferred.

To confirm this, the expected acceptor enhancement was calculated by multiplying the FRET efficiency with the donor:acceptor absorption ratio, A_D/A_A, at the excitation wavelength [14, 95]. The absorption ratio was calculated as the ratio of the donor and acceptor concentrations weighted by the respective extinction coefficients at the excitation wavelength used in the experiment: $A_D/A_A = c_{Don} \cdot \epsilon_D / (c_{Acc} \cdot \epsilon_A)$. Multiplying E_{FRET} with A_D, one obtains a number representing photons that are absorbed by the donors and transferred to the acceptors. By dividing this value with A_A this becomes equivalent to the additional energy transferred to a single acceptor: the acceptor enhancement ($E_{Enh} = (I_{AD} - I_A)/I_A$). The basic idea behind this conversion is, that the number of donor-excitons decaying non-radiatively due to energy transfer to an acceptor (Δ_{Don}), giving rise to the PL quenching, $(I_D - I_{DA})/I_D$, is equivalent to the number of additional excitons created in the acceptor QDs by energy transfer (Δ_{Acc}) (first line of equation (4.4)). Due to energy transfer the donor PL decrease by $(I_D - I_{DA})$, however as an exciton is only recombining radiatively with a probability of Q_D, the donor quantum yield, in total $\Delta_{Don} = (I_D - I_{DA})/Q_D$ excitons are transferring energy. The same holds for the acceptor PL increase of $I_{AD} - I_A$ that only represents a fraction Q_A of the excitons, those recombining radiatively, so that $\Delta_{Acc} = (I_{AD} - I_A)/Q_A$. The third line of equation (4.4) is obtained from the second line by replacing the donor PL decrease and the acceptor PL increase by the donor PL quenching, equivalent to E_{FRET}, and the acceptor enhancement (E_{Enh}) respectively. Taking into account the definition of the quantum yield, Q, as the ratio of the emitted over the absorbed photons, one obtains the last line of equation (4.4), which shows that the acceptor PL enhancement is equivalent to the FRET efficiency multiplied by the donor:acceptor absorption ratio, as states above.

$$\begin{aligned} \Delta_{Don} &= \Delta_{Acc} \\ \frac{I_D - I_{DA}}{Q_D} &= \frac{I_{AD} - I_A}{Q_A} \\ \frac{I_D}{Q_D} \cdot E_{\mathrm{FRET}} &= \frac{I_A}{Q_A} \cdot E_{Enh} \\ A_D \cdot E_{\mathrm{FRET}} &= A_A \cdot E_{Enh} \end{aligned} \tag{4.4}$$

As can be seen in Figure 4.12(a) the acceptor enhancement estimated by multiplying E_{FRET}, calculated with theory for $R_0 = 3.6$ nm and r = 0.8, with the absorption ratio (dashed line) confirms the trend of the increasing acceptor enhancement with decreasing acceptor concentration. However, it underestimates the measured values at low acceptor concentrations. An explanation for this discrepancy could be the efficient recycling of excitons trapped in donor defect states as observed for other nanocrystal FRET structures [12, 120]. This effect is more significant at low acceptor concentrations as a single acceptor can receive energy from multiple donors, whereas it does not seem to have a large impact at high acceptor concentrations. The exciton recycling effect is increasing the acceptor enhancement but is probably not affecting E_{FRET} or the donor PL quenching to the same extent.

Multiplying the measured FRET efficiency with the donor:acceptor concentration ratio only (dotted line in Figure 4.12(a)), the measured acceptor enhancement is overestimated at high acceptor concentrations and too low values are calculated at the lowest acceptor concentration investigated. By multiplying E_{FRET} with $A_D/A_A \cdot 3$ (dash-dot line) the measured acceptor enhancement seems to be reasonably well approximated, but again the strong increase of the acceptor enhancement with decreasing acceptor concentration is not well reproduced. To obtain a good fit of the measured data, the expression $E_{FRET} \cdot A_D/A_A \cdot (1 + 0.9/c_{Acc})$ was used (solid line in Figure 4.12(a)). This indicates that the efficiency of the exciton recycling process does not follow the same acceptor concentration dependence as the FRET efficiency. However, the cause of this difference in concentration dependence is not clear yet and also the question which other parameters might influence the energy recycling has still to be answered. A more detailed understanding of this effect is the subject of future investigations.

4.2.3 Relative Quantum Efficiency

The impact of FRET on the total PL emission of the mixed QD monolayer was investigated by comparing the values of the integrated time-resolved PL decays, measured without filter, of the mixed monolayer and a reference structure with non-interacting donor and acceptor monolayers. The total PL emission of the reference was calculated as the sum of the integrated PL decays measured for monodispersed donor and acceptor monolayers with similar donor or acceptor concentrations as in the mixed monolayer. The donor and acceptor emission values at the respective concentrations were obtained from a linear fit of the integrated PL decays in dependence of the QD concentration. The relative quantum efficiency, QE_{rel}, of the mixed monolayer, the PL ratio of the mixed monolayer and the reference structure, is shown as a function of the acceptor:donor ratio in Figure 4.12(b). QE_{rel} increases with decreasing acceptor:donor ratio, following a very similar trend as observed for the acceptor PL enhancement. At high

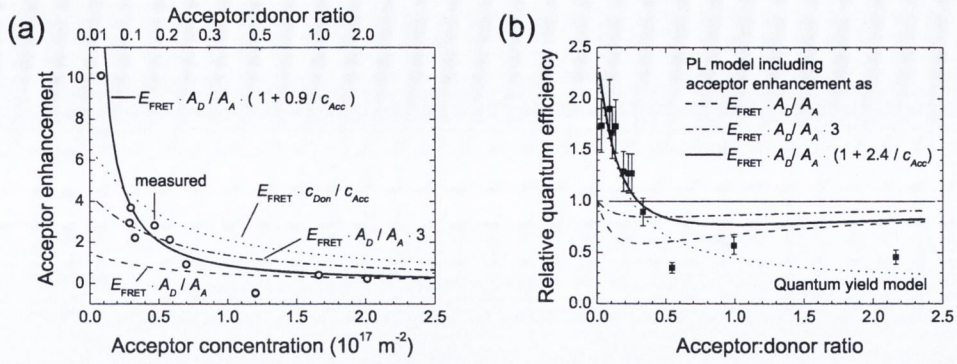


Figure 4.12: (a) Acceptor concentration dependence of the acceptor enhancement determined from the integrated acceptor PL decays (open circles) as well as by multiplying the theoretically calculated FRET efficiency ($R_0 = 3.6$ nm and r = 0.8) with the donor:acceptor concentration ratio A_D/A_A (dashed line), with $3 \cdot A_D/A_A$ (dash-dot line), with c_{Don}/c_{Acc} (dotted line) and with $A_D/A_A \cdot (1 + 0.9/c_{Acc})$. (b) Dependence of the relative quantum efficiency (black squares) on the acceptor:donor ratio. The trends calculated for a PL model including the acceptor enhancement as $E_{FRET} \cdot A_D/A_A$ (dashed line), $E_{FRET} \cdot A_D/A_A \cdot 3$ (dash-dot line) and $E_{FRET} \cdot A_D/A_A \cdot (1 + 2.4/c_{Acc})$ (solid line) as well as a model based on the addition of the quantum yields (dotted line) are also shown.

acceptor:donor ratios, the PL emission of the mixed monolayer is lower than that of the reference structure. The reason for this is that energy is transferred efficiently to the acceptor QDs, but is emitted less efficiently from the acceptor QDs with $Q_A = 1\%$ than it would be from the donor QDs with a higher quantum yield of $Q_D = 4\%$. Therefore, due to $Q_A/Q_D < 1$, energy is lost at high acceptor concentrations in the mixed monolayer prepared from Don3 and Acc1 QDs. However, at an acceptor:donor ratio of 1:4, the relative quantum efficiency becomes 1 (indicated by the dotted line) and despite the lower quantum yield of the acceptors, an enhancement of the total PL emission is observed at very low concentration ratios. It is interesting to note that the transition to the regime of an enhanced quantum efficiency occurs when the concentration ratio is equivalent to the quantum yield ratio. However, it is not yet clear if this is a coincidence or if it has a physical meaning.

A model of the PL emission ratio was developed to better understand the influence of the different parameters, such as the donor and acceptor quantum yields and concentrations, on the relative quantum efficiency. This model is going to be referred to as PL model in the following. Based on equations (4.4), the total emission of the mixed monolayer I_{Mix} can be written as:

$$I_{Mix} = I_{DA} + I_{AD} = I_D \cdot (1 - E_{FRET}) + I_A \cdot \left(1 + E_{FRET} \cdot \frac{A_D}{A_A}\right) .$$

The relative quantum efficiency can therefore be expressed as

$$\begin{aligned} QE_{rel} &= \frac{I_{Mix}}{I_D + I_A} \\ &= 1 + E_{FRET}(c_{Acc}) \frac{I_A \cdot \frac{A_D}{A_A} - I_D}{I_D + I_A} \\ &= 1 + E_{FRET}(c_{Acc}) \frac{Q_A/Q_D - 1}{1 + Q_A/Q_D \cdot \frac{A_A}{A_D}} \end{aligned} \tag{4.5}$$

and depends on the donor and acceptor quantum yields Q_D and Q_A, the acceptor and donor concentrations as well as their extinction coefficients. It is important to keep in mind that the donor quantum yield and acceptor extinction coefficient also influence the value of R_0 which, along with the acceptor concentration, determines the FRET efficiency.

The trend of QE_{rel} calculated with equation (4.5) as a function of the acceptor:donor ratio is shown as a dashed line in Figure 4.12(b) for $Q_D = 4\%$, $Q_A = 1\%$ and an average $c_{Don} = 2.7 \times 10^{17}$ m^{-2}. However, as can be seen, this does not produce a good agreement with the experimental data. One could argue that the decreasing trend with decreasing acceptor:donor ratio is reproduced fairly well at acceptor:donor ratios higher than 1:2. However, an increase of the total emission to values higher than that of the reference structure is not predicted by the model, which only produces values below or equal to 1 for this combination of donor and acceptor quantum yields. As seen in Figure 4.12(a), the acceptor enhancement is not represented well by multiplying E_{FRET} with the absorption ratio A_D/A_D. Therefore it is not surprising that the simple PL model is not reproducing the trend of the relative quantum efficiency very well. The values of the acceptor enhancement are better fitted by $E_{\mathrm{FRET}} \cdot 3 \cdot A_D/A_A$, but if this expression is included in the PL model (dash-dot line in Figure 4.12(b)) again good agreement with the experimentally determined relative quantum efficiency is not achieved. In particular, all calculated values are again lower than 1.

One can clearly see, that the shape of the calculated QE_{rel} curves has to be modified in order to better reproduce the observed trends. Describing the acceptor PL enhancement by $E_{\mathrm{FRET}} \cdot A_D/A_A \cdot (1 + 2.4/c_{Acc})$ results in a good agreement with the acceptor concentration dependence of the relative quantum efficiency when included in the PL model (solid line), in particular at the lower acceptor:donor ratios where there is a large discrepancy with the other two curves. It should be noted, that while the constants used in the modelling of the acceptor enhancement and QE_{rel}, 0.9 and 2.4 respectively, are different, the form of the acceptor-concentration dependent expression for the acceptor enhancement, that has to be included in both models to obtain a good agreement with the measured data, is the same. Although the exact origin of the additional concen-

tration dependent term is not understood yet, it is an important result that, once the right expression for the dependence of the acceptor PL enhancement on the acceptor concentration is found also the experimentally determined QE_{rel} can be well reproduced with this extended PL model.

Furthermore, it is interesting to note, that the trend and values of the relative quantum efficiency can be well reproduced by the following dependence, shown as a dotted line in Figure 4.12:

$$QE^{\star}_{rel} = 1 + E_{FRET}\frac{Q_A \cdot \frac{c_{Don}}{c_{Acc}} - Q_D}{Q_A + Q_D} \tag{4.6}$$

which is based on the idea of summing the quantum yields. However, the quantum yields cannot be simply added, but the quantum yield of the mixed monolayer would rather have to be calculated as an absorption weighted sum, as done in the PL model. Nevertheless, the good agreement of this quantum yield model with the data might help to understand the origin of the additional concentration dependent term needed to correctly model the measured acceptor enhancement and the relative quantum efficiency.

It is important to note that all the models are not valid in the range of very low acceptor concentrations, where a constant acceptor enhancement is expected once the acceptor:donor ratio decreases below a critical value. This has to be considered when evaluating the calculated values of QE_{rel}, as this means that the relative quantum efficiency cannot be increased infinitely by decreasing the acceptor concentration. The maximum enhancement of the PL emission that can be achieved in the Don3-Acc1 monolayers might already be reached for the lowest acceptor concentrations investigated. An indication for this could be that even though the acceptor enhancement is observed to continue to increase, the relative quantum efficiency is fairly constant or even starts to decrease for the mixed monolayer with a acceptor:donor ratio of 1:33.

Although the PL model described in Equation (4.5) does not represent the relative quantum efficiency measured for the mixed Don3-Acc1 monolayers well, it shows the effect of FRET on the total PL emission without taking into account the exciton recycling effect that can occur in QD systems. Therefore, the simplest version of the PL model, where the acceptor enhancement is included as $E_{\mathrm{FRET}} \cdot A_D/A_A$, can be considered as a lower limit of the PL enhancement that can be achieved in a QD FRET structure. In the following equation (4.5) has been evaluated for different acceptor quantum yields, acceptor and donor concentrations.

The ratio of the donor and acceptor quantum yields has a strong impact on the relative quantum efficiency as can be seen in Figure 4.13(a), which shows the dependence of the calculated QE_{rel} on the acceptor:donor ratio for $c_{Don} = 2.7 \times 10^{17}$ m^{-2}, a donor quantum yield $Q_D = 4\%$ and different acceptor quantum yields Q_A. The results from the calculation with the PL model taking into account $E_{Enh} = E_{\mathrm{FRET}} \cdot A_D/A_A \cdot (1 + 2.4/c_{Acc})$, referred to as extended PL model in the following, are shown in the inset

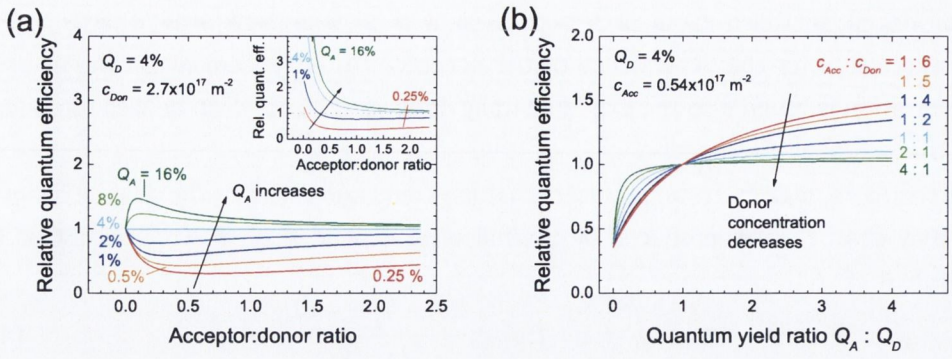


Figure 4.13: (a) Dependence of the relative quantum efficiency on the acceptor:donor concentration ratio for different acceptor quantum yields Q_A calculated with a simple model for the PL intensity ratio. The donor quantum yield and concentration were set to $Q_D = 4\%$ and $c_{Don} = 2.7 \times 10^{17}$ m^{-2} respectively. The inset shows the results of the PL model including the acceptor enhancement $E_{Enh} = E_{\mathrm{FRET}} \cdot A_D/A_A \cdot (1 + 2.4/c_{Acc})$ for the same donor properties and a selection of different values of Q_A. (b) Dependence of the relative quantum efficiency calculated with the simple PL model on the acceptor:donor quantum yield ratio for different donor concentrations. The donor quantum yield was kept constant at 4% and the acceptor concentration was set to $c_{Acc} = 0.54 \times 10^{17}$ m^{-2}.

of Figure 4.13(a) for the same conditions. The values of the acceptor concentration dependent FRET efficiency used in the calculation of QE_{rel} were obtained from FRET theory for a ratio of r = 0.8. Most importantly, the simple model suggests that the emission of a FRET structure is always the same as that in absence of FRET when the donor and acceptor quantum yields are equal. This clearly shows that, as mentioned above, the simple version of the PL model does not take into account the possibility of energy transfer from excitons trapped in donor defect states to acceptor QDs and the subsequent emission from the acceptors. The recycling of the trapped excitons increases the total emission of a FRET structure which should be reflected in a relative quantum efficiency greater than 1 for structures with donor and acceptor QDs with the same quantum yield, as it is the case for the extended PL model shown in the inset. Consequently, for the cases in which Q_A is smaller than Q_D, the simple PL model predicts that QE_{rel} is smaller than 1 for all acceptor:donor ratios as the energy transferred to the acceptors is emitted with a lower probability than it would be emitted from the donors in the reference structure. Also with the extended PL model values of $QE_{rel} < 1$ are obtained at high acceptor:donor ratios, however an enhanced relative emission should be observed even for structures with $Q_A < Q_D$ for low acceptor:donor ratios according to this model.

For acceptor:donor quantum yield ratios larger than 1, the emission in the FRET

structure is always larger than for the reference structure and it goes through a maximum for low acceptor:donor concentration ratios for the calculation with the simple PL model. The maximum is determined by the trade off of the decreasing FRET efficiency with decreasing acceptor concentration and an increasing number of donors than funnel energy into a single acceptor. The position of the maximum is determined by the quantum yield ratio and shifts to lower concentration ratios with increasing acceptor quantum yield. For the calculation with the extended PL model no maximum but a continuing increase of QE_{rel} is observed with decreasing acceptor:donor ratio.

The main observation from the comparison of the two PL models is that this simple PL model does not predict any transition from a regime of total emission loss ($QE_{rel} < 1$) to total emission enhancement ($QE_{rel} > 1$) as a function of the acceptor:donor concentration ratio. An empiric description of the recycling effect has to be explicitly included in the PL model to obtain this transition, observed for the relative quantum efficiency in the mixed Don3-Acc1 monolayers. Furthermore, in the simple as well as in the extended PL model, the relative quantum efficiency is increasing with increasing acceptor quantum yield. The values of QE_{rel} calculated with the extended PL model are larger than those determined with the simple PL model under the conditions investigated. In addition to the above discussion of the experimentally determined relative quantum efficiency, even for an acceptor quantum yield as high as 16% the measured relative quantum efficiencies would not be represented well by the calculation with the simple PL model, which clearly shows again that there is an additional effect contributing to the acceptor enhancements that needs to be taken into account.

In Figure 4.13(b) QE_{rel} calculated with the simple PL model is shown as a function of the acceptor:donor quantum yield ratio for different donor concentrations, $Q_D = 4\%$ and $c_{Acc} = 0.54 \times 10^{17}$ m^{-2}. Keeping Q_D and c_{Acc} constant means that the FRET efficiency is the same for all cases considered. As can be seen, again, for equal donor and acceptor quantum yields, the model always predicts a relative quantum efficiency of 1. For low acceptor:donor quantum yield ratios the emission from the FRET structure is always lower than one and decreases with decreasing acceptor quantum yield and / or increasing donor concentration. QE_{rel} is always higher than 1 for $Q_A : Q_D > 1$ and increases with increasing acceptor quantum yield and / or increasing donor concentration. Calculations with varying donor concentration were not carried out with the extended PL model, as the influence of the donor concentration on the exciton recycling could not be investigated for the mixed Don3:Acc1 monolayer.

Comparing the trends shown in Figures 4.13(a) and (b), it can be seen that the quantum yield ratio has a larger impact on the relative quantum efficiency than the concentration ratio. Taking the calculated values as a lower limit for what can be achieved in QD structures due to the exciton recycling effect [12, 120], acceptor QDs

with high quantum yields should be used in structures with relatively low acceptor:donor concentration ratios in order to obtain high total PL emission enhancements.

4.3 Conclusion

In this chapter a theory of FRET in two dimension taking into account exclusion zones around the donors [100], previously only used to describe FRET in molecular systems, was applied to analyse FRET in monodispersed QD monolayers and mixed donor-acceptor QD monolayers. It was shown that FRET theories, which were mostly developed representing donors and acceptors as point-dipoles, can be used to describe FRET in QD structures if the size of the QDs and the thickness of their ligand shells are taken into account in form of exclusion zones with radius R_{ex}.

In the nominally monodispersed QD monolayers, a red-shift of the ensemble emission peak, a decrease of the PL lifetime measured on the blue side of the ensemble emission spectrum and an increase of the lifetime difference on the blue and red side of the ensemble emission with increasing QD concentration were observed for different QD samples. The lifetime decrease on the blue side of the ensemble emission spectrum can be well reproduced by the theory of FRET in two dimensions. This confirms that the concentration dependent effects on the optical properties of the monodispersed QD monolayers are caused by energy transfer via the FRET mechanism from smaller to larger QDs within the QD ensemble. Other processes, such as tunneling or surface effects, can be neglected. Furthermore, the values of the Förster radius R_0 and R_{ex}, obtained from the theoretical modelling of the lifetime decrease, agree well with those obtained from the spectral analysis. This shows that it is appropriate to use R_0 calculated from the spectral self-overlap to describe intra-ensemble FRET arising from a small Stokes shift and a large inhomogeneous broadening.

FRET efficiencies as large as 80% were observed in closely packed layers of QDs with a large self-overlap. By selecting QDs with a smaller self-overlap, the impact of FRET on the optical properties is reduced. Additionally, the decrease of the probability of FRET within the monodispersed QD monolayers with decreasing self-overlap was shown to agree very well with the trend expected from theory. This demonstrates that intra-ensemble FRET in monodispersed QD structures can be controlled by tuning the QD concentration or by selecting QDs with a smaller or larger inhomogeneous broadening and / or Stokes shift.

For the mixed QD monolayers also an excellent agreement of the experimentally determined FRET efficiency in dependence of the acceptor concentration and FRET theory was found. The values of R_0 and R_{ex} used in the theoretical modelling of the concentration dependence agreed well with those obtained from the evaluation of

the spectral data, validating the calculation of R_0 from the spectral overlap of the donor emission spectrum with the full acceptor absorption spectrum. Furthermore, the measured donor PL decays in presence of the acceptor QDs can be well reproduced by the curves calculated with the two-dimensional FRET theory in dependence of R_0 and R_{ex}. The values of R_0 and R_{ex} extracted from the fitting agree well with those determined from the concentration study and the analysis of the spectral properties of the QDs. Therefore, the fitting of the donor decay with FRET theory represents a reliable means to evaluate all important FRET parameters, such as the FRET efficiency, FRET rate and R_0, from one type of measurement only.

FRET efficiencies of 90% and FRET rates as high as $(0.5\ \text{ns})^{-1}$ were achieved in the mixed QD monolayers at high acceptor concentrations. At low acceptor:donor concentration ratios an acceptor PL enhancement of 10 was observed, indicating that donors from within three shells contribute to energy transfer to a central acceptor. Additionally, it was found that the total emission in this structure is enhanced by a factor of approximately two at low acceptor:donor ratios compared to the emission in absence of FRET. No emission enhancement is predicted by a simple model calculating the relative increase of the total PL emission due to FRET. The observed emission increase is attributed to efficient energy recycling from excitons trapped in donor defect states that would combine non-radiatively in the absence of acceptor QDs. Good agreement of the modelled PL ratio with the experimentally determined values is found when an additional acceptor concentration dependent factor is included in the calculation of the acceptor enhancement.

5 FRET between separated donor-acceptor QD layers

The first report on Förster resonant energy transfer (FRET) in QD assemblies has been published by Kagan et al. in 1996 [32]. Since then, most effort was focused on the improvement of the FRET rate in QD structures by decreasing the donor-acceptor QD distance [108, 115, 145] and the demonstration of applications based on FRET including QDs as energy donors and / or acceptors [12, 22, 24, 30]. There have also been some reports on the temperature dependence of the FRET process [99, 119, 158]. However, so far only very qualitative comparison with FRET theories have been carried out [32, 114] and in particular no detailed investigation of the concentration dependence of the FRET process has been reported [99, 120].

The acceptor concentration dependence of FRET between QDs for monodispersed and mixed donor-acceptor QD monolayers has already been discussed in the previous chapter. In this chapter, FRET between separated donor and acceptor QD layers is presented. The detailed analysis of FRET in this structure is important for different types of devices making use of FRET between planar donor and acceptor layers [12, 22] and has also been predicted as the most promising geometry for surface plasmon enhanced FRET [130], discussed in the next chapter. In addition to tuning the acceptor:donor concentration ratio, as in the mixed donor-acceptor monolayer, the bilayer structure also allows for the variation of the donor-acceptor separation and offers the possibility to tune the acceptor and donor concentrations independently.

Therefore, the different FRET signatures, the FRET efficiency, acceptor enhancement and overall PL emission, will by analysed as a function of the donor-acceptor layer separation and the donor and acceptor concentrationsThe measured FRET efficiencies will be compared to calculations with a theory of FRET between donor and acceptor planes taking into account homogeneous donor and acceptor ensembles, referred to as the Homogeneous Theory (Hom.-Theory) in the following. Furthermore, the impact of intra-ensemble energy transfer, discussed in the previous chapter, on donor-to-acceptor FRET will be presented. The observed donor concentration dependence of the FRET efficiency, caused by the competition of donor-acceptor inter-layer FRET and energy transfer within the donor monolayer, is not predicted by Hom.-Theory. Two ways to include this effect, arising from the inhomogeneous broadening of the donor QD ensemble,

in FRET theory will be suggested.

The distance dependence of the FRET efficiency and the acceptor enhancement for bilayer structures with donor and acceptor QDs similar to those used in this chapter have been published in Lunz et. al., Superlattices and Microstructures, 47, p. 98 (2010). A summary of the results presented in this chapter has been submitted for publication.

5.1 FRET in Bilayer Structure

The bilayer structures presented in this chapter were prepared with Don1 and Acc2 QDs. The optical properties of the monodispersed Don1 and Acc2 monolayers have been discussed in section 4.1. The Don1 and Acc2 decays presented in the following were recorded with 500 and 650 nm broad band filter respectively.

Due to the long time over which the study of the bilayer structures was carried out, the donor quantum yield in the monolayer decreased from initially 10% to 5% and subsequently to 2.5%, for the latter measurements. Consequently, the Förster radius also decreased with time and the value of R_0 calculated from the spectral overlap reduced from 3.9 to 3.4 to 3.1 nm. For the analysis of the different data sets, the corresponding R_0, calculated with the quantum yield valid at the time of the measurement, was used in the calculations with FRET theory and is given in the discussion of each sample set. The acceptor quantum yield in the monolayers was more stable at 11%.

A fitting of the bilayer spectra with two Gaussian curves did not work accurately for these samples, especially in the case of strong donor quenching, due to the spectral proximity of the two PL peaks and their relatively large peak width. To separate the donor and acceptor contributions to the bilayer PL spectra and to remove the emission of the polyelectrolyte, the bilayer spectra were fitted with actual donor PL spectra, measured for monodispersed reference monolayers with different concentrations. Particular attention was paid to use the most suitable donor spectrum with respect to the emission peak wavelength. This was ensured by carefully monitoring the agreement of the two spectra on the blue side of the emission peak while varying the peak intensity of the donor reference spectrum. Then, the polyelectrolyte emission was added to the donor spectrum and its intensity adjusted to reproduce the intensity of the bilayer spectrum between 540 and 560 nm. The acceptor emission was then calculated as the difference of the bilayer spectrum and the donor and polyelectrolyte emission.

In Figure 5.1 the PL spectrum of a bilayer structure with donor concentration $c_{Don} = 3.1 \times 10^{17}$ m^{-2} and acceptor concentration $c_{Acc} = 0.22 \times 10^{17}$ m^{-2} is shown (solid black triangles) along with the corresponding donor (open green squares) and acceptor monolayer reference spectra (open red circles). The donor and acceptor layers in the bilayer structures were separated by a single PDDA. The thickness of the polyelectrolyte spacer

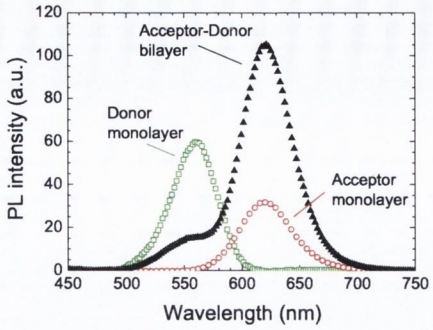


Figure 5.1: PL spectrum of a donor-acceptor bilayer sample (solid black triangles) for a donor-acceptor centre-to-centre distance of 3.6 nm and with donor concentration $c_{Don} = 3.1 \times 10^{17}$ m^{-2} and acceptor concentration $c_{Acc} = 0.22 \times 10^{17}$ m^{-2}. The reference spectra of donor (open green squares) and acceptor (open red circles) monolayer samples, with similar donor and acceptor concentrations as in the bilayer, are also shown.

layer and the interpenetrating ligand shell give rise to a donor-acceptor layer separation of approximately 0.5 nm, with a corresponding minimum donor-acceptor centre-to-centre separation of $R_{ex} = 3.6$ nm. The donor emission in the bilayer is quenched by 50%, whereas the acceptor emission is enhanced by 270%, due to the large donor:acceptor ratio of 13.7. The donor PL quenching and acceptor PL enhancement are clear signatures for energy transfer from the Don1 QDs to the Acc2 QDs.

The donor quenching can also be observed as a large intensity difference of the donor PLE spectra recorded for the bilayer (black line) and donor monolayer (green line) shown in the inset of Figure 5.2(a). This is also reflected in the low donor PLE ratio shown as a green line in Figure 5.2, which has been multiplied by five to allow for a better examination of the data. The donor PLE ratio is more or less flat as both PLE spectra were recorded at similar emission wavelengths, in contrast to the donor PLE ratio shown for the mixed monolayer in Figure 4.9(b) in the previous chapter.

The acceptor PLE spectra, shown in the main panel of Figure 5.2(a), reflect the enhanced emission of the acceptors in the presence of donor QDs (black line) with respect to the acceptor reference (red line). As for the mixed monolayer, the acceptor PLE in the bilayer shows an additional feature, here in the wavelength range between approximately 500 and 550 nm, that is not observed in the PLE spectrum of the acceptor monolayer. This feature is very distinct in the acceptor PLE ratio of the bilayer and reference monolayer shown as a red line in Figure 5.2(b). It occurs at the same wavelength as the first absorption peak in the donor absorption spectrum, also included in the figure (grey line, right-hand axis), and is, as discussed in the previous chapter, a signature of energy transfer from the donor to the acceptor QDs.

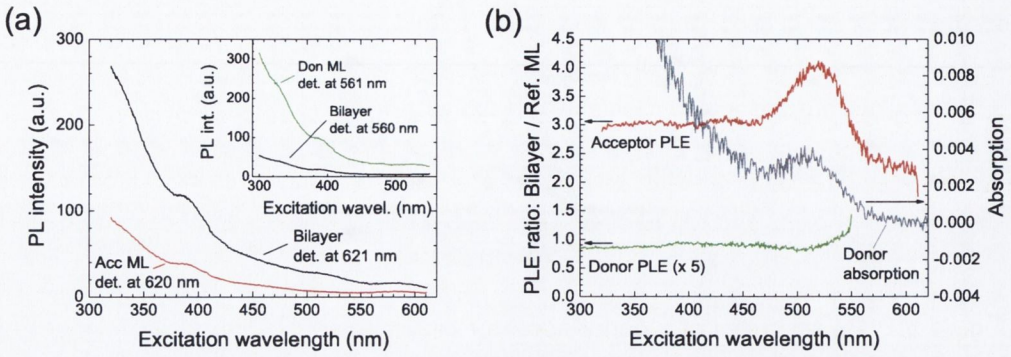


Figure 5.2: (a) PL excitation (PLE) spectra detected at the acceptor peak emission wavelength in the bilayer (black line) and acceptor monolayer (ML) reference (red line). The inset shows the PLE spectra recorded for the donor emission in the bilayer (black line) and donor monolayer reference (green line). (b) Ratio of the bilayer and monolayer PLE spectra (left-hand axis) detected at the acceptor (red line) and donor peak wavelength (green line). The absorption of the donor monolayer is also shown (grey line, right-hand axis).

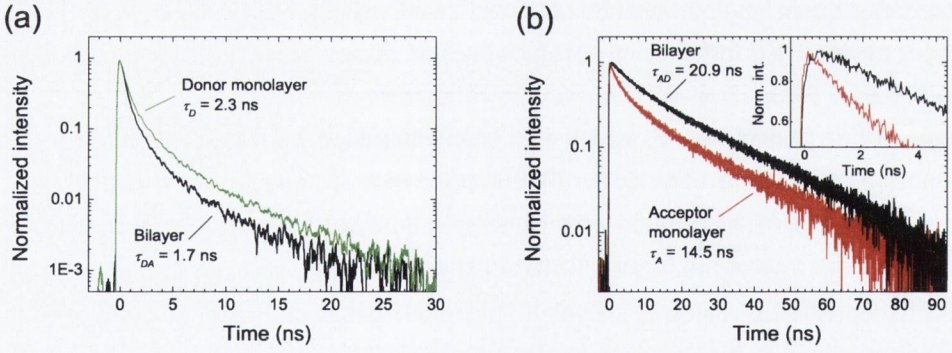


Figure 5.3: (a) Donor PL decays in the donor-acceptor bilayer structure (black line) and in a donor reference monolayer (green line), with similar donor concentration as in the bilayer. (b) Acceptor PL decays in the bilayer (black line) and in an acceptor monolayer (red line), with similar acceptor concentration as in the bilayer. The inset shows a close-up of the acceptor decays over the first 5 ns to highlight the prolonged rise-time in the bilayer structure.

The donor and acceptor PL decays in the bilayer structure are shown in Figures 5.3(a) and (b) respectively (black lines), along with the reference decays recorded for the donor (green line) and acceptor monolayers (red line). The donor PL lifetime is reduced from $\tau_D = 2.3$ ns, in the reference monolayer, to $\tau_{DA} = 1.7$ ns, in the presence of the acceptors. This lifetime decrease corresponds to a FRET efficiency of $(26 \pm 5)\,\%$. The acceptor PL lifetime increases from $\tau_A = 14.5$ ns to $\tau_{AD} = 20.9$ ns in the donor-acceptor bilayer structure. Furthermore, the intensity maximum of the time-resolved acceptor PL occurs at a later time in the bilayer structure than in the reference monolayer. The time-delay of the maximum acceptor emission is increased from 0.20 ns to 0.64 ns. The larger rise-time of the acceptors in the presence of the donors is a signature of the additional pumping of the acceptor QDs by energy transfer from the donors.

5.2 Distance dependence

A strong distance dependence is expected for energy transfer via the Föster mechanism. Varying the polyelectrolyte spacer layer thickness, the distance dependence of the FRET process between the donor and acceptor QD layers can be probed. The PL spectra of bilayer samples with different donor-acceptor layer separations, corresponding to the spacer layer thickness, are shown in Figure 5.4(a). The donor and acceptor concentrations of these samples were $c_{Don} = (3.4 \pm 0.3) \times 10^{17}$ m^{-2} and $c_{Acc} = (0.76 \pm 0.08) \times 10^{17}$ m^{-2}. The donor quenching is largest for the smallest layer separation and increases towards the value of the reference donor monolayer with increasing separation. Similarly, in the acceptor emission the largest effect, in form of the strongest acceptor enhancement, is seen for the smallest layer separation and the enhancement decreases with increasing spacer layer thickness. The PL spectrum of the sample with a 6 nm donor-acceptor layer separation is indicated by a thicker line, as this sample was prepared and measured at a later time than the other samples. The donor quantum yield had decreased from 10% to 2.5%, reducing probability for FRET. Due to the smaller R_0, arising from the reduced donor quantum yield, and a lower acceptor concentration for the sample with a 6 nm donor-acceptor layer separation, the acceptor emission of this sample is smaller than for the 9 nm separation.

The distance dependence of the energy transfer is also reflected in the acceptor PLE ratios shown in Figure 5.4(b). For the smallest donor-acceptor layer separation of 0.5 nm, a strong donor absorption feature, indicated by the green line, is observed in the wavelength range between 470 and 540 nm. The intensity of this feature is lower for the 3 nm donor-acceptor separation and an increase at higher wavelengths is seen due to a difference in detection wavelength for the bilayer and reference monolayer PLE spectra. For the 6 nm donor-acceptor separation the feature is further decreased; and it

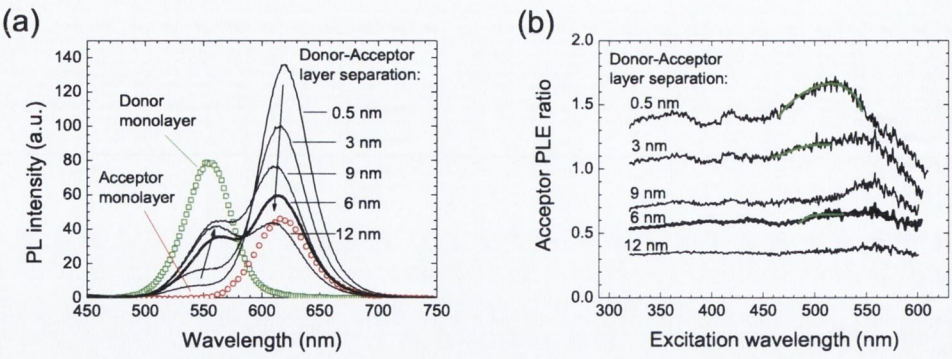


Figure 5.4: (a) PL spectra of donor-acceptor bilayer structures for different donor-acceptor layer separations (lines). Donor (open green squares) and acceptor (open red circles) monolayer spectra at similar donor and acceptor concentrations as in the bilayer structure are also shown for comparison. (b) Ratio of the acceptor PLE spectra calculated for the spectra of the bilayer structures presented in (a) and an acceptor reference monolayer. It is important to note that the sample with a 6 nm separation was prepared and measured at a later time than the other samples and therefore shows a lower acceptor enhancement as expected due to a reduced donor quantum yield. The data recored for this sample is indicated by a thicker line in Figures (a) and (b).

is no longer observed for the 9 nm and 12 nm separations. This indicates that energy is only transferred from donor to acceptor QDs over layer separations smaller than 9 nm, corresponding to a minimum donor-acceptor centre-to-centre distance of approximately 12 nm in the bilayer structure. For a R_0 of 3.9 nm, no energy transfer is expected at these "large" separations as will be discussed in more detail below.

This trend is further confirmed by the donor PL decays shown in Figure 5.5(a). The shortest decay with a lifetime of $\tau_{DA} = 0.8$ ns, corresponding to the highest FRET rate $k_{DA} = (0.9\ \text{ns})^{-1}$ and efficiency $E_{\text{FRET}} = 71\%$, is observed for the smallest donor-acceptor layer separation of 0.5 nm (blue line). For a 3 nm layer separation (dark blue line) a longer decay with a characteristic lifetime of 2.0 ns is recorded and for the larger separations of 9 and 12 nm (grey and black blue line respectively) the decay is the same as for a donor monolayer in the absence of any acceptor QDs, characterized by a lifetime of $\tau_D = 2.8$ ns. The decay for the 6 nm separation is not included in the Figure as it cannot be compared directly to the other decays due to the change in the donor recombination dynamics reflected in the decreased quantum yield.

The acceptor PL decays for a 0.5 nm (blue line) and 12 nm donor-acceptor layer separation (black line) are shown in Figure 5.5(b). As can be seen, the decay for the smaller layer separation is longer than that for the larger separation and it also shows a larger rise-time due to the additional excitation of the acceptor QDs by energy transfer from the donors. As the probability for energy transfer decreases with increasing layer

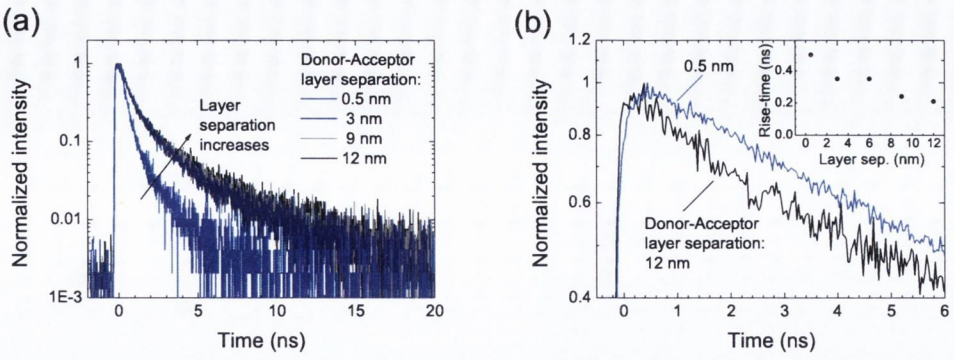


Figure 5.5: (a) Donor decays in the bilayer structure for donor-acceptor layer separations of 0.5 nm (blue), 3 nm (dark blue), 9 nm (grey) and 12 nm (black line). The donor decay of the bilayer with a 6 nm separation is not included, because of the reduced donor quantum yield at the time of the measurement which is indicative of modified decay dynamics, and therefore this decay cannot be compared directly to the other decays. (b) Acceptor decays in the bilayer structure for layer separations of 0.5 nm (blue) and 12 nm (black line). The rise-time, extracted as the time-delay of the maximum intensity in the acceptor decay, as a function of the layer separation is shown in the inset.

separation, the time-delay of the maximum acceptor intensity, shown in the inset of Figure 5.5(b), decreases from approximately 0.5 ns to 0.2 ns, the time-delay of the peak intensity measured in the time-resolved PL of a monodispersed Acc2 monolayer.

5.2.1 FRET Efficiency and Acceptor Enhancement

The FRET efficiency, $E_{\mathrm{FRET}} = 1 - \tau_{DA}/\tau_D$, can be calculated from the donor PL lifetimes at each donor-acceptor layer separation. The experimentally determined values of E_{FRET} are shown in Figure 5.6(a) along with theoretical trends calculated for different values of R_0 with equation (2.14) derived in section 2.2.1 and repeated in equation (5.1):

$$E_{\mathrm{FRET}} = \frac{1}{1 + \frac{2 \cdot R_{ex}^4}{c_{Acc} \cdot \pi \cdot R_0^6}} \,. \tag{5.1}$$

As can be seen the observed decrease of the FRET efficiency with increasing donor-acceptor layer separation agrees well with theory. A good qualitative agreement with the theoretically expected trend has already been reported for the distance dependence of the FRET rate, determined for energy transfer between QDs in an LbL assembled layer structure [114]. Here also a good quantitative agreement of the measured and calculated distance dependence of the FRET efficiency can be seen for the theory with $R_0 = (3.9 \pm 0.2)$ nm, the value of the Förster radius determined from the spectral overlap. For comparison the values calculated for $R_0 = 4.3$ nm are too high at small

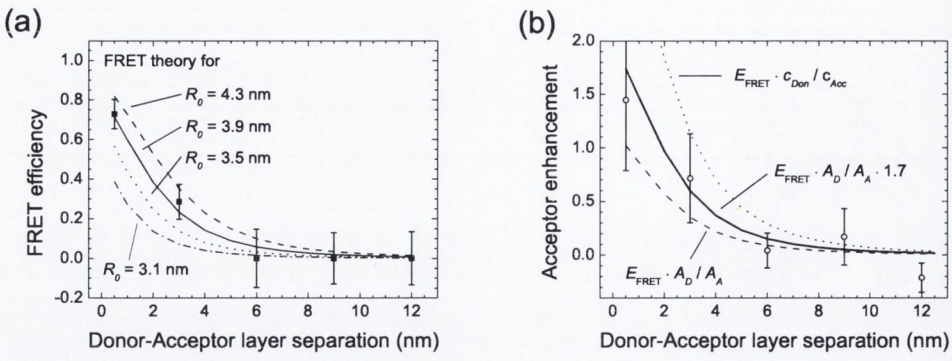


Figure 5.6: (a) Dependence of the FRET efficiency (black squares), calculated from the donor lifetime decrease in the bilayer structure, on the donor-acceptor layer separation. Theoretically calculated trends for the distance dependence of the FRET efficiency are included for $R_0 = 3.1$ nm (dash-dot line), 3.5 nm (dotted line), 3.9 nm (solid line) and 4.3 nm (dashed line). (b) Acceptor enhancement (open black circles), calculated from the integrated acceptor spectra in the bilayer structure and acceptor monolayer reference, in dependence of the donor-acceptor layer separation. The expected acceptor enhancement, calculated by multiplying the calculated FRET efficiency ($R_0 = 3.9$ nm) with the absorption ratio A_D/A_A (dashed line), $A_D/A_A \cdot 1.7$ (solid line) and by multiplying with the concentration ratio c_{Don}/c_{Acc} (dotted line), is also shown.

layer separations, whereas those for $R_0 = 3.5$ nm are too low. The experimental value of E_{FRET} for the 6 nm layer separation is almost zero and lies below the expected value for $R_0 = 3.9$ nm, even though it still agrees within error. However, as mentioned above, the donor quantum yield for this measurement had reduced to 2.5% and taking into account a reduced $R_0 = 3.1$ nm, the measured FRET efficiency also agrees very well with that expected from theory using the appropriate R_0.

In Figure 5.6(b) the acceptor PL enhancement, $I_{AD}/I_A - 1$, (open black circles), determined from the spectrally integrated acceptor emission in the bilayer and monolayer spectra with the same acceptor concentration, is shown as a function of the layer separation. The acceptor enhancement decreases with increasing separation following a trend similar to that of the FRET efficiency. The expected acceptor enhancement, $E_{Enh} = E_{\mathrm{FRET}} \cdot A_D/A_A$, has been determined for the theoretically calculated distance dependence of the FRET efficiency for $R_0 = 3.6$ nm, and is indicated by the dashed line. As can be seen, similar to observations for the mixed Don3-Acc1 monolayers, the measured acceptor enhancement is underestimated by multiplying the FRET efficiency with the donor:acceptor absorption ratio A_D/A_A. This indicates that, also for the Don1-Acc2 bilayer structure, energy of excitons trapped in donor defect states is recycled by energy transfer to the acceptor QDs. Multiplying E_{FRET} with the concentration ratio

c_{Don}/c_{Acc} (dotted line) results in larger values than the measured acceptor enhancement, which is best represented by $E_{Enh} = E_{\mathrm{FRET}} \cdot A_D/A_A \cdot 1.7$ (solid line). The good qualitative agreement of the distance dependence of the FRET efficiency with the trend for the acceptor PL enhancement indicates that enhancement of the acceptor emission is due to FRET and that no other energy transfer mechanisms, such as radiative energy transfer or tunelling, play an important role. Quantitative agreement for the acceptor enhancement is found by multiplying by a constant factor, suggesting that exciton recycling mediated by FRET can be taken account of in this way.

5.2.2 Relative Quantum Efficiency

The relative quantum efficiency QE_{rel} of the bilayer structures has been calculated in a similar way as for the mixed donor-acceptor monolayer. The integrated PL spectra of the bilayer structure were compared to the sum of the spectrally integrated emission of a donor and acceptor monolayer with the same donor and acceptor concentrations as in the bilayer structure. As can be seen in Figure 5.7(a), the relative quantum efficiency is close to one for the largest layer separations and it seems to increase to a value of approximately 1.5 at the lowest layer separation investigated, however, the error on the values is relatively large. Such a large increase is not expected from the modelling of the QE_{rel} (dashed line) calculated with the PL model discussed in section 4.2.3 and represented by equation (4.5), given again in equation (5.2).

$$QE_{rel} = 1 + E_{FRET}(c_{Acc}) \frac{Q_A/Q_D - 1}{1 + Q_A/Q_D \cdot \frac{A_A}{A_D}} \tag{5.2}$$

This enhanced PL emission is attributed to the recycling effect of the excitonic donor energy already observed for the acceptor enhancement discussed just above.

However, the effect is not as large as in the mixed monolayer, for which the data showed a much larger efficiency than predicted by the PL intensity model (e.g. a two-fold increase was observed for $c_{Acc}/c_{Don} = 0.2$) and was well reproduced by a quantum yield model (equation (4.6)) based on the idea of summing the quantum yields:

$$QE^{\star}_{rel} = 1 + E_{FRET} \frac{Q_A \cdot \frac{c_{Don}}{c_{Acc}} - Q_D}{Q_A + Q_D} \,. \tag{5.3}$$

Here, the quantum yield model (dotted line), reproduced in equation (5.3), gives values larger than those observed. The relative quantum efficiency measured for the bilayer samples actually lies between these two calculated curves for low donor-acceptor layer separations. A good agreement with the data is obtained by taking into account $E_{Enh} = E_{\mathrm{FRET}} \cdot A_D/A_A \cdot 1.7$ in the PL model (solid line), the same expression for which also a good fit with the measured acceptor enhancement was obtained as shown in Figure

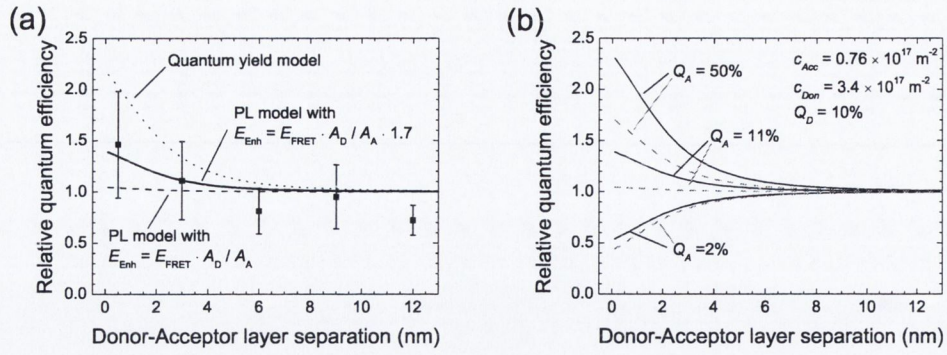


Figure 5.7: (a) Relative quantum efficiency, determined from the ratio of the integrated PL emission of the bilayer structure and a reference structure without FRET, in dependence of the donor-acceptor layer separation. The trends calculated with a model of the integrated PL intensities for $E_{Enh} = E_{\mathrm{FRET}} \cdot A_D/A_A$ (dashed lines) and $E_{Enh} = E_{\mathrm{FRET}} \cdot A_D/A_A \cdot 1.7$ (solid line) as well as for a model based on additive quantum yields (dotted lines) are also shown. (b) Relative quantum efficiency as a function of the donor-acceptor layer separation calculated with the PL model including the acceptor enhancement as $E_{Enh} = E_{\mathrm{FRET}} \cdot A_D/A_A$ (dashed grey lines) and $E_{Enh} = E_{\mathrm{FRET}} \cdot A_D/A_A \cdot 1.7$ (solid black lines) for different acceptor quantum yields. The distance dependence of the FRET efficiency was calculated by theory for $R_0 = 3.9$ nm and $c_{Acc} = 0.76 \times 10^{17}$ m^{-2}, the donor properties used were $c_{Don} = 3.4 \times 10^{17}$ m^{-2} and $Q_D = 10\%$.

5.6(b). This indicates, that the same effect that is increasing the acceptor enhancement to values higher than those expected, is also responsible for the increased total PL emission from the bilayer samples.

Figure 5.7(b) shows the distance dependence of QE_{rel} calculated with the PL model for three different acceptor quantum yields Q_A. The donor quantum yield $Q_D = 10\%$ was kept constant in order not to change R_0. The values of E_{FRET} included in the model were calculated by FRET theory for $R_0 = 3.9$ nm (solid line in Figure 5.6(a)). The dashed lines are the results of the calculation with the simple PL model including the acceptor enhancement as $E_{\mathrm{FRET}} \cdot A_D/A_A$, whereas the solid lines represent the calculation with the PL model taking into account $E_{Enh} = E_{\mathrm{FRET}} \cdot A_D/A_A \cdot 1.7$, which gives the better agreement with the data. As can be seen, for both models QE_{rel} increases with increasing Q_A at a fixed donor-acceptor separation. The extended PL model always predicts a higher total emission from the bilayer structure than the simple PL model, as it includes an empiric factor for the exciton recycling effect. Therefore, the transition from a decreased total PL emission to an enhanced emission, with respect to the reference emission value, occurs at a lower Q_A than for the simple PL model. The difference between the two models decreases with decreasing Q_A.

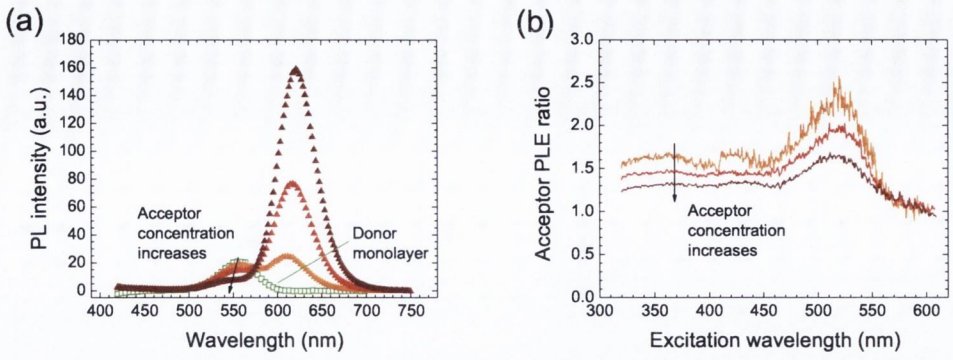


Figure 5.8: (a) PL spectra of three donor-acceptor bilayer samples with different acceptor concentrations increasing from 0.19 to 0.39 and 0.76×10^{17} m^{-2} (solid triangles). The donor concentration varied between 3.2 and 3.5×10^{17} m^{-2} for these samples. A spectrum of a donor monolayer (open green squares) with similar donor concentration is also included for reference. (b) Ratio of the acceptor PLE spectra of the bilayers and corresponding acceptor reference monolayers for the samples presented in (a).

5.3 Acceptor concentration dependence

In addition to the minimum donor-acceptor separation, the acceptor concentration also has an important influence on the FRET efficiency as can be seen in equation 5.1. To investigate the acceptor concentration dependence of the FRET process, bilayer structures with different acceptor QD concentrations and a single PDDA layer separating the donor and acceptor layers were prepared, giving rise to a donor-acceptor centre-to-centre separation of $R_{ex} = 3.6$ nm. The donor concentration was kept constant at $c_{Don} = (3.1 \pm 0.5) \times 10^{17}$ m^{-2} and Q_D at the time of the measurement was 2.5%, corresponding to $R_0 = 3.1$ nm.

PL spectra recorded for three bilayer structures with different acceptor concentrations are shown as examples in Figure 5.8(a). The reference spectrum for a donor monolayer with a concentration adjusted to $c_{Don} = 3.2 \times 10^{17}$ m^{-2} is also included for comparison. The acceptor QD concentration in the bilayer structures increased from 0.19 ($c_{Don} = 3.2 \times 10^{17}$ m^{-2}) to 0.38 ($c_{Don} = 3.5 \times 10^{17}$ m^{-2}) to 0.76×10^{17} m^{-2} ($c_{Don} = 3.2 \times 10^{17}$ m^{-2}). Due to the increasing number of acceptors available to each donor QD for energy transfer, the probability for FRET is expected to increase with increasing c_{Acc}. In line with this expectation, the donor PL emission decreases with increasing acceptor concentration and as the c_{Don} is constant, this indicates that the donor PL quenching due to FRET is increasing, reflecting an increase in FRET efficiency. The acceptor emission is increasing with increasing c_{Acc}, but without further analysis of the data it is difficult to determine to which extend this is due to energy transfer or just caused by

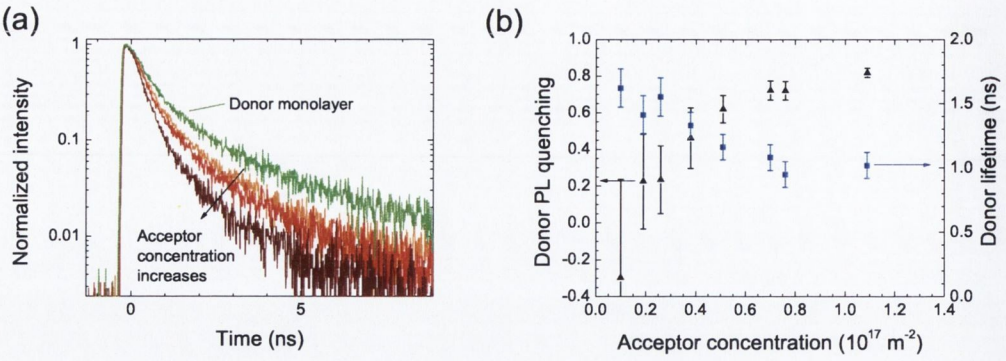


Figure 5.9: (a) Donor PL decays of the donor-acceptor bilayer structures with different acceptor concentrations presented in Figure 5.8, and of a donor reference monolayer (green line). (b) Acceptor concentration dependence of the donor PL quenching (black tirangles) and the donor lifetime (blue squares) measured in the donor-acceptor bilayer structure. The donor concentration was $c_{Don} = (3.1 \pm 0.5) \times 10^{17}$ m^{-2} for the complete sample set shown in (b).

the increase of the acceptor concentration.

A first inditcation of the actual trend of the acceptor enhancement can be obtained from the acceptor PLE ratios shown in Figure 5.8(b). The PLE ratio for the lowest acceptor concentration is noisier than the other spectra, due to the lower PL intensity of the acceptor PLE reference spectrum at this low acceptor concentration. The value of the PLE ratios at low excitation wavelengths indicates that the acceptor PL enhancement is decreasing with increasing c_{Acc}. Furthermore, the feature corresponding to the transfer of energy from donors excited in resonance with the first donor absorption peak, also shows a decrease with increasing c_{Acc}. This means that, despite the increasing FRET efficiency, with increasing acceptor concentration the acceptor PL enhancement is decreasing as the energy is transferred to a larger number of acceptor QDs, so that on average each acceptor QD receives less energy. The reason for this is the sublinear dependence of the FRET efficiency on c_{Acc}, as can be seen in equation (5.1), that leads to a slower increase in E_{FRET} for larger acceptor concentrations.

In Figure 5.9(a), the donor decays of the three bilayer structures as well as a donor reference decay (green line) can be seen. The donor decays in the bilayer structures are clearly faster than the reference decay and the respective donor lifetimes decrease from $\tau_{DA} = 1.4$ ns to 1.3 ns to 0.95 ns with increasing acceptor concentration. The acceptor decays for the bilayer structures are not discussed as they cannot be compared directly due to the varying acceptor concentration.

The donor PL quenching, $1 - I_{DA}/I_D$, as a function of the acceptor concentration is shown in Figure 5.9(b) for the whole sample set (black triangles, left-hand axis). As can be seen the quenching of the donor emission is increasing with increasing acceptor

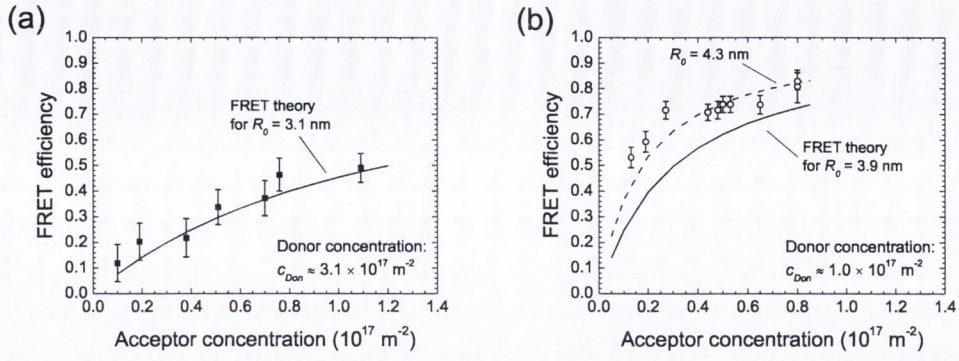


Figure 5.10: (a) FRET efficiency in dependence of the acceptor concentration for bilayer samples with high donor concentration, $c_{Don} = (3.1 \pm 0.5) \times 10^{17}$ m^{-2}. The line represents the theoretical calculation of the FRET efficiency for $R_0 = 3.1$ nm, as calculated from the spectral overlap of the Don1 and Acc2 reference spectra for $Q_D = 2.5\%$. (b) Acceptor concentration dependence of the FRET efficiency at a lower donor concentration, $c_{Don} = (1.0 \pm 0.2) \times 10^{17}$ m^{-2}. The theoretical calculations are included for $R_0 = 3.9$ nm (solid line), as calculated from the spectral overlap and $Q_D = 10\%$, and for $R_0 = 4.3$ nm (dashed line).

concentration over the whole concentration range investigated. The donor lifetime is also presented as a function of c_{Acc} in Figure 5.9(b) (blue squares, right-hand axis). As already indicated by the three donor decays shown in (a) the donor lifetime becomes continuously shorter with increasing c_{Acc}. The decrease of the donor lifetime along with the increasing donor PL quenching are both signatures of increasing FRET with increasing acceptor concentration.

5.3.1 FRET Efficiency and Acceptor Enhancement

The dependence of the FRET efficiency, calculated from the donor lifetime decrease in the bilayer structure, on the acceptor concentration is shown in Figure 5.10(a). The solid line represents the theoretical trend calculated with equation (5.1) including $R_0 = 3.1$ nm, the value of the Förster radius determined via the spectral overlap and for a donor quantum yield of 2.5%. It is important to note that the calculated trend is not a fit, but that all parameters included in the calculation were obtained from independent measurements. As can be seen, the increase of the experimentally determined FRET efficiency with increasing acceptor concentration agrees very well with the values calculated with FRET theory. The good agreement of theory and measurement for the acceptor concentration dependence as well as the distance dependence discussed in the previous section, clearly show that FRET theory, predominantly developed for molecular systems, is suitable to describe FRET in QD structures.

Another set of donor-acceptor bilayer structures with varying acceptor concentrations and a lower donor concentration $c_{Don} = (1.0 \pm 0.2) \times 10^{17}$ m^{-2} was also characterized. The samples were prepared and measured at the same time as those for the distance dependence discussed above. Therefore, $Q_D = 10\%$ has to be considered in the calculation of the Förster radius: $R_0 = 3.9$ nm. The FRET efficiencies determined from the donor lifetime meausrements for this sample set are shown in Figure 5.10(b). The values of E_{FRET} are larger in this case than those in (a) due to the higher donor quantum yield and the larger R_0 at the time of the measurement. Also for this lower donor concentration, the FRET efficiency is increasing with increasing c_{Acc}.

However, in this case, only the trend but not the values of the FRET efficiency calculated for $R_0 = 3.9$ nm, determined from the spectral overlap, agree with the measured FRET efficiencies. A larger R_0 of 4.3 nm has to be used to also obtain a quantitative agreement of theory and experiment. This is quite surprising as the distance dependence measured at the same time as this acceptor concentration dependence, does agree well with the theoretically calculated trend for $R_0 = 3.9$ nm. The FRET efficiencies obtained for the calculation of the distance dependence with $R_0 = 4.3$ nm are too large and even outside the error range, as can be seen in Figure 5.6(a). The difference between these two sample sets is the donor concentration. It seems that a good quantitative agreement with FRET theory for R_0 calculated from the spectral overlap is obtained for high but not for low donor concentrations. The discrepancy of theory and experiment at low donor concentrations is attributed to donor intra-ensemble energy transfer and the effect of energy transfer within the donor monolayer on the characterisation of donor-acceptor inter-layer FRET is going to be investigated in detail in the next section.

The acceptor PL enhancement in the bilayer structures, calculated from the integrated acceptor PL spectra, is shown as a function of c_{Acc} in Figure 5.11(a) for the sample set with the higher donor concentration $c_{Don} = (3.1 \pm 0.5) \times 10^{17}$ m^{-2} (black squares). As indicated by the comparison of the PLE ratios for three different acceptor concentrations discussed above, the acceptor enhancement is decreasing with increasing acceptor concentration. The expected acceptor enhancement obtained by multiplying the theoretically calculated FRET efficiency ($R_0 = 3.9$ nm) with the donor:acceptor absorption ratio A_D/A_A or concentration ratio c_{Don}/c_{Acc} are represented by the dashed and dotted lines respectively. Both calculations support the decreasing trend of the acceptor enhancement with increasing acceptor concentration. However, as for the distance dependence of the acceptor enhancement shown in Figure 5.6(b), the multiplication with A_D/A_A underestimates the acceptor PL enhancement a little, again showing an increased acceptor enhancement due to exciton recycling, whereas the values obtained using $E_{FRET} \cdot c_{Don}/c_{Acc}$ are too large. The best agreement of the measured and calculated acceptor enhancement for the distance dependence was found for $E_{FRET} \cdot A_D/A_A \cdot 1.7$.

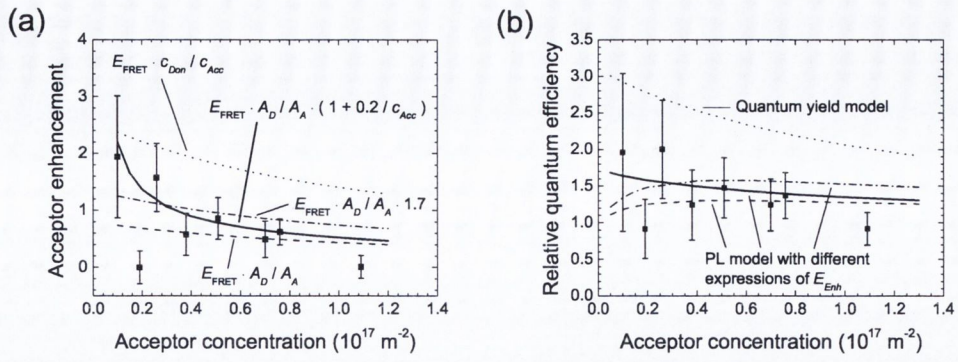


Figure 5.11: (a) Acceptor PL enhancement (black squares) in dependence of the acceptor concentration in the bilayer. The lines indicate theoretical trends calculated from the theoretically modeled FRET efficiency ($R_0 = 3.9$ nm) by multiplying with the donor:acceptor absorption ratio A_D/A_A (dashed line), $A_D/A_A \cdot 1.7$ (dash-dot line), $A_D/A_A \cdot (1 + 0.2/c_{Acc})$ or the concentration ratio (dotted line). (b) Experimentally determined relative quantum efficiency as a function of the acceptor/donor concentration ratio (black squares). The lines represent the relative quantum efficiency calculated with a PL model for the integrated PL intensities including the acceptor PL enhancement in form of $E_{\mathrm{FRET}} \cdot A_D/A_A$ (dashed line), $E_{\mathrm{FRET}} \cdot A_D/A_A \cdot 1.7$ (dash-dot line) and $E_{\mathrm{FRET}} \cdot A_D/A_A \cdot (1 + 0.2/c_{Acc})$ (solid line); the dotted line indicates the results of a quantum yield model.

For the acceptor concentration dependence this expression (dash-dot line) shows a better agreement with the data than the multiplication with the donor:acceptor absorption or the concentration ratio. However, it still doesn't fit the data very well at the very low and high acceptor concentrations and doesn't predict a strong change in the acceptor enhancement with varying acceptor concentration as observed in the measured data. Therefore, an additional concentration dependent term was included to better model the acceptor enhancement, similar to the calculation of the acceptor enhancement in the mixed monolayer. The acceptor concentration dependence of the acceptor enhancement is well reproduced by $E_{Enh} = E_{\mathrm{FRET}} \cdot A_D/A_A \cdot (1 + 0.2/c_{Acc})$ (solid line). Therefore, the increase of the acceptor enhancement due to exciton recycling can be described by the same acceptor concentration in both structures, even though the origin of this concentration dependence is not yet fully understood.

5.3.2 Relative Quantum Efficiency

In Figure 5.11(b) the relative quantum efficiency, QE_{rel}, the ratio of the spectrally integrated PL emission of the bilayer structure and the sum of the emission of the respective donor and acceptor reference monolayers, is presented as a function of the

acceptor concentration. The experimentally determined values follow a similar trend to that observed for the acceptor enhancement. At low acceptor concentrations the total emission is increased by a factor of two due to energy transfer in the bilayer structure.

The values of QE_{rel} calculated with the simple PL model described in equation (5.2) and the quantum yield model, summarized in equation (5.3), are shown as dashed and dotted lines respectively in Figure 5.11(b). In general the PL model reproduces the values of QE_{rel} better than the quantum yield model, which overestimates the total PL enhancement as for the distance dependence of QE_{rel}. However, the simple PL model only predicts efficiencies of below 1.3 and shows a decrease for decreasing acceptor concentrations below 0.4×10^{17} m^{-2}, whereas the experimentally determined efficiencies seems to continue to increase for decreasing acceptor concentrations in this range. Including $E_{Enh} = E_{\mathrm{FRET}} \cdot A_D/A_A \cdot 1.7$ in the PL model (dash-dot line) doesn't improve the agreement with the data, as the calculated values of QE_{rel} seem a little too large at high acceptor concentrations and the decrease with decreasing c_{Acc} is starting at even higher acceptor concentrations than for the simple PL model.

Good agreement with the measured acceptor enhancement was obtained for $E_{Enh} = E_{\mathrm{FRET}} \cdot A_D/A_A \cdot (1 + 0.2/c_{Acc})$ and if this expression is included in the PL model, the trend and the values of QE_{rel} are represented fairly well. This seems to indicate that the acceptor concentration dependence of QE_{rel}, as well as the acceptor enhancement, in the the mixed donor-acceptor monolayer and in the bilayer structure can be explained by the same concentration dependent factor to take account of the exciton recycling in the QD structures. However, due to the large errors and the strong variation of the measured data for the bilayer structure in the region of the lowest acceptor concentrations investigates, it is difficult to say if the efficiencies are actually continuing to increase with decreasing c_{Acc} or if they actually show a decrease of the emission enhancement at low acceptor concentrations. It is more physical to expect QE_{rel} to decrease towards 1 for low c_{Acc} as E_{FRET} decreases to zero, however if additional energy is transferred from excitons trapped in donor defect states, the efficiency would show larger values than predicted by the PL model at low c_{Acc} due to a larger acceptor enhancement and would probably only start to decrease at lower acceptor concentrations than predicted by the simple PL model. Furthermore, the increase of QE_{rel} with decreasing c_{Acc} would also be in agreement with the observations for the mixed donor-acceptor monolayer.

5.4 Donor concentration dependence

As discussed in chapter 2, FRET theory, based on homogeneous donor and acceptor ensembles, do not predict an influence of the donor concentration on the FRET efficiency, as can for example be seen in equation (5.1). However, the discrepancy

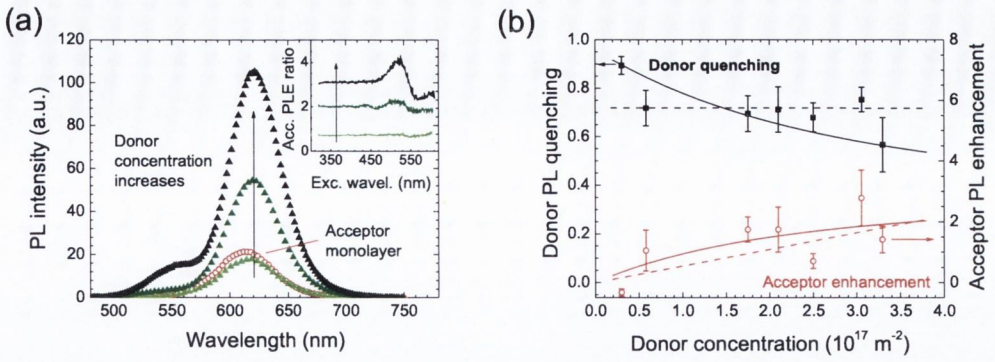


Figure 5.12: (a) PL spectra for donor-acceptor bilayer structures with $c_{Don} = 0.28$, 0.58 and 3.1×10^{17} m^{-2} (solid triangles). The acceptor concentration was kept constant at $c_{Acc} = 0.22 \times 10^{17}$m^{-2} for these three samples. An acceptor reference monolayer spectrum with this concentration is also included (open red circles). In the inset the acceptor PLE ratios of the samples are shown. (b) Donor concentration dependence of the donor PL quenching (solid black squares, left-hand axis) and acceptor PL enhancement (open red circles, right-hand axis) for the whole sample set with $c_{Acc} = (0.33 \pm 0.12) \times 10^{17}$ m^{-2}. Linear (dashed) and concentration dependent trends (solid lines) are included as possible fitting curves for the data.

between theory and experiment observed for the acceptor concentration dependence discussed above indicates that c_{Don} might have an impact on E_{FRET} and this is thought to be associated with donor intra-ensemble energy transfer. Furthermore, by increasing the donor:acceptor ratio the acceptor PL enhancement should become larger, making the donor concentration also an important parameter to study for FRET applications. Therefore, the origin and consequences of the donor concentration dependence are investigated in more detail in this section.

Three representative PL spectra of bilayer structures with $R_{ex} = 3.6$ nm and an acceptor concentration of 0.22×10^{17} m^{-2} can be seen in Figure 5.12(a), along with an acceptor reference spectrum at the same acceptor concentration (open red circles). As the donor concentration increases from 0.28 to 0.58 to 3.1×10^{17} m^{-2} the donor PL as well as the acceptor PL increase. It is difficult to obtain any information on the donor quenching from the PL spectra without further processing of the data. However, as the acceptor concentration is the same for all samples the increase in the acceptor PL can be unambiguously attributed to an increase of the acceptor PL enhancement with increasing donor concentration. This is further confirmed by the acceptor PLE ratios, shown in the inset, as the relative intensity of the PLE spectra increases and the donor absorption signature becomes larger with increasing donor concentration.

For a more detailed analysis of the FRET signatures in the PL spectra of all samples, the donor PL quenching (solid black squares, left-hand axis) and the acceptor PL en-

hancement (open red circles, right-hand axis) are shown in Figure 5.12(b). It is difficult to say if the donor quenching is constant within error (dashed line) or if it is decreasing (solid line, fit based on the rate model for the FRET efficiency given in equation (5.4) discussed below) with increasing c_{Don}, as there are always two data points, at the very low and high concentrations, that don't fit the trend. From theory a constant quenching, corresponding to a constant E_{FRET}, would be expected. However, taking into account that c_{Acc} is only $(0.33 \pm 0.12) \times 10^{17}$ m^{-2}, the donor:acceptor ratio is relatively large for samples with high donor concentrations, such that not all donors might be able to transfer their energy to an acceptor QD. The competition for available acceptors could therefore lead to a decrease of the donor PL quenching.

The acceptor PL enhancement is increasing with increasing donor concentration as expected. The solid and dashed line indicate the trends calculated from a donor-concentration dependent and constant E_{FRET} respectively, determined from the rate model and Hom.-Theory discussed in section 5.4.1 below, by multiplying with the donor:acceptor absorption ratio and a factor 1.8, taking account of the recycling effect. Both trends fit the data reasonably well, and therefore do not offer an indication whether the donor PL quenching and the FRET efficiency are constant or decrease with increasing donor concentration. However, for the optimization of applications based on FRET between QDs it is important to understand the donor concentration dependence of the FRET efficiency and the acceptor PL enhancement. For example, for a sensing structure it would be important to work at the donor concentration giving the highest sensitivity, i.e. the strongest increase in the acceptor enhancement for a small change in donor concentration. And for light harvesting structures one would like to engineer the highest FRET efficiency possible to maximize the energy flow. In order to clarify the influence of the donor concentration on the energy transfer between the Don1 and Acc2 QDs in the bilayer structure the time-resolved PL decays are investigated in the following.

The donor and acceptor PL decays recorded for the three bilayer samples with donor concentrations of 0.28, 0.58 and 3.1×10^{17} m^{-2} are shown in Figure 5.13(a) and (b) respectively. Due to the large donor PL quenching, the donor decays are very noisy. However, one can see that with increasing c_{Don} the decays are becoming faster and the PL lifetime reduces from 3.2 to 2.2 to 1.6 ns. In the inset of Figure 5.13(a) the donor concentration dependence of the donor lifetimes τ_{DA} for all bilayer structures investigated can be seen. The decrease of τ_{DA} with increasing donor concentration could be due to the underlying concentration dependence of the donor lifetime τ_D in absence of the acceptor QDs and the FRET efficiency and rate have to be calculated to see if there is an actual donor concentration dependence of the donor-acceptor FRET process.

In contrast to the donor decays, the acceptor decays become longer with increasing

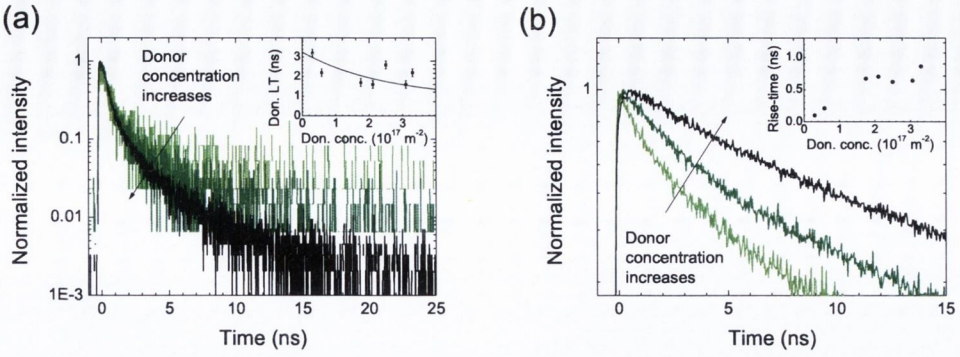


Figure 5.13: (a) Donor PL decays of the donor-acceptor bilayer structures with different donor concentrations, $c_{Acc} = 0.22 \times 10^{17} \mathrm{m}^{-2}$. In the inset the average lifetimes are shown for the whole sample set as a function of the donor concentration in the bilayer, the line is included as a guide to the eye. (b) Acceptor decays measured for the bilayer structures presented in (a). The rise-time of the acceptor decay, determined as the time-delay of the maximum intensity, is shown in dependence of the donor concentration in the inset for all samples included in this sample set.

donor concentration, which agrees well with the increase in acceptor PL observed in the spectral measurements. A prolonged rise-time is observed for the acceptor decay recorded at $c_{Don} = 3.1 \times 10^{17}$ m^{-2} (black line) in comparison with the two other decays recorded for samples with lower donor concentrations. As shown in the inset of Figure 5.13(b), the rise-time, represented by the time-delay of the intensity maximum in the acceptor decays, is increasing with increasing donor concentration.

5.4.1 FRET efficiency

The FRET efficiency for the bilayer structures with different donor QD concentrations ($c_{Acc} = (0.33 \pm 0.12) \times 10^{17}$ m^{-2} and $R_{ex} = 3.6$) is calculated from the donor lifetimes τ_{DA} measured in the Don1-Acc2 bilayers structure, shown in the inset of Figure 5.13(a), and the donor reference lifetimes τ_D at the respective donor concentration in the bilayer. The lifetimes τ_D were taken from the fit of the concentration dependence of τ_{blue} in the Don1 monolayers, discussed in section 4.1.2 and shown as a solid line in Figures 4.6(a) (as the lifetime yield) and 5.15(a) on page 99. In the following the lifetime measured on the blue side of the monodispersed donor monolayer ensemble emission spectrum, named τ_{blue} in section 4.1, is going to be referred to as τ_D, the donor reference lifetime. As can be seen in Figure 5.14(a), E_{FRET} is decreasing from approximately 67% to 27% with increasing donor concentration. However, a donor-concentration independent FRET efficiency of 32%, calculated with equation (5.1), is expected from FRET theory for homogeneous donor and acceptor ensembles for $R_0 = 3.4$ nm and $c_{Acc} = 0.33 \times 10^{17}$ m^{-2},

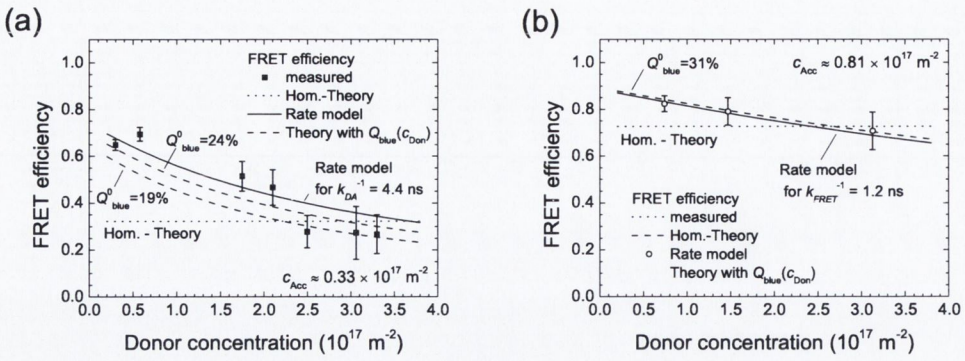


Figure 5.14: (a) FRET efficiency (solid squares) as a function of the donor concentration for $R_{ex} = 3.6$ nm and $c_{Acc} = (0.33 \pm 0.12) \times 10^{17}$ m^{-2}. The lines indicate the values of the FRET efficiency calculated with the Homogeneous Theory (Hom.-Theory) for $R_0 = 3.4$ nm (dotted line), the rate model for $k_{DA}^{-1} = 4.4$ ns (solid line) and the modified theory with donor concentration dependent donor quantum yield Q_{blue} (dashed lines). (b) Donor concentration dependence of the FRET efficiency (open circles) for $R_{ex} = 3.6$ nm and $c_{Acc} = (0.81 \pm 0.03) \times 10^{17}$ m^{-2}. The lines represent calculations of the FRET efficiency with Hom.-Theory for $R_0 = 3.9$ nm (dotted line), the rate model for $k_{DA}^{-1} = 1.2$ ns (solid line) and the modified theory with donor concentration dependent donor quantum yield Q_{blue} (dashed line).

indicated by the dotted line in Figure 5.14(a). As this theory is only considering homogeneous donor and acceptor ensembles and consequengly neglects donor intra-ensemble energy transfer due to the inhomogeneously broadened donor QD ensemble, this theory will be referred to as Hom.-Theory in the following. This discrepancy of the experimentally determined FRET efficiencies and the theoretically expected values could arise from the competition of donors for acceptors, as already mentioned in the discussion of the donor concentration dependence of the donor PL quenching shown in Figure 5.12(b). However, in that case a good agreement of the measured and calculated values would be expected at low c_{Don} followed by a decrease to values below the theoretically calculated ones at high c_{Don}. The measured E_{FRET} at low donor concentrations is however much larger than the expected 32% and decreases to values that seem to agree with theory at high donor concentrations.

A similar trend is observed for the donor concentration dependence measured for bilayer structures with a higher acceptor concentration, $c_{Acc} = (0.81 \pm 0.03) \times 10^{17}$ m^{-2}, shown in Figure 5.14(b). For this acceptor concentration and $R_0 = 3.9$ nm, a FRET efficiency of 73% is determined with Hom.-Theory. The experimentally determined E_{FRET} is however decreasing from 82% to 71% with increasing donor concentration, again showing agreement with Hom.-Theory at the highest donor concentrations.

This is also in line with the observations for the distance and the acceptor con-

centration dependence, where a good agreement of experiment and theory was found for E_{FRET} determined for samples with high donor concentrations (Figures 5.6(a) and 5.10(a)) and a larger R_0 than calculated from the spectral overlap had to be used to obtain a quantitative agreement for the concentration dependence measured at lower donor concentrations (Figure 5.10(b)). Therefore, the competition of donor QDs for available acceptor can be ruled out as origin of the donor concentration dependence, also because not all donor and acceptor QDs are excited at the same time for the measurement conditions used in the experiments presented here.

Another explanation for the donor concentration dependence of the FRET efficiency could be the competition of donor intra-ensemble and donor-acceptor energy transfer. To investigate the effect of donor intra-ensemble FRET on E_{FRET} determined for the donor-acceptor bilayer structure, a FRET rate model, represented by equation (5.4), was applied to fit the donor concentration dependence of E_{FRET}:

$$E_{FRET} = \frac{k_{DA}}{\tau_D\,(c_{Don})^{-1} + k_{DA}} = \frac{k_{DA}}{k_{D0} + k_{DD}\,(c_{Don}) + k_{DA}} \,. \tag{5.4}$$

The measured, concentration-dependent donor lifetime is included as $\tau_D\,(c_{Don})$, and therefore the only free fitting parameter is the donor-acceptor FRET rate k_{DA}. As $\tau_D = (k_{D0} + k_{DD}\,(c_{Don}))^{-1}$ is measured on the blue side of the donor ensemble emission spectrum, it is determined by the undisturbed donor lifetime described by the rate k_{D0} and the donor concentration dependent donor intra-ensemble energy transfer rate $k_{DD}\,(c_{Don})$. The measured τ_D for Don1 monolayers (solid squares), with an average ensemble quantum yield of 5%, as well as the theoretically calculated values (solid line), for $R_0 = 3.0$ nm and $R_{ex} = 3.0$ nm, are shown as a function of c_{Don} in Figure 5.15(a). The calculated τ_D is well approximated by the two-exponential decay

$$\tau_D = 4.89392 \cdot \exp\left(-\frac{c_{\mathrm{Don}}}{0.51545}\right) + 6.24292 \cdot \exp\left(-\frac{c_{\mathrm{Don}}}{1.9464}\right) + 1.14642 \,,$$

which has been implemented in the fitting function of the rate model for the analysis of the donor concentration dependent FRET efficiency. In the inset the measured lifetime $\tau_D^\star$ and its fit with theory, for $R_0 = 3.1$ nm and $R_{ex} = 3.25$ nm, are shown for Don1 monolayers measured at an earlier time, with an average ensemble quantum yield of 10%. The fitting curve based on the two-dimensional theory was approximated by

$$\tau_D^\star = 4.27308 \cdot \exp\left(-\frac{c_{\mathrm{Don}}}{0.52093}\right) + 6.27155 \cdot \exp\left(-\frac{c_{\mathrm{Don}}}{1.97049}\right) + 1.24204 \,.$$

As outlined in chapter 2.2 k_{DA}, describing the energy transfer from a donor to several acceptors, is only determined by the donor-acceptor separation and the number of acceptors surrounding this donor or the acceptor concentration in a solid structure.

Therefore, k_{DA} should be independent of the donor concentration. Applying the rate model to the data presented in Figure 5.14(a), a good agreement with the measured FRET efficiencies was obtained for $k_{DA} = (4.4\ \text{ns})^{-1}$ (solid line). As can be seen, the model reproduces the observed decrease of the FRET efficiency very well. For the measured FRET efficiencies determined for samples with higher acceptor concentration $c_{Acc} = (0.81 \pm 0.03) \times 10^{17}\ \text{m}^{-2}$, presented in Figure 5.14(b), a higher donor-acceptor FRET rate $k_{DA} = (1.2\ \text{ns})^{-1}$ was determined by fitting with the rate model. As expected from theory, the donor-acceptor FRET rate is increasing with increasing acceptor concentration. However, the difference in donor quantum yield for these two data sets has to be taken into account, but the decrease of Q_D from 10% to 5% would only reduce $k_{DA} = (1.20\ \text{ns})^{-1}$ to $(2.4\ \text{ns})^{-1}$, which is still larger than $k_{DA} = (4.4\ \text{ns})^{-1}$ measured for $c_{Acc} = (0.33 \pm 0.12) \times 10^{17}\ \text{m}^{-2}$.

The good agreement of the rate model including a constant k_{DA} with the measured FRET efficiencies, confirms that the donor concentration dependence of E_{FRET} is due to the competition of donor intra-ensemble FRET and donor-acceptor inter-layer FRET. As the c_{Don} increases donor-to-donor energy transfer becomes more likely, as reflected by the increasing k_{DD} shown as a function of the donor concentration in Figure 5.16(b) and therefore the probability for these donors to transfer energy to acceptors is decreasing. Therefore, it is important to take the concentration dependence of τ_D into account in the experimental determination of E_{FRET}. Otherwise, by using a constant donor reference lifetime in the calculation of the FRET efficiency, the decrease of τ_{DA} with increasing donor concentration could be interpreted as an enhancement of the donor-acceptor FRET efficiency with increasing donor concentration.

The decrease of the E_{FRET} can now be understood in terms of two competing energy transfer processes. The question why the experimentally determined FRET efficiency agrees with theory at high donor concentrations and not at the low ones, has however still to be addressed. On the one hand, one could argue that at low concentrations donor intra-ensemble FRET should be so slow that it can be neglected and therefore the measured FRET efficiency should agree with the value calculated with Hom.-Theory at low c_{Don}. On the other hand, at high concentrations the energy transfer between two donors is so fast, that a two-step process is established where energy is first transferred from one donor to another and then transferred on to an acceptor. In this scenario the measured donor monolayer lifetime would be the "right" reference lifetime to use to calculate E_{FRET} and therefore an agreement could be expected at high c_{Don}.

As outlined above, it has to be kept in mind that the lifetime used for the calculation of the E_{FRET} was measured on the blue side of the donor ensemble emission spectrum. Therefore, in the calculation of R_0, also the quantum yield of the emission on the blue side of the donor ensemble spectrum, Q_{blue}, should be used. This is important because,

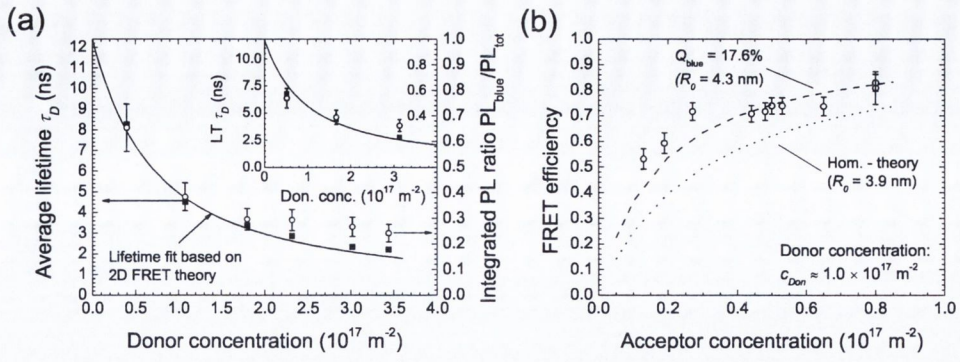


Figure 5.15: (a) Donor lifetime τ_D (solid squares, left-hand axis) and ratio of the integrated PL intensity on the blue side of the ensemble emission and the total emission I_{blue}/I_D (open circles, right-hand axis) for the Don1 monolayers ($Q_D = 5\%$) as a function of the donor concentration. The line is a fit of τ_D with the two dimensional FRET model. The inset shows the respective data for Don1 monolayers measured at an earlier time ($Q_D = 10\%$). (b) Acceptor concentration dependence of the FRET efficiency for $c_{Don} = (1.0 \pm 0.2) \times 10^{17}\text{m}^{-2}$ (also shown in Figure 5.10(b)). The theoretical trends are calculated with Hom.-Theory for $R_0 = 3.9$ nm (dotted line) and with the modified theory for $Q_{blue} = 17.6\%$, corresponding to $R_0 = 4.3$ nm (dashed line).

as discussed in section 4.1 presenting FRET in monodispersed QD monolayers, the donor emission red shifts with increasing concentration in the monolayer. This red-shift, due to energy transfer from the smaller donor QDs emitting on the blue side of the ensemble emission spectrum to the larger QDs emitting on the red side, is equivalent to a reduction of the quantum yield on the blue side.

To verify this idea, the emission on the blue side of the donor QD ensemble, I_{blue}, was determined by integrating over the PL spectra of Don1 monolayers with different concentrations between 486 nm, a wavelength just below the donor emission, and 545 nm, the wavelength at which the transmission of the 500 nm broad-band filter has decreased to 10%. The dependence of the ratio of I_{blue} and the total ensemble emission I_D is shown in Figure 5.15(a) for Don1 monolayers with an average ensemble quantum yield $Q_D = 5\%$ and in the inset for monolayers with $Q_D = 10\%$ (open circles, right-hand axis). It is important to note that the scale for τ_D shows values between 0 and the initial lifetime τ_D^0 determined from the lifetime fit with FRET theory in section 4.1. The PL ratio is shown between 0 and its maximum value of 1. It can be clearly seen that the PL ratio follows the same concentration dependence as the Don1 lifetime τ_D in both cases and that also the values of the ratios τ_D/τ_D^0 and I_{blue}/I_D agree well.

As the fraction of the blue emitting QDs within the donor ensemble, c_{blue}/c_{Don}, does not change with concentration, the absorption ratio of the blue emitting QDs

(with concentration c_{blue}) and the overall ensemble is also not changing, as the extinction coefficients of the blue subensemble and the overall ensemble are concentration-independent: $A_{\text{blue}}/A_D = \epsilon_{\text{blue}}/\epsilon_D \cdot c_{\text{blue}}/c_{Don}$. Therefore, the concentration dependence of $I_{\text{blue}}/I_D = (Q_{\text{blue}} \cdot A_{\text{blue}}) / (Q_D \cdot A_D)$ is equivalent to that of the quantum yield ratio Q_{blue}/Q_D. The average donor ensemble quantum yield Q_D has been used in the calculations so far and is concentration independent, as has been shown in Figure 4.3(a) on page 49. Therefore, the decrease of I_{blue}/I_D with increasing Don1 concentration is determined by the concentration dependence of Q_{blue}.

This similarity of the concentration dependences of Q_{blue} and τ_D can be understood by thinking of Q_{blue} in terms of rates. The quantum yield is defined as the ratio of the radiative rate k_r over the sum of all decay rates. Normally, the only decay rates that have to be considered would be k_r and the non-radiative recombination rate k_{nr}. However, for the Don1 QDs emitting on the blue side of the ensemble spectrum also the intra-ensemble transfer rate k_{DD} has to be included in the calculation of Q_{blue}, as shown in equation (5.5):

$$Q_{\text{blue}} = \frac{k_r}{k_r + k_{nr} + k_{DD}(c_{Don})} = \frac{k_r}{k_{D0} + k_{DD}(c_{Don})} = k_r \cdot \tau_D(c_{Don}) \ . \qquad (5.5)$$

This explains the close agreement of the lifetime and the PL ratio measured on the blue side of the donor ensemble emission spectrum, that can be seen in Figure 5.15(a), and shows that the concentration dependence of Q_{blue} can be modeled by the fit of $\tau_D(c_{Don})$ with FRET theory. However, it is quite difficult to determine the absolute values of Q_{blue} as either the radiative rate on the blue side of the Don1 ensemble emission spectrum or the absorption of the blue sub-ensemble, A_{blue}, have to be know. As these two parameters are difficult to determine reliably, Q_{blue} is estimated in both ways.

For the estimation of $Q^0_{\text{blue}} = k_r \cdot \tau^0_{blue}$ via the radiative rate and the initial Don1 lifetime τ^0_{blue}, the assumption that k_r is not changing across the ensemble emission spectrum is made. It is also assumed, that the decrease of the quantum yield upon deposition in the layers is only caused by an increase in non-radiative recombination path-ways rather than a modification of k_r. Furthermore, the decrease of Q_D in the Don1 monolayer with time from 5% to 10% is expected to be caused by an increase of k_{nr}, rather than a decrease in k_r, due to the slow degradation of the QDs and consequently an increase in defects. Therefore, k_r can be taken as constant over time and can be estimated from the solution ensemble quantum yield $Q_{\text{D-sol}}$ and lifetime τ_{noF}, measured without filter: $k_r = Q_{\text{D-sol}}/\tau_{noF} = 0.32/19.8\text{ns} = 0.016\ \text{ns}^{-1}$. The Q^0_{blue} for both sample sets shown in Figure 5.15(a) are therefore

$$Q^0_{\text{blue}} = \tau^0_D \cdot k_r = 12.3\ \text{ns} \cdot 0.016\ \text{ns}^{-1} = 20\%$$

$$Q^{\star 0}_{\text{blue}} = \tau^{\star 0}_D \cdot k_r = 11.8 \text{ ns} \cdot 0.016 \text{ ns}^{-1} = 19\%$$

for the Don1 monolayers with $Q_D = 5\%$ and $Q^{\star}_D = 10\%$ respectively. The values seem fairly reasonable as they are both smaller than $Q_{\text{D-sol}}$. It is however surprising that despite the difference in Q_D, both values of Q^0_{blue} are very similar. This might be explained by a larger error on the value of $\tau^{\star 0}_D$, as it was determined from a fit of only three data points. Furthermore, it has to be pointed out that Q_{blue} is four or two times larger than the Q_D for the respective sample sets. One would think that k_{nr} is larger for the smaller QDs emitting on the blue side of the ensemble emission spectrum than for the larger QDs emitting on the red side as defect states play a more important role for smaller QDs due to the larger surface-to-volume ratio, even though it could be expected that the difference is probably not very significant for QDs of the same ensemble. Taking this into account, the assumption that k_r is the same for all QDs in an ensemble is probably not right as this would mean that the quantum yield on the blue side should be smaller than that on the red side and the average quantum yield should then be larger than Q_{blue}. Nevertheless, this would only introduce the same factor in the calculations of Q^0_{blue} and $Q^{\star 0}_{\text{blue}}$, so that the values would still be very similar.

To estimate Q^0_{blue} from the measured average donor quantum yields Q_D, the absorption ratio A_{blue}/A_D has to be determined at 400 nm, the excitation wavelength used for recording the PL spectra. The absorption spectra for QDs with different sizes, as for example shown in Figures 4.1 and 4.2 on pages 47 and 48, show a similar wavelength dependence but shift to the blue with decreasing QD size. Therefore, the extinction coefficient at 400 nm of the Don1 QDs emitting on the blue side of the ensemble emission spectrum is smaller than the average value for the ensemble. Additionally, at most half of the QDs are emitting in the blue region between 486 and 545 nm, the detection range for the 500 nm filter, further reducing A_{blue} in comparison to the ensemble absorption A_D. To estimate $A_{\text{blue}}\,(400 \text{ nm})$, the Don1 solution spectra was shifted to the blue by 31 nm, the difference of the emission peak wavelength of 547 nm in solution and 516 nm, the centre wavelength of the QD emission recorded with the 500 nm filter. The absorption of the blue-shifted Don1 spectrum at 400 nm is equivalent to the absorption of the original spectrum at 431 nm, $A_D\,(431 \text{ nm}) = 0.1762$, and $A_{\text{blue}}\,(400 \text{ nm})$ can be estimated as half this value. Therefore, with the absorption ratio

$$\frac{A_{\text{blue}}\,(400 \text{ nm})}{A_D\,(400 \text{ nm})} = \frac{0.1762 \cdot 0.5}{0.2665} = 0.33\,,$$

Q^0_{blue} can now be estimated as $Q_D \cdot A_D/A_{\text{blue}}$, and one obtains $Q^0_{\text{blue}} = 15\%$ and $Q^{\star 0}_{\text{blue}} = 30\%$ for the two Don1 data sets shown in Figure 5.15. The value estimated via the absorption ratio is about 25% smaller than that estimated for a constant k_r for the samples with a $Q_D = 5\%$ and 58% larger for the monolayers with $Q_D = 10\%$. Due to

the difficulty of determining Q^0_{blue} the agreement of the values estimated in both ways is not too bad and it is assumed that the real values lie between 10% and 35%.

Taking into account a donor concentration dependent Q_{blue} in the calculation of $R_0 = 0.0211 \cdot \left(\kappa^2 \cdot Q_D \cdot n^{-4} \cdot J\right)^{1/6}$, one can see that due to the same concentration dependence of Q_{blue} and τ_D, the donor concentration dependences in the calculation of k_{FRET} with Hom.-Theory for bilayer structures, cancel:

$$k_{\text{FRET}} = \frac{c_{Acc} \cdot \pi \cdot R_0^6}{2 \cdot R_{ex}^4 \cdot \tau_D} ,$$

whereas a donor concentration dependence is introduced in the expression for E_{FRET}:

$$E_{\text{FRET}} = \frac{1}{1 + \frac{2 \cdot R_{ex}^4}{c_{Acc} \cdot \pi \cdot R_0^6}} .$$

The FRET efficiencies calculated with a modified Hom.-Theory taking into account $Q_{\text{blue}}(c_{Don})$ are included in Figure 5.14(a) and (b) for different values of Q^0_{blue} (dashed lines). It can be clearly seen, that the same donor concentration dependent trend of E_{FRET} as seen for the FRET rate model is obtained by the modified Hom.-Theory. In particular, the solid line can be reproduced in both cases for $Q^0_{\text{blue}} = 29\%$, confirming once more that the concentration dependence of the efficiency of the donor-acceptor energy transfer process is strongly influenced by the competition with donor intra-ensemble FRET. Therefore, it is important not to neglect the possibility of donor-to-donor energy transfer in the characterization of FRET in QD structures and also to include this effect in FRET theory for QD systems.

The rate model can be applied to any FRET structure without modification by taking into account the concentration dependence of the donor reference lifetime, the trend of which will however depend on the geometry of the structure investigated. For the calculation of E_{FRET} via R_0, the concentration dependence of the donor quantum yield can be applied to the calculation of R_0, which can then be included in the equation to calculate E_{FRET} for a given structure. Therefore, also this second method of including the effects of donor intra-ensemble energy transfer in FRET theory can be applied to any FRET structure.

It is important to note, that by including $Q_{\text{blue}}(c_{Don})$ in the calculation of R_0, the Förster radius itself becomes donor concentration dependent. This concentration dependence is a direct consequence of the concentration dependence of the donor lifetime arising from intra-ensemble FRET. As R_0 is defined as the distance at which k_{FRET} is equal to all other donor decay rates, including the intra-ensemble FRET rate k_{DD}, R_0 has to decrease with increasing donor concentration as k_{DD} is increasing. This also explains why a larger R_0 had to be used to achieve a quantitative agreement of the

measured acceptor concentration dependence of the FRET efficiency with theory at low donor concentration, as shown in Figure 5.15(b). For $c_{Don} = (1.0 \pm 0.2) \times 10^{17} \mathrm{m}^{-2}$, the appropriate donor quantum yield to use is 17%, as calculated from the concentration dependence of $Q^{\star}_{\mathrm{blue}}$, shown in the inset of Figure 5.15(a) for Don1 monolayers with $Q_D = 10\%$, and $Q^{\star 0}_{\mathrm{blue}} = 29\%$, as obtained from the fit of the FRET efficiency shown in Figure 5.14(b). With $Q^{\star}_{\mathrm{blue}} = 17\%$ an $R_0 = 4.3$ nm is calculated from the spectral overlap of Don1 and Acc2, which corresponds to the value for which a good agreement of FRET theory and experimentally determined FRET efficiency is achieved. This further confirms, that by taking into account the effects of donor intra-ensemble energy transfer, arising form the inhomogeneous broadening of the QD ensembles, a good quantitative agreement is obtained with FRET theory, which was originally developed for homogeneous ensembles of molecules.

The donor concentration dependence of the FRET efficiencies has also been determined for larger donor-acceptor layer separations of $R_{ex} = 6.1$ nm. The measured FRET efficiencies are shown in the upper and lower panel of Figure 5.16(a) for bilayer structures with $c_{Acc} = (0.77 \pm 0.03) \times 10^{17}\ \mathrm{m}^{-2}$ ($Q_D = 10\%$) and $c_{Acc} = (0.40 \pm 0.14) \times 10^{17}\ \mathrm{m}^{-2}$ ($Q_D = 5\%$) respectively. An increased donor-acceptor separation leads to a lower donor-acceptor FRET rate, so that the competition of the two energy transfer process should be reduced once donor intra-ensemble FRET becomes much faster than donor-acceptor FRET. However, as can be seen in comparison with the FRET efficiencies calculated with Hom.-Theory (dotted line), also at the larger separations in the Don1-Acc2 bilayer structures, still a significant concentration dependence is observed despite the reduced FRET rate. In particular for the high acceptor concentration the impact of donor intra-ensemble energy transfer is stronger at the larger (top panel in Figure 5.16(a)) than for the smaller layer separation (Figure 5.14(b)).

For a comparison of the four structures with different acceptor concentration and layer separation, the donor-acceptor FRET rates k_{DA} in the bilayer structures with $R_{ex} = 6.1$ nm were also determined by fitting the measured FRET efficiencies with the rate model (solid lines in Figure 5.16 (a)). As expected, for the structure with the higher acceptor concentration $k_{DA} = (7.4\ \mathrm{ns})^{-1}$ is larger than $k_{DA} = (10.2\ \mathrm{ns})^{-1}$ determined for the lower acceptor concentration. Both values are also smaller than those determined for the structures with similar acceptor concentrations and $R_{ex} = 3.6$ nm, $(1.2\ \mathrm{ns})^{-1}$ and $(4.4\ \mathrm{ns})^{-1}$ respectively. The k_{DA} determined for the Don1-Acc2 bilayer structures compare well with those reported in literature such as for example $(20\ \mathrm{ns})^{-1}$ [114] $(0.75\ \mathrm{ns})^{-1}$ [108], $(0.2\ \mathrm{ns})^{-1}$ [115] and $(0.07\ \mathrm{ns})^{-1}$ [145].

The donor intra-ensemble FRET rates k_{DD}, determined from the lifetimes measured in the monolayers with $Q_D = 5\%$, are shown as solid squares in Figure 5.16(b) and the theoretical trend is indicated as dotted line. The initial donor decay rate $k_{D0} =$

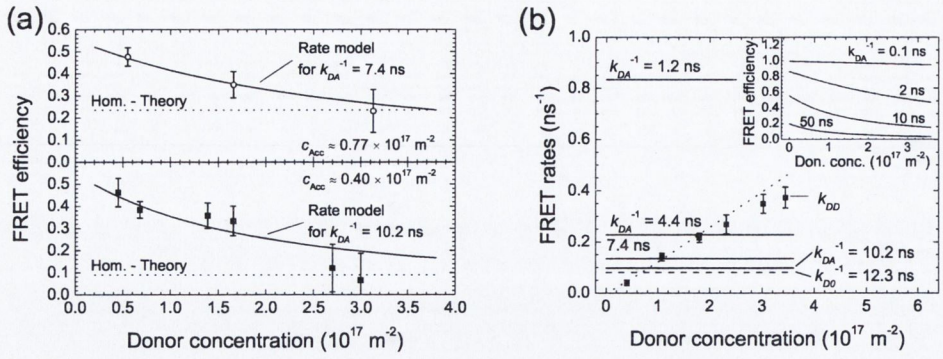


Figure 5.16: (a) Donor concentration dependence of the FRET efficiency for bilayer structures with $R_{ex} = 6.1$ nm and $c_{Acc} = (0.77 \pm 0.03) \times 10^{17}$ m^{-2} (average donor ensemble quantum yield $Q_D = 10\%$) (open circles, top panel) as well as $c_{Acc} = (0.40 \pm 0.14) \times 10^{17}$ m^{-2} ($Q_D = 5\%$) (solid squares, bottom panel). The calculated trends with Hom.-Theory (dotted line) and fits with the rate model (solid line) are also shown. (b) Comparison of the undisturbed donor lifetime k_{D0} (dashed line), the donor intra-ensemble FRET rate k_{DD} (solid squares) and the donor-acceptor FRET rates k_{DA} (solid lines), determined for the Don1-Acc2 bilayer structures. The dotted line represents the fit of k_{DD} with the two dimensional FRET theory. The inset shows the donor concentration dependence of the FRET efficiency calculated for different donor-acceptor FRET rates with the rate model, based on the measured donor lifetime dependence in the Don1 monolayers.

$(\tau_D^0)^{-1} = (12.3 \text{ ns})^{-1}$, determined by the radiative and non-radiative decay rate only, is represented by the dashed line. The solid lines show the different values of k_{DA} obtained from the fit of the donor concentration dependence of the FRET efficiency with the rate model for the four different Don1-Acc2 bilayer structures discussed above.

As can be seen in Figure 5.16(b), except for the smallest acceptor-donor layer separation and the higher acceptor concentration, resulting in a $k_{DA} = (1.2 \text{ ns})^{-1}$, the k_{DA} show values equal to k_{DD} in the range of concentrations investigated. For these conditions, the competition between the two energy transfer processes is strong and therefore a strong concentration dependence can be observed as seen for the measured FRET efficiencies and as also shown in the inset of Figure 5.16(b). For very fast energy transfer, corresponding to $k_{DA} = (0.1 \text{ ns})^{-1}$, or very slow energy transfer, represented by $k_{DA} = (50 \text{ ns})^{-1}$, only a relatively small decrease of the FRET efficiency with increasing donor concentration is observed. However, working with a small donor-acceptor FRET rate is not an option for FRET applications. Therefore, optimizing the donor-acceptor FRET rate [115, 145] and reducing the donor intra-ensemble FRET rate k_{DD} can help to limit the donor concentration dependence of the FRET efficiency.

5.4.2 FRET efficiency in Bilayers with Different Donor QDs

As discussed in section 4.1 intra-ensemble energy transfer can be reduced by using QDs with a small self-overlap. In Figure 5.17(a) the donor concentration dependence of the FRET efficiency in Don2-Acc2 bilayer structures with different donor-acceptor centre-to-centre separations of $R_{ex} = 3.35$ nm (top panel) and $R_{ex} = 5.85$ nm (bottom panel) are shown for low acceptor concentrations of $(0.23 \pm 0.05) \times 10^{17}$ m^{-2} and $(0.33 \pm 0.06) \times 10^{17}$ m^{-2} respectively. R_{ex} is smaller than for the Don1-Acc2 bilayer structures due to the smaller size of the Don2 QDs. The donor quantum yield of the monodispersed Don2 monolayers is approximately $Q_D = 4.5\%$ and $R_0 = 3.4$ nm for donor-acceptor FRET. Due to the reduced intra-ensemble FRET, evidence for which was shown in Figures 4.6(a) and 4.7, the decrease of E_{FRET} observed for the Don2-Acc2 bilayer structures is less strong compared to those observed for the Don1-Acc2 bilayers at the lower acceptor concentration (shown in Figure 5.14(a) and in the lower panel of Figure 5.16(a)). However the donor-acceptor FRET rates of $(8.5\ \mathrm{ns})^{-1}$ and $(14.2\ \mathrm{ns})^{-1}$, obtained from the fitting with the rate model, are still comparable to k_{DD} in the Don2 monolayers, ranging from $(36.3\ \mathrm{ns})^{-1}$ to $(7.1\ \mathrm{ns})^{-1}$ over the concentration range investigated. The values of k_{DD} were calculated from the measured τ_D and τ_D^0 (given in Table 4.2) obtained from the lifetime modelling discussed in section 4.1.2.

To further reduce the donor concentration dependent decrease of E_{FRET} Don4 QDs were used as donors in the bilayer structure with Acc2 QDs. The solution spectra of the Don4 QDs are shown in Figure A.3 in the Appendix. These QDs have a diameter of 1.3 nm, giving a minimum donor centre-to-centre separation of $R_{ex} = (1.8 \pm 0.2)$ in monodispersed Don4 monolayers, and show a self-overlap of only $0.26 \times 10^{-15} \frac{\mathrm{nm}^4}{\mathrm{M \cdot cm}}$, resulting in a R_0 for intra-ensemble FRET of (1.6 ± 0.2) nm, taking into account $Q_D = 2.5\%$. Consequently, the impact of intra-ensemble energy transfer is very small in the monodispersed Don4 monolayers as can be seen in the comparision of the lifetime difference, $1 - \tau_{\mathrm{blue}}/\tau_{\mathrm{red}}$, of different green-emitting QDs shown in Figure 4.7 and for the concentration dependence of τ_D ($= \tau_{\mathrm{blue}}$), shown in the inset of Figure 5.17(b). The lifetime trend is well reproduced by FRET theory for $R_0 = (1.3 \pm 0.2)$ nm, $R_{ex} = (1.95 \pm 0.2)$ nm and $\tau_D^0 = (6.4 \pm 0.3)$ ns. Also for Don4, the values of R_0 and R_{ex} obtained from the fitting of the concentration dependence of the lifetime are in good agreement with those calculated from the spectral data. The fastest value of k_{DD} measured in the monolayers is $(34\ \mathrm{ns})^{-1}$ at the highest concentration investigated.

The donor concentration dependence of the FRET efficiency in the Don4-Acc2 bilayer samples, with $R_{ex} = 5.4$ nm and $c_{Acc} = (0.54 \pm 0.06) \times 10^{17}$ m^{-2}, is shown in the main panel of Figure 5.17(b). From fitting with the rate model (solid line), a donor-acceptor FRET rate of $(22.3\ \mathrm{ns})^{-1}$ is determined. As the donor-acceptor FRET rate is faster than the highest value of k_{DD}, even at this relatively large donor-acceptor distance,

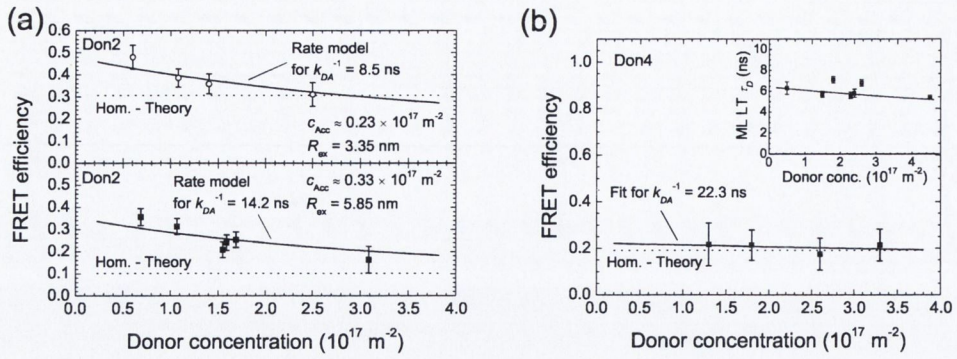


Figure 5.17: (a) FRET efficiency as a function of the donor QD concentration for Don2-Acc2 bilayer structures with $R_{ex} = 3.35$ nm and $c_{Acc} = (0.23 \pm 0.05) \times 10^{17}$ m^{-2} (open circles, top panel) as well as $R_{ex} = 5.85$ and $c_{Acc} = (0.33 \pm 0.06) \times 10^{17}$ m^{-2} (solid squares, bottom panel). The calculated trends with Hom.-Theory (dotted line) and curves fitted with the rate model (solid line) are also shown. (b) Donor concentration dependence of the FRET efficiency in a Don4-Acc2 bilayer structure with $R_{ex} = 5.4$ nm and $c_{Acc} = (0.54 \pm 0.06) \times 10^{17}$ m^{-2}. The FRET efficiency calculated with Hom.-Theory for $R_0 = 3.65$ nm (dotted line) and the fit with the rate model (solid line) are also included. In the inset the concentration dependence of the lifetime (LT) on the blue side of the ensemble emission τ_D (solid squares) of Don4 QD monolayers is shown along with the fit based on the two-dimensional FRET theory (solid line).

only a very small dependence of the FRET efficiency on the donor concentration is observed. Therefore, the measured values all agree well with $E_{\mathrm{FRET}} = 19\%$ calculated with Hom.-Theory for $R_0 = 3.65$ nm (dotted line), obtained from the spectral overlap.

Decreasing the probability for donor intra-ensemble energy transfer, by using donor QDs with a small spectral self-overlap, reduces the donor concentration dependence of the measured FRET efficiency caused by donor intra-ensemble energy transfer. This shows, how important it is to consider the impact of donor intra-ensemble energy transfer on FRET in QD structures and to carefully choose the spectral properties of the QDs used for applications. However, it has to be kept in mind that E_{FRET} presented here was determined from the lifetime measured on the blue side of the donor ensemble emission spectrum. The effect is certainly reduced or can even be neglected if the overall donor ensemble properties are characterized, which are however difficult to assess in QD systems with overlapping donor and acceptor PL emission. Additionally, the analysis of FRET as presented here is the standard technique used in the literature, therefore these results show the importance of taking account of the intra-donor ensemble FRET in the analysis and interpretation of FRET in QD systems characterised in this way.

A more detailed investigation of the dependence of the donor lifetime and emission

properties in FRET structures has to be carried out to determine if donor intra-ensemble energy transfer also has an impact on donor-acceptor FRET when considering the overall donor ensemble properties in the FRET analysis. In the data presented here the spectral cross-talk of the donor and the acceptor emission prevented the reliable investigation of the overall donor ensemble lifetime and PL properties in the donor-acceptor bilayer structure. Therefore, it is difficult to argue, whether the donor PL quenching shown in Figure 5.12(b) is constant or shows a decrease with increasing donor concentration. It can be noted, that the donor PL quenching shows larger values than the FRET efficiency shown in Figure 5.14(a), which reduces from approximately 67% to 27% whereas the PL quenching varies between 89% and 57% or could be interpreted as constant at 72%. The larger values of the PL quenching can be explained by a larger donor-acceptor FRET efficiency for the whole donor ensemble than that for the blue side only. First of all, donor intra-ensemble energy transfer only impacts on the emission on the blue side of the ensemble emission, reducing the probability for donor-acceptor FRET. Furthermore, energy transfer from donors emitting on the red side of the donor ensemble emission to the acceptor QDs might be increased due to the better overlap with the first acceptor absorption peak which could facilitate a better energy transfer at these energies. Consequently, the only conclusions that can be drawn from this comparison for now is that the impact of donor intra-ensemble energy transfer is definitely reduced when characterizing the average donor ensemble properties.

5.4.3 Relative Quantum Efficiency

An indication of whether or not donor intra-ensemble energy transfer has an important impact on the overall donor-acceptor energy transfer, and not just that for donors emitting on the blue side of the donor ensemble emission spectrum, might be found in the analysis of the relative quantum efficiency, QE_{rel}, of the FRET structure in dependence of the donor concentration shown in Figure 5.18(a). QE_{rel} was calculated from the integrated PL spectra of Don1-Acc2 bilayers with $R_{ex} = 3.6$ and $c_{Acc} = (0.33 \pm 0.12) \times 10^{17}$ m^{-2}, the sample set discussed in most detail in this section.

As can be seen the experimentally determined quantum efficiency is greater than 1 for most donor concentrations investigated. The best fit of the data with the PL model, given in equation 5.2, taking into account a FRET efficiency calculated with Hom.-Theory for $Q_D = 5\%$ and $R_0 = 3.4$ nm (dashed line), as well as for the modified theory, taking into account donor intra-ensemble energy transfer for $Q^0_{\text{blue}} = 29\%$ (solid line), were obtained for $E_{Enh} = E_{\text{FRET}} \cdot A_D/A_A \cdot 1.8$. The model taking into account intra-ensemble energy transfer is predicting higher values than that including E_{FRET} calculated with Hom.-Theory, due to the larger donor quantum yield used in the calculation. If $Q_D = 29\%$ and consequently $R_0 = 4.5$ nm are used for the calculation with the PL

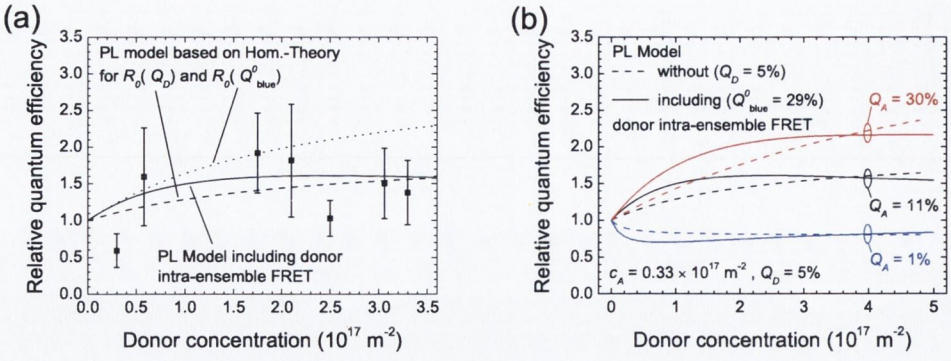


Figure 5.18: (a) Donor concentration dependence of the relative quantum efficiency for Don1-Acc2 bilayer structures with $R_{ex} = 3.6$ nm and $c_{Acc} = (0.33 \pm 0.12) \times 10^{17}$ m^{-2}. The lines represent the calculation for a PL intensity model including (solid line) and neglecting donor intra-ensemble energy transfer (dashed and dotted line). (b) Trends calculated with the PL models including (solid line) and neglecting (dashed line) donor intra-ensemble energy transfer in dependence of the donor concentration for different acceptor quantum yields Q_A. The calculations were based on an acceptor concentration of $c_{Acc} = 0.33 \times 10^{17}$ m^{-2}.

model based on Hom.-Theory (dotted line), the values of QE_{rel} are similar for both models at low donor concentrations, but then a reduced PL enhancement is seen for the calculation including donor intra-ensemble energy transfer compared to that neglecting donor-to-donor FRET. This shows that it is really important to find out if donor intra-ensemble energy transfer has an impact on the overall donor-acceptor energy transfer, as it could reduce the total light emission of a FRET structure at high donor concentrations. However, the dotted line only shows a good agreement with the data at low donor concentrations. The experimentally determined PL enhancement seems to decrease at high donor concentration in the FRET structure, which indicates that donor intra-ensemble energy transfer might have an impact on the overall energy transfer from the donor QD ensemble to the acceptor QD ensemble. However, as pointed out above, both a PL model for $Q_D = 5\%$ and neglecting donor intra-ensemble energy transfer as well as a model including donor intra-ensemble energy transfer and $Q^0_{\text{blue}} = 29\%$ are in good agreement with the data.

In order to be able to distinguish between these two different trends, FRET structures using donors with a large inhomogeneous broadening and consequently a large self-overlap should be used. Furthermore, from the evaluation of the PL model for $c_{Acc} = 0.33 \times 10^{17}$ m^{-2} and different acceptor quantum yields shown in Figure 5.18(b), one can be see that the largest difference between the two trends is observed for large acceptor:donor quantum yield ratios. It has to be kept in mind that different donor

quantum yields, Q_D and Q^0_{blue}, are used in the calculation of the FRET efficiency. Furthermore, the FRET efficiency determined from the lifetime decrease on the blue side of the donor ensemble emission spectrum might not reflect the trend of the FRET efficiency for the entire donor ensemble. Therefore, the best concentration to investigate is most likely not an intermediate donor concentration of 1.0 to 2.0 $\times$ 10^{17} m^{-2}, for which the strongest difference between the values calculated with the two models is seen in Figure 5.18(b), but a high donor concentration, for which a large difference between the dotted and solid line is seen in Figure 5.18(a).

5.5 Conclusion

Förster resonant energy transfer in a donor-acceptor QD bilayer structure was investigated as a function of the donor-acceptor layer separation as well as of donor and acceptor concentrations. The FRET signatures observed in the PL and PLE spectra show good agreement with the trends expected by FRET theory. However, the detailed analysis of the FRET efficiency as well as the acceptor enhancement and the relative quantum efficiency indicate that there are more effects to take into account in the analysis of FRET in QD structures than are considered in the basic FRET theory developed for ensembles of homogeneous molecules (Hom.-Theory).

It was found that the distance and acceptor concentration dependences of the FRET efficiency agree well with theory for Förster radii, R_0, calculated from the spectral overlap, for high donor concentrations. At low donor concentrations, FRET efficiencies larger than those predicted by Hom.-Theory were measured and a larger value of R_0 had to be used to achieve a good agreement with theory. Therefore, the donor concentration dependence of the FRET efficiency was investigated and a decrease of the FRET efficiency with increasing donor concentration was observed, which is not expected from FRET theory. It is important to note, that the concentration dependence of the donor reference lifetime has to be taken into account when calculating the FRET efficiency from the measured lifetime decrease. If a constant donor reference lifetime was used to determine the FRET efficiency, the decreasing donor lifetime in the donor-acceptor structure would be misinterpreted as an increase rather than a decrease of the FRET efficiency with increasing donor concentration.

The donor concentration dependence of the FRET efficiency was fitted with a rate model, taking into account the concentration dependent donor reference lifetime, and a good agreement with the measured values was found for a constant donor-acceptor FRET rate. Thus, the unexpected donor concentration dependence of the FRET efficiency can be attributed to the competition of donor-acceptor FRET and donor intra-ensemble energy transfer, arising from the large inhomogeneous broadening of the donor

QD ensemble. Therefore, rather than the FRET efficiency, the FRET rate should be used to compare the donor-acceptor FRET process in different QD structures. Furthermore, it was shown that the decrease of the FRET efficiency with donor concentration can also be reproduced with a modified Hom.-Theory, by including the concentration dependent quantum yield of the donor emission on the blue side of the donor ensemble emission in the calculation of the Förster radius instead of the constant ensemble quantum yield. This also shows, that R_0 depends on the donor concentration due to donor intra-ensemble energy transfer. Additionally, it was demonstrated that the dependence of the FRET efficiency on the donor concentration can be reduced by using donor QDs with a low self-overlap, showing a reduced probability for intra-ensemble energy transfer in closely packed structures.

The analysis of dependence of the acceptor enhancement as well as of the relative quantum efficiency on the donor-acceptor layer separation, acceptor and donor concentrations all showed acceptor enhancements stronger than expected from the FRET efficiency. The increased acceptor enhancement is attributed to exciton recycling, as has already been observed for other nanocrystal QD assemblies [12, 120]. The exciton recycling effect showed an acceptor concentration dependence similar to that observed for the mixed donor-acceptor monolayer. However, a more detailed analysis of this effect is necessary to enable accurate modelling of its impact on the acceptor enhancement and the total emission of a FRET structure. Furthermore, the relative quantum efficiency determined as a function of the donor concentration seems to decrease at high donor concentrations. This could be an indication of energy losses due to donor intra-ensemble energy transfer and would suggest that donor intra-ensemble energy transfer has an impact on the FRET efficiency determined for the entire donor ensemble and not only that for the blue side of the donor ensemble emission. Therefore, it is important to investigate the impact of intra-ensemble energy transfer on the overall PL emission in more detail, as it would require the selection of QDs with small self-overlap for the use in FRET devices if donor intra-ensemble FRET was reducing the emission enhancement arising from donor-to-acceptor energy transfer and the exciton recycling effect.

6 Surface Plasmon Effects on FRET in QD Structures

As discussed in the previous two chapters, Förster resonant energy transfer in QD structures is influenced by the QD size and the inhomogeneous broadening of the QD ensemble. In particular, the exclusion zone created by the donor and acceptor QD radii is limiting the maximum FRET rate and efficiency that can be achieved in QD assemblies and therefore the sensitivity and performance of QD FRET devices. It has been proposed that FRET can be enhanced by interaction with localized surface plasmons [124, 125, 130]. The sensitivity of nano-sensors and the performance of light-harvesting devices could be improved by increasing the FRET efficiency, FRET rate and / or the Förster radius by incorporating metal nanoparticles supporting localised surface plasmons in these structures. First observations of surface plasmon modified FRET have been reported in literature, though mostly for molecular systems [126, 127, 128, 129]. Recently, also work on the modification of FRET between QDs by surface plasmons has been published [131, 132, 133]. However, no detailed analysis of the process or characterization of the conditions under which enhanced FRET can be achieved has been reported.

In this chapter, the influence of localized surface plasmons, supported by gold nanoparticles (NPs) with an approximate diameter of 4 nm, on energy transfer between QDs in different structures will be investigated. Firstly, the modification of the optical properties, PL intensity and PL lifetime, of monodispersed donor and acceptor monolayers deposited on top of gold NP layers will be presented. Then, the impact of surface plasmons on the energy transfer between separated donor and acceptor layers will be analysed for an acceptor-gold-donor sandwich structure. This structure with gold NPs between the donor and acceptor QDs was proposed as the most effective geometry to observe surface plasmon enhanced FRET [130]. Different donor QDs were tested in this sandwich structure and a strong dependence of the surface plasmon effects on the donor properties has been observed. The QD-gold layer distance dependences as well as the influence of the gold NP concentration in the sandwich structure will be discussed. Finally, preliminary results for the distance dependence of the surface plasmon interaction in other sample geometries, a separated donor-acceptor bilayer and a mixed donor-acceptor monolayer deposited on top of a gold NP layer, will be presented.

6.1 Monodispersed QD Monolayers in Proximity to Gold Nanoparticle Layers

In order to be able to differentiate between a modification of the energy transfer process and a direct enhancement or quenching of the QD emission by surface plasmons, [76, 77] the influence of the gold NPs on the individual donor and acceptor QD monolayers has to be characterised in detail. The strongest surface plasmon effects in the sandwich structure were observed for Don1 and Acc2 QDs, and therefore the impact of surface plasmons on the optical properties of monolayers of these QDs will be presented in detail in this section. All other donor QDs used in the following showed similar effects to those observed for the Don1 monolayer deposited on top of a gold NP layer and will be presented in the subsequent sections where necessary for the analysis of FRET in the gold NP-QD structures. Details on the gold NPs used can be found in section 3.2.3.

6.1.1 Surface Plasmon Effects on Donor QDs

In Figure 6.1(a) PL spectra (lines) for Don1 monolayers with QD concentrations of $c_{Don} = (3.6 \pm 0.5) \times 10^{17}$ m^{-2} for different gold-Don1 separations, represented by the polyelectrolyte spacer thickness d, of 3 to 15 nm are shown. The gold concentrations for the samples were $c_{Au} = (0.22 \pm 0.03) \times 10^{17}$ m^{-2}. A reference spectrum for a Don1 monolayer deposited (on the polyelectrolyte buffer layer) on quartz, is also included in the Figure (open green squares). The original donor concentration of the reference monolayer is $c_{Don} = 2.6 \times 10^{17}$ m^{-2}, but the concentration of the reference spectrum and all other spectra shown in Figure 6.1(a) were adjusted to $c_{Don} = 3.5 \times 10^{17}$ m^{-2}. As can be seen, the emission of the Don1 QDs in proximity to a gold NP layer is quenched and blue-shifted compared to that of the reference monolayer. Furthermore, all spectra for the Don1-gold samples show similar intensities and no typical surface plasmon distance dependence [76, 77] is observed for the range of gold-QD separations investigated here.

The emission of samples with a gold-QD separations of 12 and 15 nm seems to be further quenched than for smaller separations. This is also reflected in the Don1 PL quenching $1 - I_{onAu}/I_D$, calculated from the spectrally integrated emission of the Don1-gold samples I_{onAu} and the reference monolayer I_D, shown in Figure 6.1(b) (solid squares, left-hand axis). At small layer separations the quenching is approximately 77% and then increases to 83% for $d = 12$ and 15 nm. This increased quenching is attributed to the larger gold NP concentration for these samples, also indicated in the Figure (open triangles, right-hand axis).

The PL decays on the blue side of the Don1 ensemble emission spectrum for the Don1-gold samples, recorded with a 500 nm filter, are shown in Figure 6.2(a), along

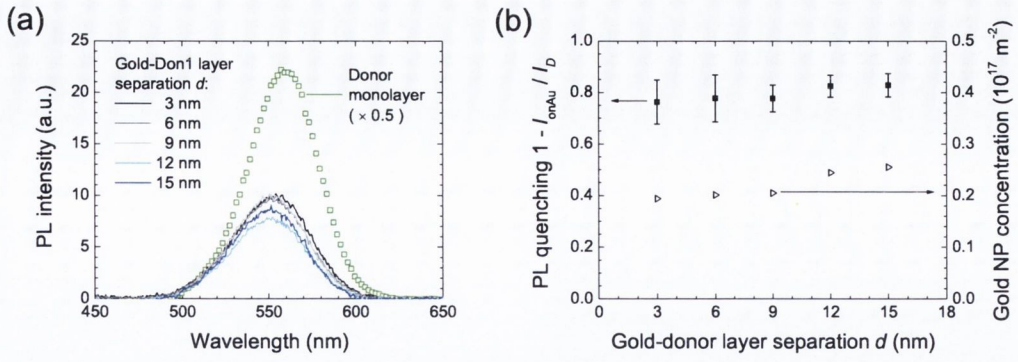


Figure 6.1: (a) PL spectra (lines) of Don1 QD monolayers deposited at different separations to a gold nanoparticle (NP) layer with concentration $c_{Au} = (0.22 \pm 0.03) \times 10^{17}$ m^{-2}. The gold-donor layer separations, given as the polyelectrolyte spacer thickness d, are indicated in the legend. The reference spectrum of a Don1 monolayer on quartz is also shown (open green squares). The Don1 concentration was adjusted to $c_{Don} = 3.5 \times 10^{17}$ m^{-2} for all spectra. (b) PL quenching of the Don1 emission in proximity to the gold NP layer (solid squares, left-hand axis) in dependence of the gold-QD layer separation d. The gold NP concentrations of the samples are indicated on the right-hand axis (open triangles).

with the reference decay of a Don1 monolayer on quartz (green line). The decay for $d = 3$ nm (black line) is the shortest and with increasing gold-Don1 separation the decays become longer and tend towards that of the reference monolayer.

The donor concentration is varying from sample to sample and, as discussed in section 4.1, this is influencing the average lifetime τ_{blue}. Hence, for a better comparison, relative lifetimes $\tau_{\text{onAu}}/\tau_D$ have been calculated for the PL lifetimes τ_{onAu} determined for the Don1-gold samples with different layer separations d and reference lifetimes τ_D of Don1 monolayers with the same QD concentrations as in the Don1-gold samples. The values of τ_D at the respective Don1 concentrations were obtained from the Don1 lifetime fit discussed in section 4.1.2. As can be seen in Figure 6.2(b), the lifetime ratio is increasing with increasing gold-Don1 separation and values close to one are observed for layer separations as small as $d = 9$ nm, due to a decreasing impact of the surface plasmons on the donor decay dynamics with increasing gold-Don1 distance.

It has been reported that the quenching of fluorophores in proximity of metal particles, can be explained with FRET theory [80, 81, 84, 86]. For the samples with separated QD and gold NP layers discussed here, the dependence of the relative lifetime on the gold-Don1 separation should therefore follow the trend described by equation (6.1), the same expression as used in the analysis of the donor-acceptor FRET efficiency in the separated bilayer structure discussed in chapter 5, converted to a lifetime yield $q_r = \tau_{\text{onAu}}/\tau_D$. Equation (6.2) will be used to describe the gold concentration dependence of the lifetime

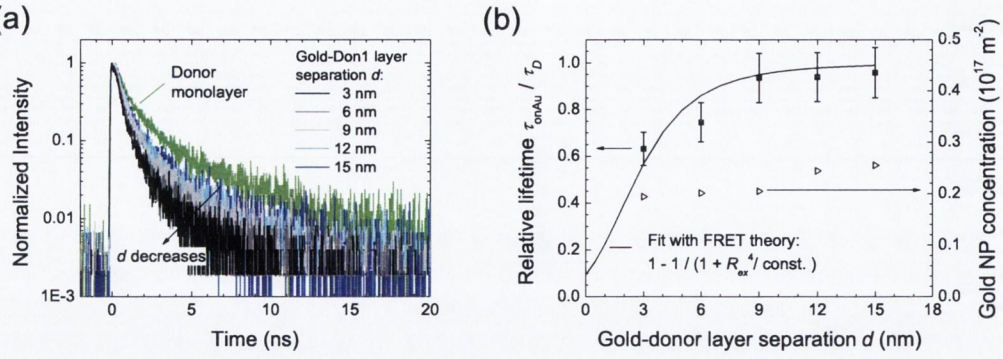


Figure 6.2: (a) PL decays of gold-Don1 structures with different layer separations d, indicated in the legend. The decay of the donor reference monolayer is shown as well (green line). (b) Distance dependence of the relative PL lifetime $\tau_{\text{onAu}}/\tau_D$ of Don1 monolayers in proximity to a gold nanoparticle (NP) layer with a donor lifetime τ_{onAu} and reference lifetimes τ_D of Don1 monolayers with similar QD concentration as in the respective Don1-gold sample (solid squares, left-hand axis). The distance dependence was fitted with a theory of FRET between two planes (solid line). The gold NP concentration of the samples is shown on the right-hand axis (open triangles).

yield discussed below.

$$q_r = 1 - E_{\text{FRET}} = 1 - \frac{1}{1 + R_{ex}^4/c_1} \tag{6.1}$$

$$= 1 - \frac{1}{1 + c_2/c_{Au}} \tag{6.2}$$

The constants c_1 and c_2 in equations (6.1) and (6.2) are used as fitting parameters here and depend on the gold concentration c_{Au} and gold-QD centre-to-centre separation, R_{ex}, respectively as well as a characteristic interaction distance, the Förster radius. $R_{ex} = d + r_{QD} + r_{Au}$ is calculated as the sum of the polyelectrolyte spacer thickness, d, and the radii of the QDs, r_{QD}, and gold nanoparticles, r_{Au}. A detailed interpretation of the QD-metal NP interaction with FRET theory is currently in progress. The in-depth investigation of the QD-metal interaction is however beyond the scope of this chapter and FRET theory will only be used to accurately model the observed trends of the optical properties of QDs in proximity to gold NPs. Therefore, the fitting parameters c_1 and c_2 will be given in the following, but no detailed analysis or explanation of their values will be presented.

The dependence of the lifetime ratio on the Gold-Don1 separation can be well fitted with equation (6.1). The best agreement with the data, shown as a line in Figure 6.2, was obtained for $c_1 = 1236$ nm^4 for this distance dependence at $c_{Au} = (0.22 \pm 0.03) \times 10^{17}$ m^{-2}. It should be noted, that the fit of the relative lifetime is not zero for $d =$

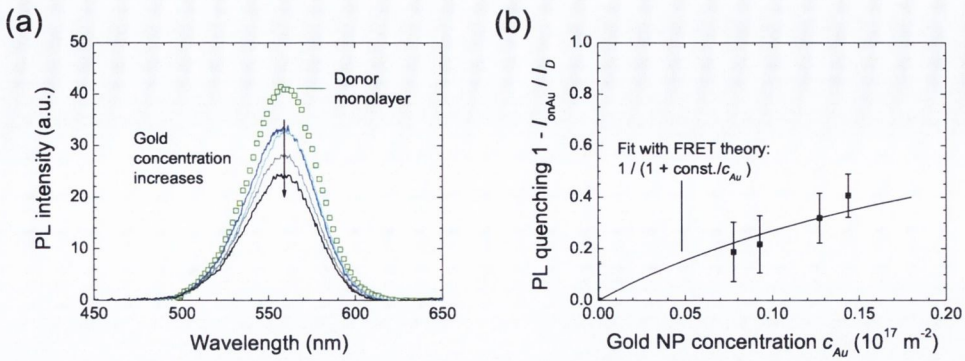


Figure 6.3: (a) PL spectra of Don1-gold structures with a layer separation of 3 nm for different gold nanoparticle (NP) concentrations (lines) and a reference monolayer on quartz (open green squares). The Don1 concentration was adjusted to $c_{Don} = 2.5 \times 10^{17}$ m^{-2}. (b) Dependence of the PL quenching in the Don1-gold structures on the gold NP concentration c_{Au}. The line represents a fit of the concentration dependence with FRET theory.

0 nm, as d is not the Gold-Don1 centre-to-centre distance R_{ex}, but represents the polyelectrolyte spacer thickness to which the gold NP and Don1 QD radii have to be added to obtain $R_{ex} = d + 3.35$ nm.

It has been mentioned above, that the Don1 emission intensity seems to be more strongly influenced by the gold NP concentration than the gold-QD separation. In Figure 6.3(a) the PL spectra (lines) of Don1-gold samples with $d = 3$ nm, are shown for four different gold NP concentrations. The Don1 concentration was approximately $(2.3 \pm 0.3) \times 10^{17}$ m^{-2} and the spectra were all corrected to show the emission for $c_{Don} = 2.5 \times 10^{17}$ m^{-2}. As for the distance dependence, the emission of all samples is quenched with respect to the reference spectrum (open green squares). Furthermore, the emission intensity is decreasing strongly with increasing gold NP concentration, as more gold NPs are available to receive energy from the Don1 QDs. This trend can also be clearly seen in the gold NP concentration dependence of the PL quenching, $1 - I_{\mathrm{onAu}}/I_D$, shown in Figure 6.3(b). The increase of the PL quenching with increasing c_{Au} can be well reproduced by a fit with FRET theory for $1 - q_r$, with the concentration dependence of q_r given in equation (6.2). The best fit, shown as line in Figure 6.3(b), was obtained for $c_2 = 0.271 \times 10^{17}$ m^{-2}.

In Figure 6.4, the PL decays measured on the blue side of the Don1 emission spectrum are presented for different gold NP concentrations in the Don1-gold structures with $d = 3$ nm. The PL decay of the Don1 reference monolayer on quartz is also shown (green line). The decays for the Don1 QDs in proximity to gold NPs are shorter than the reference decay and become faster with increasing c_{Au}.

As for the distance dependence, the relative lifetime $\tau_{\mathrm{onAu}}/\tau_D$ was determined for

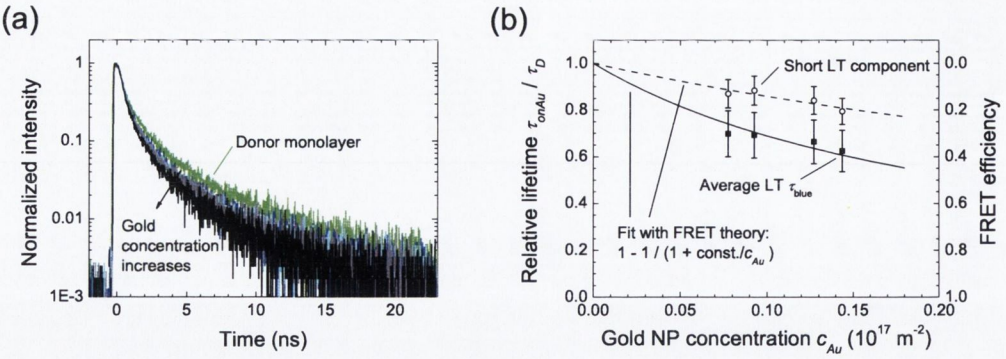


Figure 6.4: (a) PL decays of Don1-gold structures with a gold-Don1 separation of 3 nm for different gold nanoparticle (NP) concentrations c_{Au} and $c_{Don} = (2.3 \pm 0.3) \times 10^{17}$ m^{-2}. The reference decay for a Don1 monolayer on quartz is also shown (green line). (b) Relative donor lifetime in Don1-gold structures calculated for the average lifetime τ_{blue} (solid squares), measured on the blue side of the Don1 ensemble emission spectrum, as well as its short lifetime component (open circles) in dependence of c_{Au} (both left-hand axis). The lifetime trends of the average lifetime and short lifetime component were fitted with FRET theory (solid and dashed line respectively). The corresponding FRET efficiencies are indicated on the right-hand axis.

each Don1-gold structure to compensate for the concentration effects on the lifetimes. The gold NP concentration dependence of τ_{onAu}/τ_D calculated for the average lifetimes (solid squares) as well as for the short lifetime components (open squares) of the donor PL decays are shown in Figure 6.4(b). The short lifetime component is investigated as well, as it will be important for the analysis of the effect of surface plasmons on FRET in donor-acceptor QD structures on the donor decay dynamics. Both lifetime ratios decrease with increasing c_{Au} and in addition, both trends can be well fitted with equation (6.2). For the average lifetime $c_2 = 0.222 \times 10^{17}$ m^{-2}, a value similar to that obtained from the fit of the PL quenching, was obtained for the best fit of the data, and for the short lifetime component a value of $c_2 = 0.607 \times 10^{17}$ m^{-2} was found. The lifetime ratios can also be converted into an efficiency (shown on the right-hand axis) and at the highest gold concentration investigated, $c_{Au} = 0.14 \times 10^{17}$ m^{-2}, the Don1-gold NP energy transfer efficiency reaches 37% (calculated for the average lifetime).

In summary, the observed distance and gold NP concentration dependences of the optical properties of Don1 QDs in proximity to gold NPs can be well explained by FRET from the QDs to the gold NPs. Only PL quenching and reduced average lifetimes have been observed for all donor QDs used in the following. This is an important finding, as it excludes the misinterpretation of signatures arising from direct enhancement of the donor PL emission by interaction with surface plasmons as enhanced FRET from donor to acceptor QDs in proximity to gold NPs.

6.1.2 Surface Plasmon Effects on Acceptor QDs

The distance and gold NP concentration dependences of the optical properties of Acc2 QDs deposited on top of gold NP layers were also investigated. This is important to find out if a direct PL enhancement of the Acc2 QDs can be observed by interaction with the gold NPs only.

The PL spectra for Acc2 QDs deposited on gold NP layers with varying Acc2-gold layer separations are shown in Figure 6.5(a) for polyeletrolyte spacer thicknesses of $d = 3$ to 21 nm. The spectra were adjusted to show emission intensities for $c_{Acc} = 1.5 \times 10^{17}$ m^{-2}. As for the donor QDs, the emission of the Acc2 monolayers, in proximity of a gold NP layer, is quenched for all gold-Acc2 layer separations investigated and no clear distance dependence is observed. The six Acc2-gold samples show a similar level of quenching, $1 - I_{onAu}/I_A$, as can be seen in Figure 6.5(b) (solid squares, left-hand axis). The slightly stronger decrease of the emission intensity at $d = 18$ and 21 nm is again explained by an increased gold NP concentration (open triangles, right-hand axis) for these samples. The only exception to the trend occurs at $d = 6$ nm, for which a small reduction of the quenching is observed. The effect is however only within error of the general quenching level.

The Acc2 decays for the Acc2-gold structures with varying layer separations d and an Acc2 monolayer on quartz (red line) are shown in Figure 6.6(a). The decays were recorded on the red side of the Acc2 ensemble emission spectrum using the 650 nm filter. All decays are faster than the reference decay and become longer with increasing gold-Acc2 layer separation. The dependence of the lifetime ratio τ_{onAu}/τ_A (solid squares, left-hand axis) on the gold-Acc2 layer separation is shown in Figure 6.6(b). As for the relative Don1 lifetimes presented above, the reference PL lifetimes τ_A, at the respective Acc2 concentration in the Acc2-gold structure, were determined from a fit of the Acc2 concentration dependence of the acceptor lifetimes measured on the red side of the Acc2 emission spectrum . Except for $d = 21$ nm, the lifetime ratio is increasing with increasing layer separation, due to a decreasing effect of the surface plasmon on the Acc2 decay dynamics. The distance dependence of the relative Acc2 lifetime is best fitted with equation (6.1) for $c_1 = 6852$ nm^4, indicated by the line in Figure 6.6(b). The divergence from the fit at large layer separations d can be explained with the increasing trend of the gold NP concentration with increasing layer separation (open circles, right-hand axis). This suggests that, as for the Don1 QDs, the influence of the gold NP concentration on the optical properties of the Acc2 QDs is stronger than the dependence on the gold-QD separation.

PL spectra (lines) for Acc2 QDs deposited on top of a gold NP layer, covered by a polyelectrolye spacer with thickness $d = 12$ nm, are shown for four different gold NP concentrations c_{Au} in Figure 6.7(a). The Acc2 concentrations were adjusted to

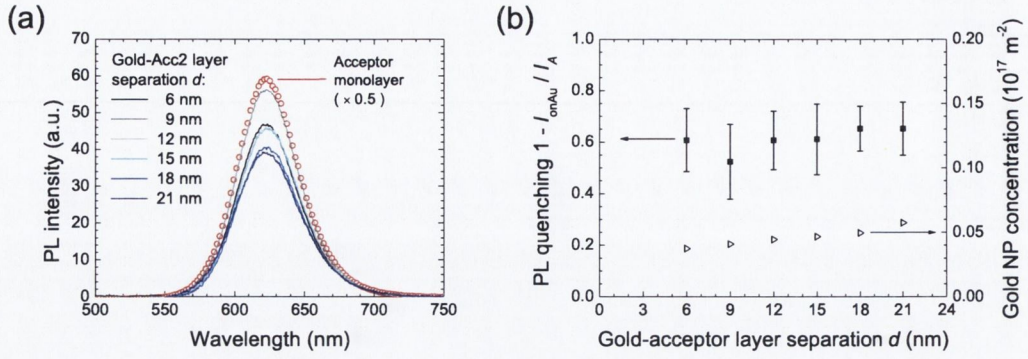


Figure 6.5: (a) PL spectra (lines) of Acc2 monolayers deposited on a gold nanoparticle (NP) layer with different layer separations d, indicated in the legend, and gold NP concentration $c_{Au} = (0.047 \pm 0.010) \times 10^{17}$ m^{-2}. The reference spectrum for an Acc2 monolayer on quartz is also shown (open red circles). The Acc2 concentration was adjusted to $c_{Acc} = 1.5 \times 10^{17}$ m^{-2} for all spectra. (b) Dependence of the Acc2 PL quenching on the gold-Acc2 layer separation d (solid squares, left-hand axis). The gold NP concentration of each sample is shown as well (open triangles, right-hand axis).

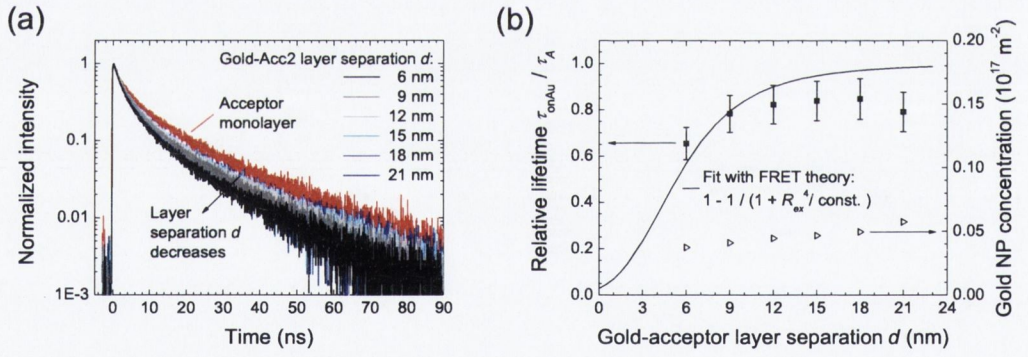


Figure 6.6: (a) PL decays of the Acc2-gold structures with different gold-Acc2 separations d, indicated in the legend, and an Acc2 reference monolayer on quartz (red line). The gold concentration was maintained at $c_{Au} = (0.047 \pm 0.010) \times 10^{17}$ m^{-2}. (b) Relative PL lifetimes of the Acc2-gold structures in dependence of the gold-Acc2 layer separation (solid squares, left-hand axis). The line represents a fit of the lifetime ratio with FRET theory. The gold concentration of each sample is also indicated (open triangles, right-hand axis). The PL decays and lifetimes were measured on the red side of the Acc2 ensemble emission spectrum.

$c_{Acc} = 1.0 \times 10^{17}$ m^{-2}. The emission intensity of all Acc2-gold samples is lower than that of the reference spectrum recorded for an Acc2 monolayer on quartz (open red circles). Except for the sample with $c_{Au} = 0.13 \times 10^{17}$ m^{-2} (light blue line), the Acc2 emission intensity is decreasing with increasing gold NP concentration. The same trend is observed for the Acc2 PL quenching, calculated from the integrated PL intensities, shown in Figure 6.7(b) (solid squares). A good agreement of the dependence of the Acc2 PL quenching on c_{Au} with FRET theory was obtained for fitting the data with $1 - q_r$, with q_r given in equation (6.2), for $c_2 = 0.185 \times 10^{17}$ m^{-2}.

The PL decays, recorded on the red side of the Acc2 ensemble emission spectrum, for the Acc2-gold samples with varying gold NP concentration c_{Au} are presented in Figure 6.8(a). The Acc2 reference sample shows the longest decay (red line) and with increasing gold NP concentration the decays become shorter. The dependence of the relative lifetime on c_{Au} is shown in Figure 6.8(b) for the lifetimes of the PL decays measured on the red (solid squares) and blue (open circles) side of the Acc2 ensemble emission spectrum. Both relative lifetimes are decreasing with increasing gold NP concentration, with only the lifetime ratio for the blue side of the ensemble emission showing the deviation from the trend for the sample with $c_{Au} = 0.13 \times 10^{17}$ m^{-2}. The two lifetime ratios show similar values for all samples investigated, indicating that the presence of the gold NPs is influencing all QDs in the ensemble in the same way. The concentration dependence of the relative lifetimes was fitted with equation (6.2) and the best agreement was found for $c_2 = 0.445 \times 10^{17}$ m^{-2}. This shows that the increasing quenching of the Acc2 intensity with increasing gold NP concentration is due to increasing energy transfer to the gold NP layer. For the Acc2 monolayers on gold smaller energy transfer efficiencies (indicated on the righ-hand side of Figure 6.8(b)) are observed as for Don1, with an efficiency of approximately 26% at $c_{Au} = 0.16 \times 10^{17}$ m^{-2}. The lower energy transfer efficiency is due to the reduced spectral overlap of the Acc2 emission and the gold NP extinction spectrum. However, it has to be noted that the PL quenching is actually larger for the Acc2 QDs on gold than for the Don1 QDs, indicating that there might be another quenching mechanism influencing only the emission of the QDs and not their lifetimes. This is further supported by the distance dependence, for which only a FRET-like trend is observed for the relative lifetimes and not for the fairly constant PL quenching. A more detailed investigation of these effects is necessary to fully explain the QD-metal NP interactions, but as mentioned above, this lies beyond the scope of the work presented here.

The main objective of this section was to show that also for the Acc2-gold layer structures only PL quenching was observed over the range of layer separations and gold concentrations investigated. This is important, as any acceptor enhancement observed for the samples presented in the following can be attributed to energy transfer from the

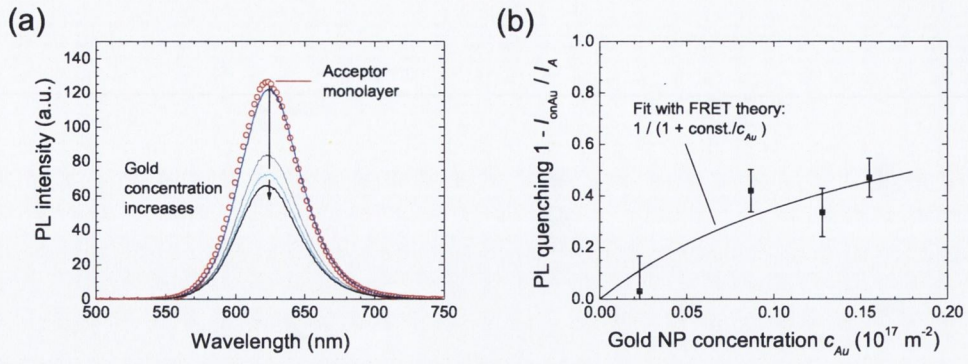


Figure 6.7: (a) PL spectra of Acc2-gold layer structures with a layer separation of 12 nm for different gold nanoparticle (NP) concentrations (lines). An Acc2 reference spectrum for a monolayer on quartz is also included in the graph (open red circles). The Acc2 concentrations were adjusted to $c_{Acc} = 1.0 \times 10^{17}$ m^{-2}. (b) Gold NP concentration dependence of the Acc2 PL quenching (solid squares). The line represents a fit of the concentration dependence with FRET theory.

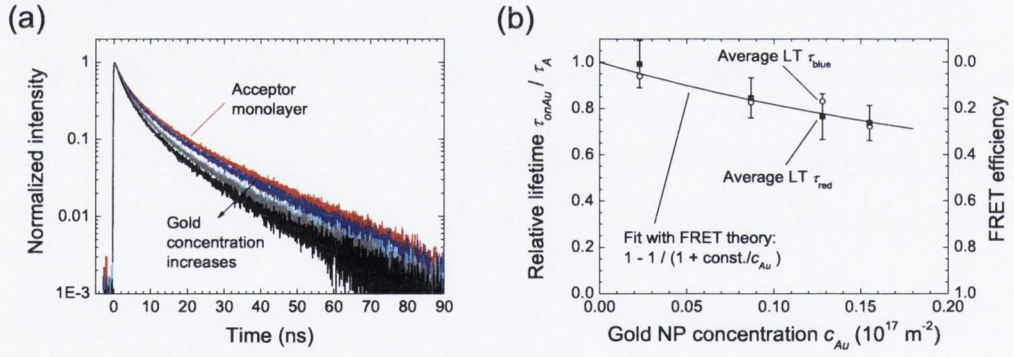


Figure 6.8: (a) PL decays for Acc2 monolayers deposited on a gold nanoparticle (NP) layer with varying gold NP concentration and a gold-Acc2 layer separation of 12 nm. The reference decay for the Acc2 monolayer on quartz is also included (red line). The PL decays were measured on the red side of the Acc2 ensemble emission spectrum. (b) Gold NP concentration dependence of the relative lifetime determined for decays recorded on the red (solid squares) and blue (open circles) side of the Acc2 emission spectrum. For the relative lifetime measured on the red side, a fit of the gold NP concentration dependence with FRET theory is shown as well (line).

donor QDs and is not caused by an enhanced absorption or emission of the Acc2 QDs in proximity to gold NPs.

6.2 Acceptor-Gold-Donor Sandwich Structure

For the investigation of the impact of surface plasmons on FRET between donor and acceptor QDs, gold NPs with a diameter of approximately 4 nm were used. Depending on the NP concentration, monolayers of these gold NPs show a surface plasmon resonance centred at 530 to 540 nm in their absorption spectra, presented as a dashed black line in Figure 6.9(a) (right-hand axis). Therefore, the resonance occurs in the wavelength region where energy transfer is observed from Don1 to Acc2 QDs due to their spectral overlap, indicated by the PL spectrum of a Don1 monolayer (solid green squares, left-hand axis) and the absorption spectrum of an Acc2 monolayer (solid red line, right-hand axis). The emission spectrum of the Acc2 monolayer (open red circles, left-hand axis) is also shown for completeness. Therefore, a resonant interaction of the surface plasmon field with the energy transfer between the QDs can be expected.

As outlined in chapter 3, absorption and PL spectra are recorded after each semiconductor or metal nanoparticle deposition step during the preparation of the acceptor-gold-donor sandwich structures. Examples of these PL spectra are shown in Figure 6.9. The emission of the acceptor monolayer (open red circles) is fully quenched after the deposition of polyelectrolyte bilayers (here 4 bilayers with a thickness $d = 12$ nm) and a gold NP layer and only emission from the polyelectrolyte is observed (solid black line). For the inverse structure with an Acc2 monolayer on gold ($d = 12$ nm), the emission is quenched by more than 50% (solid red line). Once the donor QDs are deposited on top of the acceptor-gold structure (here for one PE bilayer, $d = 3$ nm), some of the acceptor emission can be recovered. The PL spectrum of the completed sandwich structure is presented by the solid black triangles and the acceptor contribution to this spectrum is indicated by the solid red circles. As can be seen, the acceptor emission in the sandwich structure is shifted to the blue compared to that of the reference spectra for Acc2 monolayers on quartz and gold. It shows a small quenching with respect to the acceptor monolayer on quartz, but a larger emission compared to the Acc2 monolayer on gold.

This first comparison of the PL spectra already indicates, that energy transfer from the donors is able to overcome some of the quenching of the acceptor emission in proximity of metal NPs. This leads to the observation of acceptor emission in the sandwich structure, which was not detected in the structure without donor QDs. Enhanced radiative energy transfer can be excluded as a mechanism for the observed increase in acceptor emission as there is no evidence for an enhanced donor emission or acceptor absorption in the

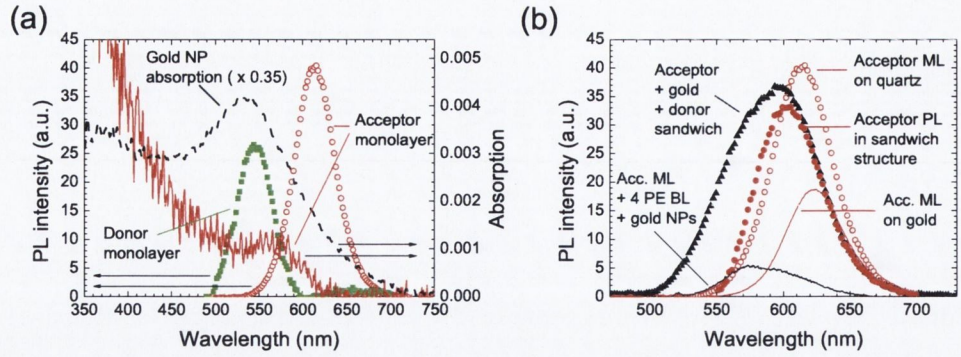


Figure 6.9: (a) Don1 (solid green squares) and Acc2 (open red circles) monolayer PL spectra (left-hand axis) as well as acceptor (solid red line) and gold nanoparticle (NP) (dashed black line) monolayer absorption spectra (right-hand axis). (b) PL spectra of an Acc2 monolayer (ML) on quartz (open red circles), an Acc2 ML on gold (separation $d = 12$ nm) (solid red line), Acc2 ML covered with 4 polyelectrolyte bilayers (PE BL) ($d = 12$ nm) and a gold nanoparticle (NP) layer (solid black line). The spectrum of a full acceptor-gold-donor sandwich structure (solid black triangles) as well as the acceptor contribution to this spectrum (solid red circles) are also shown.

study of the monodispersed QD monolayers in proximity to gold NPs, discussed above in section 6.1. Due to the large QD separation, tunnelling can also be excluded as a possible mechanism for the observed acceptor emission enhancement. Therefore, this suggests that the observed acceptor emission is due to FRET. In the separated donor-acceptor bilayer structure discussed in the previous chapter, FRET between donor and acceptor QDs has only been observed for maximum centre-to-centre distance of 12 nm, see section 5.2. These first spectra for the Acc2-gold-Don1 sandwich structure indicate that, by including gold NPs in the structure, this distance can be extended to at least $R_{ex} = 1.75\text{ nm} + 12\text{ nm} + 4\text{ nm} + 3\text{ nm} + 1.35\text{ nm} = 22.1\text{ nm}$, taking into account the QD radii, the gold NP diameter and the spacer layer thicknesses between the QD layers and the intermediate gold NP particle layer. These results are especially interesting for sensing structures, as acceptor emission from below the gold NP layer is only visible when a suitable energy donor is sufficiently close to the gold NP layer, which could be achieved by selective binding to functionalized gold NPs. Furthermore, the extension of the energy transfer distance is important for all applications to overcome the limitations of the FRET efficiency due to exclusion zone radii arising from the size of the donor and acceptor species or introduced by the device design, as for example in light emitting structures [22, 24].

6.2.1 Comparison of Different Donor QDs

For the preparation of the acceptor-gold-donor sandwich structures, six different QD donors: Don1, Don5, Don6, Don7, Don8 and Don9; were tested. The absorption, PL and PLE spectra of the Don1 QDs in solution can be seen in Figure 3.8(a) and 4.1(a), the spectra of the other five QDs in solution can be found in appendix A.2. The PL spectra of monolayers of these six QDs with concentrations of $(0.65 \pm 0.20) \times 10^{17}$ m^{-2} are shown in Figure 6.10(a). For a better comparison of the spectral properties of the QD monolayers, the peak intensities of the spectra have been normalized. As can be seen, all emission spectra overlap with the surface plasmon resonance of the gold NP layer (dashed black line, right-hand axis). With respect to the centre wavelength of the surface plasmon resonance of the gold NP layer, the emission peak of the Don5 monolayer (blue line) occurs to the blue of this wavelength and that of the Don6 monolayer (dark green line) is right in resonance. The Don1, Don8, Don9 and Don7 QDs in the monolayers emit mostly to the red of the surface plasmon centre wavelength. Due to the broad PL peak of the Don1 monolayer (light green line), its emission is still very high in the wavelength region of the maximum gold NP absorption, whereas the Don7 QDs (yellow line) only emit very little in this region, as their PL is shifted the furthest to the red. The quantum yields determined for these monolayers are 6% for the Don5 and Don6 monolayers respectively, 10% for Don1, 3% for Don7, 5% for Don8 and 2% for the Don9 monolayer.

The PL spectra of the completed acceptor-gold-donor structures for all six donor QD samples are shown in Figure 6.10(b). The acceptor-gold layer separation was $d = 12$ nm and the separation between the gold and donor layer was $d = 3$ nm. The gold NP concentration c_{Au} was approximately $(0.09 \pm 0.02) \times 10^{17}$ m^{-2} for all six samples. The polyelectrolyte emission has been removed from the spectra following the fitting procedure outline in the beginning of chapter 5. Furthermore, for the structure containing Don1 QDs, the acceptor emission was reduced from 11% to 6% for a better comparison with the other sandwich structures which were measured at a later time when the acceptor quantum yield had reduced to 6%. Therefore, the spectrum of the Don1-gold-Acc2 spectrum was separated into its Don1 and Acc2 contributions and the Acc2 spectrum was multiplied with the quantum yield ratio 6/11 before adding it back to the donor spectrum (light green line).

As can be seen, the only donor QDs for which some of the acceptor emission can be recovered in the full sandwich structure are Don5 (blue line), Don6 (dark green line) and Don1 (light green line). There is no emission that can be attributed to the acceptor QDs at wavelength greater than 600 nm for Don7 (dark yellow line), Don8 (orange line) or Don9 (yellow line). This indicates that there is a strong donor PL wavelength dependence of the surface plasmon mediated energy transfer process.

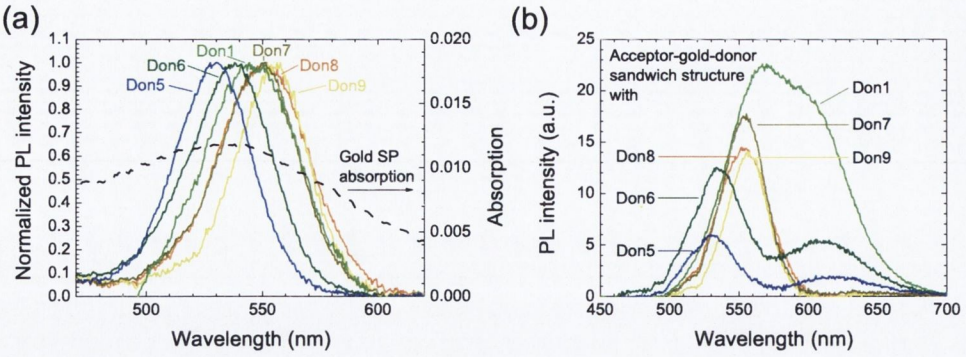


Figure 6.10: (a) PL spectra of Don5, Don6, Don1, Don7, Don8 and Don9 QD monolayers with normalized peak intensities. The QD concentration of the monolayers was $(0.65 \pm 0.20) \times 10^{17}$ m^{-2}. The surface plasmon (SP) resonance in the absorption spectrum of a gold nanoparticle (NP) layer is also shown (dashed black line, right-hand axis). (b) PL spectra of acceptor-gold-donor sandwich structures for all six donor QDs with acceptor-gold separation $d =$ 12 nm and gold-donor separation $d = 3$ nm. The gold NP concentration was approximately $(0.09 \pm 0.02) \times 10^{17}$ m^{-2} for all samples.

In Figure 6.11(a) the donor decays for different Don6 structures are shown. The PL decay of a Don6 monolayer with a QD concentration of $c_{Don} = 0.6 \times 10^{17}$ m^{-2} (light green line) is characterized by an average lifetime of $\tau_D = 5.8$ ns. This PL lifetime is reduced to $\tau_{\text{onAu}} = 3.0$ ns for a Don6 monolayer, with $c_{Don} = 0.6 \times 10^{17}$ m^{-2}, on a gold NP layer with concentration $c_{Au} = 0.085 \times 10^{17}$ m^{-2} ($d = 3$ nm). This decrease in the donor lifetime is due to energy transfer from the donors to the gold NPs with a rate $k_{Au} = (1/\tau_{\text{onAu}} - 1/\tau_D) = (6.2 \text{ ns})^{-1}$. The PL decay in the full sandwich structure (red line), with $c_{Don} = 1.0 \times 10^{17}$ m^{-2} and $c_{Au} = 0.072 \times 10^{17}$ m^{-2}, is described by a lifetime of $\tau_{DAuA} = 3.5$ ns and is longer than that of the Don6-gold structure. This is quite surprising as a shorter lifetime would be expected due to additional energy transfer to the acceptors in the full sandwich structure. However, differences in donor QD and gold NP concentrations can result in a larger donor lifetime in the sandwich structure than in the Don6-gold structure. This highlights, that the effect of surface plasmon enhanced FRET on the donor decay dynamics is not very large. Therefore, donor PL decays for structures with very similar donor and gold concentrations have to be compared in order to resolve the signatures of the gold NP mediated energy transfer in the donor PL decay.

To enable the observation of the effect of the energy transfer on the Don6 PL lifetime in the presence of gold NPs the donor-acceptor energy transfer rate k_{DA} has to be larger than $(30 \text{ ns})^{-1}$. This would lead to a decrease of the donor lifetime in the sandwich structure to below 2.7 ns compared to 3.0 ns measured for the Don6 monolayer on

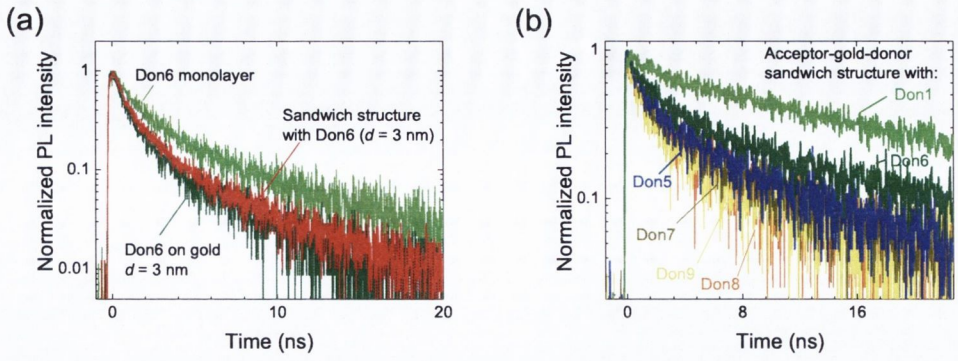


Figure 6.11: (a) Donor PL decays for a Don6 monolayer (light green line), Don6 monolayer on gold with a layer separation of $d = 3$ nm (dark green line) and for the full acceptor-gold-donor sandwich structure (red line). (b) Acceptor PL decays of the Acc2-gold-donor sandwich structures for all six donor QDs investigated.

gold. As no clear decrease of the lifetime in the Acc2-gold-Don6 sandwich structure is observed, but the lifetime is dominated by variations due to the donor QD and gold NP concentrations, the energy transfer observed for the sandwich structure has to be slower than $(30\ \text{ns})^{-1}$. However, even for $k_{DA} = (30\ \text{ns})^{-1}$ a FRET efficiency of 9% can be expected, from a calculation with equation (6.3), which seems high enough to overcome the total quenching of the acceptor QDs deposited under the gold NP layer.

$$E_{\text{FRET}} = \frac{k_{DA}}{1/\tau_D + k_{Au} + k_{DA}} \tag{6.3}$$

PL decays recorded with the 650 nm filter for the sandwich structures prepared with the six different QD donors are shown in Figure 6.11(b). The decays for the samples containing Don7 (dark yellow line), Don8 (orange line) and Don9 monolayers (yellow line) look the same and are most likely only arising from polyelectrolyte emission. Compared to these PL decays, the decay measured for the Acc2-gold-Don5 sandwich structure (blue line) is a little longer, which is attributed to the small acceptor emission that has been measured for this sample. The PL decays for structures with Don6 (dark green line) and Don1 QDs (light green line) are much longer than the other decays, in line with the larger acceptor emission observed in their PL spectra. Furthermore, for Don1 also a rise-time can be observed for the acceptors in the sandwich structure, as the maximum emission occurs at a later time than for the other decays.

In order to better understand the strong donor-dependence of the surface plasmon effect on the energy transfer in the sandwich structure, the integrated acceptor PL emission is presented as a function of the donor emission peak wavelength in solution in Figure 6.12(a). The bars indicate the FWHM of the donor QD emission. Compared

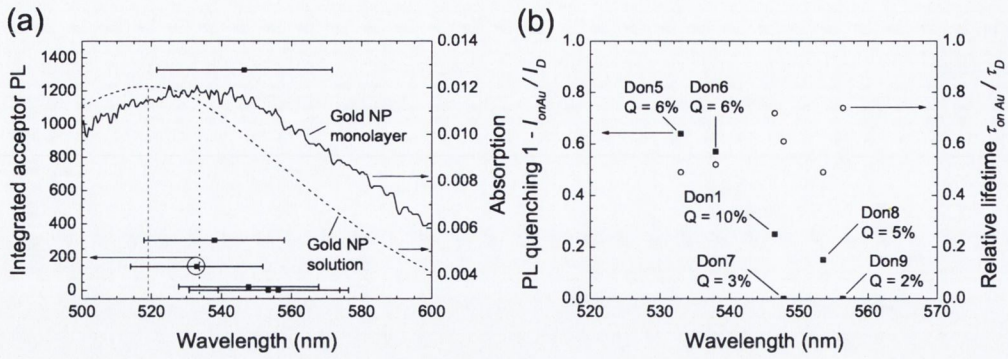


Figure 6.12: (a) Dependence of the integrated acceptor PL in the acceptor-gold-donor sandwich structures on the donor centre emission wavelength in solution (solid squares, left-hand axis). The x-bars indicate the full-width-at-half-maximum of the donor PL emission in solution. The absorption spectra of the gold nanoparticles (NP) in solution (dashed line) and in a monolayer (solid line) are also included (right-hand axis). (b) Donor PL quenching (solid squares, left-hand axis) and the relative donor lifetime (open circles, right-hand axis) for the donor monolayers on gold $c_{Au} = (0.09 \pm 0.02) \times 10^{17}$ m^{-2} in dependence of the donor emission peak wavelength in solution.

to the surface plasmon resonances observed for the gold NP solution (dashed line) and monolayer (solid line), an acceptor PL signal is observed for sandwich structures prepared with those donors that show emission peak wavelengths closest to the centre wavelength of the gold NP absorption feature for the monolayer and which still show a significant emission at the central wavelength region of the surface plasmon resonance in solution. This indicates that surface plasmon mediated energy transfer only occurs for those QDs that interact strongly with the gold NPs.

To support this observation, the interaction of the donor QDs with the gold NPs is characterised by the decrease of the donor emission and PL lifetimes in proximity to the gold NPs. The PL quenching (solid squares, left-hand axis) and the relative lifetime (open circles, right-hand axis) of donor monolayers deposited on gold, with $d = 3$ nm, are shown in dependence of the donor peak emission wavelength in solution in Figure 6.12(b). As can be seen, the strongest effects of the gold NPs on the donor emission properties are observed for Don5 and Don6, for which a PL quenching larger than 55% and donor lifetime ratios of approximately 0.5 were determined. For Don1 and Don8 the PL quenching is still 25% and 15% respectively, whereas no quenching is observed for Don7 and Don9. Furthermore the lifetime ratios for these QDs, with exception of Don8, are larger than for Don5 and Don6. This indicates a stronger interaction with the gold NPs for Don5 and Don6 than for the other donor QDs. However, the strongest signature for surface plasmon enhanced FRET, in form of the largest acceptor

PL emission, is observed for Don1. Furthermore, the transition from the donor emission wavelength region for which an acceptor emission is measured in the sandwich structure to larger donor PL peak wavelengths for which no acceptor emission is observed is very abrupt. This suggests that the donor peak emission wavelength is not the only parameter giving rise to this strong donor dependence.

For the regular FRET process, not only a large spectral overlap but also a large donor quantum yield is necessary for efficient energy transfer. Therefore, the donor quantum yield is another donor-dependent property that could strongly influence the surface plasmon mediated energy transfer. The quantum yield of the donor QDs in the monolayers is also given in Figure 6.12(b). An acceptor emission is observed for those QDs that show a good interaction with the surface plasmon, indicated by the PL quenching, and that have a large quantum yield. In particular, the large acceptor emission observed for the Acc2-gold-Don1 is thought to be mainly facilitated by the larger donor quantum yield. Due to the low quantum yield and a weak interaction with the gold NPs for Don7 QDs, no surface plasmon mediated energy transfer is observed in Acc2-gold-Don7 sandwich structures even though these QDs have a similar peak emission wavelength in solution as Don1, but a smaller PL FWHM. Don8 has a quantum yield of 5%, similar to Don5 and Don6, but is emitting further to the red than these QDs and is therefore interacting more weakly with the surface plasmon resonance, only showing a PL quenching of 15%. Therefore, no acceptor emission is observed in the Acc2-gold-Don8 PL spectrum.

6.2.2 Acceptor-Gold Distance Dependence

In order to investigate and optimize the surface plasmon mediated FRET process, the QD-gold NP distance dependences were analyzed. The PL spectra of two sets of Acc2-gold-Don1 sandwich structures with a constant gold-donor separation of 3 nm and varying acceptor-gold separations d are presented in Figure 6.13(a) and (b). Figure 6.13(a) shows spectra for d = 3 to 15 nm and gold concentrations of $c_{Au} = (0.18 \pm 0.05) \times 10^{17}$ m^{-2}. The donor and acceptor concentrations were $c_{Don} = (1.5 \pm 0.4) \times 10^{17}$ m^{-2} and $c_{Acc} = (0.49 \pm 0.11) \times 10^{17}$ m^{-2} respectively. Figure 6.13(b) includes the spectra for sandwich structures with larger separations d of 12 to 21 nm as well as a reference spectrum of a donor-acceptor bilayer structure, with $c_{Don} = 2.9 \times 10^{17}$ m^{-2} and $c_{Acc} = 0.42 \times 10^{17}$ m^{-2} and a layer separation of 21 nm (solid black squares). For this second sample set the gold concentration $c_{Au} = (0.06 \pm 0.04) \times 10^{17}$ m^{-2} was lower, but the QD concentrations $c_{Don} = (1.3 \pm 0.5) \times 10^{17}$ m^{-2} and $c_{Acc} = (0.42 \pm 0.05) \times 10^{17}$ m^{-2} were similar to those of the first sample set.

As can be seen in Figure Figure 6.13(a), the donor and acceptor emission are strongly quenched for the acceptor-gold separation of 3 nm. A clear broadening of the measured

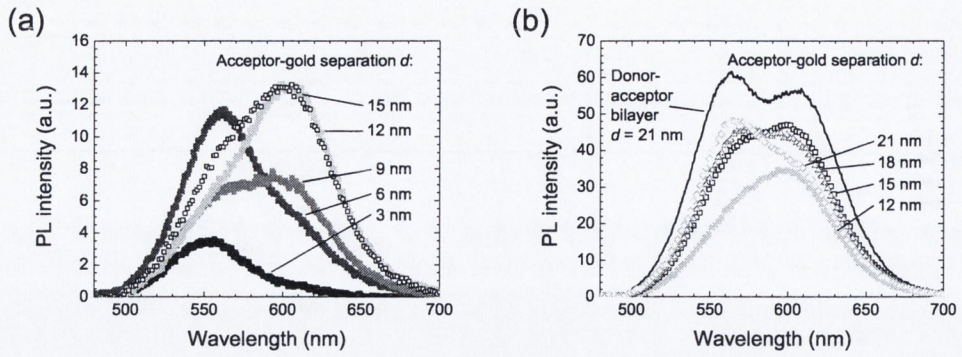


Figure 6.13: (a) PL spectra of Acc2-gold-Don1 sandwich structures with acceptor-gold separations d increasing from 3 to 15 nm for samples with gold-donor separations of 3 nm and a gold nanoparticle (NP) concentration of $c_{Au} = (0.18 \pm 0.05) \times 10^{17}$ m^{-2}. The donor and acceptor QD concentrations were $c_{Don} = (1.5 \pm 0.4) \times 10^{17}$ m^{-2} and $c_{Acc} = (0.49 \pm 0.11) \times 10^{17}$ m^{-2} respectively. (b) PL spectra of Acc2-gold-Don1 sandwich structures with larger acceptor-gold separations increasing from 12 to 21 nm, with a gold-donor separation of 3 nm and $c_{Au} = (0.06 \pm 0.04) \times 10^{17}$ m^{-2}. The QD concentrations were $c_{Don} = (1.3 \pm 0.4) \times 10^{17}$ m^{-2} and $c_{Acc} = (0.42 \pm 0.05) \times 10^{17}$ m^{-2}. A reference spectrum of a donor-acceptor bilayer structure (without gold NPs) with a donor-acceptor separation of 21 nm is also included (solid line). The QD concentrations of the reference structure were $c_{Don} = 2.9 \times 10^{17}$ m^{-2} and $c_{Acc} = 0.42 \times 10^{17}$ m^{-2}.

emission feature is observed for increasing acceptor-gold separations in the sandwich structures, along with a red-shift of the wavelength at which the maximum emission is recorded. These modifications of the spectra are caused by an increasing emission from the acceptor QDs, which is going to be analysed in more detail below.

For the spectra of the sandwich structures with larger acceptor-gold separations, presented in Figure 6.13(b), the increasing contribution of the acceptor emission to the spectra can be seen again for $d = 12$ and 15 nm. However, for larger separations of 18 and in particular 21 nm, the acceptor emission is reducing and the donor emission starts to dominate again. This causes the wavelength at which the maximum emission is observed in these spectra to shift back to the blue.

The emission intensity of all sandwich structures presented in Figure 6.13(a) and (b) is reduced compared that of the reference spectrum of a donor-acceptor bilayer structure without gold NPs and a layer separation of 21 nm (solid line). Moreover, the intensities measured for the second samples set, with lower gold concentrations, are all larger than for the first set, which shows that the gold NP concentration has an important impact on the overall emission of the sandwich structure. The influence of the gold concentration on the surface plasmon mediated energy transfer will be investigated in more detail in

section 6.2.4.

For a more detailed investigation of the influence of the acceptor-gold layer separation on the donor and acceptor emission, the donor and acceptor contributions to the spectra of the sandwich structures were separated. The integrated donor emission, corrected to show the intensity for $c_{Don} = 1.0 \times 10^{17}$ m^{-2}, is presented in Figure 6.14(a) in dependence of the acceptor-gold layer separation (solid and open green squares, left-hand axis). In addition, the gold NP concentration c_{Au} of each sample is also included in the Figure (solid and open triangles, right-hand axis). The general observation was that the number of gold NPs deposited on an increasing number of polyelectrolyte layers covering the acceptor QD layer, was decreasing for a constant immersion time. Therefore, c_{Au} is decreasing with increasing acceptor-gold layer separation for these samples and this has to be taken into account when analysing the data.

As can be seen, the integrated donor intensity seems to be relatively constant with increasing acceptor-gold layer separation d for the small acceptor-gold separations included in the first sample set (solid squares). For the second sample set (open squares) it is increasing with increasing d. If the donor QDs were only interacting with the gold NPs, a constant PL intensity would be expected for a fixed gold-donor separation. However, as mentioned above, the gold concentration was actually not constant for the samples, so an increasing donor emission should be observed with increasing acceptor-gold layer separation in the sandwich structures due to the decreasing gold concentration. Therefore, another effect has to be influencing the donor emission at small acceptor-gold separations, leading to the observed constant donor PL intensity. This additional donor quenching mechanism is the energy transfer to the acceptors. The energy transfer starts to decrease at the largest acceptor-gold separations investigated, as the integrated donor PL is increasing and even recovering to the value observed for the reference bilayer structure (value indicated at $d = 30$ nm), as the gold concentration for the samples with $d = 18$ and 21 nm is relatively low.

In Figure 6.14(b), the gold-acceptor distance dependence of the integrated acceptor PL intensity is shown for the two samples sets (solid and open circles respectively). The acceptor concentrations were adjusted to $c_{Acc} = 0.5 \times 10^{17}$ m^{-2}. As already seen for the full spectra of the sandwich structures discussed above, the acceptor emission is increasing with increasing acceptor-gold separation and reaches a maximum at 15 nm, before it starts to decrease. The emission increase of the acceptor QDs can not only be attributed to the increasing acceptor-gold separation, as a more or less constant acceptor PL quenching was determined for the distance dependence of Acc2 monolayers on gold, as presented in Figure 6.5(b). Even though a decreasing gold concentration could explain the increase in acceptor PL, c_{Au} is fairly constant for $d = 3$, 6 and 9 nm, for which the acceptor emission is already increasing. Furthermore it doesn't explain the

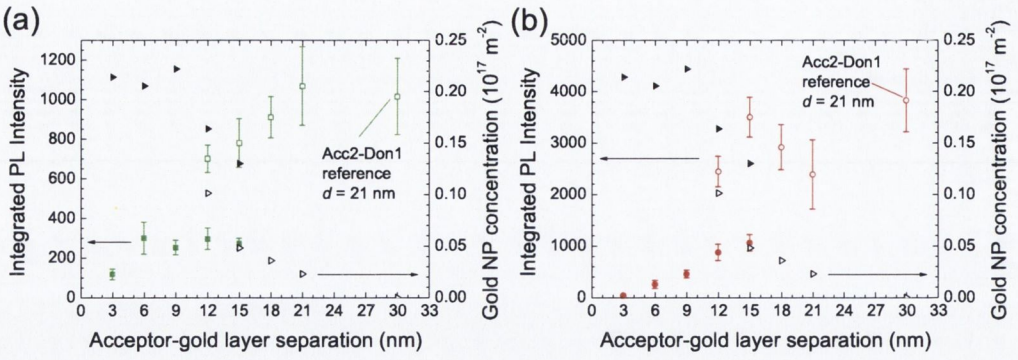


Figure 6.14: (a) Acceptor-gold distance dependence of the integrated donor PL intensity in the Acc2-gold-Don1 sandwich structure (green squares, left-hand axis). Solid and open symbols represent the data recorded for two different sample sets. The value at a separation of 30 nm shows the integrated donor PL intensity of a donor-acceptor bilayer sample with a layer separation of 21 nm. The solid and open black triangles indicate the gold nanoparticle (NP) concentration for each sample (right-hand axis). (b) Dependence of the integrated acceptor PL, of the same samples as shown in (a), on the acceptor-gold separation (solid and open red circles, left-hand axis). The reference value for the donor-acceptor bilayer sample with a layer separation of 21 nm is again indicated at 30 nm and the gold NP concentration is represented by the solid and open triangles (right-hand axis).

decrease of the acceptor emission at the largest acceptor-gold separations investigated. Also, the acceptor emission in the sandwich structure is enhanced over that of the acceptors deposited on a gold NP layer for acceptor-gold separations of 12 nm as shown in Figure 6.9(b). Altogether, the gold acceptor distance dependences of the donor and acceptor PL intensities show clear signatures for energy transfer from the donor to the acceptor QDs via the intermediate gold NP layer.

For FRET between QD layers a decreasing acceptor enhancement with increasing donor-acceptor separation is expected, as discussed in section 5.2 and shown in Figure 5.6(b). The initially increasing acceptor and constant donor emission with increasing gold-acceptor separation clearly show that the distance dependence of the energy transfer process between the donor and acceptor QDs is modified by the gold NPs. The decrease of the acceptor emission and the increase of the donor emission at large separations indicate that the influence of the surface plasmon is reducing. However, the trade off between the acceptor PL quenching in proximity to the gold NPs and the enhancement of the acceptor emission due to surface plasmon mediated energy transfer, result in an absolute acceptor emission quenching for all sandwich structures presented above. This trade off and the observed distance dependence are similar to the trend reported for a direct surface plasmon PL enhancement for QD-metal NP structures

[76, 77]. However, it has to be emphasized again that for the conditions presented here, no direct PL enhancement but only quenching in the presence of the gold NPs has been observed for the donor and acceptor QDs. Therefore, this surface plasmon effect cannot be attributed to an enhanced donor emission or an increased acceptor absorption in the proximity to the gold NPs, but must occur because of interaction of the surface plasmon field with the energy transfer mediated by dipole-interactions.

In Figure 6.15(a) the donor PL decay of the Acc2-gold-Don1 sandwich structure (black line), with $d = 12$ nm, $c_{Au} = 0.164 \times 10^{17}$ m^{-2}, $c_{Don} = 1.10 \times 10^{17}$ m^{-2} and $c_{Acc} = 0.46 \times 10^{17}$ m^{-2}, is shown along with the donor reference decay (green line) recorded for a Don1 monolayer ($c_{Don} = 3.1 \times 10^{17}$ m^{-2}) deposited on a gold NP layer ($c_{Au} = 0.194 \times 10^{17}$ m^{-2}) with a donor-gold separation of 3 nm as in the sandwich structure. As can be seen, the two decays are very similar. However, the close-up in the inset shows that, over the first two nanoseconds, the donor decay in the sandwich structure (black line) is a little faster than the reference decay (green line). This is also reflected in the short lifetime components of 0.45 ns and 0.53 ns determined from the fitting of the donor decays in the sandwich and reference structure respectively. The difference between the decays is however very small. On the longer timescales, the reference decay is faster due to the larger donor and gold concentrations in the Don1-gold sample, which both lead to a lower average donor PL lifetime τ_{onAu} of 1.2 ns, compared to $\tau_{\text{blue}} = 2.9$ ns determined for the sandwich structure.

As the donor and gold concentrations in the reference Don1-gold structure were higher than in the sandwich structure, making the reference decay faster, the impact of the surface plasmon mediated energy transfer on the donor decay should actually be larger than the effect observed. Despite these differences, a lower limit for the FRET rate and efficiency for this Acc2-gold-Don1 sample can be estimated from the lifetime values determined for these decays. The FRET rate can be calculated as $k_{\text{FRET}} = 1/\tau_{\text{blue}}^{\text{short}} - 1/\tau_{\text{onAu}}^{\text{short}}$ with the short lifetime components $\tau_{\text{blue}}^{\text{short}}$ and $\tau_{\text{onAu}}^{\text{short}}$ in the sandwich and reference sample respectively. The FRET rate for this structure is $(3.0\text{ ns})^{-1}$ and from the ratio of the short lifetime components a FRET efficiency of 15% was determined. From FRET theory a FRET rate of $(2774\text{ ns})^{-1}$ is expected for $= 22.1$ nm, $R_0 = 3.9$ nm and $c_{Acc} = 0.42 \times 10^{17}$ m^{-2}. To highlight the small impact of energy transfer with a FRET rate of $(3.0\text{ ns})^{-1}$ on the average donor lifetime, the average donor lifetime for a sandwich structure is calculated based on the donor lifetime $\tau_D = 2.8$ ns measured for a Don1 monolayer and $\tau_{\text{onAu}} = 1.2$ ns for the Don1-gold structure (corresponding to a transfer rate to the gold NPs of $(1/1.2\text{ ns} - 1/2.8\text{ ns}) = (2.1\text{ ns})^{-1}$). The expected lifetime is the inverse sum of all donor recombination rates and the estimated value in this case is $(1/2.8\text{ ns} + 1/2.1\text{ ns} + 1/3.0\text{ ns})^{-1} = 0.86$ ns. Compared to the average lifetime of the Don1-gold structure of 1.2 ns, the expected lifetime of 0.86 ns is only a

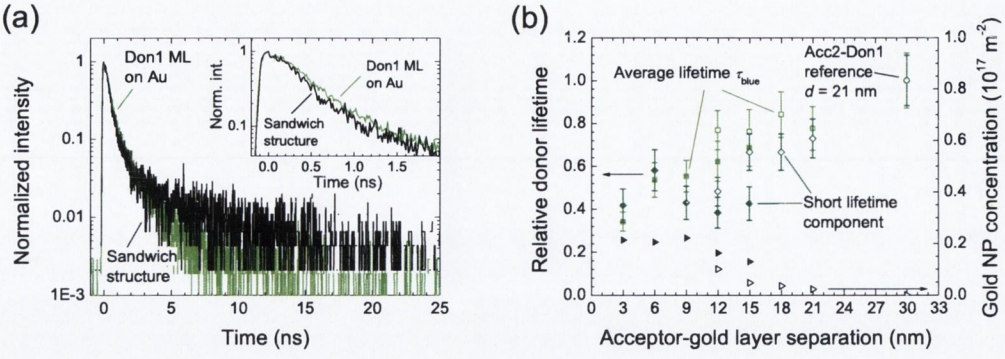


Figure 6.15: (a) Donor PL decays for an Acc2-gold-Don1 sandwich structure with $d = 12$ nm (black line) and a Don1 monolayer (ML) on gold (green line) for gold-donor separations of 3 nm. The inset shows a close-up of the two decays over the first 2 ns. (b) Acceptor-gold separation dependence of the relative donor lifetime of the average lifetime τ_{blue} (light green squares) and the short lifetime component (dark green diamonds) determined for donor decays of the Acc2-gold-Don1 sandwich structures with respect to the PL lifetimes measured for Don1 monolayers at the same donor concentration. The reference values for an Acc2-Don1 bilayer structure with a layer separation of 21 nm are included at $d = 30$ nm. The solid and open symbols represent values determined for two different sample sets. The gold nanoparticle (NP) concentration (black triangles) can be read off the right-hand axis.

little smaller and lies within the error range. However, this lifetime decrease corresponds to a FRET efficiency of $1 - 0.86$ ns$/1.2$ ns $= 28\%$ which can lead to a quite significant acceptor enhancement despite not being "visible" in the donor decay. This shows, that a careful comparison of the donor decays with the right reference decays for the same donor and gold concentrations has to be carried out in order to observe the signatures of the surface plasmon mediated energy transfer in the donor decays.

For the comparison of the donor lifetimes in dependence of the acceptor-gold separation, the relative values of the average lifetime as well as the short lifetime component were calculated with respect to the lifetimes in Don1 monolayers at the same concentration (obtained from the lifetime fit discussed in section 4.1.2). As can be seen in Figure 6.15(b), the average lifetime (solid and open light green squares) is first increasing with increasing accptor-gold separation and reaching a constant value of approximately 0.8 at the largest separations investigated. As indicated by the comparison of the donor decays shown in (a), the average lifetime is mostly dominated by the quenching by the gold NPs, and the average donor lifetime is therefore increasing with d as the gold concentration (solid and open black triangles, right-hand axis) is decreasing. The donor lifetime at $d = 21$ nm is still lower than the reference value measured for a Don1-

Acc2 bilayer structure with a layer separation of 21 nm, indicated at $d = 30$ nm, but is similar to the relative lifetime value of 0.9 expected for a Don1-gold structure with $c_{Au} = 0.03 \times 10^{17}$ m^{-2}.

As seen in the comparison of the donor PL decays, it is more important to consider the short lifetime component than the average lifetime to investigate the effect of surface plasmon mediated energy transfer on the donor PL decay. The relative values of the short lifetime components are therefore also shown in Figure 6.15(b) (open and solid dark green diamonds). For the Don1 monolayer on gold, the same trends of the average lifetime and the short lifetime component in dependence of the gold NP concentration were observed, as shown in Figure 6.4(b), with larger relative lifetimes determined for the short lifetime component than for the average lifetime. For the sandwich structure, however, a large discrepancy between the two relative lifetime trends is found for $d = 12$ and 15 nm. Furthermore, the relative short lifetime component is clearly lower than the relative average lifetime for acceptor-gold separations of 9 to 18 nm. This is a strong indication that at these acceptor-gold separations the fastest energy transfer rates occur. The FRET rate must be lower for small d as the short lifetime component shows similar values as the relative average lifetime, even though the donor-gold separation and the gold NP concentration are the same as for $d = 9$ nm. For $d = 21$ nm, the relative short lifetime is again showing a value similar to that of the relative average lifetime, indicating that the impact of surface plasmon mediated energy transfer on the donor decay is reduced corresponding to a decreased FRET rate and efficiency.

In Figure 6.16(a) the acceptor PL decay for an Acc2-gold-Don1 sandwich structure ($d = 12$ nm, $c_{Au} = 0.164 \times 10^{17}$ m^{-2}, $c_{Don} = 1.10 \times 10^{17}$ m^{-2} and $c_{Acc} = 0.46 \times 10^{17}$ m^{-2}) is shown along with the acceptor PL decays for a Don1-Acc2 bilayer structure (layer separation 21 nm and $c_{Acc} = 0.42 \times 10^{17}$ m^{-2}) and an Acc2 monolayer on gold ($d = 12$ nm, $c_{Au} = 0.155 \times 10^{17}$ m^{-2} and $c_{Acc} = 2.3 \times 10^{17}$ m^{-2}). Due to the quenching of the acceptor emission by the gold NPs, the acceptor decay of the acceptors on gold (dark red line) with an average lifetime $\tau_{\text{onAu}} = 8.1$ ns is faster than that of the acceptor monolayer on quartz (orange line), characterized by an average lifetime of $\tau_A = 11.0$ ns. The acceptor decay in the sandwich structure (black line), with an average lifetime $\tau_{\text{red}} = 16.9$ ns, is longer than that in the Acc2-gold structure. The longer lifetime of the acceptor PL emission in the sandwich structure is mostly attributed to the lifetime change due to the covering of the acceptor monolayer with polyelectrolyte, as seen for the longer acceptor PL decay with a lifetime $\tau_{AD} = 24.1$ ns in the Don1-Acc2 bilayer structure (red line) with respect to the acceptor monolayer. The increased acceptor lifetime in the reference bilayer, with a layer separation of 21 nm, is not due to energy transfer but arises most likely from an increased stabilization of the QDs by covering them with polyelectrolyte [160, 161]. Therefore, the right reference decay to compare to

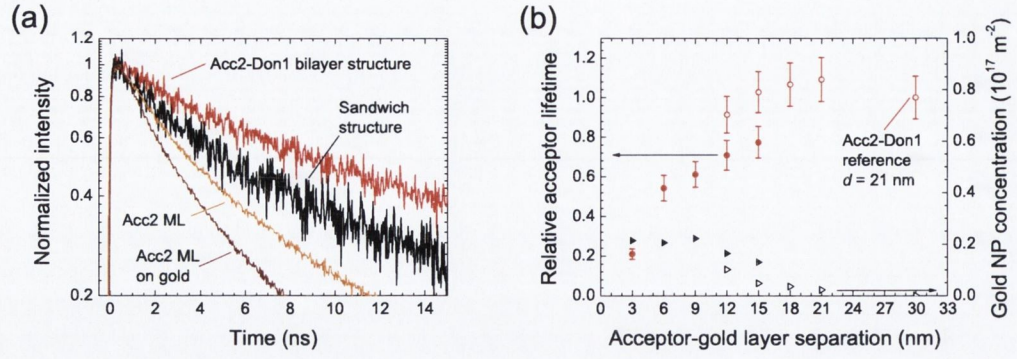


Figure 6.16: (a) Acceptor PL decays for the Acc2-gold-Don1 sandwich structure (black line) and an Acc2 monolayer (ML) on gold (dark red line) for acceptor gold separations of 12 nm. The acceptor reference decay for a Don1-Acc2 bilayer structure with a layer separation of 21 nm (red line) and an Acc2 monolayer on quartz (orange line) are also shown. (b) Dependence of the relative acceptor lifetime τ_{red} (red circles, left-hand axis) on the Acc2-gold separation. The reference values for the relative acceptor lifetime of the Acc2-Don1 bilayer structure with a layer separation of 21 nm is included at $d = 30$ nm. The solid and open symbols represent values determined for two different sample sets. The gold nanoparticle (NP) concentrations (black triangles) are indicated on the right-hand axis.

is the one of the bilayer structure. Due to the large gold concentration and consequently a strong PL quenching, the lifetime in the sandwich structure is reduced compared to that observed for the Don1-Acc2 structure without gold NPs. Furthermore, no change in the rise-time for any of the decays is apparent in the time-resolved PL measurements.

As can be seen in Figure 6.16b, the relative acceptor lifetime (solid and open red circles) is increasing with increasing acceptor-gold layer separation. This trend is partially due to the increasing separation between the Acc2 QDs and the gold NPs and the decreasing gold concentration (black triangles, right-hand axis). The relative acceptor lifetime is also influenced by the energy transfer from the donor QDs as values greater than one were determined for $d = 15$ nm and larger, signifying that the acceptor lifetime in the sandwich structure becomes larger than the reference lifetime in the Don1-Acc2 structure with a layer separation of 21 nm, indicated at $d = 30$ nm. This shows that the additional pumping of the acceptors by the donor QDs via energy transfer is overcoming the acceptor PL quenching by the gold NPs at the large separations. However, the increasing trend of the acceptor PL lifetime also slows down at these separations, indicating that the energy transfer becomes weaker.

The modelling of the donor lifetime in dependence of the donor and gold concentration as well as the donor-gold separation is currently in progress to enable the calculation of the FRET rates and efficiencies from the donor lifetimes measured in the sandwich

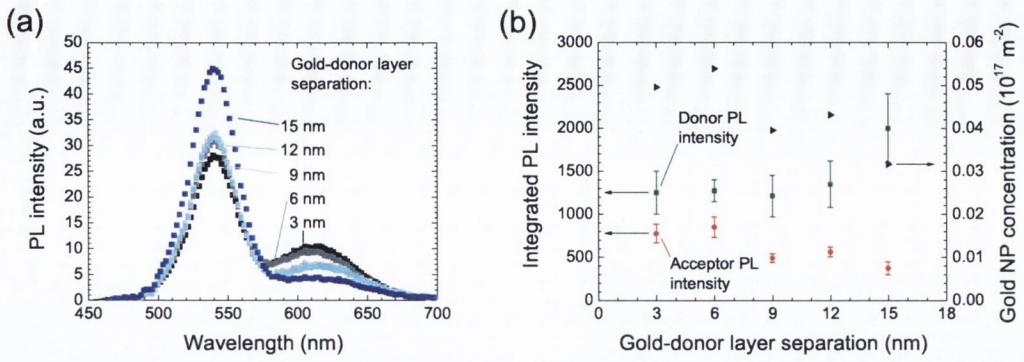


Figure 6.17: (a) PL spectra of Acc2-gold-Don6 sandwich structures for different gold-donor layer separations. The acceptor-gold separation is 12 nm and the gold nanoparticle (NP) concentration $c_{Au} = (0.043 \pm 0.011) \times 10^{17}$ m^{-2}. (b) Gold-donor distance dependence of the integrated donor (green squares) and acceptor (red circles) PL intensities for donor and acceptor concentrations adjusted to 1.0×10^{17} m^{-2} (left-hand axis). The gold NP concentration of each sample is also indicated in the graph (black triangles, right-hand axis).

structure at each acceptor-gold separation investigated. This will shed further light on the distance dependence of the surface plasmon modified FRET between donor and acceptor QDs in the sandwich structure.

6.2.3 Gold-Donor Distance Dependence

The PL and lifetime analysis presented in the previous section indicates that the maximum enhancement of FRET in proximity to the 4 nm gold NPs occurs at acceptor-gold separations of 12 to 15 nm. Therefore, the gold-donor distance dependence was carried out for structures with a acceptor-gold separation of 12 nm. The sample set presented below was prepared with Don6 QDs. The gold-donor distance dependence was also measured for Acc2-gold-Don1 structures and similar effects were observed, but as very low acceptor and gold NP concentrations for sandwich structures with Don1 QDs didn't allow for an accurate determination of c_{Acc} and c_{Au} the measurements for the samples with Don6 QDs are presented instead.

In Figure 6.17 the PL spectra of Acc2-gold-Don6 structures with gold-donor layer separations increasing from 3 to 15 nm are shown for gold concentrations of $c_{Au} = (0.043 \pm 0.011) \times 10^{17}$ m^{-2}. The donor and acceptor concentrations were $c_{Don} = (1.09 \pm 0.09) \times 10^{17}$ m^{-2} and $c_{Acc} = (0.94 \pm 0.14) \times 10^{17}$ m^{-2} respectively. As can be seen the donor intensity is not changing a lot for separations of 3 to 12 nm and then increases for a separation of 15 nm. In contrast, the acceptor intensity shows a strong decreasing trend with increasing gold-donor separation.

The integrated donor (green squares) and acceptor (red circles) intensities in dependence of the gold-donor layer separation can be seen in Figure 6.17(b) (left-hand axis). The intensities are shown for concentrations of 1.0×10^{17} m^{-2} for the donor and acceptor emission. Additionally, the gold concentration of the samples is also included in the Figure (black triangles, right-hand axis). As seen in the PL spectra, the donor intensity is not changing for layer separations of 3 to 9 nm. For a 12 nm gold-donor separation the intensity is a little increased, however still within error of the other intensity values, and at 15 nm it is clearly higher than for the smaller separations. However, as the gold concentration is decreasing a little with increasing gold-donor separation, the donor PL increase is probably not as strong as indicated by the data.

On the other hand, the acceptor emission is highest at low gold-donor separations and decreases for gold-donor separations of 9 nm and larger. It is important to note that the acceptor PL intensity is decreasing with increasing gold-donor separation, even though the acceptor-gold separation is 12 nm for all samples and the gold concentration is decreasing. In contrast, the acceptor emission is increasing with decreasing gold concentration in acceptor-gold structures without donor QDs for a constant acceptor-gold separation (shown in Figure 6.7(a) and (b)). This clearly shows that the acceptor emission is strongly influenced by the gold-donor separation. The maximum acceptor enhancement due to surface plasmon mediated energy transfer occurs for smaller gold-donor separations than acceptor-gold layer separations. This suggests that the distance between gold NPs and donor QDs is influencing the probability for energy transfer more strongly than the acceptor-gold separation.

For a more detailed investigation of the gold-donor distance dependence of the surface plasmon mediated FRET process, the relative lifetimes of the donor and acceptor PL decays have been investigated. In Figure 6.18(a), the relative donor lifetime calculated for the short lifetime component in the sandwich structure (solid squares, left-hand axis), with respect to that of a Don6 monolayer with the same donor concentration, can be seen in dependence of the gold-donor layer separation. For comparison the distance dependence of the relative value of the short lifetime component for a Don6 monolayer on gold is also shown (open squares). The gold NP concentration of the two sample sets were very similar and the values of c_{Au} for the respective sandwich (solid triangles) and Don6-gold structures (open triangles) are also indicated in the Figure (right-hand axis). The short donor lifetime component in the sandwich structure is always lower than that for the Don6-gold structure. Furthermore, both values are increasing with increasing gold-donor layer separation, however, the lifetime in the sandwich structure is increasing less strongly. This would indicate that there is still quite a significant probability for energy transfer even at a gold-donor layer separation of 15 nm and that the energy transfer rate is increasing with increasing gold-donor separation in contrast

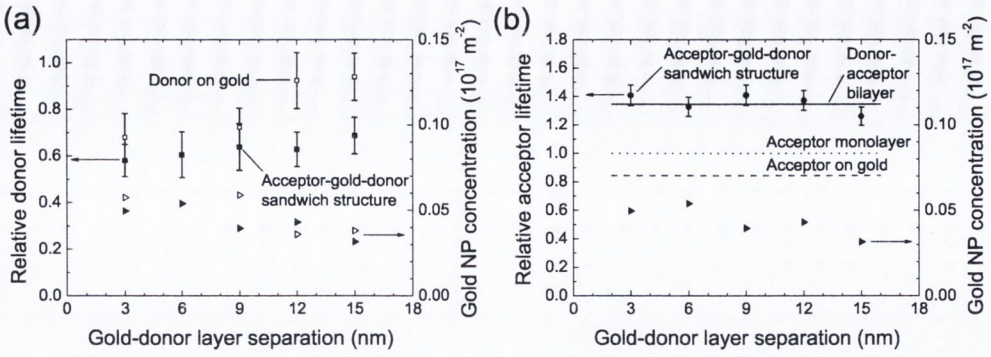


Figure 6.18: (a) Gold-donor distance dependence of the relative short lifetime component of the donor PL decays for the Acc2-gold-Don6 sandwich structure (solid squares) and Don6 monolayers on gold (open squares) (both left-hand axis). The gold nanoparticle (NP) concentrations of the sandwich structure (solid triangles) and of the Don6-gold structures (open triangles) are also shown (right-hand axis). (b) Dependence of the relative average acceptor lifetime on the gold-donor separation in the Acc2-gold-Don6 structures (solid circles, left-hand axis). For comparison the average acceptor lifetimes of an Acc2 monolayer (dotted line), an Acc2 monolayer on gold (dashed line) and an Acc2-Don6 bilayer structure with a layer separation of 21 nm (solid line) are also included. The gold NP concentration of the sandwich structures is also indicated (solid triangles, right-hand axis).

to conclusions drawn from the donor and acceptor PL data. For the verification of this trend, a more detailed analysis of the concentration dependence of the Don6 PL lifetime and the interaction with gold NPs is currently been carried out.

The dependence of the relative acceptor PL lifetime on the gold-donor separation in the sandwich structure (solid circles), calculated with respect to the lifetime of an acceptor monolayer (dotted line), is shown in Figure 6.18(b). It should be noted that the relative acceptor lifetime in an Acc2-Don6 structure with a layer separation of 21 nm, is 1.35 (solid line). This increase of the acceptor lifetime in the Acc2-Don6 bilayer structure, compared to an Acc2 monolayer with the same acceptor QD concentration, is due to the covering of the acceptor QDs with polyelectrolyte as outlined above. Therefore, the acceptor lifetime in the sandwich structure is not increased over that in the Acc2-Don6 bilayer sample without gold. It is similar to this value for small gold-donor layer separations and a little lower at 15 nm. Moreover, a decrease of approximately 15% is observed for the acceptor lifetime in proximity to gold NPs (dashed line) for the acceptor on gold (d = 12 nm, $c_{Au} = 0.052 \times 10^{17}$ m^{-2}) with respect to the acceptor monolayer. Assuming that a similar decrease in lifetime occurs in an inverse structure where the gold NPs are deposited on top of the acceptor QDs, this would mean that due to energy transfer from the donor QDs in the sandwich structure the quenching

effect of the gold NPs on the acceptor PL lifetime is overcome and the effect only starts to cease at the highest separations investigated. Taking into account that the gold concentration (solid triangles, right-hand axis) is lower at the larger gold-donor separations, which should actually result in larger acceptor lifetimes than at lower gold-donor separations, this is a clear indication that the energy transfer from the donor QDs is decreaed.

The strongest effect of surface plasmon mediated energy transfer on the acceptor emission properties is observed at the smaller gold-donor separations investigated and in particular the acceptor emission is largest for gold-donor separation of 3 and 6 nm. Therefore, the study of the dependence of the energy transfer on the gold concentration, presented in the next section, will be investigated in sandwich structures with an acceptor-gold separation of 12 nm and a gold-donor separation of 3 nm.

6.2.4 Gold Concentration Dependence

As has been observed for the two sample sets discussed for the acceptor-gold distance dependence of the surface plasmon mediated energy transfer, the gold NP concentration as an important influence on the intensity levels of the acceptor and donor emission. To find out how the surface plasmon mediated energy transfer depends on the gold NP concentration, Acc2-gold-Don1 sandwich structures with different gold concentrations were prepared for an acceptor-gold separation of 12 nm and a gold-donor separation of 3 nm. This corresponds to a minimum acceptor-donor centre-to-centre separation of approximately 22.1 nm, taking into account the thicknesses of the polyelectrolyte spacers separating the QD and gold NP layers as well as the QD radii and the diameter of the gold NPs.

The spectra of four sandwich structures with gold concentrations of 0.026, 0.063, 0.086 and 0.092×10^{17} m^{-2} are shown in Figure 6.19(a), along with a reference spectrum of an Acc2-Don1 bilayer structure with a layer separation of 21 nm. The donor and acceptor QD concentrations in the structures varied around $c_{Don} = (2.1 \pm 0.3) \times 10^{17}$ m^{-2} and $c_{Acc} = (0.68 \pm 0.09) \times 10^{17}$ m^{-2}.

At an acceptor-donor layer separation of 21 nm no energy transfer via the FRET mechanism is observed in absence of gold NPs, as discussed above. However, when gold NPs are introduced between the acceptor and donor QD layers, an increased acceptor emission and a decreased donor emission can be seen for the lowest gold concentration investigated (blue line). The donor quenching could be attributed to the direct interaction with the gold NPs, but no acceptor enhancement is expected in proximity to the gold NPs, as shown in section 6.1.2. Therefore, this acceptor emission increase is attributed to energy transfer from the donor QDs, which shows that the distance over which energy can be transferred from donor to acceptor QDs is increased due to the

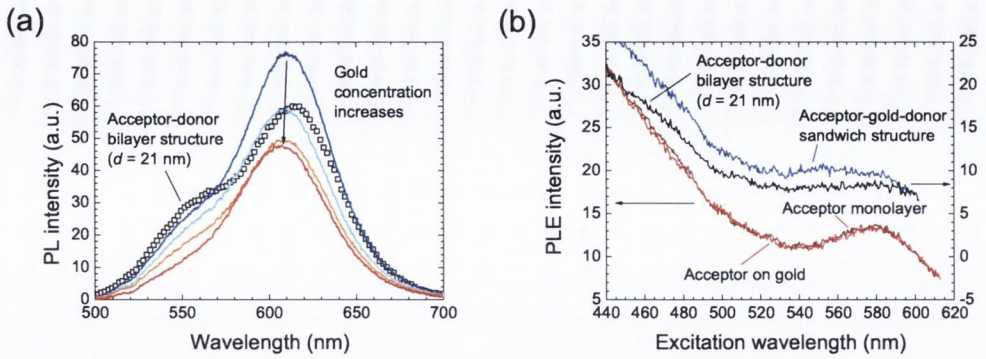


Figure 6.19: (a) PL spectra of Acc2-gold-Don1 sandwich structures with varying gold nanoparticle (NP) concentrations (lines), for an acceptor-gold separation of 12 nm and a gold-donor separation of 3 nm, as well as the reference spectrum of a Acc2-Don1 bilayer structure with layer separation $d = 21$ nm (open black squares). (b) Acceptor PLE spectra of the Acc2-gold-Don1 sandwich structure with the lowest gold concentration ($c_{Au} = 0.026 \times 10^{17}$ m^{-2}) (blue line), the Acc2-Don1 reference structure ($d = 21$ nm) (black line) (both right-hand axis) as well as of an Acc2 monolayer on quartz (dark red line) and on gold ($d = 12$ nm, $c_{Au} = 0.023 \times 10^{17}$ m^{-2}) (red line) (both left-hand axis).

presence of the gold NPs. With increasing gold NP concentration, the acceptor as well as the donor emission decrease.

Before, analysing the donor and acceptor PL trends in more detail, the acceptor PLE spectrum recorded for the sandwich structure with the lowest gold NP concentration $c_{Au} = 0.026 \times 10^{17}$ m^{-2} (blue line), presented in Figure 6.19(b), is compared to acceptor PLE spectra of an Acc2-Don1 bilayer with $d = 21$ nm (black line) as well as Acc2 monolayers on quartz (dark red line) and gold (red line). The PLE spectra were adjusted to show the emission intensity for $c_{Acc} = 0.5 \times 10^{17}$ m^{-2}. Due to the low gold NP concentration $c_{Au} = 0.023 \times 10^{17}$ m^{-2}, no quenching of the emission intensity for the acceptor monolayer on gold with a layer separation of 12 nm (red line) is observed in comparison to the PLE spectrum of the acceptor monolayer (dark red line). Also the shape of the spectra is the same, with the distinct increase in emission for excitation wavelengths in resonance with the first acceptor absorption peak. In contrast to this similarity, the acceptor PLE spectrum of the Acc2-gold-Don1 sandwich structure (blue line) shows a higher intensity than that recorded for the Acc2-Don1 bilayer without gold (black line). The spectra show a similar trend for excitation wavelengths up to 530 nm. For higher wavelengths, in the range of 530 to 590 nm, an increased emission is observed for the Acc2-gold-Don1 sandwich structure while the PLE spectrum of the bilayer structure without gold stays more or less flat. This additional intensity increase in the sandwich structure occurs in the region of the strongest overlap of the donor

emission with the surface plasmon absorption feature and is therefore a signature for energy transfer from the donor QDs via the gold NPs. The difference in the PLE spectra of the Acc2-Don1 structures with and without gold NPs confirm again that for such large acceptor-donor separations there is no "regular" energy transfer in structures without gold NPs, but that surface plasmons can increase the range of FRET to QD centre-to-centre distances of at least 22 nm.

First evidence of a gold NP concentration dependence of surface plasmon mediated energy transfer in the sandwich structures is found in the analysis of the spectrally integrated donor and acceptor emission intensities, shown as a function of the gold NP concentration in Figures 6.20(a) and (b) respectively (solid symbols). For comparison the gold NP concentration dependences of donor or acceptor monolayers on gold (open symbols) as well as their fits with FRET theory (dashed line) are also presented in (a) and (b) respectively, and have also been discussed in Figures 6.3(b) and 6.7(b). The PL intensities are presented as a relative PL ratio, calculated by dividing the integrated PL intensities in dependence of the gold NP concentration by the value determined for the respective structure without gold NPs.

As can be seen in Figure 6.20(a), at the lowest gold concentration investigated the donor emission in the sandwich structure (solid squares) is only reduced a little more than expected from the fit with theory for the PL ratio in the donor-gold reference structure (open squares). With increasing gold NP concentration the donor PL ratio for the sandwich structures is decreasing and shows a more strongly quenched emission in the sandwich structure than for the donor monolayer on gold, indicating that more energy is transferred for larger gold NP concentrations.

In Figure 6.20(b), one can see that, after correction for concentration differences, an absolute acceptor emission enhancement of approximately 19% and 14%, with respect to the Acc2-Don1 structure without gold NPs, is observed for the sandwich structures (solid circles) with the two lowest gold NP concentrations. For larger c_{Au}, the PL ratio reduces to below one and approaches the value of the emission quenching measured for acceptor monolayers on gold (open circles). This suggests that, under the conditions presented here, the PL quenching of the acceptor emission dominates over the enhancement by energy transfer from the donor QDs at gold NP concentrations larger than approximately 0.09×10^{17} m^{-2}. Furthermore, it can be noted that the donor and acceptor PL ratios show opposite trends with respect to the QD-gold reference samples, with the donor PL being further decreased while the acceptor PL is increased.

These mirrored trends are another signature of energy transfer from the donors to the acceptors via the gold NPs, despite the large donor-acceptor separation. In Figure 6.21(a) the acceptor enhancement in the sandwich structure (solid squares) is shown as a function of the gold NP concentration. The acceptor enhancement was calculated

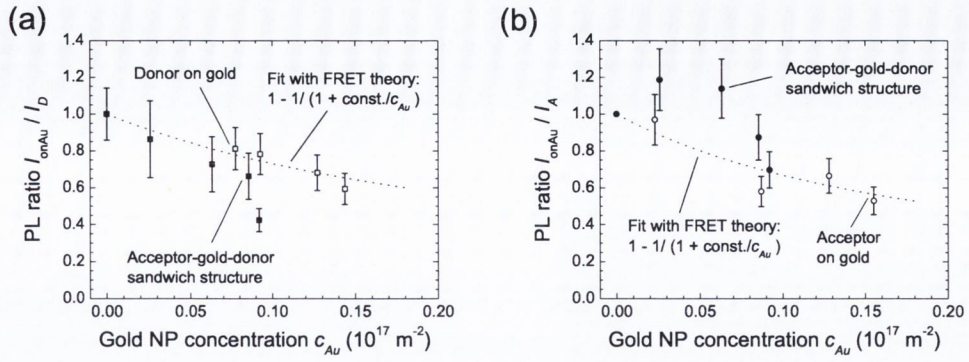


Figure 6.20: Integrated donor PL intensities shown as the ratio of intensities of sandwich and QD-gold layer structures with respect to the corresponding structures without gold. (a) Gold nanoparticle (NP) concentration dependence of the donor emission in the sandwich structure (solid squares) and for donor-gold structures (open squares). The dashed line is a fit of the gold NP concentration dependence of the donor emission in a donor monolayer on gold with FRET theory. (b) Integrated acceptor PL ratios for the Acc2-gold-Don1 sandwich structure (solid circles) and Acc2 monolayers on gold (open circles) in dependence of the gold NP concentration. The dashed line is a fit of the gold NP concentration dependence of the acceptor emission in proximity to gold NPs with FRET theory.

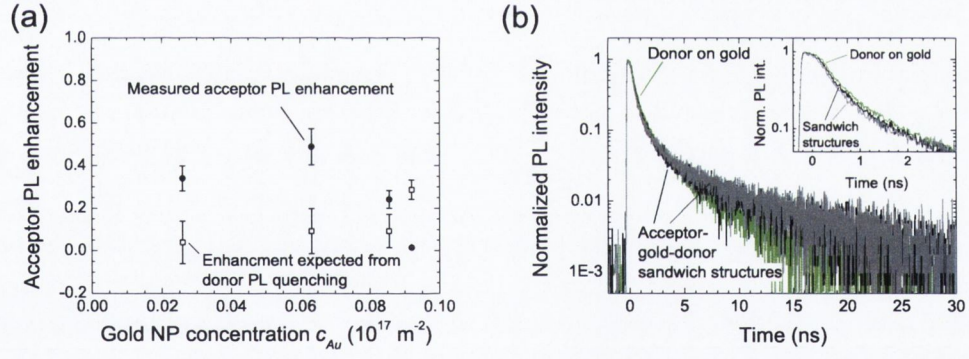


Figure 6.21: (a) Gold nanoparticle (NP) concentration dependence of the acceptor PL enhancement calculated from the acceptor emission in the sandwich structure with respect to that of acceptor-gold reference structures at the same gold NP concentration (solid circles). For comparison the acceptor enhancement expected from the donor PL quenching is also included (open squares). (b) Donor PL decays for a Don1 QD monolayer on gold ($d = 3$ nm, $c_{Au} = 0.093 \times 10^{17}$ m^{-2}) (green line) and for two Acc2-gold-Don1 sandwich structures with $c_{Au} = 0.086 \times 10^{17}$ m^{-2} (black line) and $c_{Au} = 0.092 \times 10^{17}$ m^{-2} (grey line) respectively. The donor concentrations of the three samples were $(2.1 \pm 0.3) \times 10^{17}$ m^{-2}. A close-up of the first three nanoseconds of the three donor PL decays is shown in the inset.

with respect to the acceptor emission in the acceptor-gold reference structures, with the emission at the respective gold concentrations taken from the fit shown in Figure 6.20(b). Even though the largest absolute acceptor PL emission increase of 19%, compared to the Acc2-Don1 bilayer, was observed at the lowest gold concentration investigated, the largest acceptor enhancement of 49% is achieved at the second lowest gold NP concentration of $c_{Au} = 0.063 \times 10^{17}$ m^{-2}. At the lowest gold NP concentration the acceptor enhancement is only 34%. For larger c_{Au} the enhancement is decreasing quickly. This shows, that even though at low gold concentrations the FRET enhancement is not at its maximum, a higher emission can be achieved, due to the lower quenching by the gold NPs, than at a gold concentration where a stronger enhancement by surface plamson mediated FRET is observed, but the quenching by the gold NPs is larger.

For comparison, the acceptor enhancement expected from the donor PL quenching (open squares), calculated by multiplication with the donor:acceptor absorption ratio at the excitation wavelength, is also included in Figure 6.21(a). A much lower acceptor enhancement is predicted by this calculation than that determined directly from the acceptor PL emission (solid circles). This underestimation of the acceptor enhancement has already been observed for QD FRET structures without gold NPs, discussed in the two previous chapters, and could be due to the recycling effect. The recycling effect represents the possibility of energy transfer from excitons trapped in donor defect states that do not contribute to the donor emission and are therefore not accounted for in the calculation of the acceptor enhancement via the donor PL quenching. Furthermore, the donor PL quenching is not decreasing for large gold NP concentrations as the measured acceptor PL enhancement does. This discrepancy might arise from slightly higher levels of quenching for the acceptor QD emission in the presence of the gold NPs than for the donor QDs. It highlights again, that there is a trade off between the direct interaction of the gold NPs - that only introduces a PL quenching for the materials, concentrations and separations investigated here - and the surface plasmon mediated energy transfer from donor to acceptor QDs. Therefore, it is very important to investigate and understand the QD - metal NP interactions in detail to enable the analysis of the impact of the different QD and structural properties, such as the layer separations and nanoparticle concentrations, on the modification of the energy transfer by surface plasmons.

For a confirmation of the trends observed for the donor and acceptor PL properties as a function of the gold NP concentration and attributed to surface plasmon mediated energy transfer, the time-resolved PL decays of the sandwich structures are analysed in the following. Donor PL decays for Acc2-gold-Don1 sandwich structures with $c_{Au} = 0.086 \times 10^{17}$ m^{-2} (black line) and $c_{Au} = 0.092 \times 10^{17}$ m^{-2} (grey line) are shown in Figure 6.21(b), with donor concentrations of $c_{Don} = 1.8 \times 10^{17}$ m^{-2} and $c_{Don} = 2.0 \times 10^{17}$ m^{-2} respectively. A donor reference decay (green line) for a Don1 monolayer

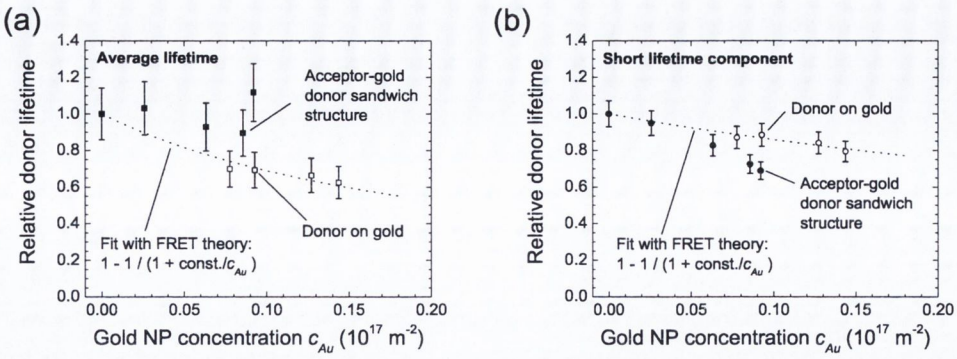


Figure 6.22: (a) Gold nanoparticle (NP) concentration dependence of the relative average donor lifetime determined for Acc2-gold-Don1 sandwich structures (solid squares) and Don1-gold structures (open squares). The dashed line represents the fit of the gold NP concentration dependence of the average lifetime for Don1 monolayers on gold by FRET theory. (b) Gold NP concentration dependence of the relative short lifetime component for the sandwich structures (solid circles) as well as the Don1 monolayers on gold (open circles). The fit of the short donor lifetime component in the Don1-gold structure is shown as a dashed line.

with a concentration of $c_{Don} = 2.4 \times 10^{17}$ m^{-2} separated by a 3 nm polyelectrolyte layer from a gold NP layer with $c_{Au} = 0.093 \times 10^{17}$ m^{-2} is also shown. As for the donor decays shown in Figure 6.15(a), the donor decays recorded for the Don1-gold structure as well as the two sandwich structures look very similar. However, in the close-up of the first three nanoseconds of the donor decays, shown in the inset, one can clearly see that the initial decay rates are a little faster for the donors in the sandwich structures than in the donor-gold reference sample.

For a more detailed comparison of the donor PL decay dynamics the relative average lifetime as well as the relative short lifetime component of the donor decays are shown as a function of the gold NP concentration in Figures 6.22(a) and (b) respectively. The relative lifetimes were calculated for the donor decays in the sandwich structures (solid symbols) as well as for donor monolayers on gold (open symbols) by dividing with donor monolayer lifetime values at the corresponding donor concentration. The relative lifetimes of the Don1 monolayers on gold as well as the fit of their gold NP concentration dependence with FRET theory (dahsed line) are the same as shown in Figure 6.4(b). The relative average lifetimes determined for the sandwich structure (solid squares), shown in Figure 6.22(a), are all larger than those for the donor monolayers on gold (open squares).

However, considering the short lifetime component shown in Figure 6.22(b), the donor lifetimes in the sandwich structure (solid circles) are all shorter than those predicted by

a fit with FRET theory (dashed line) for the short lifetime components determined from the decays measured for Don1-gold structures (open circles). This shows again, that the influence of the energy transfer on the donor PL decays of the Acc2-gold-Don1 sandwich structures is small and only has a significant impact on the short lifetime component. Furthermore, the short lifetime component determined for the sandwich structures is decreasing more strongly with increasing gold NP concentration than that of the Don1-gold reference structures. This indicates that the FRET rate and efficiency are increasing with increasing concentration over the concentration range investigated here, in line with the trend observed for the donor PL quenching. The FRET rate, calculated with the short lifetime components, increases from $(45\ \text{ns})^{-1}$ to $(2\ \text{ns})^{-1}$ corresponding to an increase in the FRET efficiency of 1% to 21%. The estimated FRET efficiencies are in good agreement with the values of the PL quenching determined for the donor emission.

The acceptor decays for the sandwich structures with $c_{Au} = 0.086 \times 10^{17}\ \text{m}^{-2}$ (black line) and $c_{Au} = 0.092 \times 10^{17}\ \text{m}^{-2}$ (grey line), shown in Figure 6.23(a), are almost the same. Furthermore, they are both much longer than the PL decay recorded for an Acc2 monolayer on gold (red line), for the same acceptor-gold separation of 12 nm and a gold NP concentration of $c_{Au} = 0.086 \times 10^{17}\ \text{m}^{-2}$. This large difference is mainly caused by the difference in the geometry of the structures. In the sandwich structure, the acceptor monolayer is covered with many polyelectrolyte layers which leads to an increase of the lifetime as mentioned above, whereas in the acceptor-gold reference structure the acceptor QD layer is the top most layer and is therefore not covered by any material.

Therefore, it is better to compare the average acceptor lifetimes determined for the PL decays in the structures including gold NPs with respect to reference samples with the same layer structure but without gold NPs. The dependence of these relative acceptor lifetimes on the gold NP concentration for the Acc2-gold-Don1 structures (solid circles) as well as for the Acc2-gold reference structures (open circles) are shown in Figure 6.23(b). Additionally, the fit of the concentration dependence of the relative acceptor lifetime in the Acc2-gold reference structures with FRET theory is included as a dashed line. The acceptor lifetime values of the Acc2-gold structures and the fit have also been presented in Figure 6.8(b).

As one can see, the relative acceptor lifetime in the sandwich structure is larger than one for the two lowest gold NP concentrations investigated. This means that the acceptor lifetime in the sandwich structure is longer than that of the Acc2-Don1 reference bilayer, which is in line with the absolute acceptor emission enhancement determined for the PL spectra. With increasing gold NP concentration, the relative acceptor lifetime decreases to values below one. However, even though the relative acceptor lifetime in the sandwich structure is decreasing more strongly with increasing gold concentration

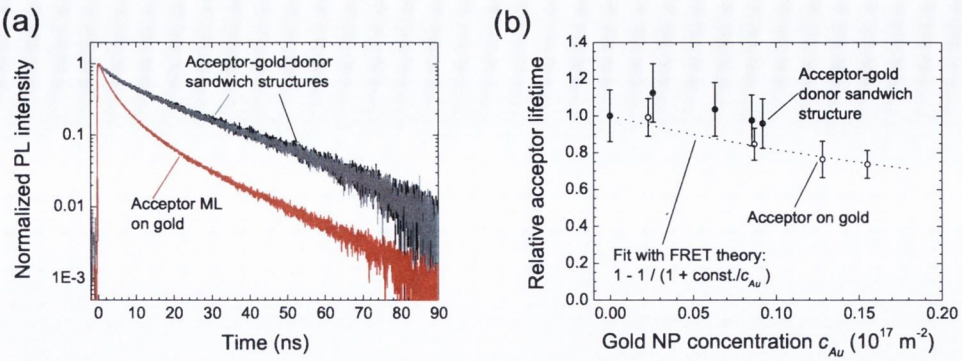


Figure 6.23: (a) Acceptor decays of Acc2-gold-Don1 sandwich structures for $c_{Au} = 0.086 \times 10^{17}$ m^{-2} (black line) and 0.092×10^{17} m^{-2} (grey line) as well as an Acc2 monolayer on gold with $c_{Au} = 0.086 \times 10^{17}$ m^{-2} (red line). The acceptor-gold separation was 12 nm for all structures and the acceptor concentration was $c_{Acc} = (0.67 \pm 0.04) \times 10^{17}$ m^{-2} in the sandwich structures and $c_{Acc} = 1.3 \times 10^{17}$ m^{-2} for the Acc2-gold structure. (b) Gold nanoparticle (NP) concentration dependence of the relative average acceptor lifetime determined for Acc2-gold-Don1 sandwich structures (solid circles) and Acc2-gold structures (open circles). The dashed line is the fit of the gold NP concentration dependence of the average lifetime for the Acc2-gold structures with FRET theory.

than in the Acc2-gold structure, it is still 15% larger than the value for the acceptor monolayer on gold at $c_{Au} = 0.092 \times 10^{17}$ m^{-2}. In contrast, the PL ratio showed a similar value for the sandwich and the acceptor-gold reference structure at this concentrations. The higher value of the relative acceptor lifetimes in the sandwich structure in comparison to those determined for the Acc2-gold reference structure at high gold NP concentrations, can be interpreted as a signature of the energy transfer from the donor QDs via the gold NPs. As has been found in the analysis of the donor PL quenching and decrease of the short donor lifetime component, the surface plasmon mediated energy transfer seems strongest at the high gold NP concentrations. However, due to the strong acceptor PL quenching an energy transfer signature is only observed in the acceptor PL lifetime but not its emission intensity at the highest gold NP concentrations investigated.

In general, the dependence of the donor and acceptor lifetimes on the gold NP concentration supports the trend of the donor and acceptor PL emission observed for the Acc2-gold-Don1 sandwich structure. Both indicate that even though the surface plasmon mediated energy transfer seems to become more efficient with increasing gold concentrations, less acceptor enhancement is observed, due to an increased quenching of the acceptor emission in the proximity of the gold NPs. More detailed investigations of the distance and concentration dependences of FRET mediated by surface plasmons

in the sandwich structure have to be carried out to determine the optimum conditions for a fast and efficient energy transfer that also leads to a large acceptor enhancement.

6.3 Different Sample Geometries

To extend the investigation of the impact of surface plasmons on energy transfer between donor and acceptor QDs, two other sample geometries were also investigated: a separated donor-acceptor bilayer on gold and a mixed donor-acceptor monolayer on gold. Only a brief overview of some preliminary results will be given in this section, as this investigation has only been started recently. The samples discussed in the following were prepared with Acc2 and Don6 QDs. The gold-acceptor separation for the separated donor-acceptor bilayer on gold and the gold-QD separation in the case of the mixed monolayer on gold, were both varied in 3 nm steps between 6 and 18 nm, as this coveres the acceptor-gold separations for which the largest effects were observed in the acceptor-gold-donor sandwich structure.

The comparison of these two structures will be of great interest for the fundamental understanding of the modification of FRET in proximity to metal NPs as the gold-QD separations can be tuned in the same way and furthermore, donor as well as acceptor QDs are deposited on top of the gold NP layer, which makes it easier to detect the emission from both types of QDs. However, the observed effect could be substantially different in the two structures, as the "energy transfer direction" in the separated donor acceptor bilayer always has a component perpendicular to the gold layer, whereas in the mixed monolayer energy transfer occurs "parallel" to the gold layer, as indicated by the arrows in Figure 6.24(a) and (b) respectively. An angle φ is defined as in the theoretical work on energy transfer between a single donor and acceptor QD in proximity to a metal NP by Govorov et al. [130], as shown in Figure 6.24(c). φ can also be used to describe the difference between the donor and acceptor positions with respect to the gold NPs in the two structures. In the mixed donor-acceptor monolayer larger values of φ are probed than in the separated donor-acceptor bilayer on gold. The average φ in the separated layer structure is 0°, independent of the gold-QD separation. For the polyelectrolyte spacer thickness between the gold and the mixed QD monolayer increasing from $d = 6$ to 18 nm, the minimum φ for the mixed monolayer on gold decreases from 23° to 10°, estimated for neighbouring donor and acceptor QDs. However, keeping in mind that energy transfer from up to the third shell around a central acceptor QD has been observed for the mixed monolayers, as discussed in section 4.2, larger φ of 40° to 50° are obtained for energy transfer between non-neighbouring donor and acceptor QDs in the mixed monolayer (for $d = 6$ nm).

Therefore, the influence of the angle φ on the modification of the FRET process in

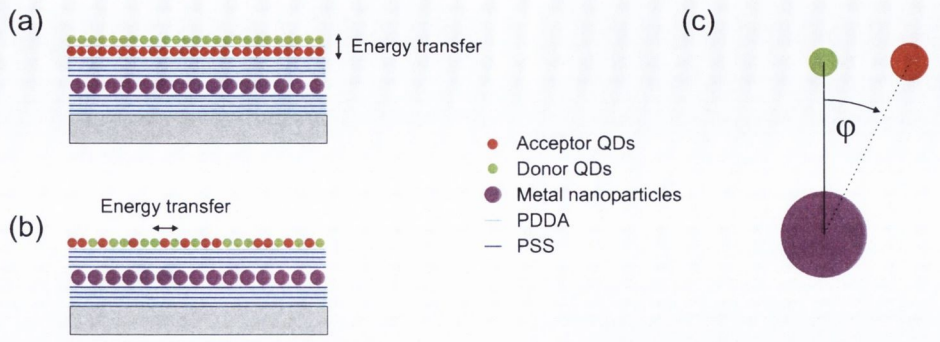


Figure 6.24: (a) Schematic of a donor-acceptor bilayer deposited on a gold nanoparticle (NP) layer, separated by a polyelectrolyte spacer formed by alternating PDDA and PSS layers. The arrow indicates the predominant direction for energy transfer in the structure. (b) Schematic of a mixed donor-acceptor monolayer on a gold NP layer with intermediate polyelectrolyte spacer. The arrow indicates the direction of the energy transfer. (c) Definition of the angle φ to describe the position of the donor (green) and acceptor (red) QDs with respect to a gold NP (purple).

the presence of metal NPs can be probed by comparing the donor-acceptor bilayer and the mixed donor-acceptor monolayer on gold. However, as mentioned in the beginning of this chapter, the most efficient surface plasmon enhancement of the FRET process is expected for $\varphi = 180°$ [130], corresponding to the sandwich structure discussed above.

6.3.1 Separate Donor-Acceptor Bilayer on Gold

Two sets of donor-acceptor bilayer structures, with a donor-acceptor separation of 0.5 nm, with different acceptor concentrations were prepared. A donor-acceptor separation of 0.5 nm (a single PDDA layer) was chosen as this gives rise to the same exclusion zone radius as in the mixed monolayer. The first set of bilayers on gold had donor and acceptor concentrations of $c_{Don} = (0.8 \pm 0.2) \times 10^{17}$ m^{-2} and $c_{Acc} = (2.1 \pm 0.2) \times 10^{17}$ m^{-2} respectively, and the gold concentration was kept constant at $c_{Au} = (0.057 \pm 0.003) \times 10^{17}$ m^{-2}. The details on the donor, acceptor and gold NP concentrations as well as the donor:acceptor concentration ratio for each of the structures in the first sample set are given in Table 6.1.

The PL spectra of the donor-acceptor bilayers on gold (lines) for different gold-QD separations as well as the reference spectrum for a bilayer on quartz (open squares) are shown in Figure 6.25(a). The respective gold-donor layer separation, calculated from the polyelectrolyte spacer thickness and the acceptor diameter, is given next to each spectrum. The spectra are dominated by a large acceptor emission, due to the large acceptor QD concentration. The high acceptor concentration should result in

Sample	c_{Don} (10^{17} m^{-2})	c_{Acc} (10^{17} m^{-2})	Don:Acc ratio	c_{Au} (10^{17} m^{-2})
Ref.	0.71	2.1	0.34	0
$d = 9.5$ nm	0.59	2.3	0.26	0.057
$d = 12.5$ nm	0.81	1.9	0.43	0.056
$d = 15.5$ nm	0.83	2.0	0.42	0.055
$d = 18.5$ nm	0.94	1.9	0.49	0.057
$d = 21.5$ nm	0.94	2.0	0.47	0.060

Table 6.1: Nanoparticle concentrations for the first set of donor-acceptor bilayer structures (donor-acceptor layer separation 0.5 nm) on gold for different gold-donor separations d: donor concentration c_{Don}, acceptor concentration c_{Acc}, donor:acceptor concentration ratio (Don:Acc ratio) and gold concentration c_{Au}. "Ref." indicates the donor-acceptor bilayer reference sample deposited on quartz without gold nanoparticle layer.

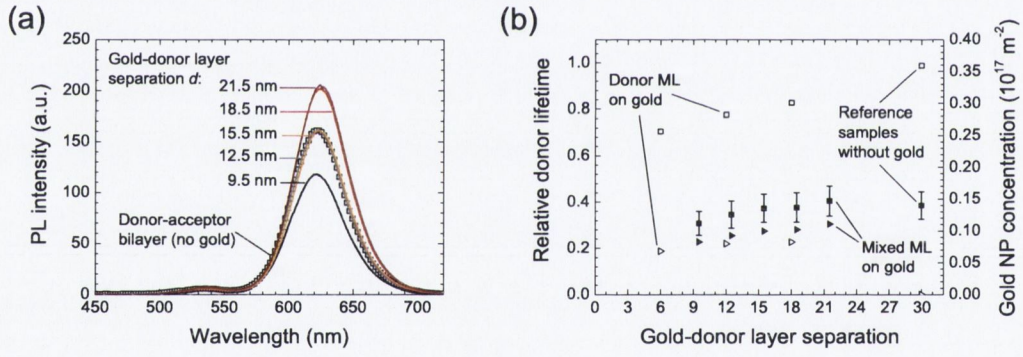


Figure 6.25: (a) PL spectra of Don6-Acc2 bilayer structures on quartz (open squares) and on gold nanoparticle (NP) layers (lines) for different gold-QD separations and an average acceptor concentration of $c_{Acc} = (2.1 \pm 0.2) \times 10^{17}$ m^{-2}. (b) Dependence of the relative donor lifetime (average value) on the gold-donor layer separation for donor-acceptor bilayers on gold (solid squares) as well as for donor monolayers on gold (open squares) (both left-hand axis). The reference values for the respective structures without gold NPs are indicated at a gold-donor separation of 30 nm. The gold NP concentration (right-hand axis) in the bilayer structure on gold (solid triangles) as well as for the donor-gold structure (open triangles) are also included in the graph.

a high FRET efficiency, which will be determined from the donor PL lifetime below. Furthermore, one can see that the acceptor emission in close proximity to the gold NPs ($d = 9.5$ nm) is smaller than that recorded for the reference, it is similar to that of the reference for $d = 12.5$ and 15.5 nm, and larger than the reference for $d = 18.5$ and 21.5 nm. The acceptor emission increase for the largest gold-QD separations is however not due to an increase in FRET, but arises most likely from the increased donor:acceptor ratio for these samples, as can be seen in Table 6.1. This is further confirmed by the time-resolved measurements of the donor PL decay.

In Figure 6.25(b) the relative donor lifetimes, calculated for the average donor lifetimes with respect to the donor lifetime in a Don6 monolayer at the same donor concentration, are shown in dependence of the gold-donor layer separation for the separated donor-acceptor bilayer structure on gold (solid squares) and donor monolayers on gold (open squares). The gold NP concentrations of these two structures are also included in the Figure (solid and open triangles, right-hand axis). The relative reference lifetimes for the reference samples without gold are indicated at a gold-donor layer separation of 30 nm. Using these reference values, a FRET efficiency of 61% and a FRET rate of $(1.8\ \text{ns})^{-1}$ are determined from the donor lifetime decrease in the bilayer structure on quartz. As can be seen, the donor lifetimes for the donor-acceptor bilayer on gold and the donor monolayer on gold increase with increasing donor-gold separation following very similar trends. The FRET efficiencies, 55% and 55%, and FRET rates, $(1.8\ \text{ns})^{-1}$ and $(1.9\ \text{ns})^{-1}$, determined for the two gold-donor layer separations of $d = 12.5$ and 18.5 nm, respectively, are very similar to those measured for the sample without gold. This confirms, as already suggested above, that the increase in acceptor emission dor $d = 18.5$ and 21.5 nm is not due to an increased FRET rate or efficiency, but results from the increased donor:acceptor ratio. Moreover, this shows that no modification of the FRET process due to surface plasmons is observed. This might be due to the high FRET rate, which is faster than the highest donor-gold transfer rate of $(6.8\ \text{ns})^{-1}$ determined for the smallest gold-donor separation ($d = 3$ nm) in the Don6-gold reference structure.

As it is more likely to see an effect of the surface plasmons on the energy transfer for lower FRET rates, a second set of donor-acceptor bilayers on gold was prepared with a lower acceptor concentration $c_{Acc} = (0.47 \pm 0.2) \times 10^{17}\ \text{m}^{-2}$. The details of the donor, acceptor and gold NP concentrations as well as the donor:acceptor ratio for these samples can be found in Table 6.2. The spectra of this second sample set with lower acceptor concentration, including a reference donor-acceptor bilayer deposited on quartz (open squares), are presented in Figure 6.26(a). One can see that all donor-acceptor bilayers on gold (lines) show lower donor and acceptor intensities than the reference structure without gold. However, it has to be pointed out that for this second sample set the donor:acceptor ratio for the reference structure is much larger than for

Sample	c_{Don} (10^{17} m^{-2})	c_{Acc} (10^{17} m^{-2})	Don:Acc ratio	c_{Au} (10^{17} m^{-2})
Ref.	0.71	0.35	2.0	0
$d = 9.5$ nm	0.47	0.59	0.8	0.088
$d = 12.5$ nm	0.59	0.59	1.0	0.070
$d = 15.5$ nm	0.59	0.59	1.0	0.063
$d = 18.5$ nm	0.65	0.53	1.2	0.043
$d = 21.5$ nm	0.54	0.59	0.9	0.083

Table 6.2: Nanoparticle concentrations for the second set of donor-acceptor bilayer structures (donor-acceptor layer separation 0.5 nm) on gold for different gold-donor separations d: donor concentration c_{Don}, acceptor concentration c_{Acc}, donor:acceptor concentration ratio (Don:Acc ratio) and gold concentration c_{Au}. "Ref." indicates the donor-acceptor bilayer reference sample deposited on quartz without gold nanoparticle layer.

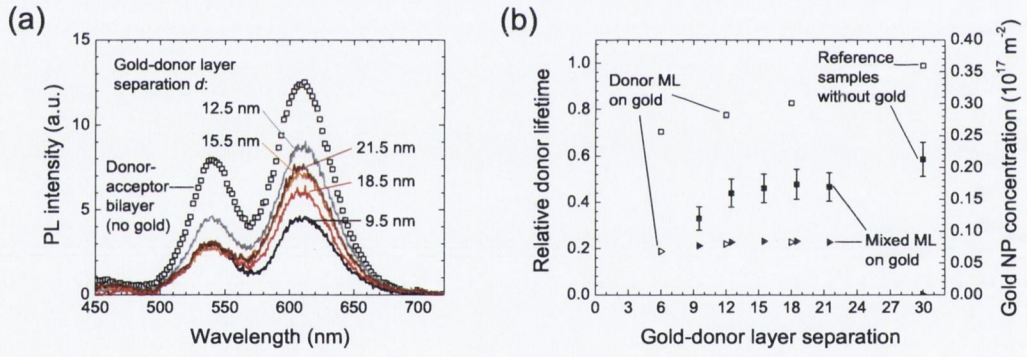


Figure 6.26: (a) PL spectra of a second set of Don6-Acc2 bilayer structures on gold (lines), for different gold-QD separations, and a reference bilayer on quartz (open squares). The average acceptor concentration of these samples is $c_{Acc} = (0.47 \pm 0.2) \times 10^{17}$ m^{-2}. (b) Dependence of the relative average donor lifetime on the gold-donor layer separation for donor-acceptor bilayers on gold (solid squares) as well as for donor monolayers on gold (open squares) (both left-hand axis). The reference values for the respective structures without gold nanoparticles (NPs) are indicated at a gold-donor separation of 30 nm. The gold NP concentrations (right-hand axis) for the bilayer structure on gold (solid triangles) as well as for the donor-gold structure (open triangles) are also shown.

the bilayers on gold. It seems a maximum acceptor emission is observed for a gold-donor layer separation of 12.5 nm, but further analysis of the PL spectra have to be carried out to verify if this is only an effect of the varying donor:acceptor ratio and gold NP concentration or due to a modification of the FRET process by the surface plasmons.

The distance dependence of the relative lifetime values, presented for the average donor lifetime measured for the donor-acceptor bilayer on gold (solid squares) and the donor monolayer on gold (open squares) in Figure 6.26(b), show similar trends as for the first sample set. The FRET rate of $(3.9\ \text{ns})^{-1}$ and efficiency of 41%, calculated for the lifetimes measured for structures without gold, included in the graph at 30 nm, indicate that the FRET process might still be too fast to observe a modification of the energy transfer by the gold NPs. Therefore, it is not surprising that only small variations of the FRET efficiency and rate are determined for the gold-donor layer separations of $d = 12.5$ nm (44%, $(2.8\ \text{ns})^{-1}$) and 18.5 nm (42%, $(3.2\ \text{ns})^{-1}$). For the other separations no lifetime values for the Don6-gold structures were available. However, the decrease of the relative donor lifetime for the donor-acceptor bilayer on gold with $d = 9.5$ nm in this second sample set seems to be stronger than for the first sample set. For an estimation of a lower limit of the FRET efficiency and FRET rate at this gold-donor separation, the relative lifetime of the donor-gold structure with $d = 6$ nm is used. A FRET efficiency of 53% and a FRET rate of $(1.7\ \text{ns})^{-1}$ indicate that an enhancement of the FRET process might occur at the smallest gold-QD separation investigated. It would be a very important result, if this modification of the FRET rate by surface plasmons can be confirmed in the separated donor-acceptor layer on gold, as theory predicts that surface plasmons should have no or only very little effect on the energy transfer rate in this geometry [130]. For verification a more detailed investigation at these low separations for samples with even lower acceptor concentrations should be carried out for the donor-acceptor bilayer on gold.

6.3.2 Mixed Donor-Acceptor Monolayer on Gold

The mixed donor-acceptor monolayer, promises to be the better geometry to observe a modification of energy transfer by surface plasmons. The donor and acceptor concentrations for the mixed monolayer prepared with different gold-QD separations d were constant within error at $c_{Don} = 0.59 \times 10^{17}\ \text{m}^{-2}$ and $c_{Acc} = 0.47 \times 10^{17}\ \text{m}^{-2}$ respectively. All relevant concentrations for these samples are given in Table 6.3.

The PL spectra of the mixed monolayers on quartz (open squares) and for different layer separations d on gold (lines) are shown Figure 6.27(a). As can be seen the donor and acceptor emission intensities for gold-QD layer separations of $d = 6$ and 9 nm are reduced compared to the reference spectrum, for $d = 12$ nm the donor emission is still lower than that of the reference, but the acceptor emission has recovered and

Sample	c_{Don} (10^{17} m^{-2})	c_{Acc} (10^{17} m^{-2})	Don:Acc ratio	c_{Au} (10^{17} m^{-2})
Ref.	0.59	0.47	1.3	0
$d = 6$ nm	0.59	0.47	1.3	0.095
$d = 9$ nm	0.59	0.47	1.3	0.066
$d = 12$ nm	0.59	0.47	1.3	0.054
$d = 15$ nm	0.59	0.47	1.3	0.053
$d = 18$ nm	0.59	0.47	1.3	0.057

Table 6.3: Nanoparticle concentrations for the mixed donor-acceptor monolayer on gold for different gold-QD separations d: donor concentration c_{Don}, acceptor concentration c_{Acc}, donor:acceptor concentration ratio (Don:Acc ratio) and gold concentration c_{Au}. "Ref." indicates the mixed donor-acceptor monolayer reference sample deposited on quartz without gold nanoparticle layer.

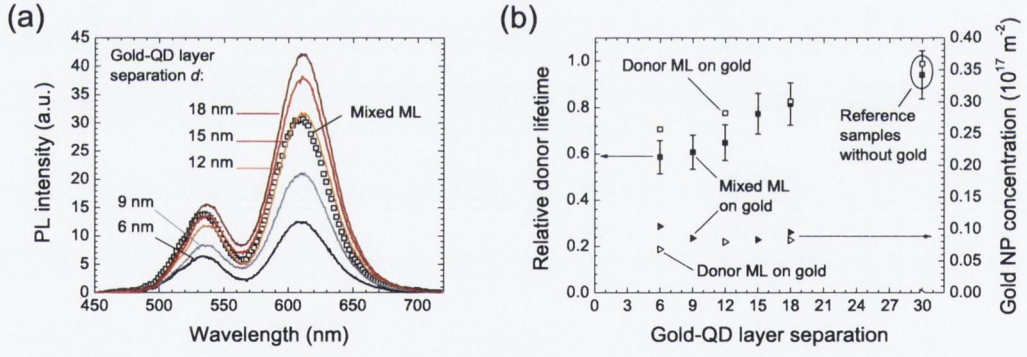


Figure 6.27: (a) PL spectra of a mixed donor-acceptor monolayer on gold (lines) for different layer separations d as well as for a mixed reference monolayer on quartz (open squares). (b) Gold-QD layer separation dependence of the relative donor lifetime (left-hand axis) in the mixed monolayer on gold (solid squares) and for a donor monolayer on gold (open squares). The reference values for the structures without gold nanoparticles (NPs) are indicated at 30 nm. The gold NP concentrations (right-hand axis) are also shown for the mixed donor-acceptor monolayer (solid triangles) as well as for the donor reference monolayer on gold (open triangles).

for $d = 15$ and 18 nm, the acceptor emission shows an increase of the acceptor peak emission intensity by 23% and 36% respectively. As the donor:acceptor ratio seems to be constant for these samples, this acceptor emission increase could be a sign for an increased energy transfer from the donors to the acceptors.

The relative donor lifetimes determined for the mixed Don6-Acc2 monolayer on gold (solid squares) and Don6 monolayers on gold (open squares) are shown in Figure 6.27(b) in dependence of the gold-QD layer separation d. The gold concentration for both structures (solid and open triangles respectively) can be read off the right-hand axis. The FRET rate is clearly reduced compared to the Don6-Acc2 bilayers discussed in the previous section, as the donor lifetimes in the mixed monolayers are not much smaller than for the Don6-gold reference samples. For the mixed monolayer a FRET efficiency of 5% and a FRET rate of $(45\ \text{ns})^{-1}$ were determined from the reference lifetime values for structures without gold NPs, indicated at $d = 30$ nm. The lifetime difference of the mixed monolayer and donor monolayer on gold seems larger for a layer separation of 6 nm than for the reference samples without gold, and this lifetime difference reduces for increasing gold layer separation. For $d = 6$ nm a FRET efficiency of 17% and a FRET rate of $(9.6\ \text{ns})^{-1}$ were obtained, and 16% and $(11.0\ \text{ns})^{-1}$ respectively at $d = 12$ nm. The values reduce to 1% and $(158\ \text{ns})^{-1}$ for the largest layer separation, $d = 18$ nm investigated. The values of the FRET rate and efficiency indicate that a FRET enhancement occurs for the smaller gold-QD separations investigated. However, a more detailed characterization of the FRET signatures in the PL and time-resolved measurements is necessary to support this increase of the FRET efficiency and rate at small gold-QD layer separations and to understand the origin of the increased acceptor emission at larger separations, for which a reduced FRET efficiency is observed.

6.3.3 Comparison

A comparison of the donor-acceptor bilayer and the mixed donor-acceptor monolayer on gold shows that larger effects on the emission spectra and donor lifetimes due to a modification of the energy transfer by the surface plasmons were observed in the gold-QD distance dependence for the mixed monolayer on gold. The FRET signatures, such as acceptor emission enhancement and a reduced donor lifetime, showed no significant modification in the donor-acceptor bilayer in dependence of its distance to an underlying gold NP layer. The observed changes in the acceptor enhancement are attributed to a variation in the donor:acceptor ratio rather than a change in energy transfer. Due to the fast FRET rate in these donor-acceptor bilayer compared to the transfer rate to the metal, not even a decrease in the energy transfer in the presence of gold NPs was observed in this structure. Only a hint for a increase of the energy transfer rate and efficiency was found for the bilayer structure with the lower acceptor concentration,

corresponding to a lower FRET rate, for the smallest gold-QD separation, giving rise to a stronger interaction of the QDs and the gold NPs. This suggests that surface plasmon modifications are strongest for slow FRET rates and small gold-QD separations.

This was confirmed in the characterization of the mixed donor-acceptor monolayer on gold, for which a four-fold increase of the FRET rate and an enhancement of the FRET efficiency by a factor of three was observed at small gold-QD separations. With increasing gold-QD separation the FRET rate and efficiency clearly decreased, showing a strong influence of the surface plasmon on the energy transfer in the mixed monolayer and no or only little effect on FRET in a separated donor-acceptor bilayer on gold.

However, it has to be taken into account that the FRET rates in the two geometries investigates were significantly different, with a lower FRET rate of $k_{DA} = (45\ \text{ns})^{-1}$ in the mixed donor-acceptor monolayer than in the donor-acceptor bilayer, with $k_{DA} = (3.9\ \text{ns})^{-1}$, which could be the reason for the different observations in these two different geometreis. Therefore, more experiments with both structures have to be carried out to investigate the influence of the surface plasmons on the energy transfer in these two geometries in more detail and to compare them with the theoretically expected results.

6.4 Conclusion

The influence of localized surface plasmons, supported by gold nanoparticles with a diameter of 4 nm, on FRET in donor and acceptor QD layer structures was investigated. In order to differentiate between direct surface plasmon PL enhancement of the donor and acceptor QD emission, a detailed analysis of the optical properties of the QD monolayers in proximity to gold nanoparticle layers was presented at the beginning of this chapter. Furthermore, a good understanding and accurate modelling of the QD-gold nanoparticle interactions in the reference structures is important to enable the evaluation of the impact of the surface plasmons on FRET efficiency and rate in the donor-acceptor FRET structures. Good agreement of the distance and concentration dependence in the QD monolayer - gold nanoparticle reference structures was found for a theory of FRET between two planes. Moreover, it was shown that for the QDs, layer separations and nanoparticle concentrations used here, only quenching of the PL intensities and a decrease of the PL lifetimes were observed for donor and acceptor QD monolayers in proximity to gold nanoparticles.

Strong evidence of energy transfer mediated by gold nanoparticles was observed for acceptor-gold-donor sandwich structures. Most importantly, no acceptor emission was observed for acceptor-gold structures due to the complete quenching of the acceptor emission after depositing polyelectrolyte layers and a gold nanoparticle layer on top of the acceptors. However, some acceptor emission re-appeared when suitable donor QDs

were deposited on top of the gold nanoparticle layer and was therefore attributed to surface plasmon mediated energy transfer. The recovery of the acceptor emission was only observed for donor QDs with a high quantum yield and a strong interaction with the gold nanoparticles.

Furthermore, a strong modification of the donor-acceptor FRET distance dependence was observed when varying the acceptor-gold separation in the acceptor-gold-donor sandwich structure. The strongest effect of the surface plasmon on the energy transfer, observed as a maximum in the acceptor emission and a decrease of the short lifetime component in the donor PL decay, was observed for acceptor-gold separations of 12 to 15 nm - corresponding to a total donor-acceptor centre-to-centre separation of 22 to 25 nm. This is a significant increase in the donor-acceptor separations over which energy transfer can be observed, as in the donor-acceptor structures without gold nanoparticles energy transfer only occurs over distances of up to 12 nm. Varying the gold-donor separation in the sandwich structure, the strongest impact on the donor and acceptor emission and the acceptor lifetime was observed for small gold-donor separations of 3 and 6 nm. The gold concentration dependence clearly highlighted the trade off between the FRET enhancement and the acceptor PL quenching by the gold nanoparticles in the sandwich structure. The largest absolute increase in the acceptor emission was observed for the lowest gold nanoparticle concentration investigated, while the largest acceptor enhancement (with respect to the acceptor-gold reference structure) was seen at an intermediate gold concentration. The FRET efficiency, determined from its impact on the donor emission and lifetime, was largest at the highest gold concentration investigated.

Due to a strong energy transfer rate to the metal, the impact of the energy transfer on the donor lifetime is only very small. On top of that, variations of the gold nanoparticle and donor QD concentrations in the sandwich and reference structures made it difficult to determine the absolute FRET rate and efficiency for all sandwich structures. FRET rates as fast as $(2\ \text{ns})^{-1}$ and $(3\ \text{ns})^{-1}$ have been determined for some of the sandwich structures with donor-acceptor centre-to-centre separations of 22.1 nm, values similar to the FRET rates determined for donor-acceptor bilayer structures with the smallest donor-acceptor centre-to-centre separations of 3.6 nm discussed in the previous chapter.

For the data available to-date, it seems that, in line with theory [130], the strongest effects of gold nanoparticles on FRET between donor and acceptor QDs have been found for acceptor-gold-donor sandwich structures, as the distance over which energy transfer can occur is greatly increased in this structure as outlined above. A surface plasmon effect on FRET has also been observed for a mixed QD monolayer on gold, for which an increase in the FRET efficiency and FRET rate has been determined, and only an indication of a small increase of the FRET rate and efficiency have been seen for the donor-acceptor bilayer on gold.

7 Conclusions

7.1 Summary of Results

In the work presented in this thesis Förster resonant energy transfer (FRET) in nanocrystal quantum dot (QD) structures was investigated. Theoretical work suggests that the basic FRET theory [90], despite having been developed for donor and acceptor molecules represented by point-dipoles, can also appropriately describe FRET between QDs [109, 110, 111, 112]. However, even though FRET in QD structures has been investigated experimentally for over a decade [32, 113] only a few reports on the qualitative agreement of FRET between QDs and theory can be found in the literature [32, 108, 114]. Therefore, FRET in different QD structures was analysed in detail and compared with theory, before turning to the investigation of the effect of surface plasmons on FRET between donor and acceptor QDs.

QD Intra-Ensemble Energy Transfer

Energy transfer within QD ensembles had been observed before and was attributed to intra-ensemble energy transfer from smaller QDs, emitting on the blue side of the ensemble emission spectrum, to larger QDs, emitting on the red side, due to the inhomogeneous broadening of the QD ensemble [99, 108, 113, 115, 158]. In the first part of chapter 4, and also published in reference [116], it was shown that the decrease in the emission lifetime of the small QDs with increasing QD concentration in monodispersed QD monolayers, can be well modelled with a theory of FRET between randomly distributed donors and acceptors taking into account an exclusion zone with radius R_{ex} around the donors [100]. Good agreement of the values of R_{ex} and the Förster radius, R_0, used in the modelling with those obtained from the QD spectra demonstrates that energy transfer within the QD ensemble is dominated by FRET. This shows that even in closely packed assemblies of chemically stabilized nanocrystal QDs, tunnelling or surface effects can be neglected. Furthermore, by comparing monolayers prepared from QD samples with varying spectral self-overlap, as determined from the QD emission and absorption spectra, it was shown that the impact of FRET on the optical properties of the QD monolayers decreases with decreasing self-overlap, following the trend predicted by FRET theory. Therefore, by tuning the QD concentration and choosing QDs with

an appropriate self-overlap, the probability for FRET in monodispersed QD structures can be controlled by another means other than by temperature [158].

FRET in Donor-Acceptor QD Structures

QDs of two different sizes were used as donors and acceptors in a mixed donor-acceptor monolayer, discussed in the second part of chapter 4 and published in reference [107], and a separated donor-acceptor bilayer structure, presented in chapter 5. The donor QDs used in the mixed monolayer structure only had a very small self-overlap and the emission lifetime was almost constant as a function of the donor concentration. Therefore, a good quantitative agreement of the two-dimensional FRET theory [100], taking into account exclusion zones created by the donor and acceptor QD radii, with the acceptor concentration dependence of the measured FRET efficiency was observed in the mixed monolayer. FRET efficiencies of 90% and FRET rates as fast as $(0.5\ \text{ns})^{-1}$ were achieved at the highest acceptor QD concentrations. Furthermore, the theory can also be used to fit the donor emission decays and an excellent agreement of the values of R_0 and R_{ex} determined from the spectral properties of the donor and acceptor QDs, the acceptor concentration dependence and the fitting of the donor decays is found. Therefore, all important FRET parameters: R_0, the FRET rate and efficiency; can be determined from time-resolved donor photoluminescence measurements alone.

In the separated bilayer structure good qualitative agreement of the FRET efficiency as a function of the donor-acceptor separation and the acceptor concentration with those calculated with theory on the basis of R_0, determined from the spectral overlap, was found. However, the absolute values of the FRET efficiency were only reproduced by theory at high donor concentrations. In the case of low donor concentrations, the trends of the experimentally and theoretically determined FRET efficiencies agreed, but a fit with the measured values was only obtained for a value of R_0 larger than that calculated from the spectral overlap. Furthermore, a strong decrease of the FRET efficiency with increasing donor concentration was observed, which is not expected from theory and has not been reported in literature. This donor concentration dependence arises from the competition of donor-acceptor FRET and intra-ensemble energy transfer within the donor monolayer. The decrease of the FRET efficiency can be well fitted with a FRET rate model for a donor concentration-independent FRET rate which takes into account the donor concentration-dependent donor lifetime. The fastest FRET rate determined from this modelling was $(1.2\ \text{ns})^{-1}$, a value in good agreement with those reported in the literature [108, 114, 115, 145]. The donor concentration dependence of the FRET efficiency can also be reproduced by theory if the donor concentration-dependent donor quantum yield of the emission on the blue side of the donor ensemble spectrum is taken into account in the calculation of R_0.

The acceptor enhancement in both the mixed monolayer and the donor-acceptor bilayer structure were larger than that expected from the FRET efficiency multiplied by the donor:acceptor absorption ratio. This is attributed to exciton recycling from donor defect states, which has also been observed by other groups [12, 120], but is not fully understood yet. An acceptor concentration-dependent factor, but independent of the donor-acceptor separation, has to be included in the calculation of the acceptor enhancement via the FRET efficiency to reproduce the experimentally determined values. An acceptor enhancement as high as 10 was determined at low acceptor concentrations in the mixed monolayer. The continuing increase of the acceptor enhancement with increasing donor:acceptor ratio in the mixed monolayer suggests that donors from within three shells around a central acceptor can transfer energy to this acceptor, which is in agreement with literature [115].

The recycling effect also results in a larger increase of the total emission intensity of the FRET structures than that predicted with a simple model of the donor and acceptor photoluminescence intensity. An enhancement of the overall emission, with respect to the emission expected for the same structure without FRET, is always obtained when the acceptor quantum yield is larger than that of the donors. An enhancement is also observed for high donor:acceptor concentration ratios for lower acceptor quantum yields. This effect is however not predicted by the photoluminescence model and shows the large impact exciton recycling can have on the total emission of a FRET structure. Further investigation is required to obtain a good model of the experimental observations, which could be used as a design tool for the engineering of higher emission intensities in light emitting structures [12, 120].

Influence of Surface Plasmons on FRET

Before investigating the impact of surface plasmons on FRET between donor and acceptor QDs, it is necessary to characterise the QD-metal nanoparticle interactions to enable the differentiation between direct surface plasmon enhancement of the donor and / or acceptor emission and any modification of the energy transfer mechanism. For the gold nanoparticles, donor and acceptor QDs used here, only quenching of the QD emission was observed over the range of separations and concentrations investigated, as shown in the first part of chapter 6. Furthermore, it was found that the distance and gold nanoparticle concentration dependences of the photoluminescence lifetime of the QDs in proximity to gold nanoparticles agree well with the trends calculated with FRET theory, as suggested in the literature [80, 81, 84, 86].

In the acceptor-gold-donor sandwich structure, discussed in the second part of chapter 6, clear signatures for enhanced FRET were observed. While the acceptor emission is fully quenched after the deposition of the gold nanoparticles, it re-appears once the

structure is completed with the appropriate donor QDs. Therefore, it is concluded that energy transfer mediated by the gold nanoparticles is overcoming the acceptor emission quenching for acceptor-donor centre-to-centre separations of 22 nm and larger. Furthermore, a strong donor QD dependence is observed and attributed to varying levels of donor-gold interaction and donor quantum yields. The gold nanoparticles are strongly modifying the FRET distance dependence, with a maximum in the acceptor emission and a decrease of the short donor lifetime component apparent at acceptor-gold layer separations of 12 to 15 nm. Alternatively, by changing the gold-donor layer separation instead, the maximum effect of the surface plasmons on FRET is observed for separations of 3 to 6 nm. The competition between the direct quenching of the QD emission in proximity to gold nanoparticles and the surface plasmon enhanced FRET is reflected in the gold nanoparticle concentration dependence. The highest acceptor emission is observed at the lowest gold concentration investigated, where the increase in the FRET efficiency is low but so also is the direct photoluminescence quenching. For the next higher gold concentration the maximum acceptor emission enhancement of 49% is observed, but the absolute emission is reduced due to the increased quenching. For even higher gold concentration the FRET efficiency and rate are largest, but due to the stronger quenching by the gold nanoparticles the acceptor emission is decreased. A direct comparison of the donor decays for the sandwich structure and the reference samples is often difficult, due to variations in the QD and gold nanoparticle concentrations that affect the donor lifetime. Taking these effects into account, FRET efficiencies and rates were determined from the decrease of the short donor lifetime component for some of the samples. FRET rates as fast as $(2.0\ \text{ns})^{-1}$, corresponding to a FRET efficiency of approximately 21%, were determined for a donor-acceptor centre-to-centre separation of 22 nm. This FRET rate is just a little lower than those mentioned above for donor-acceptor structures without gold nanoparticles, where the QDs are much closer (< 4 nm) and for which no energy transfer has been observed at these large separations. Therefore, it can be concluded that the FRET rate is strongly enhanced due to the interaction with the surface plasmons.

To complete this study, the impact of the gold-QD distance on FRET in a donor-acceptor bilayer and a mixed donor-acceptor monolayer on a gold nanoparticle monolayer were also investigated, in the final part chapter 6. No effect of the presence of the gold nanoparticles on the FRET rate and efficiency in the bilayer structure was observed, whereas a five-fold increase in FRET rate and an enhancement of the FRET efficiency by a factor of three were determined for small separations of the mixed donor-acceptor and gold nanoparticle layer. This enhancement is much lower than that observed for the sandwich structure. Based on the different geometries of these structures, it is in agreement with theory that stronger surface plasmon effects are observed for the

sandwich structure than for the mixed monolayer on gold, and no effects for the bilayer on gold [130]. However, the FRET rates in the absence of gold nanoparticles were markedly different in these structures, due to different donor-acceptor separations and concentrations. In particular the FRET rate in the bilayer structure was larger than the donor-gold transfer rate and therefore this could also be the reason for which no surface plasmon modification of the FRET rate was observed. Hence, as outlined in the next section, further study is necessary to verify these observations.

7.2 Outlook

The analysis of FRET in different QD structures provided a better understanding of FRET between QDs, for example the effect of the large QDs size and the inhomogeneous broadening of the QD ensembles, and gave first indications of the factors influencing surface plasmon mediated FRET. However, some questions remained unanswered and new ones arose. To address these, a few suggestions for future experiments are summarized in the following.

FRET in Donor-Acceptor QD Structures

In the mixed donor-acceptor monolayer structure it will be interesting to investigate in more detail the acceptor enhancement as well as the PL emission enhancement due to FRET at low acceptor:donor ratios. The acceptor enhancement is expected to be constant at very low acceptor concentrations and finding this plateau region will provide more information about the number of donors that can interact with a particular acceptor in this structure. Furthermore, a more detailed investigation of the PL enhancement in this concentration regime will provide a deeper insight into the trade-off between the decreasing FRET efficiency, increasing donor:acceptor ratio and the recycling effect.

A more detailed investigation of the recycling effect requires the careful characterisation of the integrated PL as well as time-resolved PL decay traces in the mixed donor-acceptor monolayer and donor-acceptor bilayer structure. The recycling effect describes the energy transfer from excitons trapped in donor defect states. This is an effect unique to nanocrystal QDs and should not be observed when using dye molecules as donors. Therefore, a comparison of a structure including the same acceptor QDs and using QDs or molecules as donors respectively, could confirm the actual contribution of the recycling effect to the acceptor enhancement. The bilayer structure would be best suited for this comparison as the acceptors can be deposited first by LbL and a layer of the donor species would then be added as the top-most layer either by LbL, drop-casting or spin-coating. In the structures with acceptor as well as donor QDs it will be particularly interesting to compare the dependence on the acceptor and donor

concentration to determine their impact on the recycling effect as well as to use QDs with different quantum yields to evaluate its influence on the recycling effect. These experiments will help to expand the photoluminescence model to include the recycling effect.

The detailed investigation in the mixed donor-acceptor monolayer and separated donor-acceptor bilayer structure will complement each other as low acceptor:donor ratios can be more easily achieved in the mixed monolayer structure. However for the investigation of the concentration dependence the bilayer structure is better suited, as it allows for the independent control of both concentrations.

Furthermore, the influence of donor intra-ensemble energy transfer on the different FRET signatures and the overall PL enhancement in FRET structures should be investigated in more detail by using spectrally well separated donor and acceptor QDs to compare the impact of donor-to-donor transfer on the FRET efficiency and the PL quenching determined for the blue side of the donor ensemble emission spectrum as well as for the whole donor ensemble. Photoluminescence measurements with varying excitation wavelengths could be carried out to determine how well donor intra-ensemble energy transfer and its impact on the donor-acceptor FRET efficiency can be suppressed by excitation of donor sub-ensembles, using different excitation wavelengths in resonance with the first donor absorption peak

Surface Plasmon modified FRET in QD structures

To improve and facilitate the analysis of FRET mediated by metal nanoparticles, a more detailed investigation of the QD-metal nanoparticle interactions is necessary. This should include a more detailed analysis of the quenching process and its modelling with FRET theory [80, 81, 84, 86]. A consistent analysis is the basis for the characterization of the more complex structures including donor and acceptor QDs as well as metal nanoparticles. Further experiments for QD monolayers on metal nanoparticle layers could investigate the impact of both the QD as well as the metal nanoparticle concentration in more detail. Additionally, distance dependences for different gold nanoparticle concentrations could be compared with each other and with theory to determine the parameters influencing the equivalent of the Förster radius for the QD-metal nanoparticle interaction.

In the acceptor-gold-donor sandwich structure, it would be important to investigate the dependence of the surface plasmon mediated FRET on the spectral properties of the donor QDs with respect to the surface plasmon necessary to use to achieve a large acceptor enhancement, that enables the observation of the acceptor emission, but not to fully quench the donor emission either, so that the changes in donor emission and lifetime can still be determined reliably.

Once the best donor QDs have been chosen, the impact of the QD-gold distance on the FRET signatures should be investigated in more detail. Ideally, the acceptor-gold distance dependence should be measured for two fixed gold-donor separations, and vice versa for the gold-donor distance dependence, to find out how these two separations influence each other. Furthermore, structures with the donor-acceptor separation corresponding to the largest acceptor or FRET enhancement should be prepared with the gold nanoparticle layer deposited at different position between the donor and acceptor layers. These experiments should provide a detailed understanding of the distance dependences of the surface plasmon enhanced FRET process. For the optimized separations a detailed investigation of the surface plasmon mediated energy transfer as a function of the gold concentration should be carried out to determine the optimum gold concentrations to achieve the largest absolute acceptor emission increase as well as the largest FRET acceptor enhancement.

In addition, it would be interesting to find out if the Förster radius can be further increased by including two separated metal nanoparticle layers between the donor and acceptor QD monlayers, due to the coupling of these metal nanoparticle layers. For preparation the interaction of two metal nanoparticle layers with varying layer separation should be investigated by absorption spectroscopy to identify the extent of the coupling region. It might be necessary to adjust the metal nanoparticle concentrations in the layers as more metal nanoparticles will predominantly induce more quenching, which will make the observation of any effects more difficult.

As mentioned above, a detailed comparison of the three structures discussed in this thesis: the acceptor-gold-donor sandwich, a separated donor-acceptor bilayer on gold and a mixed monolayer on gold; should be carried out and compared with the theoretical simulations [130]. In particular, the comparison of the separated bilayer and mixed monolayer on gold should be valuable as these structures are more similar with regard to gold-QD separation and donor-acceptor separation than the sandwich structure. From the initial results presented in section 6.3 it seems that the most interesting conditions to investigate are small gold-QD separations, where a larger interaction of the gold and donor QDs is expected, and low FRET rates. The FRET rate can be reduced by either decreasing the acceptor concentration or by increasing the acceptor-donor layer separation in the bilayer structure. However, to compare the bilayer and mixed monolayer structures, it would be best to prepare samples with similar acceptor concentrations and to keep the donor-acceptor separation in the bilayer as small as possible so that the donor and acceptor QDs are positioned at similar distances to the metal nanoparticles in both structures. Furthermore, in the analysis of the mixed monolayer on gold, it has to be kept in mind that the angle φ between the donor and acceptor QDs is reducing with increasing gold-QD separation and this has to be considered in the analysis.

In addition to the investigation with gold nanoparticles, all the above experiments can be carried out with nanoparticles of different metals, sizes and shapes to compare the impact of the variation of the strengths of the surface plasmon field, scattering components and surface plasmon resonance wavelengths on FRET. Furthermore, temperature dependent measurements could help to clarify the exact mechanism of the surface plasmon enhancement of FRET between donor and acceptor QDs.

Finally, once a good understanding and control of the surface plasmon enhanced FRET has been achieved, it would be important to demonstrate how this effect can increase the sensitivity of sensing structures [30, 162] and the efficiency of light-harvesting or light-emitting devices [12, 13, 20, 21, 22, 24].

Appendix

A.1 Quantum Dot Layer Concentration

To verify the values of the QD concentration in the layers determined by comparing the layer absorption spectra with those recorded for the same QDs in solution, two monodispersed QD monolayer samples were analysed by mass spectroscopy. The experiments were carried out by the Centre for Microscopy and Analysis in Trinity College Dublin with an Inductively Coupled Plasma - Mass Sepctrometer.

The monolayers investigated were prepared by the layer-by-layer deposition technique from solutions of QDs with a diameter of 2.6 nm (QD-A) and 3.4 nm (QD-B). The absorption spectra of a 5.8×10^{-6} M QD-A and 1.7×10^{-6} M QD-B solution are shown in the insets of Figures A.1(a) and (b) respectively. By fitting the monolayer absorption spectra with the solution spectra, as presented in the main panels of Figures A.1(a) and (b), QD concentrations of $c_{\text{ML QD-A}} = 0.0085 \cdot 5.8 \times 10^{-6} \cdot 3.011 \times 10^{24}\ \text{m}^2 = 1.5 \times 10^{17}\text{m}^{-2}$ for the QD-A monolayer and $c_{\text{ML QD-B}} = 1.0 \times 10^{17}\text{m}^{-2}$ for the QD-B monolayer were determined as described in detail in section 3.2.2.

For the analysis with the mass spectrometer the samples were completely digested using nitric acid and hydrogen peroxid and the mass fractions of Cd and Te of the samples were then determined from these solutions. In the case of the QD-A monolayer, the weight of Cd and Te deposited in form of QDs on the sample were 0.929×10^{-6} g and 0.326×10^{-6} g respectively, corresponding to approximately 4.98×10^{15} Cd and 1.54×10^{15} Te atoms. As the number of Cd and Te atoms should be the same, the difference to the mean value was assumed as the error on the measurements. The total CdTe weight for this sample is 1.255×10^{-6} g with an error of at least 50%. The mass of a single QD with an average diameter of 2.6 nm and a density of 6200 $\frac{\text{kg}}{\text{m}^3}$ (density of CdTe) is approximateley 5.536×10^{-20}g. Therefore, the total weight of Cd and Te measured by mass spectroscopy was contained in 2.267×10^{13} QDs on the sample or 1.133×10^{13} QDs per side. This corresponds to a QD density of $(0.6 \pm 0.4) \times 10^{17}\ \text{m}^{-2}$ on the 1.2 × 1.5 cm quartz substrate. Even though the concentration determined by mass sepctroscopy is 60% lower than that obtained by comparison of the absorption spectra, $c_{\text{ML QD-A}} = (1.5 \pm 0.2) \times 10^{17}\ \text{m}^{-2}$, the values are very close taking into account the relatively large error.

For the QD-B monolayer sample a total CdTe weight of $(1.240 + 0.415) \times 10^{-6}$ g =

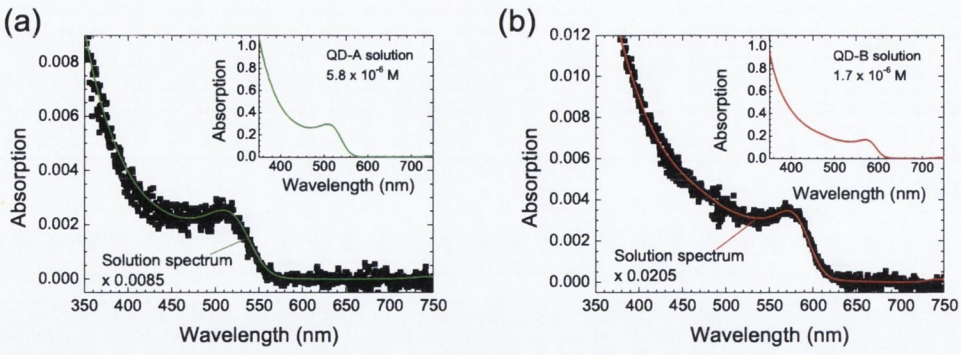


Figure A.1: (a) Absorption spectrum of a QD-A monolayer and fit with a QD-A solution spectrum (green line). The absorption spectrum of the solution as measured is shown in the inset. (b) Absorption spectrum of a QD-B monolayer and fit (red line) with the solution spectrum. In the inset the original absorption spectrum of the QD-B solution is shown.

$(1.655 \pm 0.877) \times 10^{-6}$ g was measured. Carrying out the same calculations as for QD-A, this weight corresponds to 1.2971×10^{13} QDs with a diameter of 3.4 nm on both sides of the sample and a QD layer concentration of $(0.4 \pm 0.2) \times 10^{17}$ m^{-2}. Again, the value is 60% smaller than $c_{\text{ML QD-B}} = (1.0 \pm 0.2) \times 10^{17} m^{-2}$ obtained from the comparison of the absorption spectra.

Due to the difficulty to reliably determine an absolute concentration value for these small particles, the agreement of the concentration values obtained in the two different ways is reasonable.

A.2 Quantum Dot Spectra

In this part of the Appendix, the solution photoluminescence (PL), absorption and photoluminescence excitation (PLE) spectra as well as the most important details on the QDs Acc1, Don4, Don5, Don6, Don7, Don8 and Don9 are summarized. These QDs have been used for the preparation of samples presented in this thesis, but their properties have not been discussed in the main chapters.

Figure A.2 shows the Acc1 spectra recorded for a solution with a concentration of $c_{sol} = 1.95 \times 10^{-6}$ M. The Acc1 QDs have a diameter of $d = 3.5$ nm, a quantum yield of 18% in solution and their emission and absorption features are characterized by:

Absorption peak:	581 nm	2.227 eV
PL peak:	610 nm	2.121 eV
PL FWHM:	45 nm	156 meV
Stokes shift:	29 nm	106 meV

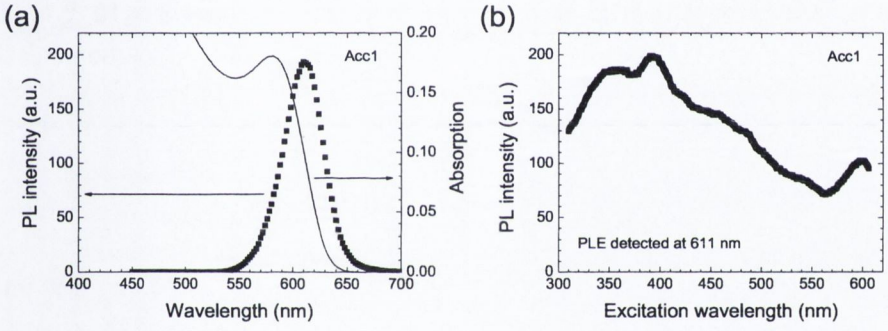


Figure A.2: (a) Photoluminescence (PL) (squares, left-hand axis) and absorption spectra (line, right-hand axis) of an Acc1 solution with a concentration of $c_{sol} = 1.95 \times 10^{-6}$ M. (b) PL excitation (PLE) spectrum of the Acc1 solution recorded at 611 nm. The PL and PLE spectra were recorded with a 1% transmission filter.

Figure A.3 shows the Don4 spectra for a solution with $c_{sol} = 1.1 \times 10^{-5}$ M. The Don4 QDs have a diameter of $d = 1.3$ nm, a quantum yield of 6.6% in solution and their emission and absorption features are characterized by:

Absorption peak:	471 nm	2.631 eV
PL peak:	511 nm	2.426 eV
PL FWHM:	34.4 nm	163 meV
Stokes shift:	40 nm	205 meV

Figure A.4 shows the Don5 spectra for a solution with $c_{sol} = 4.3 \times 10^{-6}$ M. The Don5 QDs have a diameter of $d = 2.3$ nm, a quantum yield of 29% in solution and their emission and absorption features are characterized by:

Absorption peak:	499.5 nm	2.482 eV
PL peak:	533 nm	2.326 eV
PL FWHM:	37.9 nm	165.3 meV
Stokes shift:	33.5 nm	156 meV

Figure A.5 shows the Don6 spectra for a solution with $c_{sol} = 3.3 \times 10^{-6}$ M. The Don6 QDs have a diameter of $d = 2.5$ nm, a quantum yield of 34% in solution and their emission and absorption features are characterized by:

Absorption peak:	507 nm	2.445 eV
PL peak:	538 nm	2.303 eV
PL FWHM:	40.1 nm	172 meV
Stokes shift:	31 nm	142 meV

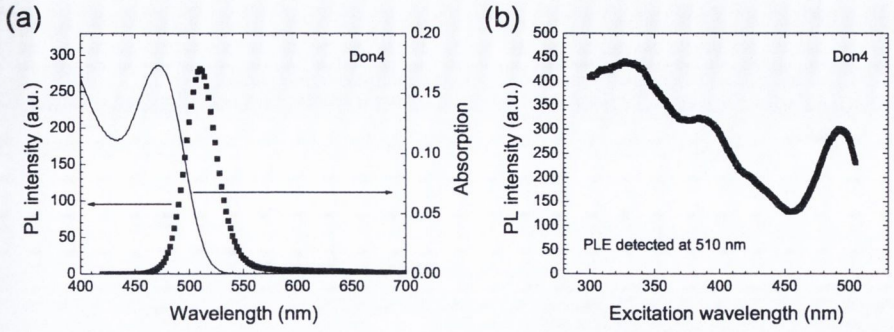


Figure A.3: (a) PL (squares, left-hand axis) and absorption spectra (line, right-hand axis) of a Don4 solution with $c_{sol} = 1.1 \times 10^{-5}$ M. (b) PLE spectrum of the Don4 solution recorded at 510 nm. The PL and PLE spectra were recorded with a 10% transmission filter.

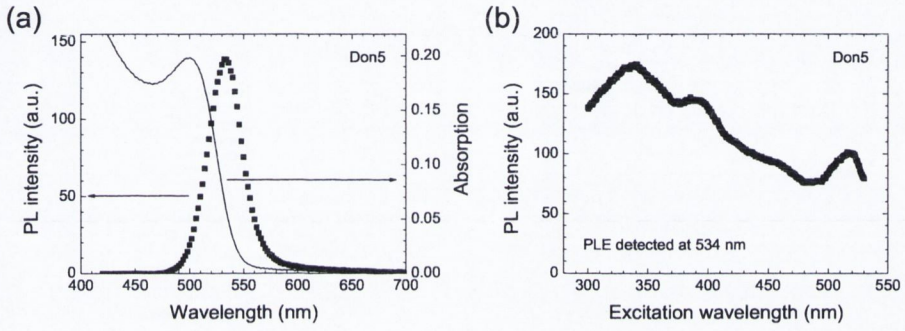


Figure A.4: (a) PL (squares, left-hand axis) and absorption spectra (line, right-hand axis) of a Don5 solution with $c_{sol} = 4.3 \times 10^{-6}$ M. (b) PLE spectrum of the Don5 solution recorded at 534 nm. The PL and PLE spectra were recorded with a 1% transmission filter.

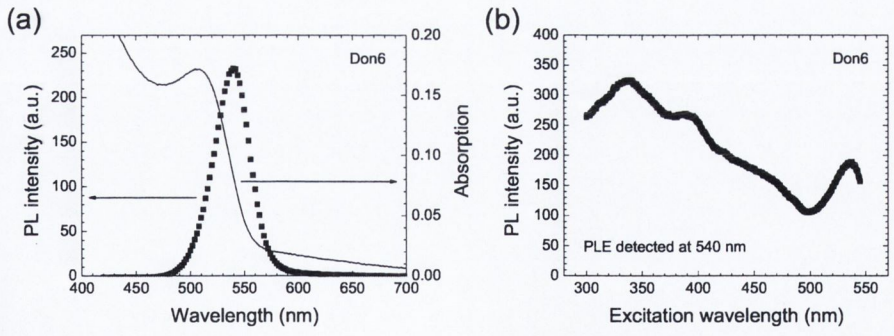


Figure A.5: (a) PL (squares, left-hand axis) and absorption spectra (line, right-hand axis) of a Don6 solution with $c_{sol} = 3.3 \times 10^{-6}$ M. (b) PLE spectrum of the Don6 solution recorded at 540 nm. The PL and PLE spectra were recorded with a 1% transmission filter.

Figure A.6 shows the Don7 spectra for a solution with $c_{sol} = 2.6 \times 10^{-6}$ M. The Don7 QDs have a diameter of $d = 2.9$ nm, a quantum yield of 37% in solution and their emission and absorption features are characterized by:

Absorption peak:	523 nm	2.371 eV
PL peak:	547.8 nm	2.263 eV
PL FWHM:	40 nm	165 meV
Stokes shift:	25 nm	108 meV

Figure A.7 shows the Don8 spectra for a solution with $c_{sol} = 2.6 \times 10^{-6}$ M. The Don8 QDs have a diameter of $d = 2.9$ nm, a quantum yield of 40% in solution and their emission and absorption features are characterized by:

Absorption peak:	525 nm	2.362 eV
PL peak:	553.5 nm	2.240 eV
PL FWHM:	45.5 nm	184 meV
Stokes shift:	28.5 nm	122 meV

Figure A.8 shows the Don9 spectra for a solution with $c_{sol} = 1.8 \times 10^{-6}$ M. The Don9 QDs have a diameter of $d = 3.1$ nm, a quantum yield of 43% in solution and their emission and absorption features are characterized by:

Absorption peak:	536 nm	2.313 eV
PL peak:	556.4 nm	2.228 eV
PL FWHM:	34.7 nm	139 meV
Stokes shift:	20 nm	85 meV

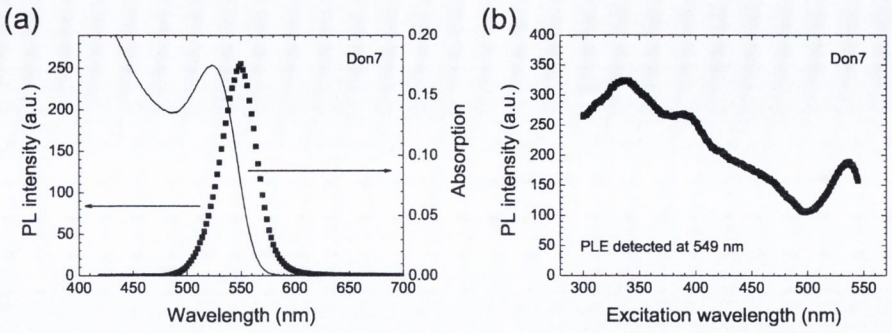


Figure A.6: (a) PL (squares, left-hand axis) and absorption spectra (line, right-hand axis) of a Don7 solution with $c_{sol} = 2.6 \times 10^{-6}$ M. (b) PLE spectrum of the Don7 solution recorded at 549 nm. The PL and PLE spectra were recorded with a 1% transmission filter.

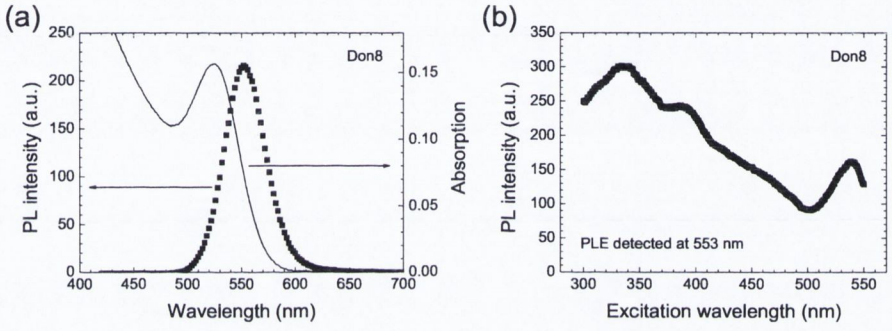


Figure A.7: (a) PL (squares, left-hand axis) and absorption spectra (line, right-hand axis) of a Don8 solution with $c_{sol} = 2.6 \times 10^{-6}$ M. (b) PLE spectrum of the Don8 solution recorded at 553 nm. The PL and PLE spectra were recorded with a 1% transmission filter.

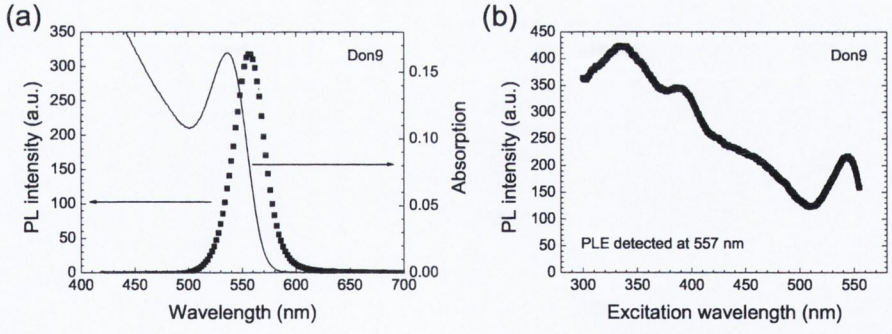


Figure A.8: (a) PL (squares, left-hand axis) and absorption spectra (line, right-hand axis) of a Don9 solution with $c_{sol} = 1.8 \times 10^{-6}$ M. (b) PLE spectrum of the Don9 solution recorded at 557 nm. The PL and PLE spectra were recorded with a 1% transmission filter.

Bibliography

[1] N. Lior, "Sustainable energy development: The present (2009) situation and possible paths to the future," *Energy*, vol. 35, p. 3976, 2010.

[2] D. J. C. MacKay, *Sustainable Energy - without the hot air*. UIT Cambridge, 2008. www.withouthotair.com.

[3] G. Meehl, T. Stocker, W. Collins, P. Friedlingstein, A. Gaye, J. Gregory, A. Kitoh, R. Knutti, J. Murphy, A. Noda, S. Raper, I. Watterson, A. Weaver, and Z.-C. Zhao, *Climate Change 2007: The Physical Science Basis. Contribution of Working Group I to the Fourth Assessment Report of the Intergovernmental Panel on Climate Change*, ch. 10 Global Climate Projections. Cambridge, United Kingdom and New York, NY, USA.: Cambridge University Press, 2007.

[4] WWF, "Climate change: Why we need to take action now." http://assets.panda.org/downloads/2_vs_3_degree_impacts_1oct06_1.pdf.

[5] J. Boe, A. Hall, and X. Qu, "September sea-ice cover in the arctic ocean projected to vanish by 2100," *Nature Geoscience*, vol. 2, p. 341, 2009.

[6] United Nations Framework Concention on Climate Change, "Kyoto protocol to the United Nations Framework Convention on Climate Change," 1998. http://unfccc.int/resource/docs/convkp/kpeng.pdf.

[7] United Nations Framework Concention on Climate Change, "Report of the ad hoc working group on long-term cooperative action under the convention on its eighth session, held in Copenhagen from 7 to 15 December 2009," 2010. http://unfccc.int/resource/docs/2009/awglca8/eng/17.pdf.

[8] R. Jones, "Nanotechnology, energy and markets," *Nature Nanotechnology*, vol. 4, no. 2, p. 75, 2009.

[9] T. Soga, *Nanostructured Materials for Solar Energy Conversion*. Amsterdam: Elsevier, 2006.

[10] W. U. Huynh, J. J. Dittmer, and A. P. Alivisatos, "Hybrid nanorod-polymer solar cells," *Science*, vol. 295, p. 2425, 2002.

[11] S. A. McDonald, G. Konstantatos, S. G. Zhang, P. W. Cyr, E. J. D. Klem, L. Levina, and E. H. Sargent, "Solution-processed PbS quantum dot infrared photodetectors and photovoltaics," *Nature Materials*, vol. 4, p. 138, 2005.

[12] T. Franzl, T. A. Klar, S. Schietinger, A. L. Rogach, and J. Feldmann, "Exciton recycling in graded gap nanocrystal structures," *Nano Letters*, vol. 4, no. 9, p. 1599, 2004.